

Controlling Non–Classical States of Light: Experimental Techniques in Quantum Information Science

Alexander (Sacha) Julien Kocsis
B.Sc., M.Sc.

School of Biomolecular and Physical Sciences
Faculty of Science, Environment, Engineering and Technology
Griffith University

Submitted in fulfilment of the requirements for the degree of
Doctor of Philosophy

January 2014

Abstract

The key task of transmitting quantum states encompasses a diverse array of techniques and applications. This thesis presents experimental work in optical quantum information science, focused on strategies for transmitting quantum states with high fidelity and security. The majority of the work in this thesis is in photonic quantum information science, although one experiment used continuous-variable states.

In the first experiment, the noiseless amplification of a photon polarisation qubit was realised, using delocalised single photon ancilla states and two single-mode amplification stages operating coherently. Artificial loss was applied to a single photon, to simulate a loss in a long-distance quantum transmission channel, and for the highest gain setting that was investigated, the qubit amplifier achieved a five-fold increase in transmission fidelity.

In the second experiment, linear optical techniques for distributing mode entanglement in a quantum network were studied. Quantum networks are based on a series of nodes, potentially separated by significant distances, and connected via quantum repeaters. Different quantum repeater architectures have been proposed, but they all include embedded distillation stages, which are based on linear optical techniques. We simulate two distinct quantum repeater scenarios, using different configurations of an entanglement swapping stage, a noiseless single-mode amplification stage, and loss. The performance of the amplification stage in overcoming the loss is characterised in both configurations. Significant distillation of mode entanglement is achieved in one configuration, and an increase in mode coherence is achieved in the other configuration.

Secure quantum communication is a highly active field of research. Device-independent protocols, such as device-independent quantum key distribution (DIQKD), offer guaranteed security even when devices are untrusted. This level of security comes at the cost of violating a Bell inequality, which is extremely challenging with current technology. A more feasible alternative is one-sided DIQKD, which involves the

violation of a steering inequality with less stringent requirements. In our experiment, we investigate a quantum-refereed steering protocol, in which both parties can be untrusted. We successfully demonstrate steering of a Bell-local state, and lay the groundwork for quantum-refereed one-sided DIQKD demonstrations. This type of protocol would seem to be the natural solution for common nodal networks, in which a secure central node communicates with many unsecured terminal nodes.

The final experiment demonstrated the coherent conversion of a squeezed vacuum state from 1550 nm, at telecommunication wavelength, to 532 nm. A frequency conversion efficiency of 89.2% was measured for a weak coherent state. Frequency conversion of non-classical optical states is an important step for interfacing various quantum technologies, or for entangling two spatially separated quantum memories, which generally operate in the visible frequency spectrum. In the end, half of a 1550 nm squeezed vacuum state was converted to 532 nm, and 1.4 dB of entanglement was measured between frequencies.

This work has not previously been submitted for a degree or diploma in any university. To the best of my knowledge and belief, the thesis contains no material previously published or written by another person except where due reference is made in the thesis itself.

Alexander (Sacha) Kocsis

List of Publications

- [1] S. Kocsis, B. Braverman, S. Ravets, M. J. Stevens, R. P. Mirin, L. K. Shalm and A. M. Steinberg, Observing the Average Trajectories of Single Photons in a Two-Slit Interferometer. *Science* **332**, 1170–1173 (2011)
- [2] S. Kocsis, G. Y. Xiang, T. C. Ralph and G. J. Pryde, Heralded noiseless amplification of a photon polarization qubit. *Nature Physics* **9**, 23–28 (2013)

Contents

List of Publications	vii
Contents	ix
List of Figures	xiii
List of Tables	xvii
1 Introduction	1
2 Classical and Quantum Theory of Light	7
2.1 Introduction	7
2.2 The Classical Wave Equation	8
2.3 Three-Wave Mixing Effects	11
2.3.1 Sum-Frequency Generation	12
2.3.2 Second Harmonic Generation	15
2.3.3 Difference-Frequency Generation	15
2.3.4 Spontaneous Parametric Down Conversion	17
2.4 Quantizing the Electromagnetic Field	20
2.4.1 Types of Electromagnetic Radiation	23
2.4.2 Correlation Measures	24
2.5 Encoding Qubits on Photons	26
2.5.1 Representing Quantum States of Light	28
2.5.2 Qubit Operations	32
2.5.3 Hong-Ou-Mandel Interference	34
2.6 Measuring Photonic Qubits	36
2.6.1 Single Photon Detection	36
2.6.2 Quantum State Tomography	36
2.7 Summary	37

3	Heralded Noiseless Amplification of a Photon Polarization Qubit	39
3.1	Acknowledgements	39
3.2	Introduction	39
3.3	Amplifying Quantum States	42
3.3.1	Strategies for Noiseless Amplification	43
3.3.2	Quantum Scissors	45
3.3.3	Generalised Quantum Scissors	48
3.4	Experimental Concept	50
3.5	Experimental Setup	52
3.5.1	SPDC Source	52
3.5.2	Noiseless Linear Amplification Stages	54
3.6	Experimental Results	55
3.6.1	Characterising the SPDC Source and Optical Circuit	55
3.6.2	Amplification	58
3.7	Discussion	63
4	Entanglement Distribution in Quantum Networks with Linear Optics	65
4.1	Acknowledgements	65
4.2	Introduction	65
4.3	Quantum Repeaters	66
4.3.1	Concept of Mode Entanglement	70
4.3.2	Entanglement of Formation and Concurrence	72
4.3.3	Teleporting Arbitrary Quantum States	73
4.3.4	Entanglement Swapping	74
4.4	Experimental Components	75
4.4.1	Photon Source Characterisation	76
4.4.2	HOM Interference Characterisation	76
4.5	Terminal Link Configuration	78
4.5.1	Experimental Concept	79
4.5.2	Linear Optical Circuit	81
4.5.3	Experimental Results	83
4.5.4	Summary	88
4.6	Intermediate Link Configuration	88
4.6.1	Experimental Concept	89
4.6.2	Linear Optical Circuit	90
4.6.3	Results	91
4.6.4	Summary	96

4.7	Discussion	97
5	Quantum-Refereed Steering for Enhanced Security	99
5.1	Acknowledgements	99
5.2	Introduction	99
5.3	Non-Classical Correlations	100
5.3.1	Einstein-Podolsky-Rosen Paradox and Entanglement	101
5.3.2	Bell Inequalities	103
5.3.3	Steering Inequalities	104
5.4	Experimental Concept	106
5.4.1	Quantum-Refereed Steering Protocol	107
5.4.2	Werner States	108
5.5	Experimental Setup	109
5.5.1	SPDC Sources	112
5.5.2	Bell State Analysis	113
5.6	Experimental Results	114
5.6.1	Characterising HOM Interference	114
5.6.2	Characterising the Werner State	115
5.6.3	Steering Inequality Measurement	118
5.7	Discussion	119
6	Frequency Conversion of Squeezed States	121
6.1	Acknowledgements	121
6.2	Introduction	121
6.3	Quantum Optical Theory in Continuous Variables	123
6.3.1	Sum-Frequency Conversion	123
6.3.2	Optical Parametric Amplification	124
6.3.3	Cavity Equation of Motion	127
6.3.4	Optical Parametric Oscillation	129
6.4	Experimental Techniques	131
6.4.1	Balanced Homodyne Tomography	132
6.4.2	Cavity Stabilization	133
6.5	Experimental Setup	135
6.5.1	Laser Preparation	135
6.5.2	Non-degenerate OPO	138
6.5.3	Squeezing Generation	140
6.5.4	Frequency Conversion	141
6.6	Results	142
6.6.1	Frequency Conversion Efficiency	142

6.6.2 Single-Mode Squeezing	144
6.7 Discussion	146
7 Conclusion	149
Appendices	
Appendix A Effect of State Renormalisation in NLA Experiments	157
Appendix B Dynamics of Optical Parametric Oscillators	163
References	167

List of Figures

2.1	Input and output frequency modes in sum-frequency generation . .	12
2.2	Phase matching function, and comparison of output field intensity for perfect and imperfect phase matching	14
2.3	Input and output frequency modes in second harmonic generation .	15
2.4	Input and output frequency modes in difference-frequency generation	15
2.5	Output field amplitudes in difference-frequency generation	17
2.6	Input and output frequency modes in spontaneous parametric down conversion	17
2.7	Energy and momentum conservation diagrams in SPDC	19
2.8	Side and front view of the down conversion cone from type-I non-collinear SPDC	20
2.9	Comparison of photon number probability distributions for thermal and coherent states, and for coherent states of different amplitude .	24
2.10	Comparison of $g^{(2)}$ functions for thermal, coherent and single photon states	25
2.11	Side view and front view of type-II spontaneous parametric down conversion	27
2.12	Systems of representing a qubit on the Poincaré sphere	28
2.13	Phase space representations of theoretical coherent and single photon states	31
2.14	Half wave plate, quarter wave plate, and an arbitrary polarisation rotation	33
2.15	Polarising beam splitter cube and beam displacer	34
2.16	Symmetric 50:50 beam splitter cube	34
3.1	Conceptual diagram of one-way DIQKD with a heralded qubit amplifier	41
3.2	Depiction of noiseless and quantum-limited amplification of coherent states in phase space	43
3.3	Original quantum scissors setup	45

3.4	Conceptual and experimental diagram of single-mode noiseless linear amplifier (NLA) based on generalised quantum scissors	49
3.5	Conceptual diagram of heralded noiseless qubit amplifier	51
3.6	Schematic representation of double-passed type-I SPDC setup	53
3.7	Experimental diagram of heralded noiseless qubit amplifier	55
3.8	Hong–Ou–Mandel interference between independent photons in NLA stage	56
3.9	Density matrices of the single photon subspaces for the six canonical polarisation inputs	60
3.10	Comparison of density matrix elements of the full state (vacuum and single photon), for the three different gain settings	62
4.1	Conceptual diagram of BDCZ quantum repeater architecture	67
4.2	Conceptual diagram of DLCZ quantum repeater architecture	68
4.3	Conceptual diagram of entanglement swapping	75
4.4	Hong–Ou–Mandel interference between signal mode and second ancilla mode, and between first and second ancilla modes	77
4.5	Conceptual diagram of terminal link configuration	78
4.6	Experimental diagram showing the optical circuit in the terminal link configuration	81
4.7	Comparison of input and output experimental density matrices for $G_m \simeq 2$ in the terminal link configuration of the setup	87
4.8	Comparison of input and output experimental density matrices for $G_m \simeq 3$ in the terminal link configuration of the setup	87
4.9	Comparison of input and output experimental density matrices for $G_m \simeq 4$ in the terminal link configuration of the setup	87
4.10	Conceptual diagram of intermediate link configuration	89
4.11	Experimental diagram showing the optical circuit in the intermediate link configuration	91
4.12	Experimental density matrix for intermediate link configuration	93
4.13	Experimental density matrix for saturated case in intermediate link configuration	94
4.14	Experimental density matrix for low loss case in intermediate link configuration	95
5.1	Hierarchy of entanglement classes	105
5.2	Hierarchy of entanglement verification tasks	106
5.3	One-sided DIQKD compared with and without a quantum referee . . .	107
5.4	Experimental setup for quantum-refereed steering protocol	111

5.5	Hong–Ou–Mandel interference in Bell state analyser	114
5.6	Density matrices of ideal and experimental Werner states	116
5.7	Experimental data for the steering payoff function	119
6.1	Input and output frequency modes in an optical parametric amplifier	124
6.2	Optical cavity in three–mirror ring configuration	127
6.3	Input and output frequency modes in an optical parametric oscillator	129
6.4	Conceptual diagram of a balanced homodyne tomography setup . . .	132
6.5	Simulated error signal in Pound–Drever–Hall stabilisation	134
6.6	Laser preparation stage of the setup	135
6.7	Full experimental setup for frequency conversion of a squeezed vacuum state, and measurement of two–mode continuous–variable entanglement	137
6.8	Non–degenerate optical parametric oscillator stage for producing 810 nm and 1550 nm pump fields	138
6.9	Conceptual diagram of cavity mode structure in a non–degenerate optical parametric oscillator; no resonance and resonance case	139
6.10	Conceptual diagram showing frequency mode overlap in a non–degenerate parametric oscillator, within phase matching bandwidth	140
6.11	Squeezed vacuum generation stage, consisting of second harmonic generation and parametric down conversion cavities	141
6.12	Frequency conversion stage, consisting of sum–frequency generation in a cavity	142
6.13	Measurement of frequency conversion efficiency, with curve fitted using nonlinear cavity simulation	144
6.14	Quadrature noise traces showing 1.1 dB squeezing and 2.9 dB anti–squeezing	145
6.15	Quadrature noise measurement while varying relative phase of local oscillator	146
A.1	Conceptual diagram of NLA stage	157
B.1	Optical parametric oscillator in a three–mirror ring cavity	163

List of Tables

3.1	Comparison of splitting ratio, nominal gain and measured gain at qubit amplifier output	59
3.2	Comparison of input fidelity and output fidelity for the three measured gain settings	61
4.1	Summary of experimental figures of merit from terminal link configuration	84
4.2	Summary of experimental figures of merit from terminal link configuration	92
5.1	Comparison of figures of merit for experimental Bell states	117

Acknowledgements

I would first like to thank my family, for their constant and unconditional support. Next, I would like to thank Geoff, for his good-natured enthusiasm for physics and his patience in explaining it to us, sometimes over and over again. I am of course also extremely grateful to everyone I've met at CQD. Studying physics has been fun and enriching in large part due to all the people I've met here.

Chapter 1

Introduction

The 1960s was a momentous decade in recent human history [1–3]. It was around this time that many of the conceptual foundations were laid for the current field of quantum information science. To be sure, the ideas that were germinating in the 1960s had important antecedents, and key concepts were developed later, but it is convenient to take this decade in the middle of the last century as a starting point to trace the development of quantum information science [4].

It was in 1961 that Maxwell’s demon was finally put to rest, by Landauer’s erasure principle [5]. Maxwell’s demon is the name given to a thought experiment first proposed by Maxwell in 1871 [6, 7]. The second law of thermodynamics states that the entropy of a closed system cannot decrease, but Maxwell imagined a machine that would apparently violate this law. He imagined a gas cylinder initially at thermal equilibrium, with a central partition dividing it into two halves. A microscopic “demon” operates a small gate at the partition, which is the only way to move between the halves of the cylinder. The demon could, in principle, individually separate the fast- and slow- moving gas particles: when a particle with a higher velocity than the ensemble mean approaches the gate from the left, the demon opens the gate and lets it through, closing the gate after it. Over time, the total entropy in the cylinder would decrease, and violate the second law of thermodynamics. Szilard considered the paradox in terms of an idealised heat engine, from which one could extract work by making appropriate measurements, and was the first to explicitly point out the connection between information and physics [8]. The paradox persisted until Landauer’s insight that the demon must measure each particle to determine its velocity, and store that information in a memory. Memory is always finite, so the demon must eventually erase some information stored in memory in order to

make new measurements. Erasing information increases entropy, and an analysis showed that this entropy increase must be at least as much as the entropy decrease due to the demon's actions, thus satisfying the second law of thermodynamics [4]. This analysis prompted Landauer to make his famous statement that “information is physical” [9, 10].

An earlier pioneering result highlighting the role of information in physics is the work by Shannon from 1948 on communication capacity [11]. Shannon quantified the physical resources required to store classical information, and how much information can reliably be transmitted across a noisy classical communication channel. The modern theory of information and communication is based on his mathematical definition of the concept of information

In 1964, Bell introduced a theorem [12, 13] concerning the famous EPR paradox [14], proving that a local hidden variable (LHV) model of nature (favoured by Einstein, Podolsky and Rosen) was incompatible with the predictions of quantum mechanics. The correlations predicted by any LHV model are limited by inequalities (now known as Bell inequalities), which are violated in quantum theory. In other words, a LHV model can reproduce measurement results predicted by quantum theory some of the time, but it cannot mimic all possible quantum correlations in an experiment. This compelled a re-appraisal of the assumptions of local realism in the original EPR paradox, as Bell's theorem confirmed that one of them must be abandoned.

In a series of papers in 1963, Glauber defined the concept of optical coherence in quantum mechanical terms [15, 16]. In their experiments on stellar interferometry in 1956, Hanbury Brown and Twiss had observed correlations between the fluctuations in photocurrents of two independent detectors illuminated by the same star. This motivated Glauber to investigate the photon statistics of radiation fields, and his results can be considered the beginning of the field of quantum optics [17]. Around that same time, the first laser system was built by Maiman in 1960 [18], based on ideas from a few years earlier due to Schawlow, Townes [19], Basov and Prokhorov [20]. The invention of the laser heralded the new field of nonlinear optics, which is the study of phenomena due to the modification of optical properties of a material system in the presence of light [21].

Within a relatively short period of time in the mid-20th century, the role of information in physics started to gain prominence, Bell's theorem re-framed the ongoing discussion about permissible models of nature, and the fields of quantum optics and nonlinear optics had emerged. In subsequent decades, these sub-fields of physics would intersect and merge in fruitful and sometimes surprising ways. By the 1980s

the idea that computation is limited by the laws of physics had been developed further [22]; in 1982 Feynman was the first to propose that simulating a quantum mechanical system would require building a quantum computer [23]. The first measurements of non-classical states of light [24] paved the way for a series of experiments demonstrating the violation of a Bell inequality; the most famous of these are the 1981–2 Aspect experiments [25–27].

A significant development in quantum optics was the first observation of interference between two single photons by Hong, Ou and Mandel in 1987 [28]. This is a purely non-classical phenomenon, now known as the Hong-Ou-Mandel (HOM) effect, and is the only known example of the interference of single photons¹. For the two photons to interfere at a 50:50 beam splitter, they must be mode-matched in all degrees of freedom, effectively making them indistinguishable. Feynman’s simple prescription [29] for calculating the probability of a certain outcome can explain the HOM effect: since the two photons are indistinguishable at the beam splitter, their probability *amplitudes* for reflection and transmission are added, and the absolute square of the result gives the probability of detecting photons in each output port. The probability amplitude for finding a photon in each output port is zero, and a photon “bunching” effect is observed. This can be thought of as another example of information (in the form of distinguishability) playing a fundamental role in physics².

One of the first great successes in the nascent field of quantum information was a theoretical proposal for teleporting an unknown quantum state, using an entanglement resource and classical communication [33]. The protocol included a joint Bell state measurement, and it was realised that this could be achieved using the recently discovered HOM effect [34, 35], which can project two photons into an anti-symmetric entangled state, *i.e.* the singlet state. The experimental demonstrations followed shortly after [36, 37], and was extended to demonstrate entanglement swapping in 1998 [38]. In any experiment involving quantum teleportation, no matter or energy is every really teleported; it is only a quantum state that is ever teleported, and a quantum state is essentially information.

Another milestone in the early history of quantum information science was the no-cloning theorem, developed in 1982 by Wootters and Zurek [39], and independently by Dieks [40]. In both papers, the point was made that a quantum

¹Cross-phase modulation in a Kerr medium is a relatively weak effect, and has so far not been demonstrated for single photons.

²The primacy of distinguishing information in the HOM effect is emphasised in “quantum eraser” experiments [30–32], in which the single photons are not mode-matched in one degree of freedom at the beam splitter, but distinguishing information is erased just before detection, to recover interference.

cloning device would, in principle, allow for faster-than-light communication. It was shown, however, that the linearity of quantum mechanics rules out the possibility of any deterministic quantum cloning device. In the quantum teleportation protocol, the initial unknown state is destroyed by measurement (so that no two copies of the state ever exist at once), and one bit of classical communication is required to be sent to the other party, confirming that communication is limited by the speed of light. Wootters and Zurek connected quantum cloning with noiseless amplification, which had implications in quantum state discrimination as well as quantum communication.

In spite of its simplicity, the no-cloning theorem has had far-reaching consequences. The first quantum cryptography scheme, known as BB84 [41], is a quantum key distribution (QKD) protocol proposed in 1984, that consists of encoding classical information on quantum states, and transmitting them over a public channel. The no-cloning theorem guarantees that, provided the error rate in transmission is lower than a certain threshold, there is no possibility of an adversary eavesdropping on the communication. The first quantum communication protocol to use entanglement was proposed in 1991 [42], and guaranteed communication security with the violation of a Bell inequality. Quantum communication has since become one of the most well-developed and promising areas of research in optical quantum information science.

The revolutionary insight that efficient quantum computation is possible with linear optics, using non-classical interference in the HOM effect and single photon detection, was due to Knill, Laflamme and Milburn in 2001 [43]. In the paper, it was shown that single qubit rotations and controlled-NOT (CNOT) gates between qubits were enough for scalable linear optical quantum computing (LOQC). Not long after this, the first photonic CNOT gate was experimentally demonstrated and characterised [44]. By the beginning of the twenty first century, the field of quantum information science had been firmly established, and incorporated principles and techniques from diverse disciplines.

The experiments in this thesis investigate techniques to enhance quantum communication in various ways. Quantum states are very fragile, and their purity degrades rapidly in a noisy environment, such as a realistic quantum transmission channel. Highly pure quantum states are required in quantum logic gates, and for most other quantum information tasks. Security is also undermined by excessive loss and mixture in transmission, which is one of the main goals of quantum communication. Finally, quantum communication serves as a link between various other quantum information systems, such as sources of non-classical light and quantum memories.

To link these different technologies, the properties of quantum states will need to be transformed in a highly controlled and precise way.

Chapter 2 presents an overview of some of the theoretical background necessary to understand the experiments in subsequent chapters. The chapter begins with a brief review of nonlinear optics, which is fundamental to the generation of non-classical states of light. In the rest of the chapter, key terms and concepts in experimental quantum information science are introduced. General details are presented in Chapter 2, while more specific theoretical background can be found in the subsequent chapters, as it relates to individual experiments.

Chapter 3 presents the experimental realisation of a heralded noiseless qubit amplifier. A qubit, a two-mode quantum state, is the quintessential model for encoding quantum information. Signal amplification, which is ubiquitous in classical communication, is limited in the quantum regime by the no-cloning theorem. A non-deterministic strategy closely related to quantum teleportation is used to overcome the limitation set by quantum mechanics. The qubit amplifier, though probabilistic, is heralded, and thus has direct applicability to device-independent quantum key distribution. A nearly five-fold increase in transmission fidelity is measured at the qubit amplifier output.

An experimental investigation of entanglement distribution with linear optics in quantum networks is described in Chapter 4. Transmission loss in a quantum network is simulated by a variable attenuator and an entanglement swapping stage, and is compensated using a single-mode noiseless amplification stage. The setup is operated in two distinct configurations: the first configuration simulates loss before the terminal node of a quantum repeater, and the second simulates loss between intermediate nodes. Distribution of high-quality entanglement is required in quantum networks, and our amplification protocol distils mode entanglement that has been degraded through transmission loss. In the first configuration, the measured concurrence of the mode-entangled state was three times higher with amplification than it would have been otherwise. The results indicate that this is a promising and robust technique that would be reasonably straight-forward to integrate into future quantum networks.

A quantum-refereed steering protocol is realised in Chapter 5. The experimental violation of a steering inequality is directly related to one-sided device-independent QKD (DIQKD). Violation of a steering inequality is an asymmetric task, in which an external referee must trust one of the parties. This can potentially undermine the security of the protocol, if Alice and Bob are in a pre-arranged conspiracy, or

if Bob's measurement device has somehow been compromised without his knowing. With the addition of quantum randomness by the referee, neither Alice nor Bob need to be trusted. A steering inequality is violated in this quantum-refereed scenario, using a Bell-local Werner state. This protocol, which has significantly less strict requirements than full DIQKD, is well-suited to situations where a secure central node in a network communicates with multiple untrusted terminal nodes.

The experiment in Chapter 6 concerns the frequency conversion of a squeezed state from 1550 nm to 532 nm. Converting the frequency of a squeezed state from telecommunication frequencies, where transmission loss is lowest, to visible frequency is a necessary step for interfacing optical continuous-variable states with quantum memories. The frequency conversion is a coherent process based on difference frequency generation, making it tunable in principle.

Chapter 7 concludes this thesis. The main results are summarised and put into context, and future directions for research are discussed.

Chapter 2

Classical and Quantum Theory of Light

2.1 Introduction

James Clerk Maxwell unified electricity and magnetism in 1873, and proposed that light is an electromagnetic wave [45, 46]. The modern theory of classical electrodynamics begins with Maxwell’s famous four equations. At the beginning of the twentieth century, one of the outstanding questions in physics was how to explain the “ultraviolet catastrophe” in the blackbody radiation spectrum. Max Planck postulated in 1900 that electromagnetic energy could only be absorbed and emitted in discrete quanta, and introduced the Planck constant h relating energy to radiation frequency [47]. This revolutionary idea inspired Albert Einstein to propose, in 1905, that all electromagnetic radiation energy is quantised, mainly in order to explain the photoelectric effect [48].

In the late 1950’s, the maser [49] and then lasers [18] were being demonstrated for the first time in laboratories. The genesis of nonlinear optics came after the invention of the laser, as only a laser was capable of producing light at high enough intensities in the optical regime to observe nonlinear effects in materials. Since then, the related field of quantum optics has progressed immensely, thanks in large part to the possibility of studying light–matter interactions with strong coherent fields, as well as the ability to generate quantum states of light using nonlinear materials.

This thesis focuses on generating, manipulating and measuring non–classical states of light, particularly in the context of the relatively new field of quantum information

science. This chapter presents an overview of the theoretical background that will be useful for understanding the experimental work discussed in subsequent chapters. To begin with, elements of classical nonlinear optics are discussed, and the connection with generating non-classical states of light will be discussed. Canonical quantisation is introduced next, and the statistical properties of different categories of electromagnetic radiation are described. In the following section, encoding qubits on single photons and physically implementing qubit operations are considered. Finally, some details concerning the detection of single photons and reconstructing their quantum states are presented.

Three of the four main chapters in this thesis describe experiments in photonic quantum information science, or quantum information with “discrete variables”. The non-classical states in these experiments are single photons, and linear optical components form the main experimental apparatus. After the single photons have been created, the only nonlinear element in the experiments are the single photon counting modules (SPCM) that detect single photons at the end of an optical circuit. This background theory in this chapter is predominantly intended to present background theory relevant to discrete variable quantum information. One chapter (Chapter 5) presents the results of an experiment using continuous variables. Most of the material in this chapter is relevant to that experiment, and the first few sections of Chapter 5 (as well as Appendix B) present additional background that will be helpful to understanding quantum optics in cavities.

2.2 The Classical Wave Equation

Here, and in Section 2.3, we closely follow the approach in [21]. Maxwell’s equations fully describe classical electromagnetic fields and associated phenomena. Their differential form (in SI units) is:

$$\nabla \cdot \mathbf{D} = \rho \qquad \nabla \cdot \mathbf{B} = 0 \qquad (2.1 \text{ a,b})$$

$$\nabla \times \mathbf{E} = -\frac{\partial \mathbf{B}}{\partial t} \qquad \nabla \times \mathbf{H} = \frac{\partial \mathbf{D}}{\partial t} + \mathbf{J} \qquad (2.1 \text{ c,d})$$

The vector fields \mathbf{E} and \mathbf{B} are the electric and magnetic fields, while \mathbf{D} is the electric displacement field, and \mathbf{H} is the magnetising field due to magnetic poles. The symbol ρ denotes distribution of free charge, and \mathbf{J} denotes free current. We are interested in the case where there are no free charges or currents, and thus:

$$\rho = 0 \text{ ,} \qquad \mathbf{J} = 0 \text{ .} \qquad (2.2 \text{ a,b})$$

We also assume that the material is not magnetic, which means

$$\mathbf{B} = \mu_o \mathbf{H} , \quad (2.3)$$

where μ_o denotes the permeability of free space.

The electric displacement field \mathbf{D} is the field arising from interaction of light with the material. It is related to the electric field in the following way:

$$\mathbf{D} = \epsilon_o \mathbf{E} + \mathbf{P} , \quad (2.4)$$

where ϵ_o denotes the permittivity of free space. In (2.4), there is a part proportional to the original field \mathbf{E} , and a part proportional to the polarisation vector \mathbf{P} . The polarisation vector describes the motion of atomic dipoles in the material. These dipoles individually behave as microscopic oscillators, which can collectively produce new electromagnetic radiation. Many interesting effects in nonlinear optics can be explained classically, without quantising the electromagnetic field. To derive several nonlinear effects in the next sections, we will treat the polarisation vector as a perturbative term in the equation of motion for the material. The polarisation vector can therefore be described as a power series expansion in \mathbf{E} :

$$\mathbf{P} = \epsilon_o [\chi^{(1)} \mathbf{E} + \chi^{(2)} \mathbf{E}^2 + \chi^{(3)} \mathbf{E}^3 \dots] \quad (2.5a)$$

$$= \epsilon_o \sum_{n=1}^{\infty} \chi^{(n)} \mathbf{E}^n \quad (2.5b)$$

$$= \sum_{n=1}^{\infty} \mathbf{P}^{(n)} . \quad (2.5c)$$

It is convenient to separate \mathbf{P} and \mathbf{D} into their linear and nonlinear components:

$$\mathbf{P} = \mathbf{P}^{(1)} + \mathbf{P}^{(NL)} , \quad \mathbf{D} = \mathbf{D}^{(1)} + \mathbf{D}^{(NL)} , \quad (2.6 \text{ a,b})$$

where

$$\mathbf{D}^{(1)} = \epsilon_o \mathbf{E} + \mathbf{P}^{(1)} . \quad (2.7)$$

Assuming that the material is lossless, the relationship between $\mathbf{D}^{(1)}$ and \mathbf{E} can be written in terms of a dielectric tensor:

$$\mathbf{D}^{(1)} = \epsilon_0 \underline{\epsilon}^{(1)} \cdot \mathbf{E} . \quad (2.8)$$

The expression is simplified in the case of an isotropic material, as the dielectric tensor reduces to a scalar quantity: $\underline{\epsilon}^{(1)} = \epsilon^{(1)} = 1 + \chi^{(1)}$. The higher order terms in

\mathbf{P} generate the nonlinear effects that we will be interested in. The relative strength of the $\mathbf{P}^{(NL)}$ terms are typically very small, which is consistent with the observation that high field intensities are required to observe any nonlinear effects. Here we will only be concerned with nonlinear effects up to order $\chi^{(2)}$, and higher order effects will be neglected.

Maxwell's wave equation can be derived in a straightforward way from the four equations in (2.1). Taking the curl of the equation for the electric field \mathbf{E} in (2.1 c,d), the order of the space and time derivatives are interchanged in the right-hand side of the resulting equation. Next, the equation for the magnetising field \mathbf{H} in (2.1 c,d) is substituted in, by noting its relation to \mathbf{B} in (2.3). The free current term \mathbf{J} vanishes due to (2.2). Finally, (2.4) is substituted in, to obtain:

$$\nabla \times \nabla \times \mathbf{E} + \frac{1}{c} \frac{\partial^2}{\partial t^2} \mathbf{E} = -\mu_o \frac{\partial^2}{\partial t^2} \mathbf{P}. \quad (2.9)$$

Recalling the vector calculus identity

$$\nabla \times \nabla \times \mathbf{E} = \nabla(\nabla \cdot \mathbf{E}) - \nabla^2 \mathbf{E} \quad (2.10)$$

and noting that the contribution of the $\nabla(\nabla \cdot \mathbf{E})$ term can be neglected in the paraxial or slowly varying amplitude approximation, equation (2.9) becomes

$$\nabla^2 \mathbf{E} - \frac{1}{c^2} \frac{\partial^2}{\partial t^2} \mathbf{E} = \mu_o \frac{\partial^2}{\partial t^2} \mathbf{P}. \quad (2.11)$$

In general, optical materials will be dispersive, meaning that the dielectric tensor will be frequency dependent. The frequency components of the electric, linear displacement, and polarisation fields should be considered separately, and a plane wave solution is tested:

$$\mathbf{E}(\mathbf{r}, t) = \sum_n \mathbf{E}_n(\mathbf{r}, t) = \sum_n [\mathcal{E}_n(\mathbf{r})e^{-i\omega_n t} + \mathcal{E}_n^*(\mathbf{r})e^{i\omega_n t}] \quad (2.13a)$$

$$\mathbf{D}^{(1)}(\mathbf{r}, t) = \sum_n \mathbf{D}_n^{(1)}(\mathbf{r}, t) = \sum_n [\mathcal{D}_n^{(1)}(\mathbf{r})e^{-i\omega_n t} + \mathcal{D}_n^{*(1)}(\mathbf{r})e^{i\omega_n t}] \quad (2.13b)$$

$$\mathbf{P}^{(NL)}(\mathbf{r}, t) = \sum_n \mathbf{P}_n^{(NL)}(\mathbf{r}, t) = \sum_n [\mathcal{P}_n^{(NL)}(\mathbf{r})e^{-i\omega_n t} + \mathcal{P}_n^{*(NL)}(\mathbf{r})e^{i\omega_n t}] \quad (2.13c)$$

Taking into account the frequency modes of these three fields, and the frequency dependence of the dielectric tensor, equation (2.11) can be re-written as:

$$\nabla^2 \mathbf{E}_n(\mathbf{r}, t) - \frac{\epsilon^{(1)}(\omega_n)}{c^2} \frac{\partial^2}{\partial t^2} \mathbf{E}_n(\mathbf{r}, t) = \mu_o \frac{\partial^2}{\partial t^2} \mathbf{P}_n^{(NL)}(\mathbf{r}, t) \quad (2.14)$$

This is the wave equation for an isotropic, dispersive nonlinear material. Each frequency mode separately satisfies (2.14), with an explicitly frequency dependent dielectric tensor. The equation has the form of a driven harmonic oscillator, with the nonlinear polarisation response of the medium on the right hand side acting as the source term. Without the source term, (2.14) simplifies to describe free waves propagating with the velocity $v = c/\sqrt{\epsilon^{(1)}}$.

2.3 Three-Wave Mixing Effects

Three-wave mixing processes are mediated by $\chi^{(2)}$, the second-order nonlinear susceptibility of the material. Some crystals are known as centrosymmetric, or equivalently they are said to have inversion symmetry. This means the medium is invariant under spatial inversion of its atomic wave functions. From (2.5), this implies that $\mathbf{P}^{(n)} = -\mathbf{P}^{(n)}$ for all even n , which can only be true if $\chi^{(n)} = 0$. Therefore even-ordered nonlinear susceptibilities, including $\chi^{(2)}$, only occur in noncentrosymmetric materials, and this is the type of material necessary to observe three-wave mixing effects.

We consider the general case where the incident field is composed of two distinct frequency components: ω_1 and ω_2 . The nonlinear polarisation is the source term in the wave equation (2.14), and as we are concerned with terms up to order $\chi^{(2)}$, this driving term is proportional to \mathbf{E}^2 . There will be five different frequency components from \mathbf{E}^2 contributing to $\mathbf{P}^{(2)}$, meaning that radiation at any of these frequencies can be emitted due to interactions in the medium:

$$\omega_1 + \omega_2 \qquad |\omega_1 - \omega_2| \qquad (2.15 \text{ a,b})$$

$$2\omega_1 \qquad 2\omega_2 \qquad (2.15 \text{ c,d})$$

$$0 \qquad (2.15 \text{ e})$$

Thus, the second-order nonlinear susceptibility can mix two waves of different frequencies, and generate a third wave. The frequencies (2.15 a,b) are the (a) *sum*-frequency and (b) *difference*-frequency, while (2.15 c,d) are the second harmonics of the fundamental frequencies. Finally, (2.15 e) is a static term known as optical rectification, which represents a constant polarisation in the material induced by the light field. The form that the three-wave mixing process takes depends on what fields are provided as inputs, the phase matching conditions, and what field is taken to be the output.

2.3.1 Sum-Frequency Generation

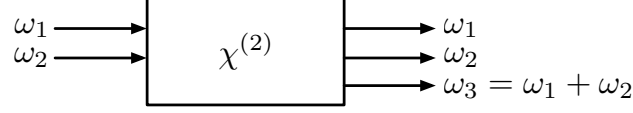


Figure 2.1: Input and output frequency modes in sum-frequency generation (SFG).

In sum-frequency generation (SFG), fields at two distinct frequencies, ω_1 and ω_2 , interact in the material to generate a third field at the sum-frequency ω_3 :

$$\omega_3 = \omega_1 + \omega_2 , \quad (2.16)$$

The frequency-dependent wave equation (2.14) governs the dynamics of the interaction. Since we can think of the polarisation source term as a small perturbation to the free-space evolution, we can propose a plane-wave solution to (2.14), assumed to be propagating in the $+z$ direction with frequency ω_3 :

$$E_3(z, t) = \mathcal{E}_3(z)e^{-i\omega_3 t} + \mathcal{E}_3^*(z)e^{i\omega_3 t} \quad (2.17a)$$

$$= A_3(z)e^{i(k_3 z - \omega_3 t)} + A_3^*(z)e^{-i(k_3 z - \omega_3 t)} \quad (2.17b)$$

The wavenumber k and linear index of refraction n are

$$k_3 = \frac{n_3 \omega_3}{c} , \quad n_3^2 = \epsilon^{(1)}(\omega_3) , \quad (2.18)$$

and A_3 is the complex amplitude of the wave. The nonlinear polarisation in sum-frequency generation can be expressed as the following scalar relationship:

$$P_3 = 4\epsilon_0 \chi A_1 A_2 e^{i(k_1 + k_2)z} \quad (2.19)$$

where $\chi \propto \chi^{(2)}$ is the effective nonlinear coupling constant. Substituting (2.19) into the wave equation (2.14) gives the expression

$$\frac{d^2 A_3}{dz^2} + 2ik_3 \frac{dA_3}{dz} = \frac{-4\chi\omega_3^2}{c^2} A_1 A_2 e^{i(k_1 + k_2 - k_3)z} \quad (2.20)$$

We can now invoke the slowly varying amplitude approximation again, but now the approximation can be quantified. It is valid as long as

$$\left| \frac{d^2 A_3}{dz^2} \right| \ll \left| k_3 \frac{dA_3}{dz} \right| \quad (2.21)$$

meaning that the amplitude of the field does not change over wavelength distance scales. This assumption, generally true, allows us to neglect the second-order derivative in (2.20), and we are left with an expression describing the spatial evolution of the ω_3 field amplitude, as a result of its coupling to the ω_1 and ω_2 waves:

$$\frac{dA_3}{dz} = \frac{2i\chi\omega_3^2}{k_3c^2}A_1A_2e^{i\Delta kz} \quad (2.22)$$

Similarly, the ω_1 and ω_2 field amplitudes evolve as:

$$\frac{dA_1}{dz} = \frac{2i\chi\omega_1^2}{k_1c^2}A_3A_2^*e^{-i\Delta kz} \quad (2.23a)$$

$$\frac{dA_2}{dz} = \frac{2i\chi\omega_2^2}{k_2c^2}A_3A_1^*e^{-i\Delta kz} \quad (2.23b)$$

These are known as the coupled-wave equations for sum-frequency generation, as the evolution of one field's amplitude explicitly depends on the amplitudes of the other two fields. We have introduced a quantity known as the wave vector mismatch:

$$\Delta k = k_1 + k_2 - k_3 \quad (2.24)$$

In general (2.24) is a vectorial relationship. Here, we are limiting the discussion to the z direction, and the the z components can therefore be written in a scalar equation. The vectorial nature of (2.24), however, is critical to the upcoming discussion of collinear and non-collinear SPDC in Section 2.3.4. For perfect phase matching, $\Delta k = 0$, the amplitude of the sum-frequency wave increases linearly with z , the distance propagated through the nonlinear medium. The argument of the complex wave function in (2.17) is $k_3z \pm \omega_3t$, and the frequency matching condition $\omega_3 = \omega_1 + \omega_2$ and the perfect phase matching condition $k_3 = k_1 + k_2$ ensure that they interact over an extended duration of time and region in space. Phase matching will also specify the direction in which the sum-frequency wave is emitted from the material. The amplitude at the end of the medium is:

$$A_3(L) = \frac{2i\chi\omega_3^2A_1A_2}{k_3c^2} \int_0^L e^{i\Delta kz} dz \quad (2.25a)$$

$$= \frac{2i\chi\omega_3^2A_1A_2}{k_3c^2} \left(\frac{e^{i\Delta kL} - 1}{i\Delta k} \right) \quad (2.25b)$$

The intensity of the field is the magnitude of the time-averaged Poynting vector:

$$I_3(L) = 2n_3\epsilon_0 c |A_3|^2 \quad (2.26a)$$

$$= \frac{8(\chi)^2 \omega_3^2 I_1 I_2}{n_1 n_2 n_3 \epsilon_0 c^2} L^2 \text{sinc}^2 \left(\frac{\Delta k L}{2} \right) \quad (2.26b)$$

This is the solution in the simple limit where the two input pump fields are undepleted throughout the interaction. It is clear that, were it not for the imperfect phase matching, the sum-frequency output intensity would increase linearly with the input field intensities, and quadratically with the length of the material. The coherence length of the three-wave interaction is commonly defined as:

$$L_{coh} \equiv \Delta k / 2 . \quad (2.27)$$

This is the length over which the three-wave mixing process will stay in phase. The phase matching function has the following form: If the length of the material

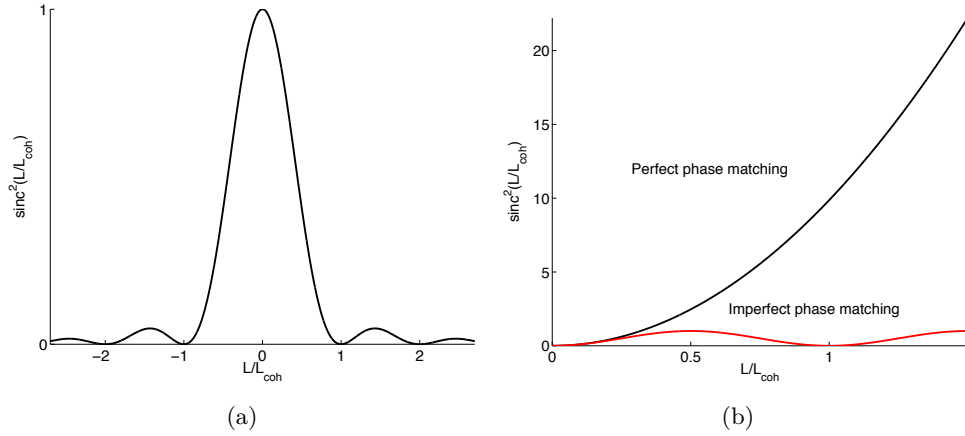


Figure 2.2: (a) Phase matching function. (b) Output intensity $I_3(L)$ for perfect and imperfect phase matching.

L is greater than L_{coh} , then the output wave gets out of phase with its driving polarisation, and energy flows from ω_3 back to the ω_1 and ω_2 fields. There is an oscillatory behaviour, as the three waves come in and out of phase over multiples of this coherence length. By contrast, for perfect phase matching the output power of the sum-frequency field simply increases quadratically.

2.3.2 Second Harmonic Generation

Second harmonic generation (SHG) is the special degenerate case of sum-frequency generation:

$$\omega_1 = \omega_2 = \omega, \quad \omega_3 = 2\omega. \quad (2.28 \text{ a,b})$$

The ω field is the strong pump field at the fundamental frequency, and some energy from the pump field is up-converted to a field at the second harmonic frequency 2ω .

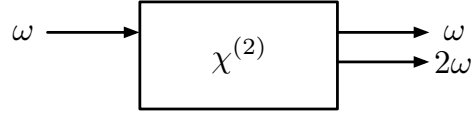


Figure 2.3: Input and output frequency modes in second harmonic generation (SHG).

The perfect phase matching condition is achieved when $2k_\omega = k_{2\omega}$. Since $\Delta k L/2$ is the argument of the phase matching function, it is apparent that the greater the length of the material L , the narrower the phase matching function (Figure 2.2(a)) becomes. In other words, the conversion efficiency is more sensitive to the phase mismatch Δk for a longer material, as long as $L \leq L_{coh}$.

2.3.3 Difference-Frequency Generation

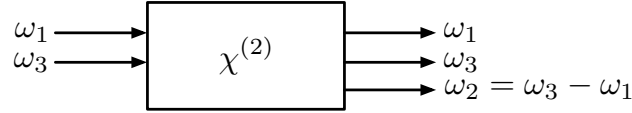


Figure 2.4: Input and output frequency modes in difference-frequency generation (DFG).

Difference-frequency generation (DFG) is the three-wave mixing process described by (2.15), in which the inputs are two fields at the frequencies ω_1 and ω_3 , and the output is the difference-frequency field at $\omega_2 = \omega_3 - \omega_1$, where ω_1 is taken to be the lower frequency field. For simplicity, we assume that the ω_3 field is a strong pump field, and is undepleted throughout the interaction, while the ω_1 field is a relatively weak input field that can be depleted. We begin by recalling the equations (2.22) and (2.23a), which determine the evolutions of the field amplitudes in three-wave mixing. In DFG, the phase mismatch is now:

$$\Delta k = k_3 - k_1 - k_2 \quad (2.29)$$

In general, we assume imperfect phase matching. As we expect the coupled $A_1(z)$ and $A_2(z)$ fields to exhibit similar spatial variation, we test solutions to (2.23a) and (2.22) of the following form:

$$A_1(z) = (Fe^{igz} + Ge^{-igz})e^{-i\Delta kz/2} \quad (2.30a)$$

$$A_2(z) = (Ce^{igz} + De^{-igz})e^{-i\Delta kz/2} \quad (2.30b)$$

Substituting these test solutions into (2.23a) and (2.22), and separately collecting terms in e^{igz} and e^{-igz} , yields two simultaneous equations for C and F , which can be written in matrix form:

$$\begin{pmatrix} i(g - \Delta k/2) & -K_1 \\ K_2^* & i(g + \Delta k/2) \end{pmatrix} \begin{pmatrix} F \\ C \end{pmatrix} = 0 \quad (2.31)$$

For convenience, we have defined the new constants:

$$K_j \equiv \frac{2i\chi\omega_j^2 A_3}{k_j c^2}, \quad (2.32)$$

where $j \in \{1, 2\}$ indexes the frequency modes. In order for the set of equations in (2.31) to have a solution, the determinant of the coefficient matrix must vanish. This sets the quantity g :

$$g = \sqrt{K_1 K_2^* - \Delta k^2/4} \quad (2.33)$$

Using the simultaneous equations for F and C , as well as for G and D , and combining them with the initial conditions

$$A_1(0) = F + G \quad A_2(0) = C + D \quad (2.34)$$

the coefficients can be derived for the general solution:

$$A_1(z) = \left[A_1(0) \left(\cosh(gz) - \frac{i\Delta k}{2g} \sinh(gz) \right) + \frac{K_1}{g} A_2^*(0) \sinh(gz) \right] e^{i\Delta kz/2} \quad (2.35a)$$

$$A_2(z) = \left[A_2(0) \left(\cosh(gz) - \frac{i\Delta k}{2g} \sinh(gz) \right) + \frac{K_2}{g} A_1^*(0) \sinh(gz) \right] e^{i\Delta kz/2} \quad (2.35b)$$

To more easily interpret this solution, we can make simplifying assumptions. We consider the case of perfect phase matching, $\Delta k = 0$, and the initial condition where there is no difference-frequency wave incident on the medium ($A_2(0) = 0$, $A_1(0) =$

arbitrary). The equations (2.35) become:

$$A_1(z) = A_1(0)\cosh(gz) \quad (2.36a)$$

$$A_2(z) = i\sqrt{\frac{n_1\omega_2}{n_2\omega_1}} \frac{A_3}{|A_3|} A_1^*(0)\sinh(gz) \quad (2.36b)$$

The size of the amplitudes $|A_1(z)|$ and $|A_2(z)|$ grow monotonically with increasing z . As before, the effect of imperfect phase matching would be to decrease the difference-frequency field amplitude. In contrast to SFG, where the fields exhibit

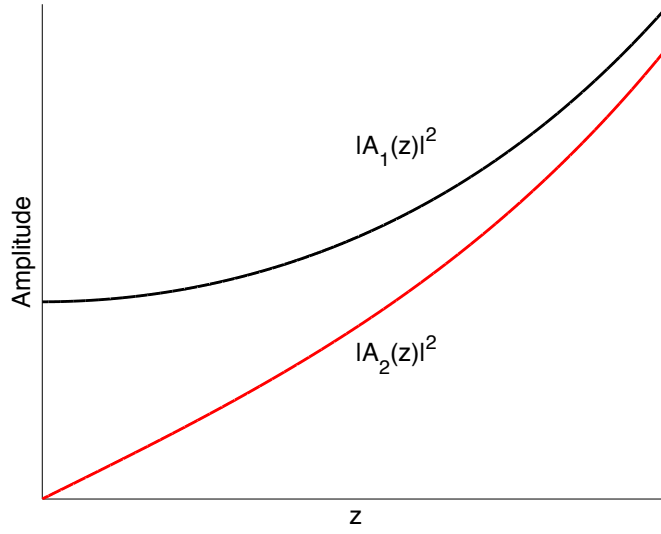


Figure 2.5: Amplitude of output fields in difference-frequency generation (DFG).

an oscillatory behaviour, the amplitudes of the two fields increase exponentially with interaction time.

2.3.4 Spontaneous Parametric Down Conversion

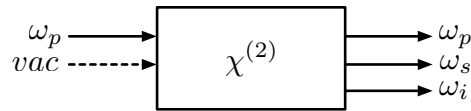


Figure 2.6: Input and output frequency modes in spontaneous parametric down conversion (SPDC). The dashed arrow indicates vacuum field input.

Spontaneous parametric down conversion (SPDC) can be considered, in some respects, to be a special case of DFG. As seen in Figure 2.5, when a strong pump field ω_3 and a weak field ω_1 are incident on the nonlinear material, both a difference-frequency field ω_2 is generated, and the lower frequency input field ω_1 is amplified.

For the initial condition $A_1(0) = 0$, meaning that there is only one input field ω_3 , the interaction is known as spontaneous parametric down conversion. “Parametric” denotes that the pump field is strong enough for its properties to remain essentially unchanged throughout the interaction. By convention, ω_3 is known as the pump field (ω_p), the higher-frequency output field is called the “signal” (ω_s), and the lower-frequency output field is called the “idler” (ω_i). The energy conservation and phase matching relations for this process are:

$$\omega_p = \omega_s + \omega_i \qquad \Delta \mathbf{k} = \mathbf{k}_p - \mathbf{k}_s - \mathbf{k}_i \qquad (2.37)$$

So far, we have considered these three-wave mixing processes from an exclusively classical point of view. SPDC is the first process we encounter that requires a quantum description. By looking at (2.36), it is clear that both $A_1(z)$ and $A_2(z)$ depend on the initial field strength $A_1(0)$, which we are assuming here is vacuum. The classical treatment predicts that no new light will be generated, but in fact this is incorrect. In the quantum theory of light, which will be described in more detail in the next section, the vacuum is not a zero-energy state. Thus, when the ω_p field enters the material, the vacuum energy fluctuations “seed” the process whereby the pump field down-converts some of its energy to fields at two lower frequencies: $\omega_s = \omega_p/2 + \Omega$ and $\omega_i = \omega_p/2 - \Omega$.

The phase matching condition is now explicitly a vector relationship in (2.37). Considering SPDC explicitly in terms of the interaction of photons: a single photon at the pump frequency ω_p is down-converted into a pair of photons at the signal and idler frequencies, in an energy-conserving process. As $\hbar \mathbf{k}$ is the momentum of a single photon, satisfying the phase matching condition ensures that momentum is also conserved. These two conservation relations are represented schematically in Figure 2.7. In quantum mechanics, conjugate variables (*e.g.* position and momentum) satisfy a minimum uncertainty relation. The nonlinear interaction occurs over the length of the crystal, L , implying that momentum need only be approximately conserved to within a fundamental uncertainty: $\Delta k \sim \hbar/L$ [50].

The phase matching condition of the material can be engineered to support down-conversion at various frequencies. In general, a range of side-band frequencies will be down-converted, where pairs of these side-band frequencies are entangled through energy and momentum conservation. The degenerate case, $\Omega = 0$, is of particular importance in the following chapters. In this case, which mode is labelled the “signal” or “idler” is arbitrary. Spatial filtering is commonly employed to select a particular signal-idler frequency pair—as seen in Figure 2.8(b), appropriate

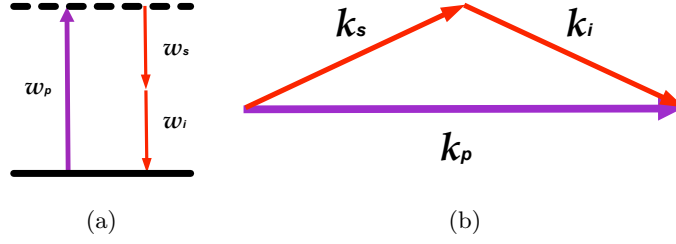


Figure 2.7: (a) Energy conservation relation in SPDC. (b) Momentum conservation relation (vectorial relation) in SPDC.

collection points on the SPDC cone can select the degenerate pair.

Finding phase matching conditions for pump, signal and idler waves in a particular material can be challenging, and is an active field of research. The main difficulty is due to the fact that most materials exhibit normal dispersion, which means that the index of refraction, $n(\omega)$, increases with frequency. This makes it impossible to simultaneously conserve energy and momentum in (2.37). Since $\chi^{(2)}$ materials are all birefringent, the solution is often to use the angle-dependence of the index of refraction to satisfy the phase matching condition. A uniaxial birefringent crystal has two fundamental indices of refraction: n_o for the ordinary polarisation, perpendicular to the crystal axis, and n_e for the extraordinary polarisation, along the crystal axis. For a beam propagating through the crystal at an angle θ to the crystal axis, its extraordinary polarisation (in the plane formed by the crystal axis and the beam direction) experiences an index of refraction $n_E(\theta)$, that is angle-dependent [51]. By precisely engineering the optic axis of a crystal, the phase matching condition can be met. Due to the finite width of the sinc function in 2.2(a), and the argument above based on the fundamental uncertainty in phase matching, it should be clear that perfect phase matching is not a requirement for down conversion, and imperfect phase matching will only reduce the efficiency.

Each instance of a pump photon down-converting into a signal-idler photon pair in the material occurs with an independent probability, due to the randomness in the fluctuation of the vacuum. From outlining the theory of three-wave mixing in the previous sections, it is reasonable to assume that the probability of a downconversion event occurring will be proportional to properties of the crystal (such as its $\chi^{(2)}$ and phase matching condition), as well as the pump power. In general, we can write the wave function of the signal-idler pair in the following way:

$$|\psi_{\text{SPDC}}\rangle_{s,i} \propto |0\rangle_s|0\rangle_i + \eta|1\rangle_s|1\rangle_i + \eta^2|2\rangle_s|2\rangle_i + \dots \quad (2.38)$$

Since the efficiency coefficient η is very small (typically of order 10^{-2} for the SPDC sources discussed in this thesis), we can neglect higher-order terms for most purposes, and use SPDC as a source of correlated single photons. Due to energy conservation, it is clear that the signal and idler photons must be correlated in time. Due to momentum conservation, the spatial modes that the photons occupy must also be correlated.

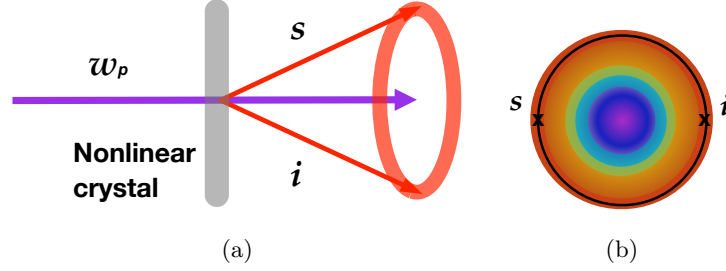


Figure 2.8: (a) Side view of the exit angle in type-I non-collinear SPDC. Here the signal and idler photons are shown to be degenerate, and exit the crystal in a symmetric diverging cone around the pump beam. By momentum conservation, a signal-idler photon pair (*i.e.* from the same down conversion event) are always on opposite sides of the down conversion cone, indicated by the red arrows. (b) Front view of down conversion light cone for type-I phase matching. Down conversion can be non-degenerate, and all frequency pairs are possible, as long as the signal and idler photon energies add up to the pump photon energy. The degenerate case is indicated by the black ring, with signal and idler photons positioned at opposite sides of the cone.

The photon pairs are also correlated in polarisation, and the type of correlation depends on the phase matching condition of the crystal. In Type-I phase matching, the pump field is polarised in one direction, and both down-converted photons are polarised in the orthogonal direction. In Type-II phase matching, the down-converted photons are orthogonally polarised, from which it is possible to generate an entangled polarisation state. Further details about these two phase matching conditions, and the output states that arise from them, will be given in Section 2.5.

2.4 Quantizing the Electromagnetic Field

The classical mode of a light field can be uniquely defined in terms of only a few properties: frequency, direction of propagation, spatial mode (for a Gaussian beam: waist size and location), intensity, absolute phase, and direction of polarisation. The concept of a photon derives from quantising the electromagnetic field. It is tempting to think of photons as massless “particles” propagating at the speed of light. It is

more accurate, however, to say that a mode of light has a photon occupation number, which is one property of the mode [52]. Photon occupation numbers of an optical mode are the result of quantising the electromagnetic field. Photons follow Bose–Einstein statistics, and hence the photon occupation number of a single mode can be greater than one.

Most textbooks begin quantising the electromagnetic field by presenting the classical Hamiltonian for the field, and noting its formal equivalence to the energy of a simple harmonic oscillator. If the field is assumed to be inside a cavity resonator, the Hamiltonian of the radiation field is a sum of independent oscillator energies. Each quantised mode of the field is dynamically equivalent to a simple harmonic oscillator, and the electric and magnetic fields can thus be identified with the canonical position and momentum variables. Canonical quantisation dictates that two classical variables, conjugates in Hamilton’s equations [53], can be replaced in the Hamiltonian by quantum mechanical operators, which are then related by the commutator instead of Poisson brackets. A detailed description of canonical quantisation can readily be found in most quantum mechanics textbooks [54], but some of the results will be presented and discussed in this chapter.

Indexing the field modes by k , the quantum mechanical Hamiltonian for the electromagnetic field is:

$$\mathcal{H} = \hbar \sum_k \omega_k \left(\hat{a}_k^\dagger \hat{a}_k + \frac{1}{2} \right) \quad (2.39)$$

The dimensionless operators \hat{a} and \hat{a}^\dagger obey the bosonic commutation relation:

$$[\hat{a}_k, \hat{a}_{k'}^\dagger] = \delta_{k,k'} \quad [\hat{a}_k, \hat{a}_{k'}] = [\hat{a}_k^\dagger, \hat{a}_{k'}^\dagger] = 0 \quad (2.40)$$

When we are discussing a single mode, the indices can be dropped. Their relation to the electromagnetic field is:

$$\hat{\mathbf{E}}(z, t) = \hat{\mathbf{E}}^{(+)}(z, t) + \hat{\mathbf{E}}^{(-)}(z, t) \quad (2.41a)$$

$$= A[\hat{a} e^{-i(\omega t - kz)} + \hat{a}^\dagger e^{i(\omega t - kz)}] \quad (2.41b)$$

$$\hat{\mathbf{B}}(z, t) = \hat{\mathbf{B}}^{(+)}(z, t) + \hat{\mathbf{B}}^{(-)}(z, t) \quad (2.41c)$$

$$= B[\hat{a} e^{-i(\omega t - kz)} + \hat{a}^\dagger e^{i(\omega t - kz)}] \quad (2.41d)$$

The coefficients A and B are for normalisation, and have the same dimensions as an electric and magnetic field, respectively. We are generally more interested in the quantised electric field, as photo-detection devices generally respond to electric fields.

At this point, it is convenient to introduce “bra-ket” notation, where a “ket” $|\psi\rangle$ denotes a vector representing a quantum state, and a “bra” $\langle\psi|$ is defined as a dual vector to $|\psi\rangle$ in Hilbert space¹. An energy eigenstate of a single-mode field is written $|n\rangle$, and denotes a state with a fixed number of photons n . The operator \hat{a} is known as the annihilation operator, and the operator \hat{a}^\dagger is the creation operator. Appropriately, they transform the energy eigenstate in the following ways:

$$\hat{a}^\dagger|n\rangle = \sqrt{n+1}|n+1\rangle \quad \hat{a}|n\rangle = \sqrt{n}|n-1\rangle \quad (2.42)$$

The appropriately named creation operator adds one photon to the energy eigenstate, and the annihilation operator removes one photon from the state. The normally ordered product of the pair is the number operator $\hat{n} = \hat{a}^\dagger\hat{a}$, whose eigenvalue is the photon excitation number of the mode: $\hat{n}|n\rangle = n|n\rangle$. The energy of the state is:

$$\mathcal{H}|n\rangle = E_n|n\rangle \quad (2.43a)$$

$$= \hbar\omega \left(n + \frac{1}{2}\right) |n\rangle \quad (2.43b)$$

The photon occupation number of the vacuum state $|0\rangle$ is zero, and yet the state contains a zero point energy $\hbar\omega/2$. This is true for every mode, and since there are an infinite number of modes, it implies that the vacuum contains an infinite amount of energy. That is misleading, however, because as in classical mechanics, the level of zero energy can be arbitrarily chosen. What is significant is that the vacuum state has a finite (*i.e.* non-zero) energy variance, which explains a variety of quantum effects. In the previous section, for example, we saw that SPDC relied on energy fluctuations of the vacuum state to enable down-conversion.

An energy eigenstate is commonly known as a *Fock* or *number* state. The single photon number state $|1\rangle$ is of special importance in this thesis, since quantum information with discrete variables typically encodes information using the properties of single photons. As mentioned in the previous section, SPDC is a common method of generating single photons at high enough flux to demonstrate many quantum information protocols. SPDC occurs with very low probability, so the down-conversion mode is dominated by the vacuum. But since two correlated photons are always produced when down-conversion does occur, it is common to use the idler photon as a herald for the signal photon, effectively filtering out the vacuum component. Higher order terms are also present in (2.38), and for this reason the outputs of an SPDC source cannot be considered “true” single photons,

¹A complex vector space with a defined inner product.

only very good approximations of them.

2.4.1 Types of Electromagnetic Radiation

Single photons are the backbone of experiments in photonic quantum information science, and they are often generated by SPDC. It is clear from the higher-order terms in (2.38), however, that the output of an SPDC source is not a pair of pure single photons. While the SPDC output state is an excellent approximation of a pair of photons, it is necessary to have a way of describing and characterising a range of states. In this section, a useful way of categorising optical states is introduced. The next section briefly introduces correlation measures, used to determine the photon statistics in electromagnetic radiation.

Thermal light—the everyday light we are most familiar with—is the result of the thermal (random) motion of charged particles in materials. At the beginning of the 20th century, Planck quantised blackbody radiation, and in doing so derived an expression for the statistical distribution of thermal photon frequencies. Blackbody radiation is emitted from an idealised cavity in thermal equilibrium, and the field mode energies are quantised as harmonic oscillators, as described in the previous section. The Boltzmann factor $P_B(n) = \exp[-E_n/k_B T] / \sum_n \exp[-E_n/k_B T]$ gives the probability that a single mode is thermally excited to its n th energy state, and thus the mean number of photons excited in a field mode is $\langle n \rangle = n P_B(n)$.

Coherent states of light are eigenstates of the annihilation operator, and can be expressed as an infinite series in the number state basis:

$$\hat{a}|\alpha\rangle = \alpha|\alpha\rangle \quad |\alpha\rangle = e^{-\frac{|\alpha|^2}{2}} \sum_{n=0}^{\infty} \frac{\alpha^n}{\sqrt{n!}} |n\rangle \quad (2.44)$$

Other important properties of the coherent state are that the probability of detecting n photons is a Poissonian distribution:

$$P_c(n) = e^{-|\alpha|^2} \frac{|\alpha|^{2n}}{n!} \quad (2.45)$$

and the average photon number $\langle \hat{n} \rangle$ and its uncertainty (standard deviation) Δn are related in the following way:

$$\langle \hat{n} \rangle = |\alpha|^2 = \bar{n} \quad \Delta n = \sqrt{\langle \hat{n}^2 \rangle - \langle \hat{n} \rangle^2} = |\alpha| = \sqrt{\bar{n}} \quad (2.46)$$

It is a general property of Poissonian distributions that the uncertainty scales as

the square root of the distribution's mean. A coherent state therefore exhibits Poissonian statistics in the photon number uncertainty of a single mode. Figure 2.9(a) graphically shows that for fixed mean photon number \bar{n} , a thermal state has a larger uncertainty than a coherent state, and is said to be super-Poissonian. In the limit $\hat{n} \gg 1$, the uncertainty scales as $\Delta n \approx \bar{n}$. If the photon number uncertainty in a field is less than the square root of the mean, $\Delta n < \bar{n}$, the state is said to have sub-Poissonian statistics, and this is one signature of a non-classical state. The most extreme example of this would be a Fock state, which has a precisely defined photon number, and hence a vanishing uncertainty. As expected, then, the output of SPDC also exhibits sub-Poissonian statistics.

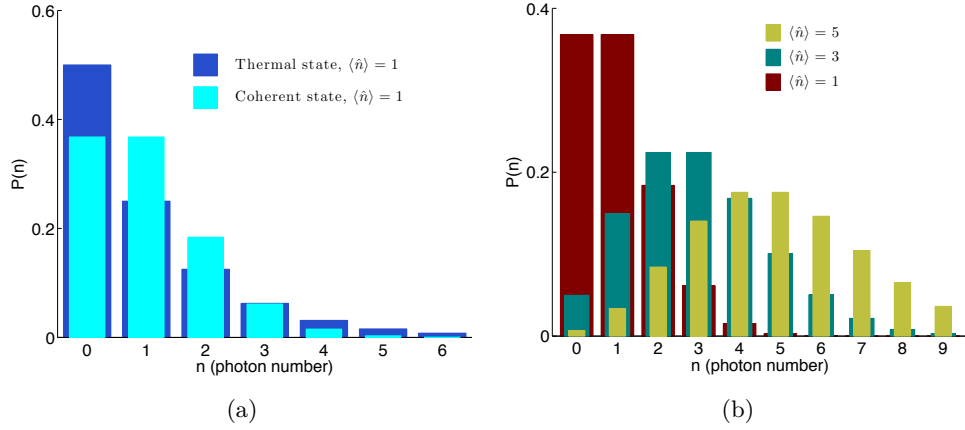


Figure 2.9: (a) Thermal *vs.* coherent state photon number probability distribution, $\hat{n} = 1$ for both. The probability of detecting photon number $P(n) = \langle n|\psi \rangle^2$, where $|\psi \rangle$ is the coherent or thermal state. (b) Photon number distribution for coherent states with different \hat{n} . As $\hat{n} \gg 1$, the discrete Poissonian distribution begins to look like a continuous normal distribution.

2.4.2 Correlation Measures

The first-order correlation function is a measure of a single field's interference with itself:

$$G^{(1)}(\tau) = \langle \hat{E}^{(-)}(t) \hat{E}^{(+)}(t + \tau) \rangle = \int dt \hat{E}^{(-)}(t) \hat{E}^{(+)}(t + \tau) \quad (2.47)$$

The correlation of the field amplitude is measured at a fixed position and polarisation, with a portion of the same field that is shifted by a time interval τ . The degree of first-order temporal coherence is defined as the normalised version of $G^{(1)}(\tau)$:

$$g^{(1)}(\tau) = \frac{\langle \hat{E}^{(-)}(t) \hat{E}^{(+)}(t + \tau) \rangle}{\langle \hat{E}^{(-)}(t) \hat{E}^{(+)}(t) \rangle} = \frac{G^{(1)}(\tau)}{\langle \hat{E}^{(-)}(t) \hat{E}^{(+)}(t) \rangle} \quad (2.48)$$

For a light source that is first-order coherent, $g^{(1)}(0) = 1$, and $g^{(1)}(\tau) \rightarrow 0$ when $\tau \gg \tau_c$. The time interval τ_c , outside of which the light will no longer interfere with itself, is known as its coherence time. The degree of first-order coherence determines the modulation amplitude of the output intensity in an interferometer, known as the classical interference visibility:

$$\langle I_{out} \rangle = \frac{\langle I_{in} \rangle [1 \pm |g^{(1)}(\tau)| \cos(\phi)]}{2} \quad \text{Vis.} = |g^{(1)}(\tau)| \quad (2.49)$$

For a coherent state, such as the output of a continuous wave laser, the coherence time is assume to be practically infinite, and hence $g^{(1)}(\tau)$ is constant.

The degree of second-order temporal coherence measures intensity correlations:

$$g^{(2)}(\tau) = \frac{\langle \hat{E}^{(-)}(t) \hat{E}^{(-)}(t + \tau) \hat{E}^{(+)}(t + \tau) \hat{E}^{(+)}(t) \rangle}{\langle \hat{E}^{(-)}(t) \hat{E}^{(+)}(t) \rangle^2} = \frac{G^{(2)}(\tau)}{\langle \hat{E}^{(-)}(t) \hat{E}^{(+)}(t) \rangle^2} \quad (2.50)$$

It gives information about the probability of detecting a photon at time $t + \tau$, when a photon has already been detected at t . Using the Cauchy inequality it can be shown that $1 \leq g^{(2)}(\tau) \leq \infty$ and $g^{(2)}(\tau) \leq g^{(2)}(0)$ for classical fields. Violation of these inequalities is a signature of non-classicality, and performing such an intensity correlation measurement is a common way of testing to what extent a state can be described as non-classical state (*e.g.* a single photon).

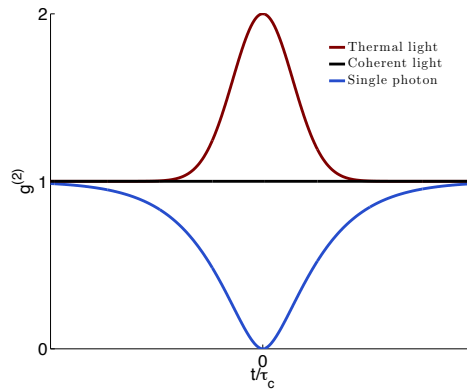


Figure 2.10: Normalised second-order correlation functions of thermal, coherent, and single photon states, for a single mode.

2.5 Encoding Qubits on Photons

A *bit* is the fundamental unit of classical information, and can take a value of either 0 or 1. A *quantum bit*, commonly known as a *qubit*, is the fundamental unit of quantum information, and can be in a linear superposition of basis states $|0\rangle$ and $|1\rangle$. In its most general form, a qubit can be written as

$$|\psi\rangle = \alpha|0\rangle + \beta|1\rangle, \quad (2.51)$$

where $|0\rangle$ and $|1\rangle$ are orthonormal basis states (called the computational basis), and α and β are complex numbers satisfying the normalisation condition $|\alpha|^2 + |\beta|^2 = 1$. Thus, the qubit $|\psi\rangle$ represents a vector in Hilbert space.

In experimental quantum information, a qubit $|\psi\rangle$ is encoded in the properties of a physical system that contains suitable basis states, such as a non-classical state of light. The polarisation state vector of a single photon is restricted to the plane perpendicular to its direction of motion. It therefore exists in a two-dimensional Hilbert space, and is particularly well-suited to encoding qubits [55]. By convention, the computational basis $\{|0\rangle, |1\rangle\}$ is designated to be the horizontal and vertical polarisation states $\{|H\rangle, |V\rangle\}$. The full set of standard polarisation basis states is:

$$\begin{aligned} \text{Horizontal} &= |H\rangle \equiv |0\rangle & \text{Vertical} &= |V\rangle \equiv |1\rangle \\ \text{Diagonal} &= |D\rangle = |H\rangle + |V\rangle & \text{Anti-diagonal} &= |A\rangle = |H\rangle - |V\rangle \\ \text{Right-circular} &= |R\rangle = |H\rangle + i|V\rangle & \text{Left-circular} &= |L\rangle = |H\rangle - i|V\rangle \end{aligned} \quad (2.52)$$

Another advantage of encoding qubits in polarisation states is that polarisation can be easily manipulated using linear optical components such as wave plates, filters and polarising beam splitters.

The SPDC process, introduced in Section 2.3.4, provides the single photon states upon which qubits can be encoded. A down-conversion event is an energy and momentum conserving process in which a pump photon splits into two photons of lower frequency. The signal and idler photons are always entangled in energy and momentum, and may also be entangled in polarisation depending on the phase matching conditions. In the parametric approximation (*i.e.* a classical, un-depleted pump field), the SPDC Hamiltonian for the type-I phase matching condition is:

$$\mathcal{H}_{\text{type-I}} = \hbar\eta\hat{a}_s^\dagger\hat{a}_i^\dagger + \text{H.c.} \quad (2.53)$$

The type-I phase matching condition produces two classically correlated photons:

the signal and idler will have the same polarisation, but it is determined and always perpendicular to the polarisation of the pump beam. A single nonlinear crystal with type-I phase matching does not generate polarisation entanglement, although two such thin crystals can be used in a “sandwiched” configuration to generate polarisation entanglement. Further details about sandwiched type-I SPDC sources can be found in Section 5.5.1.

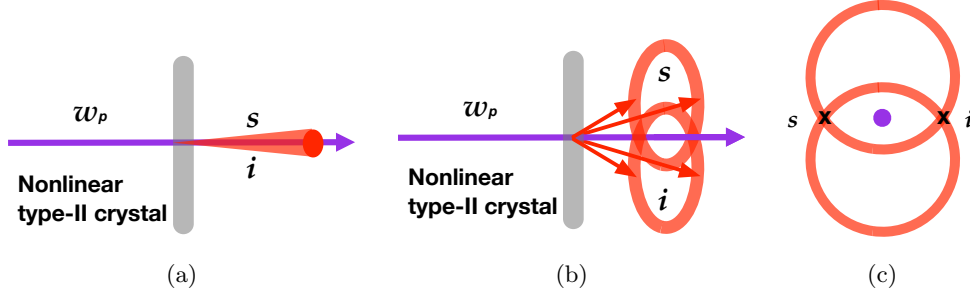


Figure 2.11: (a) Side view of collinear type-II SPDC. (b) Side view of non-collinear (crossed cones) type-II SPDC. Photons in orthogonal polarisations are down converted in separate cones, with their axes at angles symmetric about the pump beam axis. (c) Front view of crossed cones type-II SPDC. At the points where the polarisation cones overlap, polarisation-entangled photons can be collected.

A type-II SPDC source can be operated in collinear mode (Figure 2.11(a)) or with crossed down conversion cones (Figure 2.11(b) and 2.11(c)). The Hamiltonians for these two type-II sources are:

$$\mathcal{H}_{\text{type-II, coll.}} = \hbar\eta\hat{a}_{sV}^\dagger\hat{a}_{iH}^\dagger + \text{H.c.} \quad (2.54a)$$

$$\mathcal{H}_{\text{type-II, cross}} = \hbar\eta(\hat{a}_{sV}^\dagger\hat{a}_{iH}^\dagger + \hat{a}_{sH}^\dagger\hat{a}_{iV}^\dagger) + \text{H.c.} \quad (2.54b)$$

In the type-II collinear case, the two polarisation modes are in the same spatial mode, and hence they are not in an entangled state. In the type-II crossed cones case, down converted photons are typically collected at the points where the cones intersect (marked by X in Figure 2.11(c)), and this state can be written in the following way:

$$\begin{aligned} |\psi(t)\rangle_{\text{type-II}} &\simeq |0\rangle_{sV}|0\rangle_{sH}|0\rangle_{iV}|0\rangle_{iH} \\ &\quad - i\eta t(|1\rangle_{sV}|0\rangle_{sH}|0\rangle_{iV}|1\rangle_{iH} + |0\rangle_{sV}|1\rangle_{sH}|1\rangle_{iV}|0\rangle_{iH}) \end{aligned} \quad (2.55a)$$

The signal and idler photons are correlated in having orthogonal polarisations, but the individual photons are in a superposition of $|H\rangle$ and $|V\rangle$. The second term in (2.55), when normalised, is a maximally entangled polarisation state, and is

equivalent to one of the four Bell states:

$$|\psi^+\rangle = \frac{1}{\sqrt{2}}(|V\rangle_s|H\rangle_i + |H\rangle_s|V\rangle_i) \quad (2.56)$$

This output state can be transformed into any of the three other Bell states using only local operations. The Bell states are maximally entangled two-qubit states, and are commonly used in various quantum information protocols, or for fundamental tests of quantum theory [13].

2.5.1 Representing Quantum States of Light

In this section, common ways of visualising and representing qubits and non-classical states are introduced². Polarisation qubits are commonly visualised on the Poincaré unit sphere, which is the optical equivalent of the Bloch sphere—the difference between the two spheres being solely in how the axes are labeled. As $|\psi\rangle$ is a pure state, which can be described by a wave function, the vector extends from the origin to the surface of the sphere.

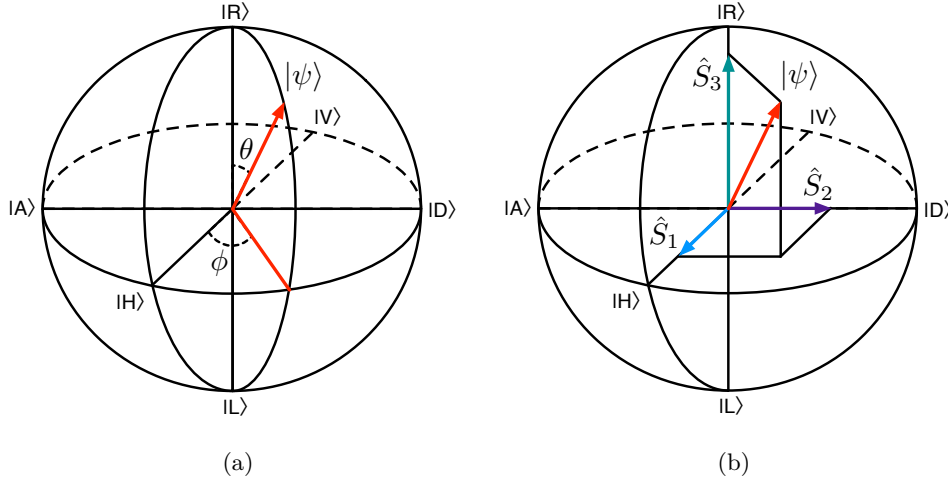


Figure 2.12: (a) A pure state $|\psi\rangle$ has fixed magnitude equal to unity on the Poincaré sphere, and therefore the two angles $\{\theta, \phi\}$ uniquely define the state vector: $|\psi\rangle = \cos(\theta/2)|H\rangle + e^{i\phi}\sin(\theta/2)|V\rangle$. (b) Projection of state vector $|\psi\rangle$ onto the Stokes parameters.

The component vectors adding to $|\psi\rangle$ in Figure 2.12(b) are the Stokes parameters, commonly used to describe polarisation states of a classical electromagnetic field.

²For a good overview, refer to [56].

In the quantum formalism, they are projection operators:

$$\begin{aligned}\hat{S}_0 &= |H\rangle\langle H| + |V\rangle\langle V| & \hat{S}_1 &= |H\rangle\langle H| - |V\rangle\langle V| \\ \hat{S}_2 &= |D\rangle\langle D| - |A\rangle\langle A| & \hat{S}_3 &= |R\rangle\langle R| - |L\rangle\langle L|\end{aligned}\quad (2.57)$$

For a pure state like $|\psi\rangle$, the \hat{S}_0 projector, representing the length of the state vector, is equal to unity.

The most general state is a *mixed state*—a statistical mixture of pure states. This state can only be described as a *density matrix*:

$$\rho \equiv \sum_j p_j |\psi_j\rangle\langle\psi_j|, \quad (2.58)$$

where $|\psi_j\rangle$ is one possible pure state, indexed by j , and p_j is the probability of finding the system in that state. If the system is in a pure state, then there is only one term in the sum:

$$\rho = |\psi\rangle\langle\psi|. \quad (2.59)$$

In matrix form, $|\psi\rangle$ is a column vector, $\langle\psi|$ is a row vector, and $|\psi\rangle\langle\psi|$ is the outer product:

$$\begin{aligned}|\psi\rangle &= \alpha|H\rangle + \beta|V\rangle & |\psi\rangle &= \begin{pmatrix} \alpha \\ \beta \end{pmatrix} \\ \langle\psi| &= \alpha^*\langle H| + \beta^*\langle V| & \langle\psi| &= \begin{pmatrix} \alpha^* & \beta^* \end{pmatrix}\end{aligned}$$

$$|\psi\rangle\langle\psi| = \alpha\alpha^*|H\rangle\langle H| + \alpha\beta^*|H\rangle\langle V| + \beta\alpha^*|V\rangle\langle H| + \beta\beta^*|V\rangle\langle V| \quad (2.60a)$$

$$= \begin{pmatrix} |\alpha|^2 & \alpha\beta^* \\ \beta\alpha^* & |\beta|^2 \end{pmatrix} \quad (2.60b)$$

In (2.60), $|\alpha|^2$ and $|\beta|^2$ are the probabilities of finding the qubit in the computational basis states $|H\rangle$ and $|V\rangle$, respectively. The off-diagonal terms are known as the *coherence* terms, which appear when the qubit is in a superposition of basis states.

A condition that a density matrix representing a real physical state must satisfy is that the trace equals one: $\text{tr}(\rho) = 1$. For a pure state, this is simply the normalisation condition $|\alpha|^2 + |\beta|^2 = 1$. For a mixed state, it ensures that the probability weightings for the different states in the ensemble (2.58) add up to one: $\sum_i p_i = 1$. A scalar quantity known as a state's *purity* is a common measure in quantum information

science:

$$\text{Purity} = \text{tr}(\rho^2) \quad \begin{cases} = 1 & \text{Pure state,} \\ < 1 & \text{Mixed state.} \end{cases} \quad (2.61)$$

The purity is a common figure of merit when measuring the quality of a prepared quantum state for quantum information processing, or when quantifying the effect of noise on the state. The purity is determined by the coherence terms in the density matrix. The minimum purity is $\mathcal{P}_{\min} = 1/d$, where d is the dimension of the state. For a qubit $d = 2$, and $\mathcal{P}_{\min} = 1/2$.

Density matrices are a complete and general description of quantum states, but they can be unwieldy and difficult to interpret when dealing with states of many dimensions. Another useful description of a state is its description in phase space [57]. Recalling the quantised electric field (2.41), two new quantities can be defined:

$$\hat{Q} \equiv \frac{\hat{a} + \hat{a}^\dagger}{\sqrt{2}} \quad \hat{P} \equiv \frac{i(\hat{a} - \hat{a}^\dagger)}{\sqrt{2}} \quad (2.62)$$

The dimensionless \hat{Q} is commonly known as the amplitude quadrature, and \hat{P} is known as the phase quadrature. The quadrature names are attributed to the fact that \hat{Q} can be identified with the coordinate variable \hat{x} in the Hamiltonian of the electromagnetic field, and \hat{P} can be identified with the momentum variable \hat{p} . The two quadratures are always orthogonal to one another, and the reference frame is arbitrary:

$$\begin{aligned} \hat{Q}_\Theta &= \frac{\hat{a}e^{i\Theta} + \hat{a}^\dagger e^{-i\Theta}}{\sqrt{2}} & \hat{P}_\Theta &= \frac{i(\hat{a}e^{i\Theta} - \hat{a}^\dagger e^{-i\Theta})}{\sqrt{2}} \\ &= \cos(\Theta)\hat{Q} + \sin(\Theta)\hat{P} & &= -\sin(\Theta)\hat{Q} + \cos(\Theta)\hat{P} \end{aligned} \quad (2.63)$$

Different parameters Θ coincide with different physical observables $\{\hat{Q}_\Theta, \hat{P}_\Theta\}$, which is the underlying principle of homodyne tomography, a powerful technique for measuring quantum states of light. Further details about homodyne tomography can be found in Section 6.4.1 of Chapter 6.

A phasor diagram graphically represents these quadratures in phase space. A classical state of light is represented by a point, since the quadratures can be simultaneously determined to arbitrarily high accuracy. For a quantum state, \hat{Q} and \hat{P} are non-commuting operators, and there is a minimum uncertainty relation: $(\Delta\hat{Q})^2(\Delta\hat{P})^2 \geq 1$. This means a quantum state of light will be represented by an area in phase space (Figure 2.13(a)), instead of a point.

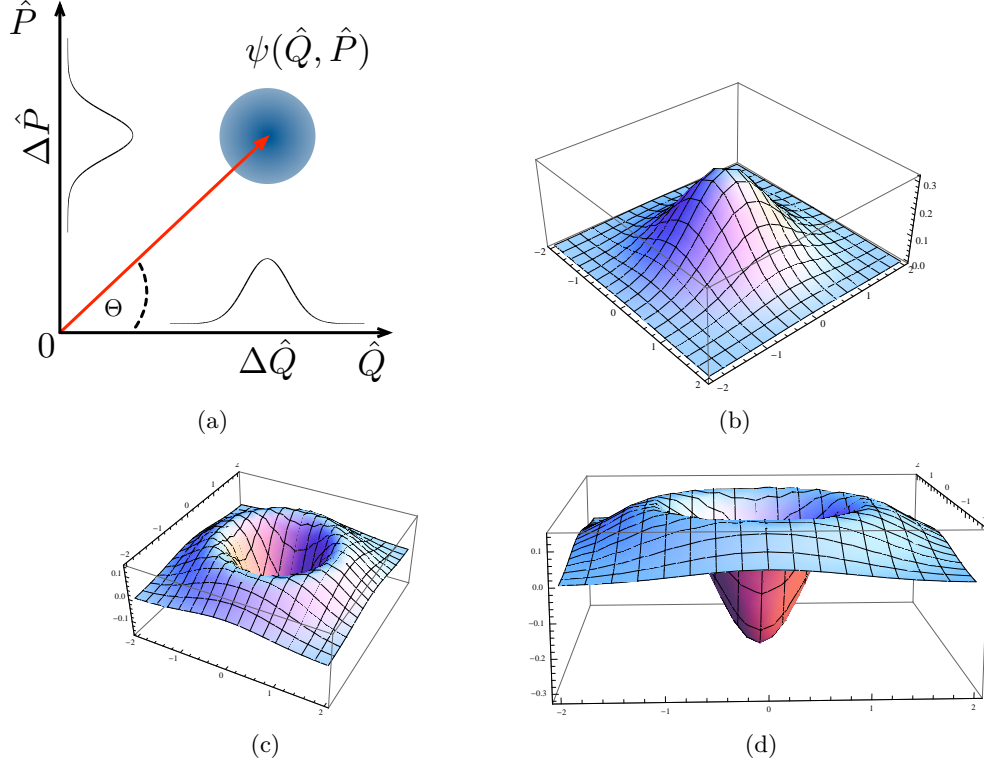


Figure 2.13: (a) Phasor diagram of a theoretical coherent state. Its amplitude is proportional to its displacement from the origin (red arrow), and it has a definite phase Θ , with the \hat{Q} quadrature acting as the zero phase reference. The fundamental uncertainty in the quadratures is given by the projections $\Delta\hat{Q}$ and $\Delta\hat{P}$. It is represented as a symmetric ball, due to the fundamental uncertainty in its quadratures. Its amplitude is represented by the red arrow, showing displacement from the origin. (b) Wigner distribution of a coherent state. (c) and (d) Wigner distribution of a theoretical single photon state. A single photon is a non-classical state, indicated by the fact the the Wigner function is negative-valued at certain points in phase space. For the single photon, the Wigner distribution is negative at the origin.

Phasor diagrams only present information about the quadrature projections of a quantum state. To graphically present the full information in a density matrix, we must go a step further, and calculate a quasi-probability distribution. There are several different ways to generate a quasi-probability distribution for a given state, but perhaps the best known is the Wigner distribution. The Wigner distribution $W(q, p)$ can be calculated from a density matrix ρ in the following way:

$$W(q, p) = \pi^{-1} \int_{-\infty}^{+\infty} e^{2ipy} \langle q - y | \rho | q + y \rangle dy \quad (2.64)$$

The Wigner distribution can be inverted to regain the density matrix. The Wigner

function gives the quadratures projections in a straight-forward way:

$$w(q) = \int_{-\infty}^{+\infty} W(q, p) dp \quad w(p) = \int_{-\infty}^{+\infty} W(q, p) dx \quad (2.65)$$

The Wigner distribution is a “quasi”-probability distribution because it can take negative values for certain states. A negative value in the Wigner distribution is often interpreted as a characteristic of non-classicality. The quadrature projections $w(q)$ and $w(p)$ are always positive definite, and give the correct quantum mechanical distributions for position and momentum. Two other quasi-probability distributions commonly used as the P function and the Q function. These three representations differ in their operator ordering conventions for calculating the distributions. The same quantum state can have quite different representations depending on which convention is used.

2.5.2 Qubit Operations

A closed system evolves via a unitary transformation:

$$|\psi(t + \tau)\rangle = \hat{U}|\psi(t)\rangle, \quad (2.66)$$

where the unitarity condition for the operator

$$\hat{U}^\dagger \hat{U} = \hat{U} \hat{U}^\dagger = 1 \quad (2.67)$$

ensures that the evolution is reversible, *i.e.* if time were to run backwards, the state $|\psi(t + \tau)\rangle$ would evolve deterministically to $|\psi(t)\rangle$. Equivalently, we can say that information is preserved under a unitary transformation. In linear optics, the operations before final detection are unitary operations. These operations include manipulating the polarisation state of photons using wave plates, splitting spatial modes using polarising or non-polarising beam splitters, classical interference and two-photon interference.

Polarisation qubits, with basis states that are polarisation modes of a single photon, are used extensively in this thesis, due to the relative ease with which they can be manipulated. A wave plate is an optically flat birefringent material that can induce a delay between the ordinary and extraordinary components of a photon’s polarisation vector. Wave plates are commonly made from quartz, which is a uniaxial crystal with positive birefringence ($n_e > n_o$). The extraordinary polarisation is defined as the polarisation component lying in the plane of the crystal’s optic axis, and

the ordinary polarisation is then the orthogonal polarisation component. A relative phase between the two polarisations is acquired due to the different phase velocities through the crystal. Wave plates are manufactured to generate a phase delay of either half of a wavelength (half wave plate, HWP) or a quarter of a wavelength (quarter wave plate, QWP). Wave plates are mounted so as to be rotatable around their surface normal axis, so the plane of the optic axis can be changed.

The operations of a HWP and QWP are given by the following unitary matrices:

$$\hat{U}_H(\theta) = i \begin{bmatrix} \cos(2\theta) & \sin(2\theta) \\ \sin(2\theta) & -\cos(2\theta) \end{bmatrix} \quad (2.68a)$$

$$\hat{U}_Q(\theta) = \frac{1}{\sqrt{2}} \begin{bmatrix} 1 + i \cos(2\theta) & i \sin(2\theta) \\ i \sin(2\theta) & 1 - i \cos(2\theta) \end{bmatrix} \quad (2.68b)$$

The angle θ is the angle between the optic axis plane of the wave plate and the laboratory reference frame. Any pure polarisation state can be transformed into any other pure polarisation state on the Poincaré sphere using the following sequence of wave plates: a QWP, followed by a HWP and then another QWP, all with the appropriate optic axis angles.

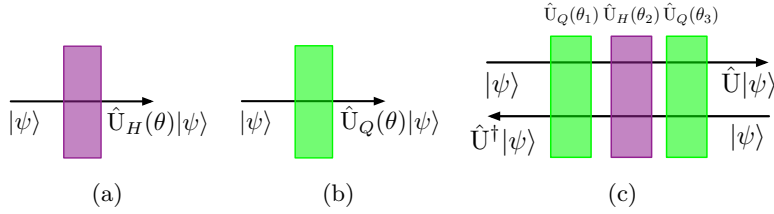


Figure 2.14: (a) Half wave plate. (b) Quarter wave plate. (c) Arbitrary polarisation rotation: $\hat{U} = \hat{U}_Q(\theta_3)\hat{U}_H(\theta_2)\hat{U}_Q(\theta_1)$.

It is often necessary to convert polarisation modes to spatial modes, and this can be achieved using polarising beam splitters (PBS) or beam displacers (BD). Beam displacers are typically calcite crystals several tens of millimetres in length, which separate orthogonal polarisations into parallel spatial modes. Polarising beam splitters are often made of two right-angle glass prisms making contact at their hypotenuse to form a cube, with a dielectric coating along the cube's diagonal interface. In contrast to the beam displacer, the polarising beam splitter cube reflects S-polarised light at a 90° angle, and transmits P-polarised light straight through.

Another common linear optical element is the non-polarising beam splitter (BS) [58]. These are similar to PBS's, but provide a splitting ratio between the two output

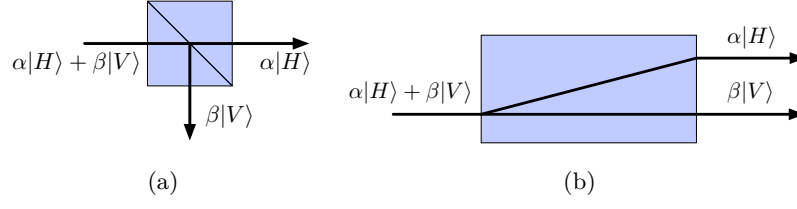


Figure 2.15: (a) Polarising beam splitter cube. (b) Beam displacer.

ports that is ideally independent of polarisation. In reality, the splitting ratio is usually slightly different for S and P polarisations. A beam splitter with reflectivity

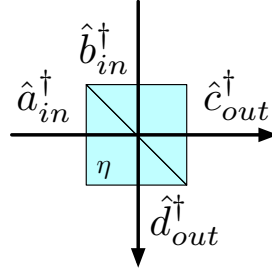


Figure 2.16: Beam splitter cube (non-polarising) with reflectivity η .

η transforms input modes in the following way:

$$\hat{a}_{in}^\dagger \rightarrow \sqrt{\eta} \hat{c}_{out}^\dagger + i\sqrt{1-\eta} \hat{d}_{out}^\dagger \quad (2.69a)$$

$$\hat{b}_{in}^\dagger \rightarrow \sqrt{\eta} \hat{d}_{out}^\dagger + i\sqrt{1-\eta} \hat{c}_{out}^\dagger \quad (2.69b)$$

In general, we will use the “symmetric” beam splitter convention, where all reflections induce a $\pi/2$ phase shift, as shown in (2.69). Such a beam splitter mixes the two input fields in the the output spatial modes. It is an important component in many optical circuits, one reason being that by carefully choosing the input fields, the 50:50 beam splitter can be used to generate Hong–Ou–Mandel interference.

2.5.3 Hong–Ou–Mandel Interference

Hong–Ou–Mandel (HOM) interference [28] is the non-classical interference of two identical photons at the input ports of a beam splitter. It is an effect that is not predicted by classical electromagnetic theory, as it depends essentially on the quantisation of the electromagnetic field. The setup to observe HOM interference is the following: a single photon is sent to each input port of a symmetric ($\eta = 0.5$) beam splitter. Apart from being in orthogonal spatial modes, the two single photons are

otherwise indistinguishable—*i.e.* their other physical properties, such as polarisation and temporal profile, are identical. Classical field theory predicts that, when single photon detectors are placed at the output ports, statistically half of the time either output detector will “click” alone, and half the time both detectors will click in coincidence (*i.e.* simultaneous detection signals). Quantum theory predicts the correct outcome, which is that the probability for coincidence detection is zero. This is due to the destructive interference of the single photon amplitudes to travel to opposite output ports:

$$\hat{a}_{in}^\dagger \hat{b}_{in}^\dagger |00\rangle \rightarrow (1/2)(\hat{d}_{out}^\dagger + i\hat{c}_{out}^\dagger)(\hat{c}_{out}^\dagger + i\hat{d}_{out}^\dagger)|00\rangle \quad (2.70a)$$

$$= (i/2)(\hat{d}_{out}^\dagger \hat{d}_{out}^\dagger + \hat{c}_{out}^\dagger \hat{c}_{out}^\dagger)|00\rangle + (1/2)(\hat{d}_{out}^\dagger \hat{c}_{out}^\dagger - \hat{c}_{out}^\dagger \hat{d}_{out}^\dagger)|00\rangle \quad (2.70b)$$

$$= (i/2)(\hat{d}_{out}^\dagger \hat{d}_{out}^\dagger + \hat{c}_{out}^\dagger \hat{c}_{out}^\dagger)|00\rangle + (1/2)[\hat{d}_{out}^\dagger, \hat{c}_{out}^\dagger]|00\rangle \quad (2.70c)$$

$$= (i/2)(\hat{d}_{out}^\dagger \hat{d}_{out}^\dagger + \hat{c}_{out}^\dagger \hat{c}_{out}^\dagger)|00\rangle \quad (2.70d)$$

It is clear from the Bose–Einstein commutation relations introduced in (2.40) that $[\hat{d}_{out}^\dagger, \hat{c}_{out}^\dagger] = 0$ in the equation above. Single photon detectors at the output ports of the beam splitter measure the electric field operators \hat{E} (see (2.41)) in modes c and d . The joint probability of detecting photons in both modes c and d , at times t and $t + \tau$ respectively, is:

$$P_{c,d}(\tau) = \langle 1_d \ 1_c | \hat{E}_c^-(t) \hat{E}_d^-(t + \tau) \hat{E}_d^+(t + \tau) \hat{E}_c^+(t) | 1_c \ 1_d \rangle \quad (2.71)$$

The form of (2.71) is similar to the second-order correlation function $g^{(2)}(\tau)$ from (2.41), the difference being that in (2.71) there are two input modes. The interference of the two identical single photons at the balanced beam splitter ensures that $P_{c,d}(0) = 0$. This effect is known as photon bunching, since the two indistinguishable but initially independent single photons occupy the same output mode after the beam splitter. As the delay τ in one input mode approaches the order of the coherence time τ_{coh} of the single photons, the distinguishing information destroys any interference, and the normalised joint probability $P_{c,d}(\tau > \tau_{coh}) \rightarrow 1$.

A major disadvantage of using linear optics for certain quantum information tasks is the difficulty of getting two photons to interact. Cross phase modulation is possible, for example, in certain nonlinear materials, but the nonlinearity is typically too weak for an observable effect at the single photon level. HOM interference, however, is one of the only practical ways of getting two photons to interfere with each other, and it is an essential component in linear optical quantum gates, such as the quantum controlled–NOT (CNOT) gate [44].

2.6 Measuring Photonic Qubits

2.6.1 Single Photon Detection

A photodetector responds to the electric field of a beam of light, converting the energy in the electric field into an electronic current via the photo-electric effect. Photodetectors are photodiodes (semi-conductors) operating in reverse bias—when an electron-hole pair is created in the depletion zone due to photoionisation, the electrons move towards the n -junction and the holes towards the p -junction along the gradient of the applied electric field [59].

An avalanche photodiode (APD) is a photodiode with a reverse bias that is high enough to cause the avalanche multiplication of photo-current. After photoionisation, the electron and hole are accelerated to a high enough velocity to generate another electron-hole pair due to impact-ionisation. Thus, impact-ionisation generates a large gain on the initial photo-current.

An APD is said to operate in *Geiger mode* if the reverse bias is well above the breakdown voltage. This means that a single photoionisation is enough to generate an avalanche of impact ionisations, and a macroscopic electronic current on the order of mA. This mode of operation is known as Geiger mode by analogy with Geiger counters, or also single photon avalanche detector (SPAD). Accordingly, commercial SPADs can only count single photon detection events, and cannot discriminate between a single photoionisation or multiple photoionisations in the detection window. Implementing photon number discrimination in SPADs is an active area of research.

SPADs have a *quantum efficiency*, which is the probability of a single photon creating an electron-hole pair. SPADs also suffer from *dark counts*, which are spurious impact ionisation avalanches due to thermal effects. To minimise dark counts, SPADs are usually cooled. SPADs for detecting single photons with visible to near-infrared wavelength are usually made from silicon, and typically have a quantum efficiency 50%. For photons at telecom wavelengths, SPADs are made from InGaAs, and their quantum efficiency is somewhat lower.

2.6.2 Quantum State Tomography

Qubit tomography is performed by measuring the Stokes parameters $\{\sigma_x, \sigma_y, \sigma_z\}$ for an ensemble of identically prepared qubits. The preparation procedure must therefore be kept constant throughout data collection, in order to collect accurate

measurement statistics. There is always noise associated with a measurement, meaning that the measurement statistics only correspond closely (but not exactly) to the theoretical probabilities of the qubit. To account for this noise, a *maximum likelihood* optimisation is performed using the measurement data. This is a numerical search of all (physically valid) theoretical density matrices that could give similar measurement results to the given data set. The theoretical density matrix with the highest probability of generating the given data set is taken to be the density matrix of the measured system [55].

2.7 Summary

This chapter has reviewed some of the theoretical background that will be helpful in understanding the experiments described in subsequent chapters. Additional background can be found in each chapter, as it relates to a specific experiment.

Chapter 3

Heralded Noiseless Amplification of a Photon Polarization Qubit

3.1 Acknowledgements

Guoyong Xiang and I constructed the SPDC photon source and optical circuit together. I collected and analysed the data, under the supervision of Geoff Pryde. The theoretical results presented in Section 3.7, characterising the effects of source and detector efficiencies, are due to Tim Ralph. The results presented in this chapter were published in [60].

3.2 Introduction

Photons are the best long-range carriers of quantum information, but the inevitable absorption and scattering of photons in a transmission channel places a serious limitation on viable communication distances. The amplification of quantum information, analogous to relay stations in classical communication networks, will be an essential feature of future quantum technologies, with direct applications to quantum communication, metrology and fundamental tests of quantum theory.

There are unique challenges involved in amplifying quantum signals. Deterministic noiseless amplification of an arbitrary quantum state is forbidden by the no-cloning

theorem [39, 40], and there is a minimum noise cost imposed by quantum mechanics for deterministic amplification [61]. A common approach to circumventing these restrictions is to make the amplification non-deterministic—some of the time, the state is amplified without adding noise, and the rest of the time the amplification fails, and the state is destroyed in the process. On average, no laws of quantum mechanics are contradicted.

The noiseless linear amplification (NLA) of single mode optical states has recently been experimentally demonstrated using a few different approaches [62–67]. Qubits, which are two-mode states, are the quintessential model for encoding quantum information. Qubits, or systems of entangled qubits, are central to most protocols for transmitting and processing quantum information [4], and play a large role in other proposed quantum technologies [68, 69], as well as proposed investigations of quantum theory [70]. A natural implementation of a travelling qubit is an excitation coherently shared between two harmonic oscillators. In optics, this implementation is a photonic qubit, in which the information is encoded in orthogonal polarisation, spatial or temporal modes of a single photon.

A great deal of attention has been devoted to the challenge of efficiently transmitting qubits over significant distances. Overcoming transmission loss is of both fundamental and practical interest. From a fundamental perspective, long-range tests of Bell inequalities have normally been vulnerable to the detection loophole: owing to losses, not all entangled pairs are detected, and the fair sampling assumption is invoked to argue that the undetected pairs would not have significantly changed the measurement statistics. Only quite recently have steering [71–73] and Bell inequality [74, 75] violations been experimentally demonstrated with the detection loophole closed. These tests, however, have relied on highly efficient superconducting transition-edge sensors (TES) [72, 74, 75] with $\sim 95\%$ quantum efficiency [76], or modified steering inequalities with lower efficiency bounds [71, 73]. Superconducting TES detectors are very expensive and technically challenging to operate, and not yet widely available, while modified inequalities with lower efficiency bounds have only been derived for asymmetric steering protocols.

Developing practical techniques to overcome *transmission* loss thus remains a highly active field. Inevitable transmission losses can in principle be compensated by amplifying the signal. A noiseless qubit amplifier, although necessarily non-deterministic, can have an independent heralding signal to notify when the state has been successfully amplified. A heralding signal allows two parties to be certain that they share an entangled pair before measurement. This implies that the overall detection efficiency

would no longer depend on transmission efficiency, but only on the intrinsic efficiency of the measurement devices.

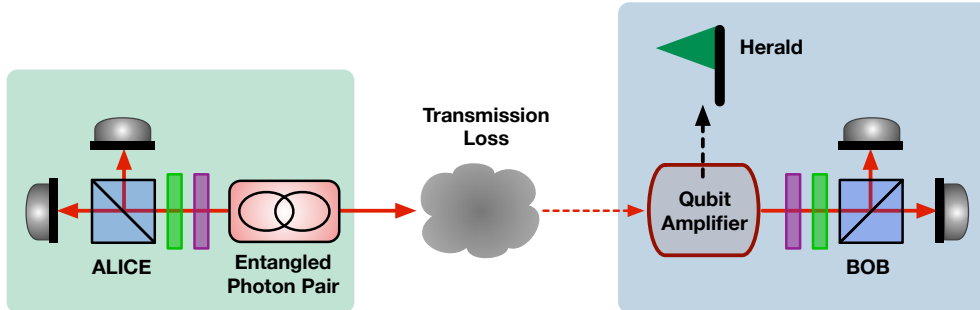


Figure 3.1: Conceptual diagram of a one-way device-independent quantum key distribution (DIQKD) protocol, using a heralded noiseless qubit amplifier to overcome transmission loss. Alice possesses a source of entangled photon pairs, and send one photon across a lossy quantum transmission channel to Bob. The state, initially a qubit encoded in the polarisation of a pure single photon, is now a mixture of single vacuum and single photon. The qubit amplifier nondeterministically increases the weight of the single photon term in the mixture, in principle arbitrarily close to a single photon. Alice and Bob only perform measurements on their respective photonic qubits when successful amplification is heralded in Bob's qubit amplifier. In this way, their detection efficiency only depends on the intrinsic quantum efficiency of their detectors, and no longer on transmission efficiency. If their detectors are reasonably efficient, Alice and Bob can violate a Bell inequality, which effectively guarantees that they share entanglement, independently of what their specific measurement procedure was.

Closing the detection loophole in an optical Bell test experiment is essentially equivalent to establishing device-independent quantum key distribution (DIQKD) between two parties, as the rigorous violation of a Bell inequality guarantees the presence of entanglement independent of the specific measurement procedure [77–80]. Another approach to closing the detection loophole, by heralding the presence of a qubit using a quantum non-demolition measurement [81], has been proposed but so far not demonstrated.

The one-way DIQKD protocol pictured in 3.1 could be implemented using a heralded noiseless qubit amplifier, as suggested in [77]. Alice, who trusts her measurement device and entangled photon source, sends half of an entangled photon pair through the transmission channel, to Bob. The transmission channel, assumed to have a low efficiency, transforms the single photon into a mixed state, in which the vacuum term dominates. Once the mixed state reaches Bob, it is sent to the qubit amplifier, which heralds the successful amplification of the single photon component—or equivalently, suppression of the vacuum term. Bob and Alice then only measure the subset of amplified states, which in principle can be maximally entangled. If Alice and Bob's detectors are reasonably efficient, they should be able to demonstrate the violation

of a Bell inequality, despite the loss present in the transmission channel.

3.3 Amplifying Quantum States

Amplifying a signal is ubiquitous in long-range classical communication networks. It is impossible to amplify a quantum signal in a similarly straightforward way, as the linearity of quantum mechanics precludes deterministically cloning an unknown quantum state [39, 40]. The early investigations that culminated in the famous no-cloning theorem were greatly motivated by the problem of distinguishing between two or more quantum states. Two perfectly distinguishable quantum states are represented by orthogonal vectors in Hilbert space, and in fact, deterministic cloning is only possible for such a restricted set of orthogonal states [82]. As two orthogonal states are perfectly distinguishable to begin with, cloning cannot increase their distinguishability. Thus, preserving the indistinguishability of quantum states [83, 84] can be seen as an equivalent restriction on permissible operations. The original no-cloning theorem was formulated for pure states, but has been extended to non-commuting mixed states [85].

A quantum state represented in phase space has a phase angle Θ and an associated phase uncertainty $\Delta\Theta$, as seen in Figure 3.2(a). Amplification increases the amplitude of the state, or displaces the state further from the origin in phase space. Noiseless amplification would reduce phase uncertainty, and increase the distinguishability of states. The process must therefore add enough noise to maintain $\Delta\Theta$ after the amplification, or the overlap of two states in 3.2(b). A rigorous derivation of the minimum noise added to an arbitrary quantum state when it is deterministically amplified can be found in [61].

Noiseless amplification of a coherent state $|\alpha\rangle$ increases its amplitude by a factor g , in the transformation

$$|\alpha\rangle \rightarrow |g\alpha\rangle, \quad (3.1)$$

where $|g| > 1$. Although deterministic noiseless amplification is impossible, noiseless amplification can be achieved by making the transformation non-deterministic [86]:

$$|\alpha\rangle\langle\alpha| \rightarrow P|g\alpha\rangle\langle g\alpha| + (1 - P)|0\rangle\langle 0|, \quad (3.2)$$

where the state is successfully amplified by the factor g with probability P , and with probability $1-P$ the transformation fails, and the output state is assumed to be vacuum (without loss of generality). It is now the probability of success that

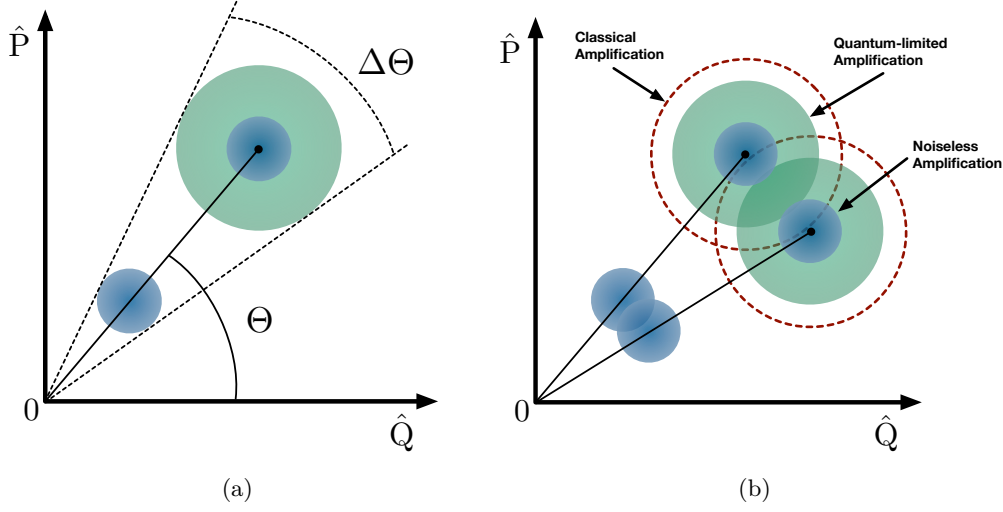


Figure 3.2: (a) A coherent state represented in phase space has a phase angle Θ , and an associated phase angle uncertainty $\Delta\Theta$. Noiselessly amplifying an arbitrary state, or displacing it further from the origin in phase space, would concentrate its phase information by reducing $\Delta\Theta$. This is prohibited by the linearity of quantum mechanics, and consequently the state's quadrature variances $\Delta\hat{Q}$ and $\Delta\hat{P}$ must increase accordingly, to preserve $\Delta\Theta$. (b) Illustration of noiseless amplification of two quantum states increasing their distinguishability, which is prohibited by the linearity of quantum mechanics. Quantum-limited deterministic amplification will preserve the distinguishability of two quantum states, while classical amplification will decrease the distinguishability.

guarantees the distinguishability of states is not increased. For the case of a small coherent state $|\alpha\rangle$, the upper bound on the success probability is:

$$P \leq \frac{1 - \exp[-|\alpha|^2]}{1 - \exp[-|g\alpha|^2]} . \quad (3.3)$$

For the maximum allowable probability, the average distinguishability of the state after amplification is equal to the distinguishability of the original state.

3.3.1 Strategies for Noiseless Amplification

The optimal strategies for deterministic noisy amplification, or optimal quantum cloning, have been investigated and realised in many cases [87, 88]. More recently, nondeterministic noiseless amplification has generated a great amount of theoretical and experimental activity, and several different approaches to noiseless linear amplification of optical states have been experimentally demonstrated [89]. Different strategies often share several features in common: they are non-deterministic, but heralded by an independent signal; they require ancillary states; and they have so

far only been demonstrated for states of relatively small amplitude.

One noiseless amplification strategy consists of coherent addition and subtraction of a single photon from the state [64]. Coherent addition and subtraction of a single photon to an optical state approximately corresponds to applying the creation and annihilation operators to the state. Exploiting the commutation relation between the two operators [90, 91], coherent photon addition followed by subtraction doubles the amplitude of a small coherent state:

$$\hat{G}_{g=2}|\alpha\rangle = \hat{a}\hat{a}^\dagger|\alpha\rangle \quad (3.4a)$$

$$\simeq \hat{a}\hat{a}^\dagger(|0\rangle + \alpha|1\rangle) \quad (3.4b)$$

$$= |0\rangle + 2\alpha|1\rangle. \quad (3.4c)$$

In (3.4), the amplitude α of the initial coherent state is taken to be small, $|\alpha| \ll 1$. In this limit, the coherent state $|\alpha\rangle$ can be approximated to a very high fidelity by a superposition of the $|0\rangle$ and $|1\rangle$ number states:

$$|\alpha\rangle \simeq |0\rangle + \alpha|1\rangle. \quad (3.5)$$

A single photon is coherently added to the initial state using a down-converter setup, and the other photon in the down converted pair acts as a heralding signal for photon addition. Successful amplification in [64] is heralded by coincidence detection between the idler from the down-converted pair, and the photon subtracted from the state. The amplifier setup requires mode matching between the down-converter and the signal state, but does not require interferometric stability, and the amplified output state is of high fidelity. This is for a fixed amplitude gain $g = 2$, however, and varying the gain factor would require a more sophisticated setup, with interferometric stability.

Another approach to amplification involves incoherently adding photons to a state, followed by photon subtraction [65]. The small coherent state in (3.5) is displaced by the addition of thermal noise. Subtraction of a pre-determined number of photons heralds the output state, which has a reduced phase uncertainty due to the conditioning. The transformation is not noiseless, as the output state is less pure than the input, but demonstrating that adding thermal noise and conditioning can concentrate the phase information of a state is nevertheless surprising and significant.

This chapter presents experimental results on the heralded noiseless amplification of a two-mode state, based on the generalised quantum scissors technique. Generalised quantum scissors are a modification of optical state truncation [92], which

is a method of limiting the number-state expansion of an optical state to leave only its vacuum and one photon components. The noiseless amplification of single mode states using the generalised quantum scissors approach has been successfully demonstrated in several experiments [62, 63, 66, 93, 94]. Loss mitigation for a single-rail qubit using generalised quantum scissors has also recently been demonstrated [67].

3.3.2 Quantum Scissors

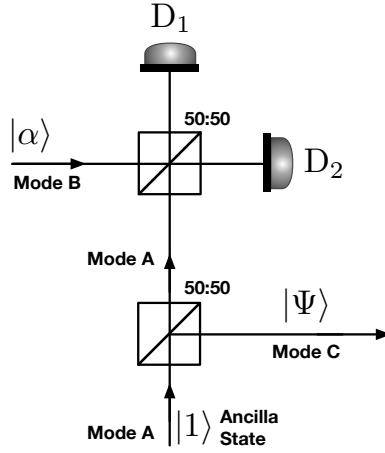


Figure 3.3: Quantum scissors setup proposed by Pegg *et al.* [92]. The original aim was to prepare an arbitrary single mode state of the form $|\Psi\rangle = \gamma_0|0\rangle + \gamma_1|1\rangle$, by sending a coherent state $|\alpha\rangle$ to the input (Mode B), and projecting it into the output (Mode C) by projective measurement in one of the two heralding detectors (D_1 or D_2). The protocol uses the mode entanglement of a de-localised single photon ancilla between Mode A and Mode C, and single photon detection to condition the correct state in the output mode. The protocol is nondeterministic but heralded, and if the input is a small amplitude coherent state $|\alpha| \ll 1$, or simply a superposition of vacuum and a single photon state, then the quantum scissors effectively teleports the state from the input mode into the output mode. As in the traditional teleportation protocol [33], no light from the original state is ever transmitted to the output, and it is the information in the wave function that is teleported into the output mode.

In the original formulation of the quantum scissors by Pegg *et al.*, the aim was to create an arbitrary superposition state of vacuum and single photon, of the form $\gamma_0|0\rangle + \gamma_1|1\rangle$, which they note is the simplest optical state containing any phase information. Other approaches to creating such superposition states have subsequently been investigated [95]. Their strategy was to use a coherent state $|\alpha\rangle$, and truncate higher order terms (hence the name *quantum scissors*), leaving only

the vacuum and single photon terms with the phase relationship intact:

$$|\alpha\rangle = \sum_{n=0}^{\infty} \gamma_n |n\rangle \rightarrow |\psi\rangle = \gamma_0 |0\rangle + \gamma_1 |1\rangle . \quad (3.6)$$

The apparatus for optical state truncation is illustrated in Figure 3.3. An ancillary single photon state in mode A of Figure 3.3 is sent to a 50:50 beam splitter, and is transformed into a de-localised single photon state in modes A and C:

$$|1\rangle_A \rightarrow |\phi\rangle_{A,C} = \frac{1}{\sqrt{2}}(|1\rangle_A |0\rangle_C + i|0\rangle_A |1\rangle_C) \quad (3.7a)$$

$$= \frac{1}{\sqrt{2}}(\hat{a}^\dagger + i\hat{c}^\dagger)|\mathbf{0}\rangle , \quad (3.7b)$$

where \hat{a}^\dagger (\hat{c}^\dagger) is the creation operator for spatial mode A (C), and $|\mathbf{0}\rangle$ is the global vacuum state. The state $|\phi\rangle_{A,C}$ is a mode-entangled state, or a de-localised single photon state [96–98]. After the first beam splitter, mode A of $|\phi\rangle_{A,C}$ is superposed at a second 50:50 beam splitter with a coherent state $|\alpha\rangle_C$ from mode C. The combined state $|\phi\rangle_{A,C} \otimes |\alpha\rangle_B$ is transformed via the beam splitter operator $\hat{U}_{A,B}$ for modes A and B:

$$|\phi\rangle_{A,C} \otimes |\alpha\rangle_B \rightarrow |\Psi\rangle = \hat{U}_{A,B}(|\phi\rangle_{A,C} \otimes |\alpha\rangle_B) \quad (3.8a)$$

$$= \hat{U}_{A,B}|\phi\rangle_{A,C} \otimes \hat{U}_{A,B}|\alpha\rangle_B. \quad (3.8b)$$

The beam splitter operator has the form

$$\hat{U}_{A,B} = \exp \left[i \frac{\pi}{4} (\hat{a}^\dagger \hat{b} + \hat{a} \hat{b}^\dagger) \right] , \quad (3.9)$$

and its effect [56] on the states $|\phi\rangle_{A,C}$ and $|\alpha\rangle_B$ is

$$\hat{U}_{A,B}|\phi\rangle_{A,C} = \frac{1}{\sqrt{2}}\hat{U}_{A,B}(\hat{a}^\dagger + i\hat{c}^\dagger)|\mathbf{0}\rangle \quad (3.10a)$$

$$= \frac{1}{\sqrt{2}} \left(\frac{1}{\sqrt{2}} (\hat{a}^\dagger + i\hat{b}^\dagger) + i\hat{c}^\dagger \right) |\mathbf{0}\rangle \quad (3.10b)$$

and

$$\hat{U}_{A,B}|\alpha\rangle_B = \hat{U}_{A,B}|\alpha\rangle_B \quad (3.11a)$$

$$= \left| \frac{i\alpha}{\sqrt{2}} \right\rangle_A \left| \frac{\alpha}{\sqrt{2}} \right\rangle_B \quad (3.11b)$$

$$= \exp \left[\frac{-|\alpha|^2}{2} \right] \left(\sum_{n=0}^{\infty} \left(\frac{i\alpha}{\sqrt{2}} \right)^n \frac{(\hat{a}^\dagger)^n}{n!} \right) \left(\sum_{m=0}^{\infty} \left(\frac{\alpha}{\sqrt{2}} \right)^m \frac{(\hat{b}^\dagger)^m}{m!} \right) |\mathbf{0}\rangle \quad (3.11c)$$

Note that, while the state in (3.10) is mode entangled, the state in (3.11) is fully factorized, and therefore has no entanglement.

The output state of the quantum scissors is heralded by a single photon detection in either mode A or mode B. Detections of single photons in both mode A and mode B, or of two photons in either of the modes, do not constitute successful heralding events. This corresponds to projecting $|\Psi\rangle$ onto either $\langle 1_A 0_B|$ or $\langle 0_A 1_B|$, to herald the desired superposition state in the output mode. The output state consists of those terms where $\langle 1_A 0_B|\Psi\rangle$ and $\langle 0_A 1_B|\Psi\rangle$ are non-zero, and both of these correspond to at most one photon in modes A and B. Higher order terms in the state (3.11) will consequently be filtered out. To calculate the quantum scissors output, the coherent states need only be expanded to first order. The two successful heralding events are:

$$\langle 1_A 0_B|\Psi\rangle = \frac{\exp\left[\frac{-|\alpha|^2}{2}\right]}{\sqrt{2}} \langle 1_A 0_B| \left(\frac{1}{\sqrt{2}} (\hat{a}^\dagger + i\hat{b}^\dagger) + i\hat{c} \right) \left(1 + i\frac{\alpha}{\sqrt{2}}\hat{a}^\dagger \right) \left(1 + \frac{\alpha}{\sqrt{2}}\hat{b}^\dagger \right) |0\rangle \quad (3.12a)$$

$$= \frac{1}{2} \exp\left[\frac{-|\alpha|^2}{2}\right] (1 - \alpha\hat{c}^\dagger) |0\rangle, \quad (3.12b)$$

$$\langle 0_A 1_B|\Psi\rangle = \frac{i}{2} \exp\left[\frac{-|\alpha|^2}{2}\right] (1 + \alpha\hat{c}^\dagger) |0\rangle. \quad (3.12c)$$

One of the heralded states, $\langle 0_A 1_B|\Psi\rangle$, is a copy of the input coherent state $|\alpha\rangle$ in the output mode, up to a normalisation factor, and with the higher order terms truncated. The other heralded state, $\langle 1_A 0_B|\Psi\rangle$, is a copy of $|\alpha\rangle$ with an additional π phase shift between the vacuum and single photon term. As this π phase shift is associated with one of the two known heralding events, it can always be corrected at the output.

Pegg *et al.* note in [92] that their protocol is similar to quantum teleportation [33], and in fact, teleportation using quantum scissors has been experimentally demonstrated [99]. The typical quantum teleportation protocol uses EPR-entangled ancillae and a Bell state measurement, while in the quantum scissors the mode entanglement of a de-localised single photon is used. Both protocols, however, require classical communication to correct for potential phase shifts in the output mode. Since it was first proposed, the quantum scissors protocol has inspired numerous theoretical investigations into possible realisations [100–102] and optimisations [103].

3.3.3 Generalised Quantum Scissors

Ralph and Lund introduced a modification to the quantum scissors [62, 104], known as the generalised quantum scissors, in which the amplitude of the single photon term in the superposition state is increased at the output. If the input state is considered to be a small coherent state ($|\alpha| \ll 1$), or a superposition of the vacuum and a single photon to begin with, the output state is then an amplified version of the input. The modification to the original quantum scissors is that the first 50:50 beam splitter in Figure 3.3 becomes a variable reflectivity beam splitter in Figure 3.4(a), with amplitude reflectivity denoted by η .

The state $|\phi\rangle_{A,C}$ in (3.7) becomes

$$|\phi\rangle_{A,C} = \frac{1}{\sqrt{2}} \left(\sqrt{1-\eta} \hat{a}^\dagger + i\sqrt{\eta} \hat{c}^\dagger \right) |0\rangle. \quad (3.13)$$

The superposition of the single photon between modes A and C is no longer equally weighted, as the beam splitter reflectivity η determines the splitting ratio. The heralded output states from the generalised quantum scissors are:

$$\langle 1_A 0_B | \Psi \rangle = \exp \left[\frac{-|\alpha|^2}{2} \right] \left(\sqrt{\frac{1-\eta}{2}} - \sqrt{\frac{\eta}{2}} \alpha \hat{c}^\dagger \right) |0\rangle \quad (3.14a)$$

$$= \sqrt{\frac{1-\eta}{2}} \exp \left[\frac{-|\alpha|^2}{2} \right] \left(1 - \sqrt{\frac{\eta}{1-\eta}} \alpha \hat{c}^\dagger \right) |0\rangle, \quad (3.14b)$$

$$\langle 0_A 1_B | \Psi \rangle = \exp \left[\frac{-|\alpha|^2}{2} \right] \left(i\sqrt{\frac{1-\eta}{2}} + i\sqrt{\frac{\eta}{2}} \alpha \hat{c}^\dagger \right) |0\rangle \quad (3.14c)$$

$$= i\sqrt{\frac{1-\eta}{2}} \exp \left[\frac{-|\alpha|^2}{2} \right] \left(1 + \sqrt{\frac{\eta}{1-\eta}} \alpha \hat{c}^\dagger \right) |0\rangle. \quad (3.14d)$$

In the new heralded output states, the single photon term in the superposition is weighted by a coefficient. Identifying the amplitude gain $g \equiv \sqrt{\eta/(1-\eta)}$, the amplitude of the single photon is probabilistically increased without adding noise to the state:

$$|\alpha\rangle \simeq |0\rangle + \alpha|1\rangle \rightarrow |0\rangle + g\alpha|1\rangle \simeq |g\alpha\rangle. \quad (3.15)$$

The generalised quantum scissors is a noiseless linear amplifier (NLA), with the amplitude gain g determined by the ratio of the amplitude reflectivity to transmissivity at the variable beam splitter. The probability of successfully heralding an amplified output state is proportional to $1-\eta = (1+g^2)^{-1}$, implying that for larger amplifications the probability of success will diminish proportionally.

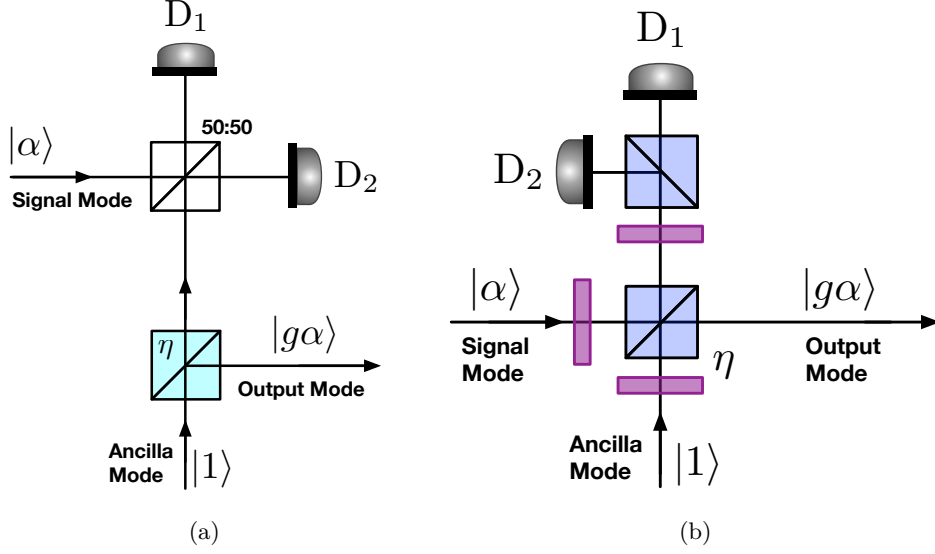


Figure 3.4: (a) Generalisation of the quantum scissors protocol. The first 50:50 beam splitter becomes a variable–reflectivity beamsplitter, where η denotes its amplitude reflectivity. This changes the weighting of the single photon in the output state, which is an effective amplitude gain. The gain factor is $g \equiv \sqrt{\eta/(1-\eta)}$, and $|g| > 1$ when $\eta > 1/2$, or when more of the single photon is reflected into the output mode than sent to the heralding detectors. The probability of success scales inversely with gain: $P \simeq (1 + g^2)^{-1}$. A higher gain leads to a lower success probability. (b) The experimental implementation of the generalised quantum scissors NLA stage. The variable reflectivity η is achieved using a HWP and PBS in the ancilla mode. The signal state is reflected at the first beam splitter, and superposed with the transmitted ancilla mode. The two modes are indistinguishable in all degrees of freedom at that point, but in orthogonal polarisations: the signal is in $|V\rangle$ and the ancilla is in $|H\rangle$. The second HWP and PBS project into the $\{|D\rangle, |A\rangle\}$ basis, effectively making the modes completely indistinguishable (erasing which–path information). The amplified output state is then heralded by D_1 or D_2 , in the same way as before.

In practice, the NLA stage based on generalised quantum scissors is constructed according to the schematic in Figure 3.4(b). The variable reflectivity beam splitter from Figure 3.4(a) is achieved using a HWP and PBS in the ancilla mode. As before, the ancilla photon is entangled between the reflected mode, at the NLA output, and the transmitted mode that is directed to the heralding detectors. The input state $|\alpha\rangle$ is reflected at the first PBS and, as before, no light from the signal mode ever directly reaches the output mode. The ancilla and signal are mode matched after the first beam splitter, except for the polarisation degree of freedom where they occupy orthogonal polarisation modes. The second HWP and PBS project the heralding beam into a polarisation basis shifted by $\pi/2$ on the Poincaré sphere, effectively erasing which–path information. Successful amplification in the output mode is again heralded by a single photon detection in either D_1 or D_2 .

3.4 Experimental Concept

In contrast to previous experiments in noiseless linear amplification [62–64, 66], now we are not interested in single mode states of the form $|\Psi\rangle = \gamma_0|0\rangle + \gamma_1|1\rangle$, but in single photons mixed with the vacuum state. The state of a single photon subspace can be a two-mode state, and in fact, a qubit encoded on the polarisation state of a single photon is just such a state. After transmission through any quantum channel with non-zero loss, a photonic qubit will be in the mixed state ρ_{in} , consisting of a vacuum and single photon component:

$$\rho_{\text{in}} = \gamma_0|0\rangle\langle 0| + \gamma_1|\psi_1^{\text{in}}\rangle\langle\psi_1^{\text{in}}|, \quad (3.16)$$

where the vacuum state will dominate ($\gamma_0 > \gamma_1$) for a very lossy channel. The qubit is encoded in the polarisation state of the single photon subspace:

$$|\psi_1^{\text{in}}\rangle = \alpha|1_{\text{H}}0_{\text{V}}\rangle + |0_{\text{H}}1_{\text{V}}\rangle \equiv \alpha|\text{H}\rangle + \beta|\text{V}\rangle. \quad (3.17)$$

The state ρ_{in} is the input to the qubit amplifier, $|\text{H}\rangle$ denotes the horizontal polarisation state and $|\text{V}\rangle$ the vertical polarisation state. The noiseless qubit amplifier is an optical circuit that works probabilistically, but with an independent heralding signal, to generate the transformation

$$\rho_{\text{in}} \rightarrow (1 - P)|00\rangle\langle 00| \otimes \Pi_{\text{f}} + P\rho_{\text{out}} \otimes \Pi_{\text{h}}. \quad (3.18)$$

Here Π_{h} is the projector on the subspace of heralding states corresponding to successful amplification, with the amplified state ρ_{out} at the circuit output:

$$\rho_{\text{out}} = \frac{\gamma_0|00\rangle\langle 00| + g^2\gamma_1|\psi_1^{\text{in}}\rangle\langle\psi_1^{\text{in}}|}{N}. \quad (3.19)$$

The projector Π_{f} (fail) projects onto the subspace of cases in which the heralding success signal is not received, and the state is discarded. The relative weighting of the qubit subspace $|\psi_1^{\text{in}}\rangle$ in the mixed state is increased by the gain factor g^2 .

Owing to amplification, the output state must be renormalised by $N = \gamma_0 + g^2\gamma_1$. With probability P , the likelihood of detecting a single photon is actually multiplied by the factor $G_{\text{nom}} = g^2/N$, where G_{nom} takes renormalisation into account. Amplification occurs when $G_{\text{nom}} > 1$, implying that $\gamma_0/N < 1$, or that the vacuum component is reduced compared to what it is in the input state.

The qubit amplifier is constructed from two noiseless linear amplification (NLA)

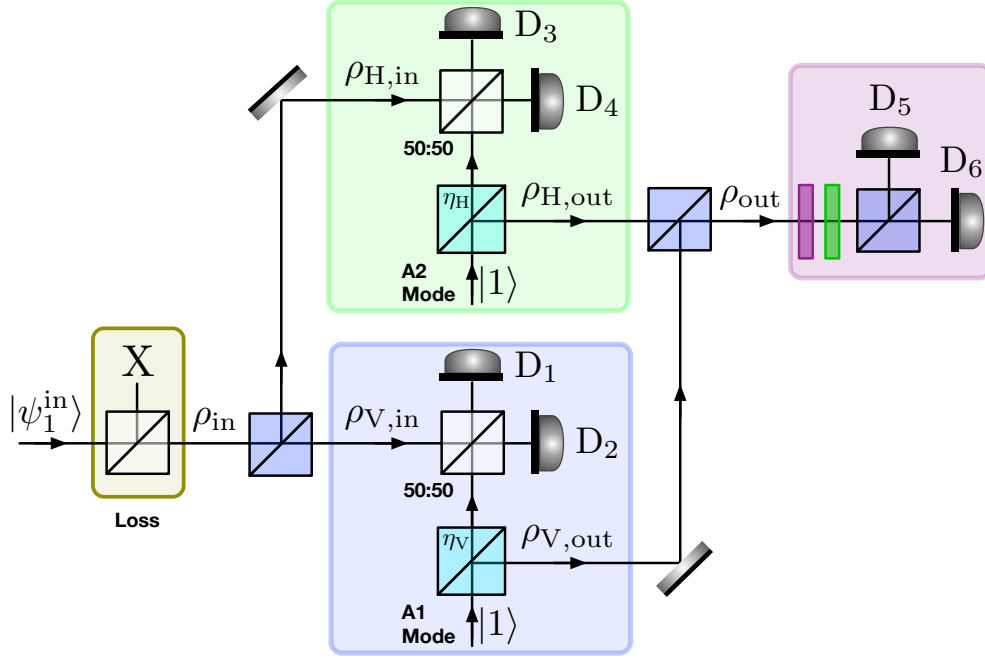


Figure 3.5: Conceptual diagram of the noiseless qubit amplifier circuit. The input signal ρ_{in} is split with a PBS into its polarisation components $\rho_{\text{H},\text{in}}$ and $\rho_{\text{V},\text{in}}$, which are individually amplified in separate NLA stages. The reflectivities η_{H} and η_{V} (always set to be equal) are related to the amplifier gains through $g = \sqrt{\eta/(1-\eta)}$. The amplified states $\rho_{\text{H},\text{out}}$ and $\rho_{\text{V},\text{out}}$ are coherently recombined to recover ρ_{out} , the amplified qubit at the output.

stages, and is depicted in 3.5. This application of single-mode NLA stages was proposed theoretically in [77]. Orthogonal polarisations $|H\rangle$ and $|V\rangle$ that are the basis states of the qubit are amplified individually in separate NLA stages, and coherent recombined at the output. Although the two NLA stages are independent, their combined effect in the qubit amplifier is to increase coherence between two output modes that do not interact.

The reflectivity of the variable beam splitter in each NLA stage (η_{H} and η_{V}) determines the nominal gain in the mode. Successful amplification is heralded by detection of a photon in only one of the detectors in each stage (either D_1 or D_2 in the stage amplifying $|V\rangle$, and either D_3 or D_4 in the stage amplifying $|H\rangle$), and the output state is analysed using detectors D_5 and D_6 . An important point is that the decision to keep a particular signal is based solely on an independent heralding event that occurs before the final measurement choice. There is no post-selection on the final measurement results.

Figure 3.5 is a conceptual depiction of the experiment. A qubit is initially encoded on the polarisation state $|\psi_1^{\text{in}}\rangle$ of a single photon. Polarisation-independent loss is

applied to the single photon, transforming it into the mixed state ρ_{in} . A PBS separates the orthogonal polarisation modes of the qubit in the single photon subspace of ρ_{in} , sending the $|V\rangle$ mode to be amplified in the lower NLA stage, and $|H\rangle$ to be amplified in the upper stage. When both amplifications are successfully heralded, the output states $\rho_{H,\text{out}}$ and $\rho_{V,\text{out}}$ from each NLA stage are coherently recombined at a PBS, to recover the final output state ρ_{out} . Quantum state tomography can then be performed on ρ_{out} to verify that the photon subspace has been increased, and that coherences in the polarisation state have survived.

3.5 Experimental Setup

The experimental setup consisted of a SPDC single photon source, described in Section 3.5.1, and an optical circuit described in Section 3.5.2. Details can also be found in [60].

The SPDC source is double-passed, allowing collection of two photon pairs into four spatial modes. Three of the photons are used directly in the circuit, and the last photon is sent directly to a single photon counting module, and acts as an external trigger. The conceptual depiction of the qubit amplifier in Figure 3.5 shows polarisation modes being separated into orthogonal spatial modes, and then recombined after amplification. This implies interferometric stability between the the two NLA stages, which would be technically very challenging to achieve. To avoid this, the two polarisation modes remain in the same spatial mode, which makes the entire optical circuit in Figure 3.7 passively stable.

3.5.1 SPDC Source

The laser used was a *Tsunami* model Ti:Sapphire laser, manufactured by *Spectra-Physics*. This laser could provide approximately 2.8 W of frequency-tunable pulsed coherent light in the TEM₀₀ spatial mode. The repetition rate was 80 MHz, with a pulse width of ~ 100 fs. The laser was operated at 780 nm wavelength, and part of the output was used as a pump field for second harmonic generation (SHG) in a 2 mm thick β -Barium Borate (BBO) crystal. The 780 nm pump frequency is filtered after the SHG using two dichroic mirrors and a pair of prisms, to ensure that only 390 nm light is sent to the SPDC crystal. A small iris is placed in between the two prisms, to additionally filter out other frequencies. Back-reflected 390 nm light is also filtered with a dichroic mirror, to prevent reflections from re-entering the laser

cavity and de-stabilising the mode locking.

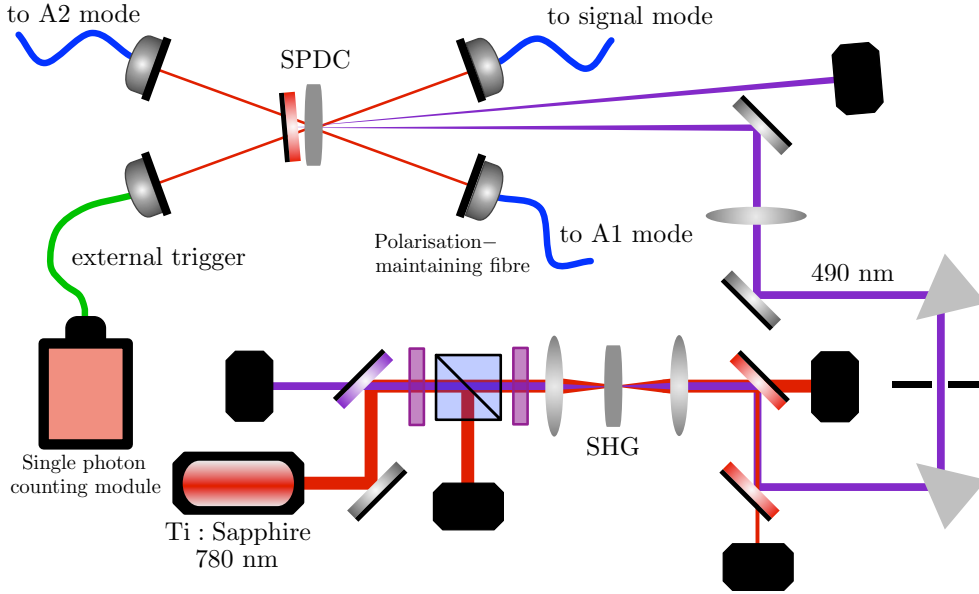


Figure 3.6: Schematic representation of the SPDC source used to generate single photon states for the qubit amplifier circuit. The SPDC crystal (BBO cut for type-I, degenerate down conversion) is pumped with 100 mW of 390 nm light from an SHG process (see text for details). The down converted photon pair from the forward pass of the pump beam passes through a dichroic mirror, and is coupled into single mode optical fibre. One of the photons is sent directly to a fibre-coupled single photon counting module, and acts as an external trigger to herald the presence of its pair in the circuit. Its pair is couple into polarisation-maintaining optical fibre, and is sent to the A2 mode (see Figure 3.7). The pump beam is retro-reflected at the dichroic mirror, and another down converted photon pair is independently generated in the backward pass through the crystal. Both photons are coupled into polarisation maintaining optical fibres, and are sent to the signal and A1 modes of the optical circuit.

The 390 nm light is used to pump a 2 mm thick BBO crystal cut for type-I (polarisation-unentangled) SPDC. The pump beam was focused using a plano-convex spherical lens with a 50 cm focal length. The pump beam is double-passed through the SPDC crystal, with a dichroic mirror retro-reflecting the 390 nm beam, while transmitting the 780 nm light down converted from the forward pass. The pump beam must be reflected at a slight angle from the forward optical path, to prevent it from re-entering the laser cavity and de-stabilising the laser. A beam dump is therefore put in the path of the retro-reflected beam some distance behind the SPDC crystal.

The down converted light is coupled into single mode optical fibres. Long-pass filters (not pictured) are placed directly before all four fibre couplers, to additionally filter out background 390 nm light. Both photons generated in the backward pass, and

one of the photons from the forward pass, are coupled into polarisation-maintaining fibres, and sent to the optical circuit. The other photon from the forward pass acts as an external trigger, to herald the presence of its pair in the optical circuit, and is coupled into regular single mode optical fibre and sent to a single photon counting module.

3.5.2 Noiseless Linear Amplification Stages

The interferometer from Figure 3.5 was experimentally realised in polarisation-mode configuration. The orthogonal polarisation modes $|H\rangle$ and $|V\rangle$ that are the basis states of the qubit remain in the same spatial mode, making the optical circuit passively stable against vibrations. The two NLA stages from 3.5 are in series in 3.7, and the polarisation modes are individually addressed using wave plates and polarising beam splitters.

One of the single photons from the backward pass of the SPDC source is sent to the signal mode of the optical circuit, depicted in 3.7. Immediately after exiting the polarisation-maintaining fibre, the photon passes through a HWP and PBS. This serves two purposes: to ensure the initial purity of the photon's polarisation state, and apply loss. Applying loss before preparing the polarisation qubit state is equivalent to applying polarisation-independent loss to the qubit. The polarisation state is next encoded onto the single photon subspace using a QWP and HWP, and the state in the optical circuit becomes ρ_{in} from Equation (3.16).

The two ancilla photons pass through a HWP and PBS (not shown in Figure 3.7) immediately after exiting the optical fibre, to ensure their highly pure polarisation states. The effective reflectivities η_H and η_V of the central beam splitters in the NLA stages are set to be equal, to apply identical gain factors to both polarisation modes. The axis of the HWP between the two NLA stages was set to 45 degrees, to flip the polarisations so the $|H\rangle$ mode is amplified in the second stage. The advantage of the setup in 3.7 is that the two amplified polarisation modes are automatically recombined in the output, in an inherently stable way. State tomography is performed on ρ_{out} using the output detector D_5 and D_6 .

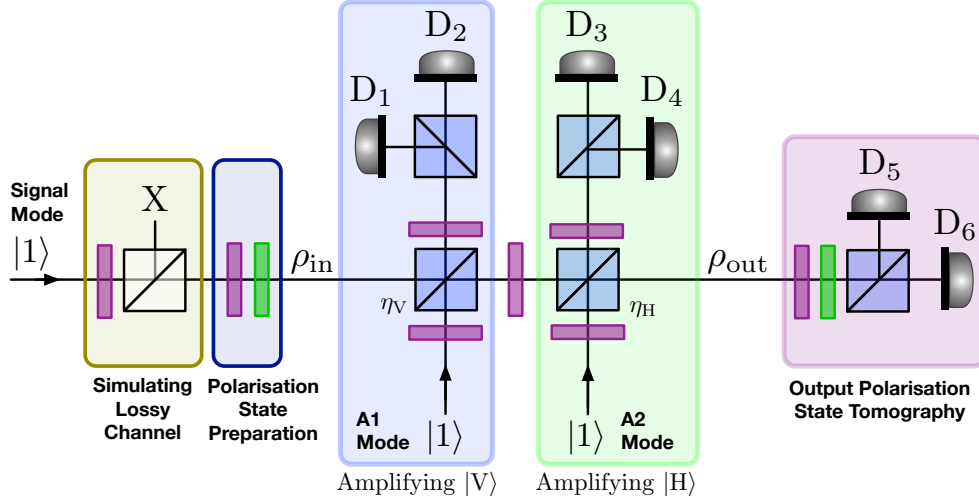


Figure 3.7: Experimental qubit amplifier circuit. The orthogonal spatial modes of the conceptual interferometer in Figure 3.5 are here superposed in the same spatial mode, to make the optical circuit passively stable. The NLA stages are implemented in series, and the $|V\rangle$ polarisation is reflected at the PBS in the first stage to be amplified, while the $|H\rangle$ polarisation passes through unchanged. A HWP with its optic axis set to 45 degrees flips the two polarisations, and the original $|H\rangle$ polarisation is reflected at the PBS in the second stage to be amplified, while the original $|V\rangle$ polarisation passes through unchanged. The amplified polarisation modes are coherently recombined in the output mode, in a way that is inherently stable, to recover the amplified qubit ρ_{out} . The initial loss was applied before qubit state preparation. This is identical to polarisation-independent loss after qubit preparation.

3.6 Experimental Results

Results were collected for three different gain settings, listed in 3.1. The loss at the beginning of the optical circuit was constant, and the size of the single photon in ρ_{in} was measured to be $\gamma_1 = 0.041 \pm 0.005$. The performance of the qubit amplifier was characterised in two ways: by directly measuring the gain factor at the output, to be compared with the gain expected from the ancilla mode splitting ratio and renormalisation; and by performing quantum state tomography on the qubit subspace of the output state, to verify that coherence was preserved, and to calculate the increase in transmission fidelity.

3.6.1 Characterising the SPDC Source and Optical Circuit

Single photon detection rates and coincidence efficiencies were measured for the source using detectors in the optical circuit. The power of the 390 nm pump beam was set to 100 mW directly before the SPDC crystal in 3.7. This is regulated using

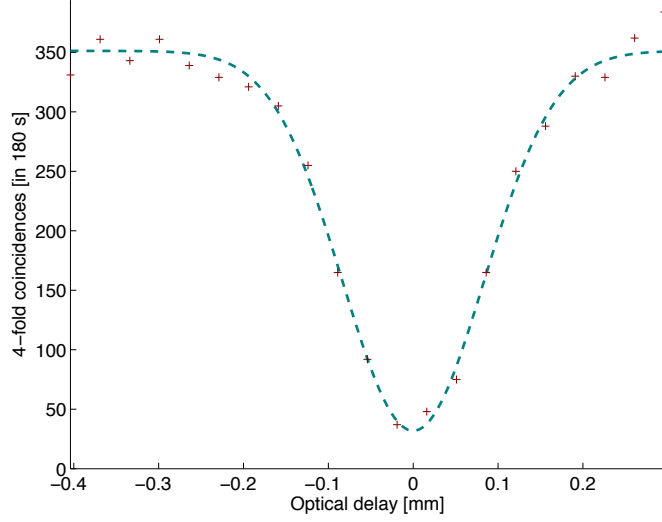


Figure 3.8: Hong-Ou-Mandel interference between the signal and A2 modes (see Figure 3.7). The optical delay was varied in A2 to match temporal modes of the two photons at the PBS. As photons in the signal and A2 modes are from independent sources (different passes in the SPDC setup), the non-classical interference must be measured using 4-fold coincidence detection between the external trigger heralding the presence of a photon in the A2 mode, and detection of an A1 photon in D_2 heralding the presence of a photon in the signal mode. The acquisition time for each data point was 180 seconds, and the fitted interference visibility was 91%.

the HWP and PBS before the SHG crystal, which controls the 780 nm power from the Ti:Sapphire laser. The 390 nm power was kept at 100 mW to limit the higher order terms created in SPDC, which would be considered noise in the qubit amplification protocol. The laser bandwidth was typically kept at a FWHM of $\sim 5.4 - 5.7$ nm, as it was found that the Ti:Sapphire laser's mode locking was less robust at narrower bandwidths. Bandpass filters of 3 nm were placed directly before the couplers at every output port of the optical circuit (not pictured), effectively setting the spectral shape of the pulses.

The photons in the signal and first ancilla (A1) mode are pairs from the backward pass of the SPDC source, and their coincidence efficiency was typically measured to be 18 – 20% in D_1 and D_2 of the circuit. The single photon detection rate from the signal mode ranged from $5.5 \cdot 10^4 \text{ s}^{-1}$ in D_1 to $4.0 \cdot 10^4 \text{ s}^{-1}$ in D_6 , while for the A1 mode it ranged from $6.5 \cdot 10^4 \text{ s}^{-1}$ in D_1 to $5.5 \cdot 10^4 \text{ s}^{-1}$ in D_6 . The photon in the second ancilla mode (A2) is from the forward pass of the SPDC source, and its pair is the external trigger photon in 3.6. The single photon detection rate from the A2 mode ranged from $1.10 \cdot 10^5 \text{ s}^{-1}$ in D_3 to $9.0 \cdot 10^4 \text{ s}^{-1}$ in D_6 , while the detection rate in the external trigger was $1.20 \cdot 10^5 \text{ s}^{-1}$. The coincidence efficiency measured between the A2 mode and the external trigger was typically $\sim 15\%$. The

lower efficiency in the forward pass was likely due to coupling more background light into those modes. Another contributing factor was that the phase matching condition was slightly different for the two passes in the source, since the reflected beam must pass through the SPDC crystal at a slightly different angle, in order to not be retro-reflected back into the laser cavity.

The signal and A1 modes are matched at the central beam splitter in the first NLA stage, to generate non-classical HOM interference that is measured in D_1 and D_2 . The two photons are matched to the same spatial and temporal mode at the central beam splitter but, as the signal photon is reflected and A1 photon is transmitted at the PBS, they are in orthogonal polarisation modes. Using the HWP and PBS in front of the two detectors, a projection on the diagonal ($|D\rangle = (|H\rangle + |V\rangle)/\sqrt{2}$) and anti-diagonal ($|A\rangle = (|H\rangle - |V\rangle)/\sqrt{2}$) polarisation basis erases which-path information, and thereby creates HOM interference that is manifested as vanishing two photon coincidence detection rate between D_1 and D_2 (see Figure 3.8).

Measuring HOM interference between the signal and ancilla photons guarantees that they are indistinguishable. As they must occupy the same temporal mode at the beam splitter, this sets a fixed phase relationship between the photon in the signal mode, and the reflected ancilla mode which is the output of the NLA stage. This is necessary to establish coherence between modes at the output. A photon detection at either D_1 or D_2 gives no information, in principle, about whether the photon came from the signal or ancilla mode, which is in essence a quantum eraser [31, 95, 105]. It is this absence of distinguishing information that induces the interference between modes, allowing a measurement in D_1 or D_2 to project the input signal into the output mode.

As the photons in the signal and A1 modes are a pair from the same source—the backward pass of the SPDC—they HOM interference can be measured in two-fold coincidence detection. The HOM interference visibility was typically measured to be $\sim 97\%$, with a small accidental coincidence rate due to detector dark counts ($< 1\%$) subtracted off. The HOM interference in the second NLA stage is between photons from independent sources, and must therefore be measured in four-fold coincidence detection. The signal mode is transmitted through the first NLA stage, and the A1 photon is sent directly to D_2 , without any mode splitting or interference. The signal and A2 modes are overlapped at the central beam splitter in the second NLA stage, and HOM interference is measured as before, in D_3 and D_4 . The photon in the A1 mode acts as a trigger to herald the presence of the presence of a photon in

the signal mode, and the external trigger similarly heralds the presence of a photon in the A2 mode. The HOM interference is thus measured in four-fold coincidence detection between the signal and A2 photons, conditioned on detection at the two triggers.

The HOM interference between the signal and A2 photons is plotted in 3.8. A Gaussian function was fitted to the data, and the interference visibility was calculated as the ratio of the Gaussian amplitude and the constant coincidence rate outside the interference region. The visibility was calculated to be 91%.

3.6.2 Amplification

Three different gain factors were investigated, for an input state with a single photon subspace size $\gamma_1 = 0.041 \pm 0.005$. To measure the size of the single photon subspace, the signal mode is transmitted directly through the circuit to D_5 and D_6 , without mode splitting or interference, and the ancillae are likewise transmitted directly to the heralding detectors (D_1 and D_2 for A1, and D_3 and D_4 for A2). The size of the single photon in ρ_{in} is the rate of detecting a single photon in D_5 or D_6 , conditioned on heralding detections in the external trigger, D_1 or D_2 , and D_3 or D_4 . The signal size is thus given by a ratio of four-fold to three-fold coincidence detections: $\mathcal{C}_4/\mathcal{C}_3$, where \mathcal{C}_3 is the appropriate combination of three-fold heralding detections, and \mathcal{C}_4 comprises an additional detection in D_5 or D_6 . To obtain a final value for γ_1 , the detected state size is scaled by the detector efficiency (ϵ_{det}) and path efficiency through the optical circuit (ϵ_{path}). We use $\epsilon_{\text{det}} = 0.5$ for our silicon avalanche photodiode detectors (*Perkin Elmer* SPCM-AQR-14FC) at 780 nm wavelength, and the optical path efficiency from the circuit input to D_5 and D_6 was measured to be $\epsilon_{\text{path}} = 0.64 \pm 0.04$. The actual input size was therefore calculated using the expression

$$\gamma_1 = \frac{1}{\epsilon_{\text{det}} \cdot \epsilon_{\text{path}}} \frac{\mathcal{C}_4}{\mathcal{C}_3} . \quad (3.20)$$

The average size of the amplified photon subspace in the output state ρ_{out} is measured using the same four-fold to three-fold coincidence detection ratio, but with the central beam splitters in the NLA stages set to the correct reflectivities η_{H} and η_{V} . Since detection and path inefficiencies affect the detected input and output states in the same way, they don't need to be included to calculate the measured gain:

$$G_{\text{m}} = \frac{(\mathcal{C}_4/\mathcal{C}_3)^{\text{amp}}}{(\mathcal{C}_4/\mathcal{C}_3)^{\text{in}}} \quad (3.21)$$

The effective reflectivities η_H and η_V for the ancilla modes in the two NLA stages were calibrated by observing the ratio of single photon detection rates D_6/D_2 for A1, and D_6/D_3 for A2. The ratio $g^2 = \eta/(1 - \eta)$ determines the nominal gain $G_{\text{nom}} = g^2/N$ after re-normalisation, where N is the normalisation factor for ρ_{out} . In the limit of $g^2\gamma_1 \ll 1$, the re-normalisation can safely be neglected, and $G_{\text{nom}} \simeq g^2$.

The performance of the qubit amplifier was characterised in two ways: in terms of its measured gain G_m , and in terms of the state fidelity between $|\psi_1^{\text{in}}\rangle$ and the output state ρ_{out} . The input photon polarisation state $|\psi_1^{\text{in}}\rangle$ was prepared in right-hand circular polarisation $|R\rangle = (|H\rangle - i|V\rangle)/\sqrt{2}$ for all three gain settings. The measured gains are compared in 3.1. In practice, successful amplification can be heralded by different combinations of coincidence detections, and the observed splitting ratios g^2 (and hence G_{nom}) varied slightly with small differences in path and detector efficiencies. To accurately estimate G_{nom} and its uncertainty, the effective splitting ratios were measured through all paths in the optical circuit that could herald successful amplification, to calculate an average value and standard deviation. Similarly, G_m was measured using a representative sample of heralding combinations: detection in D_5 or D_6 heralded by D_1 and D_3 , and detection in D_5 or D_6 heralded by D_2 and D_4 . An average measured gain and standard deviation were calculated using the four coincidence combinations.

A saturation effect can be seen in comparing the highest nominal gain $G_{\text{nom}} = 6.5 \pm 0.08$ with the corresponding measured gain $G_m = 5.7 \pm 0.5$ —this is due to the non-unit efficiency of delivering ancilla photons to the circuit, as well as to the lack of number resolution in the detectors. In the $|g| \rightarrow \infty$ limit, the attainable gain in the qubit amplifier is in principle equal to the ancilla source efficiency [60], and this is consistent with recent theory [106].

For the case of the middle gain, $G_m = 3.3$, the qubit $|\psi_1^{\text{in}}\rangle$ was prepared in the

g^2	G_{nom}	G_m
2.08 ± 0.08	2.0 ± 0.2	2.2 ± 0.2
3.48 ± 0.09	3.2 ± 0.4	3.3 ± 0.6
8.40 ± 0.45	6.5 ± 0.8	5.7 ± 0.5

Table 3.1: The nominal (G_{nom}) and measured (G_m) intensity gains were determined for three different splitting ratios g^2 (with $\eta_H = \eta_V$). The input qubit state size was $\gamma_1 = 0.041 \pm 0.005$. The nominal intensity gain was determined by measuring splitting ratios between the output detectors and heralding detectors in each NLA stage (see text for details). The measured intensity gain was determined by taking the ratio of successfully heralded photon detection rate in the output state, to the photon detection rate γ_1 in the input state.

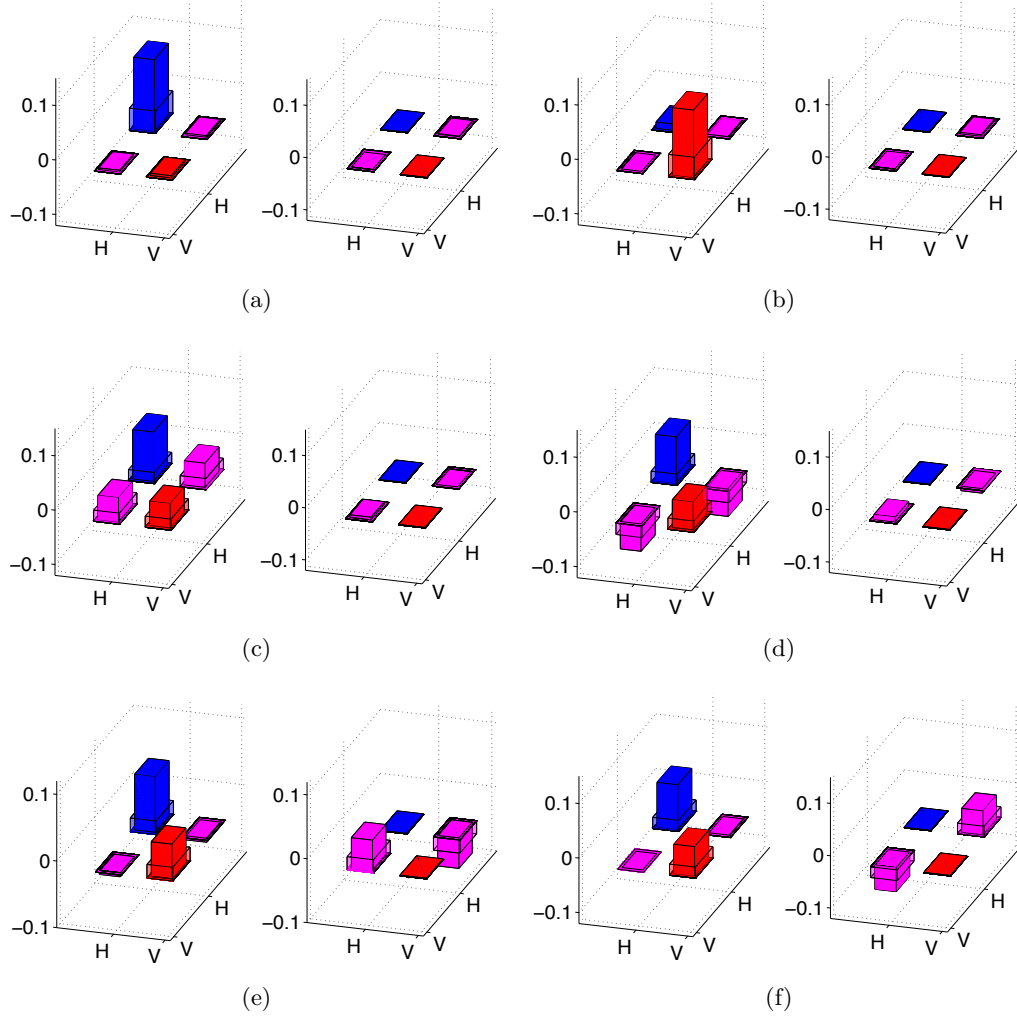


Figure 3.9: Density matrices of the single photon subspace for the six canonical polarisations inputs (a)–(f), with $G_m = 3.3 \pm 0.6$. The left-hand plots show the real elements of the density matrices, and the right-hand plots show the imaginary elements. The semi-transparent bars are the state matrix elements of the single photon qubit $|\psi_1^{\text{in}}\rangle\langle\psi_1^{\text{in}}|$ in the input state ρ_{in} , and the solid bars represent the amplified single photon subspace ρ_1^{out} of the output state ρ_{out} . The increase in the size of the single photon subspaces after amplification is apparent from the figures, as well as the fact that coherences are preserved at the circuit output. A small systematic imbalance in favour of |H⟩ is noticeable for all polarisations, and this is due to different heralding path efficiencies in the two NLA stages of the qubit amplifier. These density matrices correspond to a subspace of the system, and are consequently not normalised.

six canonical polarisation basis states $\{|H\rangle, |V\rangle, |D\rangle, |A\rangle, |R\rangle, |L\rangle\}$, and the density matrices of the output qubits were reconstructed using quantum state tomography. The un-normalised density matrices for the six output qubit subspaces are shown in Figure 3.9, with the density matrices of the corresponding input qubit subspaces

shown as semi-transparent bars. The real elements of the density matrices are plotted shown in the left subplots, and the imaginary elements in the right subplots. The increased size of the qubit subspace in the overall mixed state is apparent.

G_m	$\langle R \rho_{\text{in}} R\rangle$	$\langle R \rho_1^{\text{out}} R\rangle$	$\langle R \rho_{\text{out}} R\rangle$
2.2 ± 0.2	0.041	0.831 ± 0.005	0.071 ± 0.001
3.3 ± 0.6	0.041	0.819 ± 0.009	0.119 ± 0.008
5.7 ± 0.5	0.041	0.891 ± 0.009	0.208 ± 0.002

Table 3.2: The fidelity between the amplified output state ρ_{out} and the ideal qubit subspace $|\psi_1^{\text{in}}\rangle = |R\rangle$ was compared for all three measured gains G_m . The input fidelity $\langle R|\rho_{\text{in}}|R\rangle$ in all three cases corresponds to the size of the photon in the input (ρ_{in}), since perfect polarisation qubit preparation was assumed. The fidelity of the output qubit $\langle R|\rho_1^{\text{out}}|R\rangle$ is measured using quantum state tomography. This shows that imperfect HOM interference in the NLA stages adds polarisation mixture to the output qubit.

The fidelity between the output state and the input polarisation qubit, $\langle \psi_1^{\text{in}}|\rho_{\text{out}}|\psi_1^{\text{in}}\rangle$, is compared to the fidelity between input state and polarisation qubit, $\langle \psi_1^{\text{in}}|\rho_{\text{in}}|\psi_1^{\text{in}}\rangle$, for the three gains in Table 3.2. The fidelity $\langle \psi_1^{\text{in}}|\rho_{\text{out}}|\psi_1^{\text{in}}\rangle$ depends on the size of the qubit subspace, but also on the purity of the qubit after amplification. The qubit amplifier introduces some mixture into the polarisation qubit subspace, and ρ_{out} from (3.19) is more accurately written

$$\rho_{\text{out}} = \frac{\gamma_0|00\rangle\langle 00| + g^2\gamma_1\rho_1^{\text{out}}}{N}, \quad (3.22)$$

where the output qubit subspace ρ_1^{out} is itself a mixed state in general. This polarisation mixture is not a fundamental feature of amplification [60], but is rather a result of imperfect mode matching between the signal and ancilla modes, which translates to a decrease in the non-classical interference visibility, and hence an imprecise phase relationship between basis states in the output mode. To a lesser extent, higher order photon terms from the SPDC source that populate the ancilla modes also contribute to polarisation mixture in the qubit subspace: one down-converted photon in an ancilla pulse can trigger a heralding detector, and another photon in the same pulse can be reflected into the output mode, without fixing the phase between this second photon and the input mode. These spurious coincidence events are measured as polarisation mixture during quantum state tomography of the output mode.

For the measured gain $G_m = 3.3$, the fidelity averaged over the six polarisation states increased from $\langle \psi_1^{\text{in}}|\rho_{\text{in}}|\psi_1^{\text{in}}\rangle = 4.1\%$ to $\langle \psi_1^{\text{in}}|\rho_{\text{out}}|\psi_1^{\text{in}}\rangle = 11.7 \pm 0.8\%$. This increase in fidelity is slightly lower than the value of G_m would suggest, and it can

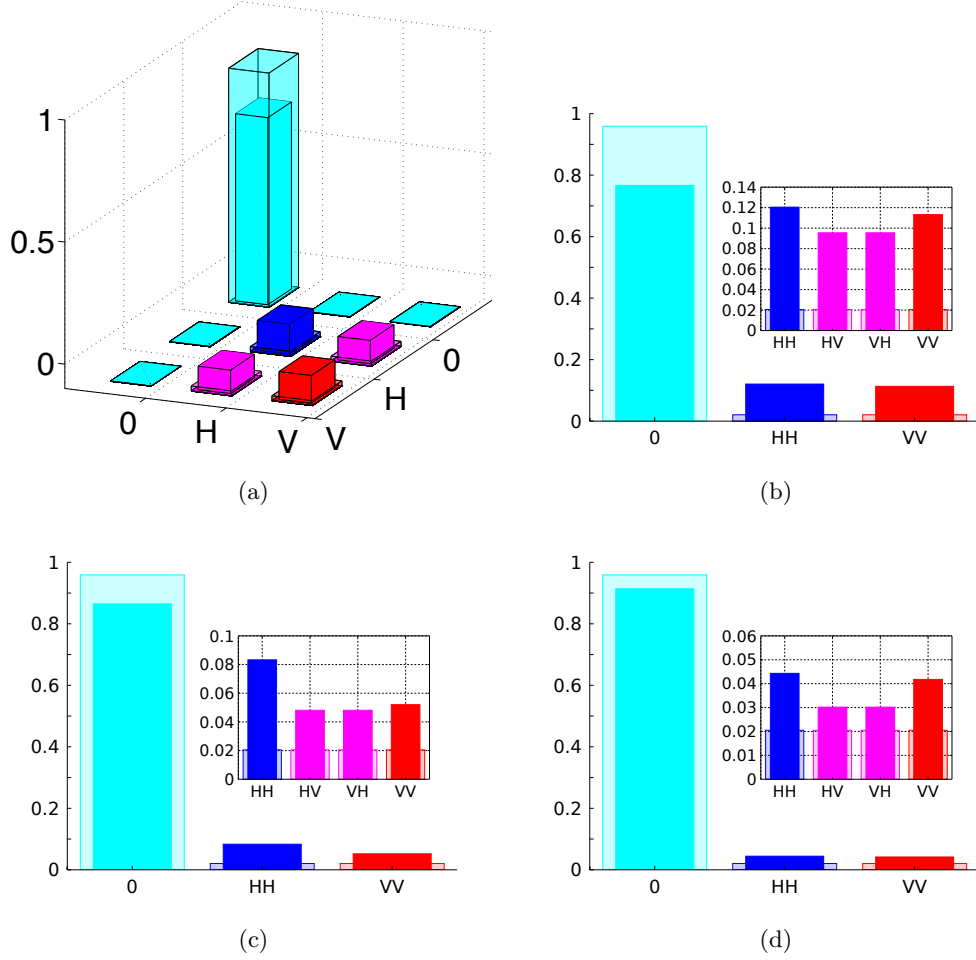


Figure 3.10: Absolute values of the ρ_{in} (semi-transparent bars) and ρ_{out} (solid bars) density matrices. (a) Absolute values of the elements from the full density matrix for gain $G_m = 5.7 \pm 0.5$ and input polarisation $|\psi_1^{\text{in}}\rangle = |R\rangle$. As the input state was an attenuated single photon, and the qubit amplifier operates on the single photon subspace, it can be assumed that no coherence exists between the vacuum and single photon subspace. The absolute values of the population and coherence terms in ρ_{in} and ρ_{out} are compared for (b) $G_m = 5.7 \pm 0.5$ (c) $G_m = 3.3 \pm 0.6$ and (d) $G_m = 2.2 \pm 0.2$, all for $|\psi_1^{\text{in}}\rangle = |R\rangle$. The comparison highlights the decrease of vacuum in the mixed state, and a corresponding increase in the size of the qubit subspace and coherences.

be explained by the polarisation mixture in ρ_1^{out} added by the qubit amplifier. The fidelities are compared for the three gain settings, with $|\psi_1^{\text{in}}\rangle = |R\rangle$, in Table 3.2. In Figure 3.10(a), the absolute value of the full density matrix for ρ_{out} (solid bars) and ρ_{in} (semi-transparent bars) is depicted. The non-zero terms in 3.10(a) are shown in 3.10(b), where it is more apparent that the vacuum term is partially suppressed and the probability of the qubit subspace is correspondingly increased as a results of amplification. The absolute values of the density matrix elements for the two

other gains are also presented in 3.10. The coherence terms between the vacuum and single photon were set to zero, as the initial state at the beginning of the optical circuit was an attenuated single photon state.

3.7 Discussion

This is the first experimental realisation of the noiseless amplification of a two-mode quantum state, which is an important advance towards meeting the challenge of establishing DIQKD [77]. The purity of the qubit remains high after amplification (Figure 3.9), and the amplifier achieves a significant improvement in transmission fidelity for qubits subjected to substantial losses (Table 3.2). Qubit amplification is completely heralded—no post-selection is required—leaving the output qubit available for subsequent quantum information processing. For the highest measured gain $G_m = 5.7$, the transmission fidelity was increased from $\langle R | \rho_{\text{in}} | R \rangle = 4.1\%$ to $\langle R | \rho_{\text{out}} | R \rangle = 20.8 \pm 0.2\%$, a five-fold increase.

There was a slight variation in output state purities that depended on the polarisation input, and this was due to different non-classical interference visibilities in the two NLA stages, and different efficiencies in the ancilla modes. From theoretically investigating the effects of source and detection efficiency on the qubit amplifier's performance [60], we conclude that the gain saturation observed in our data (Figure 3.1) is caused by source inefficiency in the ancilla mode and lack of number resolution in the detectors. A gain saturation factor, denoted by L , is calculated for the output state:

$$\rho_{\text{out}} = \frac{(\gamma_0 + L\gamma_1)|00\rangle\langle 00| + g^2\gamma_1\rho_1^{\text{out}}}{\gamma_0 + \gamma_1(g^2 + L)}. \quad (3.23)$$

The gain saturation in (3.23) only affects the relative probabilities of terms in the mixed state ρ_{out} , and does not affect the purity of the qubit subspace ρ_1^{out} . The gain saturation factor L can be expressed as

$$L = 1 + \frac{1 - \tau}{\tau(1 - \eta)} \quad (3.24a)$$

$$= \frac{1 + (1 - \tau)g^2}{\tau}, \quad (3.24b)$$

and only depends on the single photon source efficiency in the ancilla modes, denoted by τ , and the factor g^2 . From (3.23) and (3.24), the highest attainable qubit efficiency from the amplifier is τ , or the ancilla efficiency, which is consistent with other theory [106]. This maximum qubit efficiency is achieved in the $|g| \rightarrow \infty$ limit.

When factoring out detector efficiency, denoted by δ , and path efficiency through the optical circuit, we estimated our average source efficiency to be approximately 0.45. Taking into account detector and source efficiency, the theoretical probability of successfully amplifying a qubit was calculated to be

$$P = \delta^2 \tau^2 (1 - \eta)^2 (\gamma_0 + \gamma_1 (g^2 + L)) . \quad (3.25)$$

The experimental success probability was calculated from data by taking the ratio of three-fold coincidence detections heralding successful amplification, $\mathcal{C}_3^{\text{amp}}$, to three-fold coincidence detections when the circuit is not set to amplify, $\mathcal{C}_3^{\text{in}}$ (see Section 3.6.2 and (3.21)). This corresponds to the success probability conditional on ancillae photons being delivered to the circuit and being detected, *i.e.* with $\tau = \delta = 1$. For the case of $G_m = 3.3$ (shown in Figure 3.9), $P \simeq 0.05$. This is consistent with the expected value from (3.25).

Improved photon sources currently under development [107–111] can be integrated directly into the qubit amplifier, and the circuit could therefore be used to amplify a state arbitrarily close to a single photon (that is, arbitrary suppression of vacuum). Amplification is inversely related to success probability, but amplification to an extreme level is not required, for example, to violate a loophole-free Bell inequality. Heralded noiseless qubit amplification is a powerful technique, with direct applications in DIQKD, fundamental tests of quantum physics and a range of emerging quantum technologies [112–114].

Chapter 4

Entanglement Distribution in Quantum Networks with Linear Optics

4.1 Acknowledgements

Guoyong Xiang and I constructed the SPDC photon source together. I modified the optical circuit from the qubit amplifier experiment (presented in Chapter 3) for the present experiment. I collected and analysed the data, under the supervision of Geoff Pryde and with input from Tim Ralph. A manuscript on the results presented in this chapter is currently in progress.

4.2 Introduction

Entanglement is the fundamental resource in quantum information [4], and enabling efficient distribution of entanglement across a quantum network is a highly active research area [115, 116]. A quantum network consists of universal nodes—with the ability to send, receive, store and perform local operations on a quantum state—connected by transmission channels. A node essentially requires a fully functional quantum memory, and a tremendous amount of research activity is directed towards realising quantum memories in a variety of physical systems: single atoms in cavities [117, 118], trapped ions [119, 120], atomic ensembles [121], and superconducting circuits [122] are some examples. On the other hand, the transmission channel

connecting distant nodes is always an optical channel. Photons are a very appealing quantum information carrier, for their naturally low rate of decoherence and the ease of encoding and controlling information on their physical properties. Linear optics and single photon detection can mediate interaction between quantum states at spatially separated nodes of a network, thereby inducing conditional entanglement [123].

Creating entanglement across large distances could be considered a goal in itself, enabling fundamental tests at new distance scales [124, 125]. Violating a Bell inequality is equivalent to demonstrating device-independent quantum key distribution (DIQKD) [77], and recent experiments demonstrating entanglement in space-like separated bipartite systems [71, 125–127] also prove the feasibility of a secure device-independent communication link over appreciable distances. Once entanglement is established between nodes, various secure quantum communication [128] or computation [129, 130] protocols can be performed across a network.

Any realistic transmission channel includes loss and decoherence, due to absorption and scattering of photons. Shared entanglement decreases exponentially with transmission distance, and purification protocols are necessary to extend the viable transmission range. Purification in the form of entanglement concentration is possible with linear optics, and these experimental techniques can be applied in a variety of realistic conditions. This chapter investigates a linear optical technique for mitigating transmission loss in entanglement distribution that is suitable for a wide variety quantum repeater architectures. We focus on the problem of transmission in quantum networks, and do not attempt to demonstrate a working quantum node. Combining some of the key ingredients in quantum repeater proposals—single photons, entanglement swapping and purification—the performance of the purification technique is assessed for two distinct configurations of the optical circuit, by tomographic reconstruction of the quantum state at the end of the circuit.

4.3 Quantum Repeaters

The probability of a photon being absorbed or scattered increases exponentially with transmission distance, which means that distributed entanglement deteriorates at the same rate. A practical strategy to overcome loss in entanglement distribution is a quantum repeater. The first quantum repeater was proposed by Briegel, Dür, Cirac and Zoller (BDCZ) in 1998 [131], and consisted of a series of $N - 1$ entanglement swapping stages that divide a total transmission distance L into smaller elementary

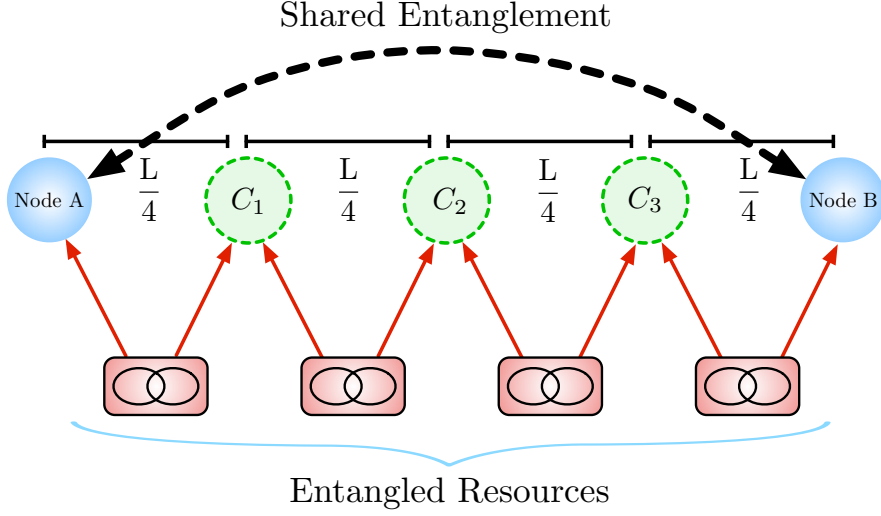


Figure 4.1: Conceptual depiction of the BDCZ repeater configuration described in [131]. Elementary links of entangled resources, usually pairs of photons, are connected at intermediary nodes ($C_1 - C_3$) via entanglement swapping, to entangle the principal nodes A and B . To entangle nodes separated by distance L , photons only traverse distances of $L/4$. Purification stages at intermediary nodes can repair the effects of noise and loss, in principle ensuring that nodes A and B become maximally entangled. Three intermediary nodes are shown here, but the number of nodes $N - 1$ is determined by the total distance L and attenuation and noise rate across the channel.

linkage distances L/N . The resource requirement is N entangled photon pairs, and each photon travels a distance $L/(2N)$ to interact with another photon from an adjacent pair at the entanglement swapping stage, thereby entangling the terminal nodes separated by the full distance L —see Fig. 4.1. The BDCZ model incorporates two-photon detection at the entanglement swapping stage, and as the entanglement swapping stages must all succeed simultaneously, the probability of successfully distributing an entangled state (or in other words, the rate at which entanglement can be transmitted) decreases exponentially with distance.

Generation of entangled photons, entanglement swapping and entanglement purification are currently all non-deterministic operations, only succeeding with independent probabilities. To realise a quantum repeater in practice, quantum memories will need to hold states until purification or entanglement swapping are successful. A quantum repeater scheme based on linear optics, single photon detection and collective excitations in atomic ensembles was proposed in 2001 by Duan, Lukin, Cirac and Zoller (DLCZ) [123].

Entangled photon pairs in the BDCZ scheme are replaced in the DLCZ protocol by spatially separated and entangled atomic ensembles. Two atomic ensembles

separated by up to an attenuation length L/N become entangled in the following way. A three-level Λ system in alkali-metal atoms is formed by two metastable ground state sub-levels and one excited electronic state. A laser pulse on the transition from one ground state to the excited state results in spontaneous emission of a single photon when the electron relaxes to the second metastable ground state. The emission modes from both atomic ensembles are matched, to erase which-path information, and interact at a beam splitter; conditioned on detection of a single photon after the beam splitter, the two atomic ensembles are projected into a maximally entangled state. As spontaneous emission from either atomic ensemble only occurs with low probability, the majority of the time no photon is detected, and this process of forming an elementary entangled link in DLCZ is non-deterministic (but heralded).

Once the elementary link is successfully heralded, entanglement can be extended beyond L/N by connecting atomic ensembles from two different elementary links. The stored excitations in two atomic ensembles are retrieved using read-out laser pulses, with close to unit efficiency due to collective enhancement [132], and combined in an entanglement swapping stage to extend the entanglement to twice the original

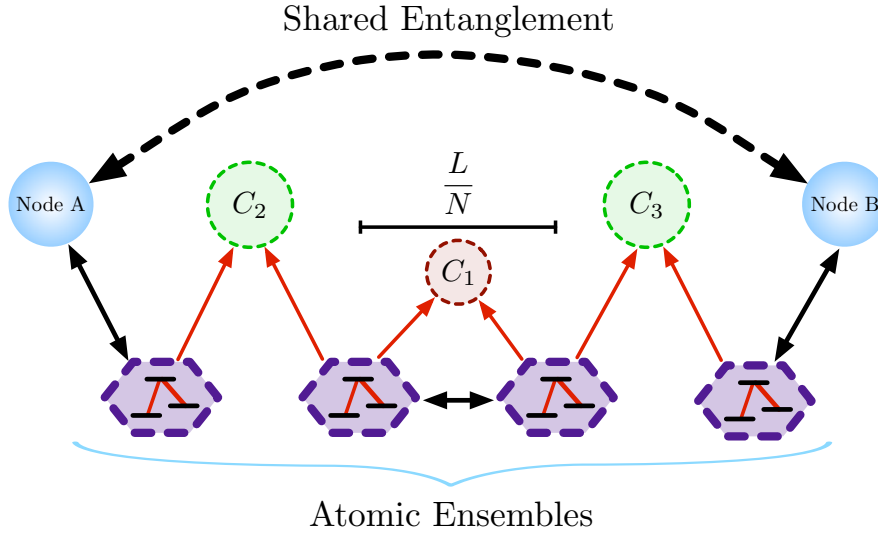


Figure 4.2: Conceptual depiction of the DLCZ repeater architecture described in [123]. The entangled photon pairs in 4.1 are replaced by atomic ensembles. An elementary link consists of two atomic ensembles within distance L/N of each other. The ensembles are conditionally entangled, at intermediary node C_1 , when spontaneous emission modes are combined at a beam splitter, and a single photon with equal amplitude of originating from both modes is detected. Elementary links are connected via entanglement swapping, at intermediary nodes C_2 and C_3 , to entangle principal nodes A and B separated by a distance L . As before, the length of an elementary link L/N is determined by transmission efficiency, and in principle, nodes A and B can become maximally entangled.

length. Using N of these links, two atomic ensembles separated by a distance L can be entangled, in a similar way to the BDCZ scheme. In BDCZ, the purifications in all N elements would need to succeed simultaneously, and this probability decreases exponentially with distance. In DLCZ on the other hand, once a quantum state has been successfully purified it is stored in an atomic ensemble quantum memory, and the communication efficiency therefore scales polynomially. It should be noted that transmission losses in DLCZ simply reduce the probability of successfully swapping entanglement between elementary links, but once entanglement swapping is successfully heralded, the states are maximally entangled. Thus, entanglement swapping in DLCZ filters out the vacuum component in a state, effectively purifying it.

Since these early proposals for quantum repeater architectures, several modifications and refinements have been proposed, and a comparison of various approaches can be found in [133]. All quantum repeaters that are discussed, however, incorporate the same key ingredients: single photons, entanglement swapping with linear optics, and quantum memories. As long as single photons are transmitted over appreciable distances, vacuum will always be mixed in with the state due to transmission loss. As mentioned, this would decrease the success probability of entanglement swapping, but the distributed entanglement would ultimately not be affected.

At this time, quantum memories are still technically extremely challenging to realise, and their performance is far from ideal [134]. For this reason, a quantum state stored in memory is a precious resource. As an NLA stage not only filters the vacuum component of a transmitted photonic state, but also incorporates an independent signal heralding successful amplification, it is a useful technique for heralding that a pure state has been sent to a quantum memory. This could be important, for example, if the quantum memory also performs local quantum information processing, which generally requires high purities. Alternatively, if two-photon detection is required in a quantum network, an NLA stage can herald when a pure single photon state is being sent to an entanglement swapping stage, signalling that the state in the adjacent quantum memory can safely be released. Another recent quantum repeater proposal [113], combining qubit amplification and quantum memories to form heralded pairs of entangled photons, and Bell state (two-photon) measurements for entanglement swapping, can also be seen as motivation for the current work.

An NLA stage integrated into a quantum network can be considered to perform quantum erasure correction. Quantum error-correcting codes [135, 136] are an

important advance towards enabling fault-tolerant quantum computing. In the continuous-variable regime, experimental quantum error correction has recently been demonstrated for decoherence [137] and loss [138] channels. In the discrete variable regime, overcoming decoherence noise in entanglement distribution has previously been demonstrated by encoding states in a decoherence-free subspace [139, 140]; correcting measurement errors in linear optics quantum gates has also been experimentally investigated [141]. Compensating for photon loss, however, remains an important goal, which the current work addresses.

In the experiment, orthogonal spatial modes of a quantum network are simulated by orthogonal polarisation modes of a single photon state. A one-to-one mapping exists between a photon polarisation qubit, which is a two-mode state, and the mode-entangled states considered in many quantum repeater proposals. Using wave plates and PBSs, the orthogonal polarisation modes can be addressed independently. The optical circuit consists of two NLA stages, one operated as a single-mode amplifier and the other as a teleportation stage to swap mode entanglement, and variable loss in one mode. A polarisation mode of each photon is sent to an entanglement swapping stage, thereby entangling the two photons' orthogonal polarisation modes that never interacted. Two configurations of the setup are investigated: in the first configuration, called the “terminal link” configuration, loss is added to the “outer” mode, between an ancilla photon source and a terminal node or quantum memory (see Fig. 4.5); in the second configuration, called the “intermediate link” configuration, loss is added to the “inner” mode, between an ancilla photon source and an entanglement swapping stage (see Fig. 4.10). In both configurations, loss is repaired with the NLA stage operated as a single-mode amplifier, which is based on the generalised quantum scissors [62, 92, 99] introduced in Chapter 3.

It should be emphasised that the details of the BDCZ and DLCZ repeater architectures have been introduced purely as illustrative examples. Both configurations that we experimentally study in this chapter could be applied in any general quantum repeater architecture.

4.3.1 Concept of Mode Entanglement

In the DLCZ repeater architecture, it is single mode entanglement that is being shared between atomic ensembles—a single photon in a superposition of two separate spatial modes. Despite considerable debate in the past, it is now clearly established that a single photon delocalised between two modes represents an entangled system.

A single photon de-localised between spatial modes A and B can be written

$$|\psi\rangle_{A,B} = |0\rangle_A |1\rangle_B + |1\rangle_A |0\rangle_B , \quad (4.1)$$

where $|0\rangle_{A,B}$ and $|1\rangle_{A,B}$ denote the occupation number of spatial modes A and B . One counter-argument, for example had been that writing (4.1) in terms of field operators

$$|\psi\rangle_{A,B} = (\hat{a}_A^\dagger + \hat{a}_B^\dagger) |0_A 0_B\rangle , \quad (4.2)$$

suggests that there is no entanglement, as it is a simple superposition of two field mode operators acting on the vacuum.

A conclusive argument [96, 98, 142] in favour of entanglement, however, can be made by imagining two cavities in spatial modes A and B that each contain single atoms. The atom-cavity system can be prepared in such a way that if a photon enters the cavity, it will be deterministically absorbed and excite the atom. The single de-localised photon $|\psi\rangle_{A,B}$ in (4.1) is transformed into the atomic state

$$|\Psi\rangle_{A,B} = |g\rangle_A |e\rangle_B + |e\rangle_A |g\rangle_B , \quad (4.3)$$

with $|g\rangle_{A,B}$ and $|e\rangle_{A,B}$ denoting the ground and excited states, respectively, of the atoms in modes A and B . This new state $|\Psi\rangle_{A,B}$ is generally agreed to be entangled, and it was created directly from $|\psi\rangle_{A,B}$ using only local operations and classical communication (LOCC). It is known that entanglement cannot be increased using LOCC alone [4, 143], and this implies that $|\psi\rangle_{A,B}$ must be equally entangled.

It would be inaccurate, however, to say it is the single photon and the vacuum state that are entangled in $|\psi\rangle_{A,B}$. It is in fact the modes A and B that are entangled in their occupation number [97]. Mode entanglement is a useful resource that has potential applications in quantum communication and computation [144–147]. As previously discussed (see Section 2.5), qubits in linear optical quantum information are often encoded in a single photon's polarisation state: $|\psi\rangle = \alpha|H\rangle + \beta|V\rangle$. The photonic qubit occupies a single spatial mode, but it can easily be transformed into a superposition of two spatial modes using a wave plate and a PBS: $\alpha|H\rangle + \beta|V\rangle = \alpha|1_H 0_V\rangle + \beta|0_H 1_V\rangle \rightarrow \alpha|10\rangle + \beta|01\rangle$. In quantum computing, this is known as dual-rail encoding, where the basis states of the qubit are orthogonal spatial modes. Polarisation encoding is formally equivalent to dual-rail encoding of a qubit [148]. An important point is that a dual-rail qubit is not an entangled state: it is a single photon with basis states $\{|01\rangle, |10\rangle\}$. A delocalised photon is only entangled if it is considered a subspace of a larger space, spanned by the basis states

$\{|00\rangle, |01\rangle, |10\rangle, |11\rangle\}$. This larger space is a two qubit space, comprised of two modes that are each limited to 0 or 1 photons. In other words, it is an entangled state of two single-rail qubits. This is an important point to keep in mind, as the full state density matrix of basis states $\{|00\rangle, |01\rangle, |10\rangle, |11\rangle\}$ is experimentally reconstructed.

4.3.2 Entanglement of Formation and Concurrence

Entanglement is the fundamental resource in quantum information, and like any resource, a method of quantifying it is essential. A pure quantum state is entangled if it is not factorizable, as in the case of the four Bell states $\{\Psi^\pm, \Phi^\pm\}$. A mixed state is entangled if it cannot be represented as a mixture of factorizable pure states. Several different measures of entanglement have been proposed for mixed states [149], and here we will focus on a measure known as the entanglement of formation.

The entanglement of formation was designed to quantify the resources needed to *create* a given entangled state [150]. In the case of a bipartite pure state, the entanglement of formation is equivalent to the von Neumann entropy of either of the two subsystems [151]. An analytic expression for the entanglement of formation of bipartite¹ mixed states has also been developed [152], and this formula is described below.

Given a bipartite mixed state ρ , a non-Hermitian matrix ϱ can be defined:

$$\varrho \equiv \rho \tilde{\rho} , \quad (4.4)$$

where $\tilde{\rho}$ is the spin-flipped state

$$\tilde{\rho} = (\sigma_y \otimes \sigma_y) \rho^* (\sigma_y \otimes \sigma_y) . \quad (4.5)$$

Here ρ^* is the complex conjugate of ρ when expressed in the standard computational bases $\{|00\rangle, |01\rangle, |10\rangle, |11\rangle\}$, and σ_y is the Pauli matrix

$$\sigma_y = \begin{pmatrix} 0 & -i \\ i & 0 \end{pmatrix} . \quad (4.6)$$

A quantity $\mathcal{C}(\rho)$ called the concurrence is now defined as

$$\mathcal{C}(\rho) = \max\{0, \lambda_1 - \lambda_2 - \lambda_3 - \lambda_4\} , \quad (4.7)$$

¹Consisting of two parts, in this case two modes.

where the λ_j s are the square roots of the eigenvalues of ϱ in decreasing order. The λ_j s are non-negative real numbers, and the concurrence is bounded between $0 \leq \mathcal{C}(\rho) \leq 1$. The entanglement of formation is then:

$$\mathcal{E}(\mathcal{C}) = \mathcal{G} \left[\frac{1 + \sqrt{1 - \mathcal{C}^2}}{2} \right] \quad (4.8)$$

with

$$\mathcal{G}[x] \equiv -x \log_2 x - (1 - x) \log_2 (1 - x) . \quad (4.9)$$

The entanglement of formation is monotonically increasing and ranges from 0 to 1, as desired for an entanglement measure. The concurrence is also monotonically increasing from 0 to 1, and can therefore be taken as a measure of entanglement in its own right. Following [153], we calculate the concurrence in Section 4.5.3 to characterise mode entanglement in our experiment.

4.3.3 Teleporting Arbitrary Quantum States

Quantum teleportation is one of the great early successes of quantum information science [33, 36, 154, 155]. If one party, Alice, possesses a quantum state $|\psi\rangle$ that she wants to transmit to another distant party, Bob, the laws of quantum mechanics impose some fundamental constraints on how it can be achieved. One straightforward method would be for Alice to measure $|\psi\rangle$, and then send Bob the classical information so he could reconstruct the state for himself. But it is impossible for Alice to accurately measure a single copy of a wave function [84].

If Alice and Bob already share a maximally entangled photon pair, Alice can send her unknown state $|\psi\rangle$ by consuming their entangled resource and communicating two bits of classical information to Bob. The procedure is for Alice to interact $|\psi\rangle$ with her half of the entangled pair. If we suppose Alice and Bob initially share the Bell state $|\Phi_{A,B}^+\rangle$, and Alice's unknown quantum state is written in the computational basis as $|\psi\rangle = \alpha|0_A\rangle + \beta|1_A\rangle$, the full three qubit state is:

$$|\psi_A\rangle \otimes |\Phi_{A,B}^+\rangle = \frac{(\alpha|0_A\rangle + \beta|1_A\rangle)(|0_A0_B\rangle + |1_A1_B\rangle)}{\sqrt{2}} . \quad (4.10)$$

It is important to realise that Alice's two-qubit state can be expressed as a super-

position of all four Bell states [156]:

$$|\psi_A\rangle \otimes |\Phi_{A,B}^+\rangle = \frac{1}{2} [|\Phi_{AA}^+\rangle(\alpha|0_B\rangle + \beta|1_B\rangle) + |\Phi_{AA}^-\rangle(\alpha|0_B\rangle - \beta|1_B\rangle)] \quad (4.11a)$$

$$+ |\Psi_{AA}^+\rangle(\alpha|1_B\rangle + \beta|0_B\rangle) + |\Psi_{AA}^-\rangle(\alpha|1_B\rangle - \beta|0_B\rangle)] . \quad (4.11b)$$

By performing a joint Bell state measurement on the two qubits in her possession, she projects Bob's qubit into one of four possible states. One of the four possibilities is exactly the state Alice wanted to send Bob in the first place, that is $|\psi\rangle$. The other three states only require local qubit rotations to be transformed into $|\psi\rangle$. After performing her Bell state measurement, Alice simply sends Bob two classical bits informing him which of the four possible outcomes she measured, and this determines the operation Bob must perform to recover $|\psi\rangle$. An important detail of this protocol is that Alice's original state $|\psi\rangle$ is destroyed in the projective Bell state measurement. If it had not been destroyed, two identical states $|\psi\rangle$ would exist in the end, in direct contradiction with the no-cloning theorem. This is, in fact, why the procedure is called quantum teleportation, instead of quantum cloning. Another detail to notice is that Alice never learned what the state was, as it was unnecessary for teleportation. Finally, the physical system—the energy of a single photon, in this example—was never teleported, but only the information contained in its wave function.

4.3.4 Entanglement Swapping

The quantum teleportation technique can be extended from teleporting an arbitrary quantum state to entangling two qubits that never directly interact with each other. This procedure is called entanglement swapping [38] (see Figure 4.3), and the main idea is that the arbitrary qubit $|\psi\rangle$ in the quantum teleportation protocol is now one half of another entangled qubit pair. Alice and Bob initially share the entangled ancilla $|\Psi_B^-\rangle$, and Alice receives a state $|\psi_2\rangle$ that is unknown to her, but which is in fact half of another singlet $|\Psi_A^-\rangle$. The four-qubit state in the computation basis is

$$|\psi_{1234}\rangle = \frac{1}{2} |\Psi_A^-\rangle \otimes |\Psi_B^-\rangle \quad (4.12a)$$

$$= \frac{1}{2} (|0_1\rangle|1_2\rangle - |1_1\rangle|0_2\rangle)(|0_3\rangle|1_4\rangle - |1_3\rangle|0_4\rangle) . \quad (4.12b)$$

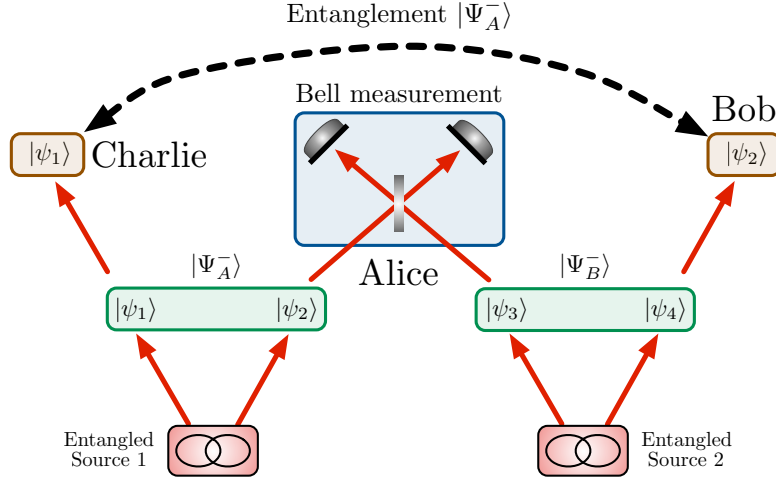


Figure 4.3: Conceptual diagram of an entanglement swapping setup. Alice possesses an unknown state $|\psi_2\rangle$, and half of a Bell state $|\psi_3\rangle$. She can teleport $|\psi_2\rangle$ to Bob by performing a two photon Bell state measurement on $|\psi_2\rangle$ and $|\psi_3\rangle$, and classically sending her measurement result to Bob. As $|\psi_2\rangle$ was originally maximally entangled with $|\psi_1\rangle$, the state Bob now possesses is also maximally entangled with $|\psi_1\rangle$. Thus, Bob has swapped his initial entanglement with $|\psi_3\rangle$ for entanglement with $|\psi_1\rangle$, never having directly interacted with $|\psi_1\rangle$ or $|\psi_2\rangle$.

Like before, the combined state can be re-expressed as a superposition of all four Bell states [38]:

$$|\psi_{1234}\rangle = \frac{1}{2}(|\Psi_{14}^+\rangle|\Psi_{23}^+\rangle + |\psi_{14}^-\rangle|\Psi_{23}^-\rangle + |\Phi_{14}^+\rangle|\Phi_{23}^+\rangle + |\Phi_{14}^-\rangle|\Phi_{23}^-\rangle). \quad (4.13a)$$

Alice performs a joint Bell state measurement on qubits 2 and 3, and projects Bob's state into one of four possible states. When Alice communicates two classical bits encoding her measurement outcome to Bob, he can correct his half of the state with local operations. Bob now possesses a subsystem that is half of the entangled state $|\Psi_A^-\rangle$, never having directly interacted with any part of the original state $|\Psi_A^-\rangle$.

4.4 Experimental Components

Two distinct configurations of the experiment—referred to as the *terminal link* configuration (Section 4.5) and the *intermediate link* configuration (Section 4.6)—were studied, using the same experimental components. They both incorporated the NLA stages used for the noiseless amplification of a polarisation qubit, described in 3.5 and [60]. Polarisation-dependent loss was also common to both, and this loss was applied by using a half wave plat and a partially-polarising beam splitter.

The location of the loss in the optical circuit, and the detection patterns at the circuit output, were the main differences between the two configurations. In the next sections, elements common to the two schemes will be described.

4.4.1 Photon Source Characterisation

The single photons for this experiment were generated using the SPDC source described in 3.5.1. As before, two pairs of degenerate polarisation-unentangled photons at 780 nm were produced in the double-passed BBO crystal. The 380 nm pump beam was held at a constant power of 100 mW to limit higher-order terms in the down-converted modes.

A 3 nm interference filter was placed directly before each single photon counting module, to minimise coupling of background light. The bandwidth of down-converted photons was typically ~ 5.5 nm FWHM directly from the source, as this was found to be the narrowest bandwidth achievable with the Ti:Sapphire pump laser while maintaining stable mode-locking over extended time intervals. The interference filters effectively limit the bandwidth of the photons in the circuit to 3 nm, which gives an expected photon coherence length $\Delta L_c \simeq \lambda^2/\Delta\lambda \simeq 0.2$ mm. This is consistent with the FWHM of the HOM interferences in Figure 5.7.

As in Chapter 3, the photons in the signal mode and the first ancilla mode are pairs generated in the backward pass of the SPDC source. The coincidence efficiency for this pair of photons in the circuit was typically measured to be 17 – 18%. The single photon detection rate from the signal mode ranged from $6.0 \times 10^4 \text{ s}^{-1}$ in *D1* to $4.5 \times 10^4 \text{ s}^{-1}$ in *D6*, while for the first ancilla mode it ranged from $9.5 \times 10^4 \text{ s}^{-1}$ to $7.5 \times 10^4 \text{ s}^{-1}$. The second ancilla mode and the photon acting as the external trigger are a pair from the forward pass of the SPDC, and the coincidence efficiency was typically measured to be 16 – 18%. The detection rate in the external trigger was $1.55 \times 10^5 \text{ s}^{-1}$ and in the second ancilla mode it ranged from $1.20 \times 10^5 \text{ s}^{-1}$ in *D3* to $1.00 \times 10^5 \text{ s}^{-1}$ in *D6*.

4.4.2 HOM Interference Characterisation

The signal and ancilla modes are matched at the central beam splitter in the entanglement swapping stage of Figure 4.6, to generate HOM interference between single photons. As in Chapter 2, the photon anti-bunching effect is measured in *D1* and *D2*. This non-classical interference is between photons of the same down-

conversion pair (both are from the backward pass in the SPDC), and the interference visibility is therefore expected to be close to unity. Interference visibility between the signal and first ancilla mode was typically measured to be 96–97%, with a small accidental coincidence rate ($< 1\%$) subtracted off.

The HOM interference in the second NLA stage of Figure 4.6 is always between photons from independent sources, since the second ancilla photon is from the forward pass of the SPDC source. The modes are overlapped at the central beam splitter in the NLA stage, and the photon anti-bunching effect is measured in $D5$ and $D6$. The non-classical interference between the signal mode and the second ancilla mode is plotted in Figure 4.4(a), and the interference between the first ancilla and second ancilla modes is plotted in Figure 4.4(b).

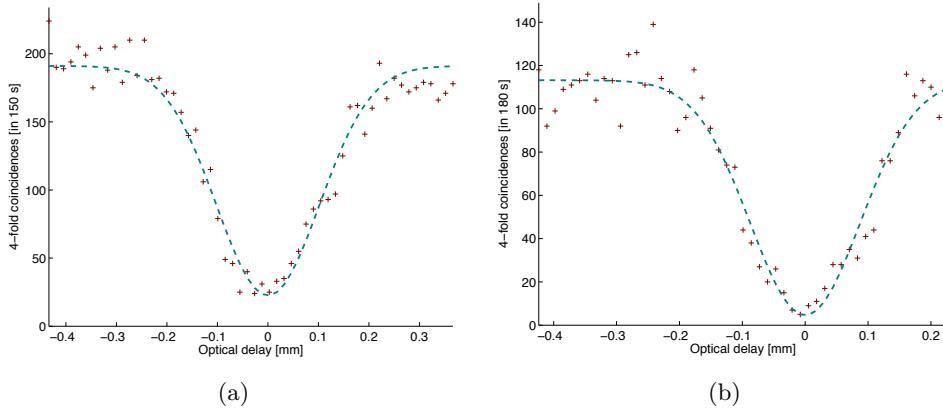


Figure 4.4: Measurement of the Hong–Ou–Mandel interference visibility between (a) the signal and second ancilla modes, and (b) the first and second ancilla modes. The optical delay was varied with a motorised linear translation stage in the second ancilla mode. The measurement was made in four-fold coincidences, with the external trigger and the other ancilla acting as extra triggers. Collection time for each data point was 150 seconds in (a), and 180 seconds in (b). The dashed curves are the Gaussian functions fitted to the data sets.

A Gaussian function was fitted to both data sets in Figure 5.7, and the interference visibility was calculated as the ratio of the Gaussian amplitude coefficient and the constant background. The visibility between the signal mode and the second ancilla mode is 88%, and the visibility between the first ancilla and second ancilla modes is 96%.

4.5 Terminal Link Configuration

In the first configuration of the experiment, the channel between an entangled resource and a principal node (quantum memory) is lossy. Two entangled photon pairs are linked by an entanglement swapping stage in the middle of the channel, which fulfils the role of an auxiliary node in 4.1. The loss in the outer channel is overcome by a noiseless linear amplification (NLA) stage. When the entanglement swapping and NLA stages work simultaneously, entanglement is shared between nodes A and B despite the loss that is present in the channel.

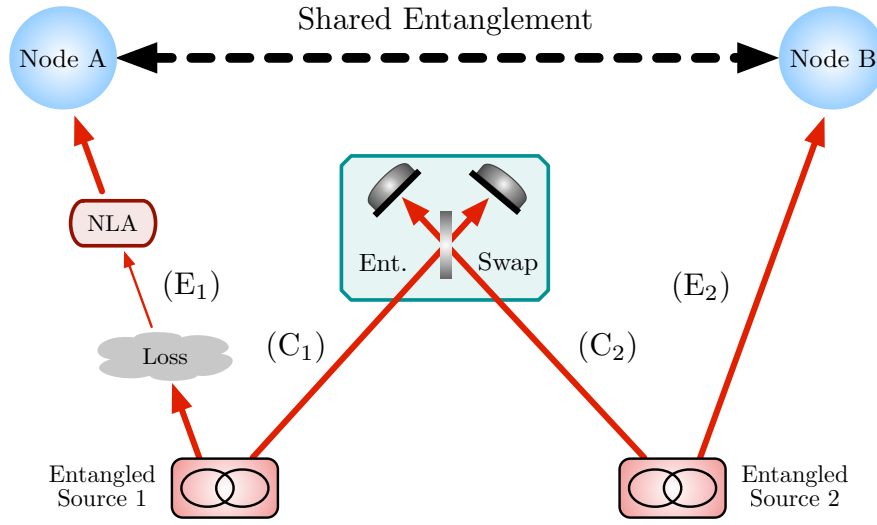


Figure 4.5: Conceptual diagram of the terminal link configuration of the experiment. The loss and amplification are in the outside mode E_1 , between an ancillary entanglement source and a terminal node, which is generally a quantum memory.

Both the entanglement swapping and NLA are achieved with linear optical elements and single photon counting modules, and consequently they are both non-deterministic transformations. Since both stages use the generalised quantum scissors [92, 99], they produce independent heralding signals when they succeed. The advantage of an independent heralding signal is that the nodes are guaranteed to share entanglement without needing to directly measure it, meaning that the entanglement can be used for quantum information tasks. Another advantage can be seen for the case where the entanglement swapping succeeds with a significantly higher probability than the NLA stage. In this situation, it would save entangled resources to wait for a successful NLA heralding signal to guarantee that the loss has been corrected, and only then send an entangled state to the entanglement swapping stage to connect the nodes. The protocol is completely flexible regarding the order

in which the operations are performed and the auxiliary modes are connected.

4.5.1 Experimental Concept

The two-mode polarisation state of a single photon used in this experiment is a perfect analogy for the spatially separated modes in quantum networks. Sending a polarisation qubit to a polarisation beam splitter will transform the state into a delocalised photon. The linear optical circuit (see Figure 4.5) uses three single photons—the spatial modes C_1 and E_1 in 4.5 are encoded in orthogonal polarisation modes of the signal photon at the beginning of the circuit, and two other photons are ancillae in the entanglement swapping and NLA stages. The polarisation state of the signal photon is in a single spatial mode, and can be written in the mode-occupation representation as:

$$|\psi_1\rangle = \alpha|1_H 0_V\rangle + \beta|0_H 1_V\rangle \equiv \alpha|H\rangle + \beta|V\rangle . \quad (4.14)$$

As discussed in Section 4.4.1, the coincidence efficiency of the SPDC source providing single photons to the optical circuit was in the range of 14 – 19%, meaning that the state at the beginning of the circuit is in fact a mixture of vacuum, single photon and higher order terms. Polarisation-independent loss was also applied to the state at the beginning of the circuit, to increase the proportion of vacuum in the mixture. This is to simulate a high-loss channel, as would be expected in a long repeater link, and it also avoids saturating the NLA gain [62], as will be discussed later in the chapter. The real state after the initial polarisation-independent loss is therefore

$$\zeta \simeq \gamma_0|0\rangle\langle 0| + \gamma_1|\psi_1\rangle\langle \psi_1| + \varepsilon|2\rangle\langle 2| , \quad (4.15)$$

where $|0\rangle$ is the vacuum state and $|2\rangle$ is the two-photon state for all modes, and higher order terms are neglected. The entanglement swapping stage next generates a non-deterministic, but heralded, transformation:

$$\zeta \rightarrow (1 - P_s)|0\rangle\langle 0| \otimes \Pi_f + P_s \rho_s \otimes \Pi_s , \quad (4.16)$$

where Π_s is the projector onto the subspace of heralding states corresponding to successful teleportation

$$\rho_s = \gamma_0|0\rangle\langle 0| + \gamma_1\rho_1^s + \varepsilon|2\rangle\langle 2| , \quad (4.17)$$

and Π_f (fail) is the projector onto the subspace of cases when the heralding success signal is not received. The specific form of the state in the failure condition is irrelevant, as it is ignored, and it is convenient to represent it as the vacuum state. The terms in the initial state ζ and entanglement swapped state ρ_s have identical coefficients in principle, and the only difference in ρ_s is that the original pure single photon polarisation state $|\psi_1\rangle\langle\psi_1|$ becomes a mixed state ρ_1^s after entanglement swapping. The small degree of mixture in ρ_1^s is predominantly due to imperfect HOM interference between the signal and ancilla photons (or between modes C_1 and C_2 in 4.5). Second-order terms $|\mathbf{2}\rangle\langle\mathbf{2}|$ in modes that can create spurious heralding signals also contribute to the mixture of the output state.

The entanglement swapping operation produces an independent heralding signal with probability P_s , and conditioned on this case the entanglement swapped state ρ_s is sent onwards. With probability $1 - P_s$ the entanglement swapping fails, the output state is discarded, and the procedure can be repeated until successful. This is equivalent to waiting until entanglement is successfully swapped between modes C_1 and C_2 in 4.5. As already mentioned in Section 4.5, the order of the stages in the protocol is arbitrary, and it is equally possible to wait for successful amplification before sending the modes onward for entanglement swapping. Next, in our experimental setup, loss is applied to $|\mathbf{H}\rangle$ in ρ_1^s (or mode E_1 in Figure 4.5), to produce the state

$$\rho_{in} = \gamma'_0|\mathbf{0}\rangle\langle\mathbf{0}| + \gamma'_1\rho_1^s + \varepsilon|\mathbf{2}\rangle\langle\mathbf{2}|. \quad (4.18)$$

The probabilities in the mixed state have now changed, to reflect the fact that loss in $|\mathbf{H}\rangle$ results in an imbalance between polarisation modes (*i.e.* $|\alpha|^2 < |\beta|^2$ in (4.14)), implying that the overall single photon probability is reduced $\gamma'_1 < \gamma_1$ and the vacuum probability is correspondingly increased, $\gamma'_0 > \gamma_0$. In addition, ε should also decrease, but this effect is small enough to be neglected here.

Finally, the NLA stage amplifies the $|\mathbf{H}\rangle$ mode back to the level of $|\mathbf{V}\rangle$. The transformation is again non-deterministic but heralded:

$$\rho_{in} \rightarrow (1 - P_a)|\mathbf{0}\rangle\langle\mathbf{0}| \otimes \Pi_f + P_a\rho_{out} \otimes \Pi_a, \quad (4.19)$$

where Π_f is the projector onto the subspace of failed amplification events as before, and Π_a is the projector onto the successfully amplified output state ρ_{out} :

$$\rho_{out} = \gamma''_0|\mathbf{0}\rangle\langle\mathbf{0}| + \gamma''_1\rho_1^a + \varepsilon|\mathbf{2}\rangle\langle\mathbf{2}|. \quad (4.20)$$

Thus, with probability P_a , the unbalanced polarisation state ρ_{in} is amplified and

transformed into ρ_{out} , which contains an equal superposition of $|H\rangle$ and $|V\rangle$ in the single photon subspace. In the ideal case $\rho_{out} = \zeta$, or $\rho_1^a = |\psi_1\rangle\langle\psi_1|$ and $\gamma_0'' = \gamma_0$, $\gamma_1'' = \gamma_1$. However, due to unavoidable mixture from imperfect HOM interference, and spurious heralded contributions from higher order terms, ρ_1^a will never be entirely pure (see Table 4.1).

The overall success probability in the full circuit is $P = P_s \cdot P_a$, and the output ρ_{out} is heralded by the state $\Pi_s \otimes \Pi_a$, which is orthogonal to $\Pi_f \otimes \Pi_f$, $\Pi_s \otimes \Pi_f$ and $\Pi_f \otimes \Pi_a$.

4.5.2 Linear Optical Circuit

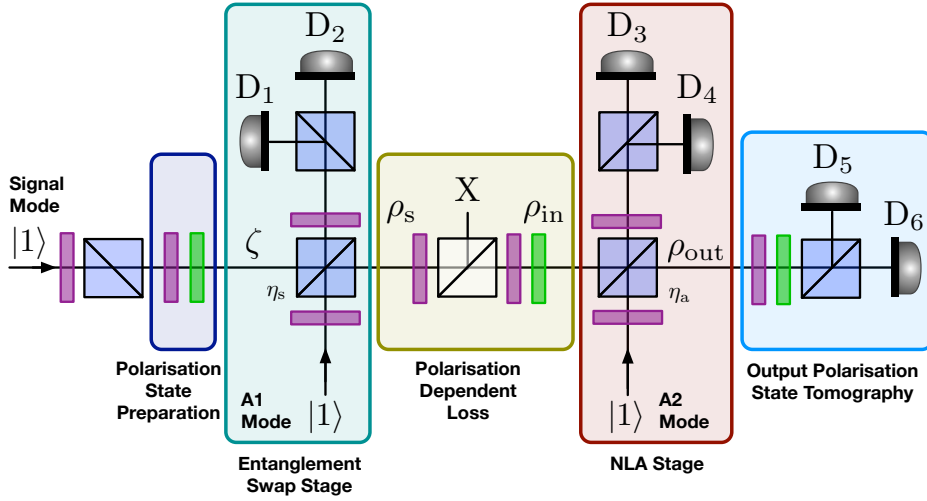


Figure 4.6: Linear optical circuit implementing loss and amplification in the terminal arm of a quantum repeater. A state having very high fidelity with a single photon enters the signal mode, and is prepared with the first HWP and PBS as a mixture of vacuum, single photon, and a very small two photon component. The polarisation state of the single photon subspace is prepared in a balanced superposition of $|H\rangle$ and $|V\rangle$, in state ξ . Polarisation mode $|V\rangle$ (equivalent to C_1 in 4.5) is swapped with the $|V\rangle$ (reflected, equivalent to E_2) mode of the first ancilla photon, while signal mode $|H\rangle$ (E_1) is transmitted through the stage, to create ρ_s . Loss is applied to mode $|H\rangle$ using a HWP and PPBS, creating ρ_{in} . Mode $|H\rangle$ is amplified in the NLA stage to compensate for the loss, while mode $|V\rangle$ is transmitted through the stage, to create ρ_{out} .

In our experiment the three single photons sent to the optical circuit depicted in Figure 4.6 each initially pass through a HWP and PBS. This is to ensure that they are in a pure polarisation state to begin with. In the case of the signal mode, the initial PBS also applies a polarisation-independent loss that reduces the size of the single photon term in the state. The loss is effectively polarisation-independent, because it is before the polarisation state of the signal photon is assigned for the

experiment. The single photon term is artificially reduced to simulate a high-loss transmission channel, and also to avoid saturation in the gain [60, 62].

For the entanglement swapping and NLA stages to operate in the linear regime, the condition $\gamma'_1, \gamma''_1 \ll 1$ must be satisfied. After this condition is met using the first HWP and PBS to attenuate the signal, the signal photon's polarisation state can be set using the next HWP and QWP. As before (see Chapter 3) polarisation modes are ideal for our purposes because they are easy to manipulate, and more importantly, an optical circuit with spatially superposed polarisation modes is passively phase stable. The polarisation state of the signal photon is prepared in the diagonal state $|D\rangle = (|H\rangle + |V\rangle)/\sqrt{2}$ —the essential feature is that this state is an equal superposition of $|H\rangle$ and $|V\rangle$, and the value of the phase between them is unimportant, as long as it is well-defined.

The spatial mode E_1 is identified with $|H\rangle$, and C_1 with $|V\rangle$, in the initial polarisation state $|D\rangle$. The spatial mode entanglement between E_1 and C_1 is equivalent to the polarisation mode entanglement between $|H\rangle$ and $|V\rangle$. The entanglement swapping stage and the NLA stage are both generalised-quantum-scissors-style amplifiers operating on polarisation modes, and are described in detail in Section 3.3.2. In the entanglement swapping stage, the signal $|V\rangle$ is teleported into the output mode, implying that the signal $|H\rangle$ becomes mode entangled with $|V\rangle$ in the output mode. This is identical to entangling E_1 and E_2 in Figure 4.5. The effective amplitude reflectivity η_s of the central beam splitter is set to $1/2$, for teleportation into the output mode without gain.

The $|H\rangle$ mode is next subjected to loss, and then amplified back to the level of $|V\rangle$ by the NLA stage. A partially-polarising beam splitter (PPBS) reflects a fraction of one polarisation, while leaving the other polarisation mostly unaffected. The reflected portion of $|H\rangle$ is sent to a beam dump, to simulate loss in the E_1 channel. The total polarisation state transmitted through the PPBS ideally comprises all of the original $|V\rangle$ mode, and the portion of $|H\rangle$ that is not reflected. In reality, the $|V\rangle$ mode will also experience a small amount of loss, but this is taken into account in the experiment. The loss to mode $|H\rangle$ is calibrated directly in the circuit, by measuring the ratio of detected photon counts in both transmitted modes. A loss factor of $1/2$ then corresponds to a detected $|H\rangle$ photon rate that is half of the detected $|V\rangle$ rate. In this experiment, the relative loss between $|H\rangle$ and $|V\rangle$ modes is of primary interest, and any overall loss due to imperfection of the PPBS can effectively be subsumed into the polarisation-independent loss at the beginning of the circuit.

The PPBS was manufactured for $1/3$ loss in one polarisation mode at 810 nm, and the loss at 780 nm was found to be approximately $1/2$ near normal incidence. Higher losses, of approximately $3/4$ and $5/6$, were also achieved by tilting the PPBS to change the in-plane angle of incidence. Loss factors of approximately $1/2$, $3/4$ and $5/6$ were then compensated in the NLA stage by tuning the reflectivity η_a to achieve the correct effective amplification factors G_m . The loss and gain factors were experimentally measured in the optical circuit (L_m and G_m , respectively), and their values are listed in Table 4.1.

The real gain in $|H\rangle$ was experimentally calibrated to correct for the three loss settings, by varying the effective reflectivity for the ancilla photon at the central beam splitter of the NLA stage (as discussed in Section 3.3.2). At the end of the optical circuit, polarisation state tomography is performed on the final output state. The density matrix is reconstructed, and mode entanglement is measured by calculating the concurrence of the full state. Although the two entangled modes are spatially superposed in the output, the protocol is equivalent to distributing mode entanglement over a distance with transmission loss, and serves as a proof-of-principle demonstration.

4.5.3 Experimental Results

Tomography of the polarisation state in the single photon subspace was performed on ρ_{in} and ρ_{out} , the states before and after the NLA stage, respectively. Detectors $D3$ and $D6$ were used for tomography of ρ_{in} , and $D5$ and $D6$ were used for tomography of ρ_{out} . The polarisation state density matrices were reconstructed from the tomographic measurements using maximum-likelihood reconstruction (see Section 2.6.2).

The results of the input and output state tomographies are presented in Figures 4.7, 4.8 and 4.9, for the three loss and gain settings. Subfigures (a) and (b) depict the absolute values of the input and output polarisation state density matrices, and subfigure (c) shows the full normalised state with the vacuum and two-photon terms. Subfigure (d) directly compares the absolute value of non-zero elements in the output density matrix depicted in (c), with the input density matrix elements (represented as semi-transparent bars). The inset shows a magnified view of the single and two-photon elements.

States in the experiment were tomographically measured with four-fold coincidence detection. For the measurement of ρ_{out} , a successful measurement signal consisted

L_m		$57 \pm 2\%$	$77 \pm 2\%$	$84 \pm 3\%$
G_m		1.98 ± 0.07	3.0 ± 0.1	4.1 ± 0.2
Input	$\langle H \rho_{in} H\rangle$	$(1.64 \pm 0.04) \cdot 10^{-2}$	$(1.06 \pm 0.03) \cdot 10^{-2}$	$(0.79 \pm 0.03) \cdot 10^{-2}$
	$\langle V \rho_{in} V\rangle$	$(3.84 \pm 0.07) \cdot 10^{-2}$	$(4.54 \pm 0.06) \cdot 10^{-2}$	$(4.83 \pm 0.07) \cdot 10^{-2}$
	$\text{tr}\{(\rho_1^a)^2\}$	$97 \pm 1\%$	$96 \pm 1\%$	$97 \pm 1\%$
	$\mathcal{C}(\rho_{in})$	$(2.5 \pm 0.2) \cdot 10^{-2}$	$(1.7 \pm 0.2) \cdot 10^{-2}$	$(1.2 \pm 0.2) \cdot 10^{-2}$
Output	$\langle H \rho_{out} H\rangle$	$(3.25 \pm 0.06) \cdot 10^{-2}$	$(3.13 \pm 0.06) \cdot 10^{-2}$	$(3.25 \pm 0.06) \cdot 10^{-2}$
	$\langle V \rho_{out} V\rangle$	$(3.49 \pm 0.06) \cdot 10^{-2}$	$(3.76 \pm 0.06) \cdot 10^{-2}$	$(3.72 \pm 0.06) \cdot 10^{-2}$
	$\langle 2 \rho_{out} 2\rangle$	$(1.4 \pm 0.2) \cdot 10^{-4}$	$(1.5 \pm 0.2) \cdot 10^{-4}$	$(1.2 \pm 0.2) \cdot 10^{-4}$
	$\text{tr}\{(\rho_1^a)^2\}$	$85.1 \pm 0.8\%$	$84.5 \pm 0.6\%$	$82.4 \pm 0.8\%$
	$\mathcal{C}(\rho_{out})$	$(3.4 \pm 0.2) \cdot 10^{-2}$	$(3.3 \pm 0.2) \cdot 10^{-2}$	$(3.2 \pm 0.2) \cdot 10^{-2}$

Table 4.1: Summary of results for the BDCZ repeater configuration of the optical circuit. Three different loss settings were tested, while the state size was kept approximately constant throughout. The performance of the protocol was assessed based on the purity of the polarisation subspaces, the probabilities of the $|H\rangle$ and $|V\rangle$ modes in the full states, and the concurrences.

of a coincidence between the external trigger directly from the SPDC source (see Section 4.4.1), a successful heralding signal from the entanglement swapping stage (in either $D1$ or $D2$), a successful heralding signal from the NLA stage (in either $D3$ or $D4$), and detection of a single photon at the circuit output (in either $D5$ or $D6$). During measurement of each polarisation basis, one state is sent to $D5$ while its orthogonal pair is sent to $D6$, and half way through tomography the optic axis of the HWP is rotated by 45 degrees, to send the orthogonal states to opposite detectors for an equal time. This averages over the different path and detection efficiencies of $D5$ and $D6$, guaranteeing that this imperfection of the optical circuit does not affect state reconstruction.

Three-fold coincidence counts, between the external trigger, $D1$ or $D2$, and $D3$ or $D4$, were also recorded during state tomography. The size of the single photon subspace relative to vacuum in the mixed state ρ_{out} was calculated as the ratio of four-fold coincidence rates to three-fold coincidence rates: $\gamma_1'' = \mathcal{C}_4/\mathcal{C}_3$. As the output state is heralded by three-fold coincidences, this ratio gives the probability of measuring a single photon at the output, conditional on heralding. The probabilities of the $|H\rangle$ and $|V\rangle$ modes in the output state are the ratio of four-fold to three-fold coincidences when measuring in the $\{H, V\}$ basis: $\langle H|\rho_{out}|H\rangle = \mathcal{C}_{4,H}/\mathcal{C}_3$ and $\langle V|\rho_{out}|V\rangle = \mathcal{C}_{4,V}/\mathcal{C}_3$.

Tomography of the input state ρ_{in} used detectors $D3$ and $D6$. As the NLA stage is not used in ρ_{in} , its ancilla photon was sent directly to $D4$ without any mode splitting,

and acted as a second trigger. The four-fold coincidences were then between the external trigger, the successful heralding signal from the entanglement swapping stage (in $D1$ or $D2$), the second trigger in $D4$, and detection of a single photon at the output (in $D3$ or $D6$). Again, orthogonal polarisations for each measurement basis swapped detectors half way through tomography, to neutralise the effect of detection efficiency imbalance between $D3$ and $D6$ in state reconstruction.

Five-fold coincidence counts were also recorded during tomography of ρ_{out} , between the usual three-fold pattern and $D5$ and $D6$. This directly measures the probability ε of the two photon term in the successfully heralded output state. As expected, $\varepsilon \ll \gamma_1'' \ll \gamma_0''$, and it was found that the vacuum, single photon and two photon probabilities each differed by two orders of magnitude (see Table 4.1). The full ρ_{out} state is depicted in (c) of Figures 4.7, 4.8 and 4.9, where the relative probabilities of the vacuum, single photon and two photon terms can be compared. It was reasonable to assume that no coherences existed between the vacuum, single photon and two photon terms, and all off-diagonal elements in (c) were set to zero, with the exception of the coherences in the polarisation subspace.

The purities of the polarisation states ρ_1^s and ρ_1^a are shown in Table 4.1. The purities after entanglement swapping are around 96 – 97%, which is slightly below the HOM interference visibility at that stage, as expected. The purities after amplification are in the range 82 – 85%, which is again slightly below the bound (~ 86 – 87%) given by the product of the ρ_1^s purity and the HOM interference visibility between independent photons in the NLA. The loss in the $|H\rangle$ mode can be seen in (a) of Figures 4.7, 4.8 and 4.9—the $|H\rangle\langle H|$ element in the density matrix is significantly lower than $|V\rangle\langle V|$. Subfigure (b) shows the two populations balanced after amplification, as desired. The inset of (d) compares the polarisation matrix elements between the input (semi-transparent bars) and output (solid bars) states. It is easier to see in the inset that the $|H\rangle\langle H|$ term increases from input to output, and the $|V\rangle\langle V|$ term essentially remains constant. The slight de-amplification of the $|V\rangle\langle V|$ population seen in (d) is most likely due to loss through the optical circuit. The single photon probability in ρ_{out} is small enough compared to the ancilla photon efficiency for us to believe that saturation in the NLA stage is not the dominant effect. Amplification increases the overall single photon subspace in ρ_{out} , and a corresponding suppression of the vacuum term in (d) can clearly be seen. The coherence terms also increase slightly after the amplification, which is the cause of the increase in the mode entanglement.

Similar to the approach in [62, 153, 157], the concurrences for the density matrices

ρ_{in} and ρ_{out} were calculated to verify mode entanglement. Having experimentally determined the non-zero elements of the density matrices, the formula for concurrence in 4.3.2 was used to calculate the values listed in Table 4.1. The two photon term was only measured in ρ_{out} , and was assumed to be equal in ρ_{in} when calculating its concurrence. This is a reasonable assumption, given that the teleportation and amplification operate on the single photon subspace, and the heralded two photon terms in ρ_{in} and ρ_{out} are regarded as noise in the protocol. For the largest loss factor $L_m = 84 \pm 3\%$, the concurrence is increased nearly three-fold, from $(1.2 \pm 0.2) \cdot 10^{-2}$ to $(3.2 \pm 0.2) \cdot 10^{-2}$, a significant improvement.

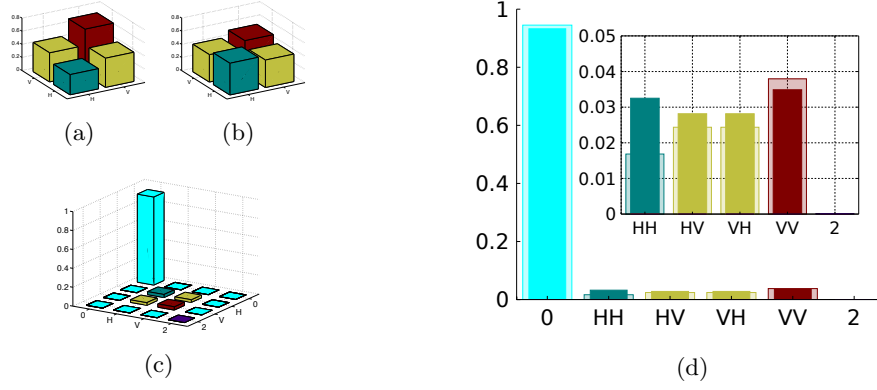


Figure 4.7: NLA gain $G_m \simeq 2$. Absolute value of (a) input and (b) output polarisation density matrix. (c) Full output density matrix. (d) Absolute values of input and output matrix elements.

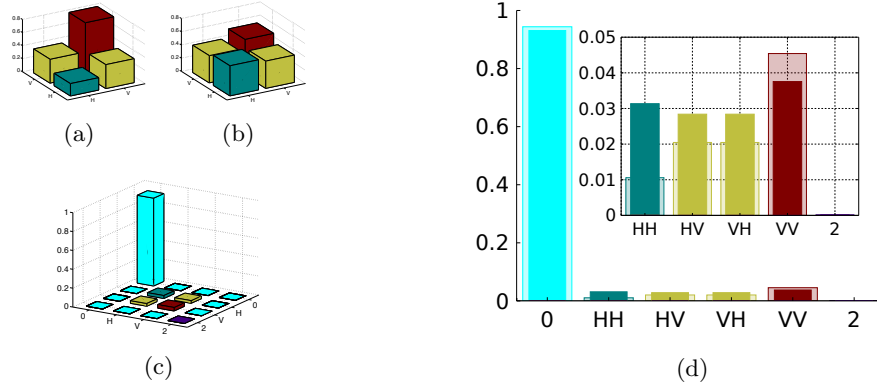


Figure 4.8: NLA gain $G_m \simeq 3$. Absolute value of (a) input and (b) output polarisation density matrix. (c) Full output density matrix. (d) Absolute values of input and output matrix elements.

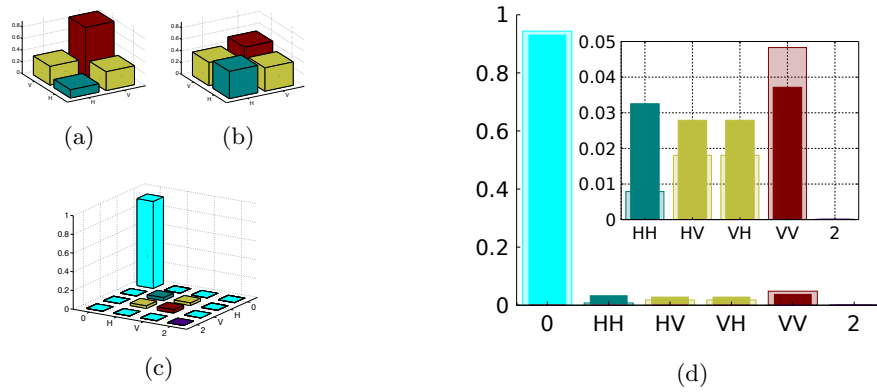


Figure 4.9: NLA gain $G_m \simeq 4$. Absolute value of (a) input and (b) output polarisation density matrix. (c) Full output density matrix. (d) Absolute values of input and output matrix elements.

4.5.4 Summary

A method of distributing entanglement between nodes of a quantum network in the presence of loss has been demonstrated. In this configuration, loss was added to the channel between an entangled resource and one of the terminal nodes or quantum memories. The experiment presented above consists of two NLA stages, one operating as an amplification stage to compensate for photon loss, and the other operating as a stage to swap mode entanglement. Both of these are key elements in proposed quantum repeater architectures.

The technique was demonstrated for three different loss settings, and for the highest loss ($L_m = 84 \pm 3\%$), the concurrence between output modes was increased almost threefold compared to what it would have been without amplification. This is therefore a valuable technique for ensuring that a highly pure entangled state is sent into a quantum memory, for future quantum information processing. This could effectively herald the entanglement of two quantum memories, or an elementary link in a quantum repeater, without the need for any post-selection to filter out a vacuum component, as proposed in [113]. Advantages of this protocol are that the NLA and the entanglement swapping stages both give independent heralding signals, and the order of the stages is unimportant. In principle, the NLA stage could successfully herald that loss in mode E_1 (in Figure 4.5) has been repaired, before entanglement swapping between modes C_1 and C_2 is attempted. Waiting for the next link in the channel to be purified before swapping entanglement could conserve valuable previously-entangled resources.

4.6 Intermediate Link Configuration

In contrast to the first configuration, here the loss is applied to the entanglement swapping channel, and the NLA stage is used to compensate for the loss directly before entanglement swapping. A useful conceptual picture might be two quantum memories separated by the entanglement swapping stage between them. It should be emphasised again, however, that this is for illustrative purposes, and the technique is applicable to a variety of situations. As mentioned already, successful entanglement swapping effectively filters out the vacuum component of the entangled state [123]. The potential advantage of this configuration, then, would be in a scenario in which the second quantum memory already stores long-range entanglement, which is being extended using the first quantum memory and entanglement swapping. If the channel between the first quantum memory and the entanglement swapping stage

is lossy, it would be beneficial to wait for the NLA to herald that the loss in this channel has been repaired, before the second quantum memory releases its stored state. The fidelity of the entanglement swapping operation can be increased in this way, by correcting the erasure error in one channel beforehand.

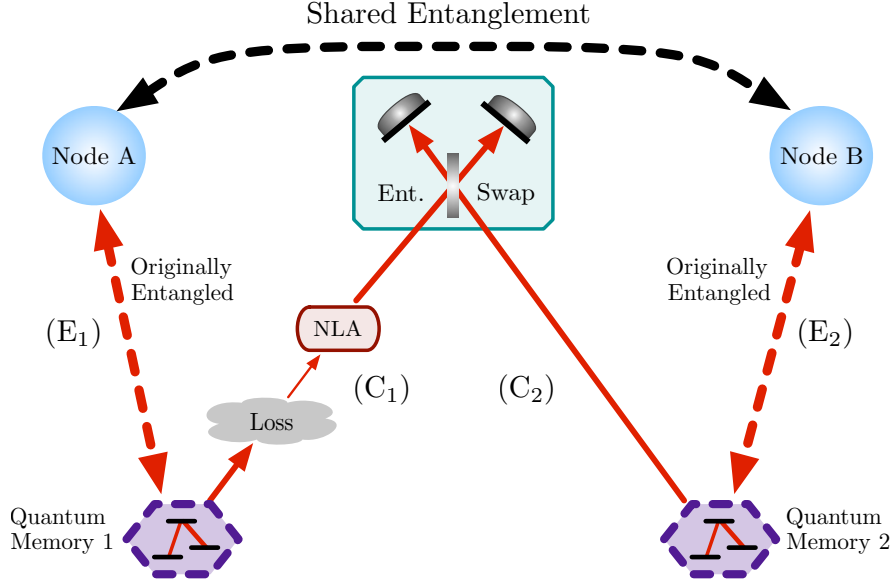


Figure 4.10: Conceptual diagram of the second experimental configuration. The loss is now in mode C_1 , one of the entanglement swapping channels. The entangled resources are depicted here as quantum memories, or atomic ensembles, but the entangled resources in the experiment are photon pairs, as before.

4.6.1 Experimental Concept

As before, the two-mode polarisation state of a single photon represents the spatial modes in a quantum network. Beginning with the state ζ from (4.15), loss is applied again to mode $|H\rangle$, while leaving mode $|V\rangle$ largely unchanged. The state after loss (and directly before amplification) is

$$\rho_{in} = \gamma_0|0\rangle\langle 0| + \gamma_1|\psi_1\rangle\langle\psi_1| + \varepsilon|2\rangle\langle 2|. \quad (4.21)$$

The single photon subspace can be represented as a pure state in ρ_{in} , because the loss only increases the vacuum probability without adding polarisation mixture. The $|H\rangle$ mode is then amplified in the NLA stage to compensate for the loss. The $|V\rangle$ mode passes through the NLA stage without any mode splitting or interference. The

NLA generates the transformation

$$\rho_{in} \rightarrow (1 - P_a)|\mathbf{0}\rangle\langle\mathbf{0}| \otimes \Pi_f + P_a \rho_a \otimes \Pi_a , \quad (4.22)$$

where Π_f is the heralding projector corresponding to failed amplification events, and Π_a is again the projector in the ancilla subspace heralding the successfully amplified output state ρ_a :

$$\rho_a = \gamma'_0|\mathbf{0}\rangle\langle\mathbf{0}| + \gamma'_1\rho_1^a + \varepsilon|\mathbf{2}\rangle\langle\mathbf{2}| . \quad (4.23)$$

The amplification adds a small amount of mixture into the polarisation subspace, due to unavoidable experimental imperfections, and the polarisation is hence represented as the mixed state ρ_1^a . After the NLA, the $|\mathbf{H}\rangle$ mode is sent to the entanglement swapping stage, where the $|\mathbf{V}\rangle$ mode again passes through unchanged. The entanglement swapping stage transforms the system into

$$\rho_a \rightarrow (1 - P_s)|\mathbf{0}\rangle\langle\mathbf{0}| \otimes \Pi_f + P_s \rho_{out} \otimes \Pi_s , \quad (4.24)$$

with the final heralded polarisation state

$$\rho_{out} = \gamma''_0|\mathbf{0}\rangle\langle\mathbf{0}| + \gamma''_1\rho_1^s + \varepsilon|\mathbf{2}\rangle\langle\mathbf{2}| . \quad (4.25)$$

The total probability of transforming the unbalanced polarisation state ρ_{in} into ρ_{out} is the same as in the previous configuration: $P = P_a \cdot P_s$.

4.6.2 Linear Optical Circuit

The three single photons are prepared in pure polarisation states to begin with, by each passing through a HWP and PBS. A polarisation-independent loss is again applied to the signal mode photon, to ensure that the single photon component in the state is always small: $\gamma'_1, \gamma''_1 \ll 1$. After this, the signal photon is prepared in the $|\mathbf{D}\rangle$ polarisation state. In this configuration, the correspondence between spatial modes in the conceptual depiction of Figure 4.10 and polarisation modes in the experimental circuit of Figure 4.11 are reversed: $|\mathbf{H}\rangle$ represents C_1 and $|\mathbf{V}\rangle$ represents E_1 .

The PPBS is now at the beginning of the optical circuit, and subjects the signal $|\mathbf{H}\rangle$ mode (C_1) to loss before the NLA and entanglement swapping stages. The signal $|\mathbf{V}\rangle$ mode (E_1) passes unchanged through the loss, NLA and entanglement swapping stages, and acts as a reference against which the final $|\mathbf{H}\rangle$ mode can be measured at each stage, for amplitude and coherence.

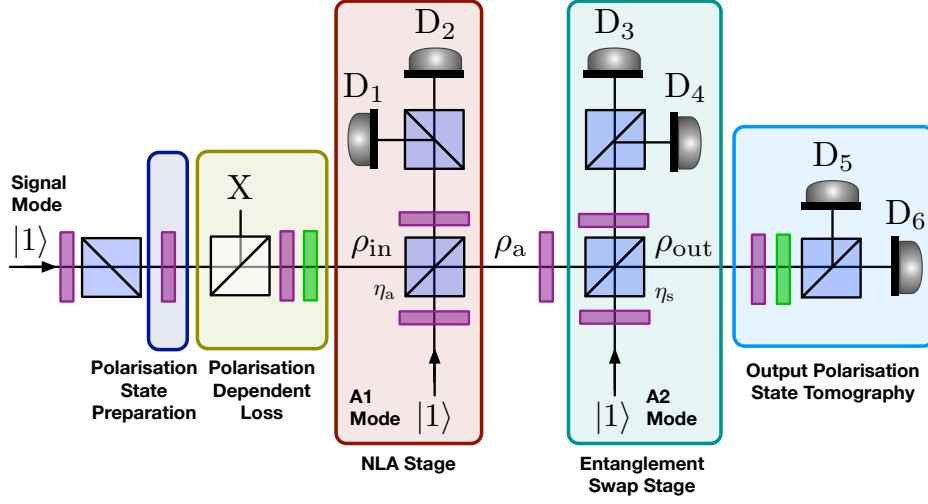


Figure 4.11: Linear optical circuit simulating the DLCZ repeater configuration. A single photon enters the signal mode, and is prepared with the first HWP and PBS as a mixture of vacuum, single photon, and a very small two photon component. The polarisation state of the single photon subspace is prepared in a balanced superposition of $|H\rangle$ and $|V\rangle$, in state ξ . Loss is applied to polarisation mode $|H\rangle$ (equivalent to C_1 in 4.10) using a HWP and PPBS, creating ρ_{in} . Mode $|H\rangle$ is amplified in the NLA stage to compensate for the loss, while mode $|V\rangle$ is transmitted through the stage, to create ρ_a . Mode $|V\rangle$ (E_1) is teleported to ancilla mode $|V\rangle$ (reflected, equivalent to E_2), to create ρ_{out} .

4.6.3 Results

A single loss setting, $L_m = 78 \pm 3\%$, was tested in this configuration, and the three states ρ_{in} , ρ_a and ρ_{out} were each tomographically reconstructed. A compensating gain factor of $G_m = 4.3 \pm 0.2$ is subsequently applied in the NLA stage. Three states were measured in four-fold coincidence detection (as before), to characterise each of the three stages in the protocol—loss in mode $|H\rangle$, noiseless amplification and entanglement swapping.

After the loss, ρ_{in} was measured in detectors $D2$ and $D6$, while the ancilla photon for the NLA stage was sent directly to $D1$ without any mode splitting or interference, and the ancilla photon for entanglement swapping was likewise sent to $D4$. The ρ_{in} tomography data collected in $D2$ and $D6$ was conditioned on these two additional (internal) triggers from the ancilla photons. Detectors $D3$ and $D6$ were used in the tomography of ρ_a , conditioned on the external trigger from the SPDC source, successful amplification heralded in detector $D1$ or $D2$, and the ancilla photon in the entanglement swapping stage acting as an extra trigger in $D4$. The final output state ρ_{out} is measured in detectors $D5$ and $D6$, conditioned on successful amplification heralded in $D1$ or $D2$, successful entanglement swapping heralded in $D3$ or $D4$, and

	$\rho = \rho_{in}$	$\rho = \rho_a$	$\rho = \rho_{out}$
$\langle H \rho H \rangle$	$(0.32 \pm 0.01) \times 10^{-2}$	$(1.40 \pm 0.05) \times 10^{-2}$	$(1.37 \pm 0.05) \times 10^{-2}$
$\langle V \rho V \rangle$	$(1.46 \pm 0.02) \times 10^{-2}$	$(1.26 \pm 0.05) \times 10^{-2}$	$(1.19 \pm 0.04) \times 10^{-2}$
$\langle \mathbf{2} \rho \mathbf{2} \rangle$	$(8.7 \pm 0.3) \times 10^{-7}$	—	$(2.0 \pm 0.3) \times 10^{-5}$
$\text{tr}\{(\rho_1)^2\}$	$99.97 \pm 0.15\%$	$92.3 \pm 0.9\%$	$79.0 \pm 1.5\%$
$\mathcal{C}(\rho)$	$(1.20 \pm 0.02) \times 10^{-2}$	$(1.56 \pm 0.08) \times 10^{-2}$	$(1.06 \pm 0.09) \times 10^{-2}$
$ \langle H \rho_1 V \rangle $	0.39	0.69	0.54

Table 4.2: Summary of results for the intermediate link configuration of the optical circuit. This is data for a single loss setting $L_m = 78 \pm 3\%$. The performance of the protocol was assessed based on the purity of the polarisation subspaces, the probabilities of the $|H\rangle$ and $|V\rangle$ modes in the full states, the concurrences and the size of the coherences.

the external trigger as always. Again, a HWP rotation of 45 degrees swapped the two detectors measuring the signal state for half of the time in every tomography, to average over unequal path efficiencies.

The two photon term $\langle \mathbf{2}|\rho_{out}|\mathbf{2} \rangle$ was measured during state tomography, by recording the five-fold coincidences between the usual three-fold coincidence patterns, a detection in $D5$ and one in $D6$. This directly measures the probability of the two photon term in ρ_{out} : $\varepsilon = \mathcal{C}_5/\mathcal{C}_3$. The two photon term $\langle \mathbf{2}|\rho_{out}|\mathbf{2} \rangle$ was not measured in the same way, because too few five-fold coincidence events were could be recorded for conclusive statistics. Instead, $\langle \mathbf{2}|\rho_{in}|\mathbf{2} \rangle$ was determined by measuring a ratio of three-fold coincidence to single photon rates. The ancilla photon in the NLA stage was sent directly to $D1$ to act as a trigger, since photons in this ancilla mode and the signal mode are generated in the same source. The signal mode is split evenly between $D2$ and $D6$, and the ratio of three-fold coincidences between $D1$, $D2$ and $D6$ and single counts detected in $D1$ is recorded: $\varepsilon = \mathcal{C}_3/\mathcal{S}$.

This procedure only measures the two photon term in the signal mode, without any contribution from the entanglement swapping ancilla mode. This is somewhat artificial, because one might want to compare the performance of the circuit with amplification, to the performance without amplification, but in both cases with teleportation. Teleportation requires an ancilla photon as well, which would contribute two-photon terms to the output state. Our experimentally determined value for $\langle \mathbf{2}|\rho_{in}|\mathbf{2} \rangle$ thus serves as a lower bound for ε . This presents the best-case scenario for the input state, but a worst-case scenario for a comparison with our output state.

The results of the tomographies are depicted in Figure 4.12: subfigures (a)–(b) show the normalised polarisation subspaces $|\psi_1\rangle\langle\psi_1|$, ρ_1^a and ρ_1^s , while (d) shows the full states ρ_{in} (semi-transparent bars) and ρ_{out} . The inset in (d) compares the

polarisation elements of the ρ_{in} and ρ_{out} density matrices. The $|H\rangle\langle H|$ probability is amplified in the output to re-balance the polarisation state. In subfigure (e) the matrix elements in (a)—(c) are directly compared: ρ_{in} from (a) is represented by the widest and lightest bars, ρ_a from (b) is represented by the middle-width and shaded bars, and ρ_{out} from (c) is represented by the narrowest solid bars. The main difference between ρ_a and ρ_{out} is a decrease in the coherence terms, which is a result of lower polarisation state purity after the entanglement swap. This is a result of imperfect interference in the entanglement swapping stage between the signal and ancilla photons, which are generated in independent sources. From the measured independent HOM visibility, and the purity of ρ_1^a from the NLA stage, the upper bound for the purity after entanglement swapping is $\sim 82\%$, compared to the measured $79 \pm 1.5\%$ purity of ρ_1^s .

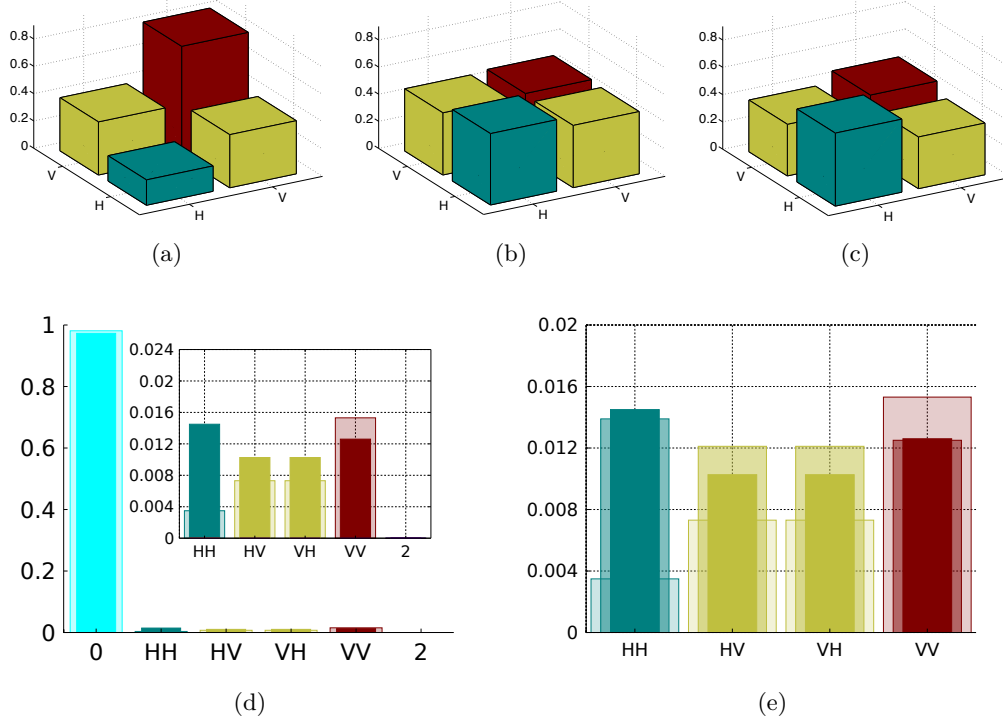


Figure 4.12: Loss factor $L_m = 78 \pm 3\%$ and NLA gain factor $G_m = 4.3 \pm 0.2$. Absolute values of the density matrix elements (a) $|\psi_1\rangle\langle\psi_1|$, (b) ρ_1^a and (c) ρ_1^s , the polarisation states after loss, amplification and entanglement swapping, respectively. (d) Absolute values of ρ_{in} (semi-transparent bars) and ρ_{out} . (e) Absolute values of $|\psi_1\rangle\langle\psi_1|$ (widest bars), ρ_1^a (middle bars) and ρ_1^s (narrowest bars).

The concurrences were calculated for ρ_{in} , ρ_a and ρ_{out} , and they are listed in Table 4.2. The concurrence increases from $(1.20 \pm 0.02) \cdot 10^{-2}$ to $(1.56 \pm 0.08) \cdot 10^{-2}$ after the NLA stage, but is reduced to $(1.06 \pm 0.09) \cdot 10^{-2}$ after entanglement swapping.

The reduced purity $\text{tr}\{(\rho_1^s)^2\} = 79.0 \pm 1.5\%$ after entanglement swapping, as well as the higher two photon probability $\varepsilon = (2.0 \pm 0.3) \cdot 10^{-2}$ can explain why the overall concurrence in ρ_{out} is approximately equal to the original concurrence in ρ_{in} . The absolute value of the coherence increases from 0.39 in 4.12(a) to 0.54 in 4.12(c), and all three coherence terms can be compared directly in 4.12(e). We note that our value for $\langle \mathbf{2} | \rho_{in} | \mathbf{2} \rangle$ was in fact a lower bound, which implies that $\mathcal{C}(\rho_{in}) = (1.20 \pm 0.02) \cdot 10^{-2}$ is the best case value. This suggests that the concurrence could be increased from ρ_{in} to ρ_{out} in an identical experiment, if single photon sources with lower rates of higher order terms were used. Developing true and deterministic single photon sources is a very active research field that incorporates diverse approaches, due to the fact that reliable single photon generation is currently a limitation in most quantum information protocols.

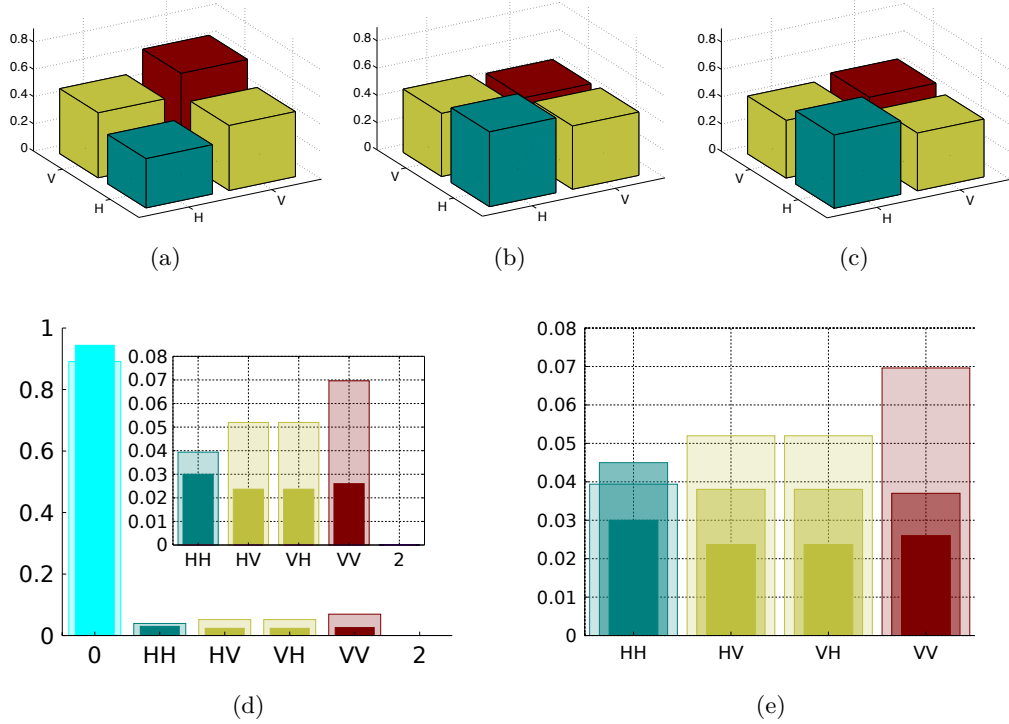


Figure 4.13: Data for input state with a single photon probability that is too large (with respect to ancilla efficiency). Absolute values of the density matrix elements (a) $|\psi_1\rangle\langle\psi_1|$, (b) ρ_1^a and (c) ρ_1^s , the polarisation states after loss, amplification and entanglement swapping, respectively. (d) Absolute values of ρ_{in} (semi-transparent bars) and ρ_{out} . (e) Absolute values of $|\psi_1\rangle\langle\psi_1|$ (widest bars), ρ_1^a (middle bars) and ρ_1^s (narrowest bars). Saturation (de-amplification) in both the NLA and entanglement swapping stages becomes evident in (d). See Appendix A for further details.

The experimental limitations of this configuration were explored in further detail:

Figure 4.13 shows data for an input state that is too large compared to the efficiency with which we can deliver ancilla states to the circuit, resulting in saturation of both the NLA and entanglement swapping stages. This saturation effect is manifested as a de-amplification of mode $|V\rangle$, which is the mode that had not been amplified. For an explanation of this effect, refer to Appendix A. Figure 4.14 shows data for a state subjected to less loss, and in this case the advantage from noiseless amplification is offset by the effect of experimental imperfections on the final output state.

It is interesting to note that from Figures 4.13(a), 4.13(b) and 4.13(c) it would appear as though the protocol works correctly—the saturation is not evident in the polarisation subspace. The problem is obvious in Figure 4.13(e), where it can be seen that the $|H\rangle\langle H|$ and $|V\rangle\langle V|$ probabilities become balanced from a de-amplification of $|V\rangle\langle V|$, instead of an amplification of $|H\rangle\langle H|$ as expected. The protocol hence weakens the mode entanglement, and the concurrence is reduced from $\mathcal{C}(\rho_{in}) \simeq 0.088$ to $\mathcal{C}(\rho_{out}) \simeq 0.029$.

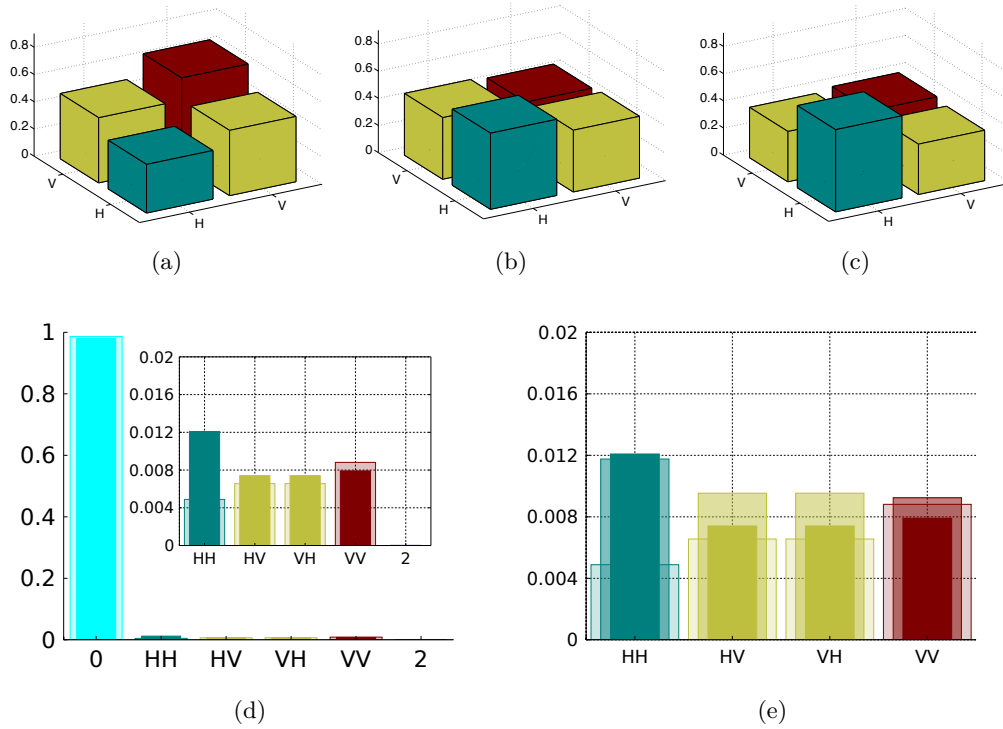


Figure 4.14: Loss factor $L_m \simeq 56\%$. Absolute values of the density matrix elements (a) $|\psi_1\rangle\langle\psi_1|$, (b) ρ_1^a and (c) ρ_1^s , the polarisation states after loss, amplification and entanglement swapping, respectively. (d) Absolute values of ρ_{in} (semi-transparent bars) and ρ_{out} . (e) Absolute values of $|\psi_1\rangle\langle\psi_1|$ (widest bars), ρ_1^a (middle bars) and ρ_1^s (narrowest bars). The loss is too small, and the advantage from the NLA stage is counterbalanced by experimental imperfections—the ρ_1^s coherences in (d) are only marginally higher than in $|\psi_1\rangle\langle\psi_1|$.

Even when the total single photon probability in ρ_{in} is reduced enough compared to ancilla efficiency for the NLA and entanglement swapping stages to work linearly, there is a loss regime in which this protocol does not offer a clear advantage. In 4.14 the loss to mode $|H\rangle$ in ρ_{in} was measured to be $L_m \simeq 56\%$. Despite a moderate over-amplification of the $|H\rangle$ mode in ρ_{out} , the coherence in the polarisation state ρ_1^s is not significantly greater than the original coherence in $|\psi_1\rangle\langle\psi_1|$, as seen in 4.14(e). Comparing concurrence in the input $\mathcal{C}(\rho_{in}) \simeq 0.011$ to concurrence in the output $\mathcal{C}(\rho_{out}) \simeq 0.007$ confirms that the protocol is not advantageous in this regime. Inevitable experimental imperfections in each stage reduce the advantage of these techniques, and this fact will need to be acknowledged for practical applications of long-distance quantum networks. This point becomes even clearer by noting that the concurrence in the state after amplification $\mathcal{C}(\rho_a) \simeq 0.011$ is equal to the input concurrence. The entanglement swapping reduces the polarisation state purity from $\text{tr}\{(\rho_1^a)^2\} = 92\%$ to $\text{tr}\{(\rho_1^s)^2\} = 80\%$, which accounts for the net loss in mode entanglement.

4.6.4 Summary

In this configuration of the optical circuit, loss was added to the entanglement swapping channel. A useful conceptual picture to motivate this configuration is two nodes or quantum memories separated by an entanglement swapping stage between them, in order to extend the range of entanglement.

The performance of the protocol was demonstrated for a loss of $L_m = 78 \pm 3\%$, and a clear increase in the coherence between modes was measured in the output state. The concurrence of the modes was moderately increased after the amplification stage, but after entanglement swapping the final concurrence decreased to approximately the same value as at the input. The fact that overall concurrence does not increase can be explained by imperfect HOM interference in the NLA and entanglement swapping stages, which introduced mixture and lead to a purity of $79.0 \pm 1.5\%$ in the single photon subspace. The ancilla photons in the two stages also contributed two photon terms to the output state, and the concurrence is highly sensitive to noise from higher order terms.

The performance of this configuration was also investigated using a larger input state size: $\langle \mathbf{1} | \rho_{in} | \mathbf{1} \rangle \simeq 0.12$ (see 4.13). In this case, as both the NLA and entanglement swapping stages are based on generalised quantum scissors, the single photon component of the input state proved to be too large, and saturation effects were observed in both stages. The coherence between modes was consequently reduced

after both amplification and entanglement swapping. A smaller loss setting was also investigated ($L_m \simeq 56\%$), and in this regime the advantage of amplification was counterbalanced by the effects of experimental imperfections, and the coherence was only marginally increased at the output.

These results suggest that this configuration offers an advantage in certain regimes, where it can increase coherence between modes. The results also highlight what improvements could be made—in particular, it is likely that the only modification to this configuration that is required to demonstrated entanglement concentration is a single photon source in the ancilla modes with suppressed higher order terms.

4.7 Discussion

The work presented in this chapter used two NLA stages based on generalised quantum scissors to investigate mitigating photon loss in quantum networks. In one configuration, loss was applied to the channel between a photon source and a quantum memory, and the distillation of mode entanglement was successfully demonstrated. In the second configuration, loss was applied to the channel between a photon source and the entanglement swapping stage, and while coherence between modes was increased with amplification, overall mode entanglement did not increase.

The greatest limitation of our approach is that the largest theoretically attainable output state size is equal to the ancilla source efficiency [106], and as the output state size approaches this limit the NLA stage saturates [60, 62, 63]. The need for deterministic single photon sources is a common theme in quantum information science, and significant progress has been made in increasing the efficiency of both generation and detection of single photons at various wavelengths [107]. In principle, with deterministic single photon sources a NLA stage could yield an output state arbitrarily close to a pure single photon. The probability of successful amplification scales inversely with the gain, so a tradeoff would need to be found between state purity and transmission rate, which would depend on the specific application. Higher-order photon number terms in the ancilla modes, which are an extra source of noise that were particularly noticeable in the second configuration of our experiment, are also an important consideration in engineering better single photon sources.

Another limitation of this approach is that it requires the stability of optical path lengths to within the coherence length of the photons. Since the goal is to extend quantum networks over large distances, this would be a serious technical challenge. More work is required to ascertain whether this could be technically feasible, or if

another approach to compensating for photon loss can be found with less stringent stability requirements.

The advantage of our technique can be seen in the scenario discussed in [113]. The authors note that heralding entanglement in an elementary link, consisting of two quantum memories separated by a linkage distance, is the necessary ingredient for high fidelity and high rate entanglement distribution. In their proposal, an entangled photo source is located close to one quantum memory, so that one photon is stored in memory without any loss. The other photon pair is transmitted to a second quantum memory. A NLA stage close to the second memory ensures that a pure state has been stored, effectively heralding entanglement creation in an elementary link. The resource requirement for the NLA is an on-demand single photon ancilla, but generated locally—that is, close to the second quantum memory. Subsequently, multiple elementary links can be connected via entanglement swapping, to extend the range of entanglement. This scenario is similar to the one depicted in Fig. 4.5, the conceptual diagram for the terminal configuration, except that a second quantum memory directly after the first photon source, in the entanglement swap arm, is not pictured there. As already mentioned, the advantage of the second configuration, where the NLA is in the entanglement swapping arm, would be evident in a scenario where long-range entanglement has previously been established, and is being extended to the next node. The memory containing the long-range entanglement should not release its state until the NLA heralds that transmission loss in the channel on the other side of the entanglement swapping stage has already been corrected. This increases the success probability of the entanglement swapping operation. Although proposed quantum repeaters such as the one in Ref. [113] explicitly consider entanglement between two particles, or qubits, we have previously demonstrated that the techniques described in this chapter can readily be extended to apply to qubits [60].

The goal of building a quantum repeater unifies several research areas, including quantum memories, quantum communication, state purification and error correction. It represents a great challenge, but also holds the key to developing a practical quantum internet [115, 116]. The value of quantum repeaters may extend beyond quantum information networks, and their potential application to metrology has recently been investigated [158]. The experimental results presented in this chapter set a benchmark for linear optical protocols that will be integrated in quantum repeater architectures, and identify areas for future improvement and further investigation.

Chapter 5

Quantum-Refereed Steering for Enhanced Security

5.1 Acknowledgements

The two SPDC sources and the Bell state analysis setup were constructed by Adam Bennet and Dylan Saunders, and I assisted in their optimisation. Adam Bennet and I characterised the Werner state and the Bell state measurement. I performed the primary data analysis, with input from Adam Bennet, and supervision from Michael Hall and Geoff Pryde. The payoff function for the quantum-refereed steering protocol, presented in Section 5.4.1, was developed by Michael Hall.

5.2 Introduction

It has been shown that one-sided DIQKD requires the violation of a steering inequality, in analogy to two-way DIQKD required the violation of a Bell inequality, which is a strong category of non-classical correlation [159]. The rigorous violation of a Bell inequality requires very high detection efficiencies in order to rule out the detection loophole, which is extremely challenging with the existing technology [74]. Steering is generally less restrictive, and it has been shown that steering can be demonstrated with arbitrarily low efficiencies [71]. This is motivation to consider scenarios in which the security of a central node in a communication network can be guaranteed, but the other nodes to which it transmits signals are not secure. In such a case, one-sided DIQKD could guarantee communication security in the network.

If two spatially separated parties, Alice and Bob, report measurement results that violate a steering inequality [160–162], this only proves to an external referee, Charlie, that Alice really is steering Bob’s system if Charlie is willing to assume that Alice and Bob did not agree on a list of measurement outcomes prior to being separated. Combining lists of measurement results is logically insufficient to guarantee that two parties truly share entanglement [163]. An added degree of security, in the form of a semi-quantum refereeing protocol, or semi-quantum game, is required to address the problem. This is the subject of the experimental results presented in this chapter.

5.3 Non-Classical Correlations

The idea of classical correlations is well-known and reasonably intuitive. Correlations exist between systems in nature that cannot be explained using classical reasoning alone, but which are predicted by quantum theory. In a general sense, these non-classical or quantum correlations can be explained by the superposition principle in quantum mechanics: a system can exist in a superposition of two eigenstates, with a fixed phase between the states.

To sketch out a somewhat simplistic example of the difference between classical and non-classical correlations: imagine that Alice and Bob know that inside a box there is one red ball and one green ball. With their eyes closed, they each take one ball out of the box, and still keeping their eyes shut Alice boards a plane to Perth (Australia) while Bob boards a plane to Hamilton (Bermuda). Once at their destinations, Alice can ascertain whether she has a red or green ball by looking at what is in her hand. If she sees a green ball, she instantaneously knows that Bob, on the other side of the world, must be holding a red ball. By making a local measurement, she immediately gains information about a system that is a great distance away—with her local measurement, she instantaneously determines if Bob’s ball is red or green, when it is on the other side of the world. Nothing mysterious or un-intuitive happens in this scenario, and this is a purely classical correlation.

The scenario can be modified to illustrate a quantum correlation. Now the two balls in the box are “quantum” balls, and before looking at them one can only describe them as having complementary colours on the colour wheel. That is, if one is red the other is green, if one is blue the other is orange, if one is purple the other is yellow, *etc.* From Perth, Alice can now choose how to “measure” the ball—she can equally ask if the ball is blue, green or red. In the quantum formalism, this is called

choosing the measurement basis for a system. The point is that the colour of Alice's ball is actually undefined until she makes a decision to test it in a specific basis, and the only defining feature is that the two balls are always opposite colours. If she tests whether the ball is green and the result is affirmative, she and Bob both know that Bob's ball is green without Bob needing to check it himself. So far, this is identical to the classical case. The difference now is that Alice can measure in any basis, and the correlation will persist. For example, if she tests whether her ball is purple, she will automatically ensure that Bob's ball is either yellow or purple, based on her measurement result. In the classical case, the balls were always either red or green (even if Alice and Bob did not know it), and they could never be any other colour. In the quantum case, Alice has the freedom to measure her ball in any colour basis, and by doing so, she collapses Bob's ball in Bermuda into the same colour basis, with the opposite colour. To truly verify that Alice and Bob are seeing non-classical (*i.e.* quantum mechanical) correlations, Bob should measure his ball in a different colour basis than what Alice measures hers in. This ensures that Alice and Bob don't simply share a list of correlated values, or in other words, that they don't share a statistical mixture of classically correlated states. By measuring in different colour bases over many trials, and looking at their measurement results, Alice and Bob can test that the exact colour of their balls is truly undetermined before measurement, existing in a superposition of possibilities. This is essentially what the inequalities that will be introduced in the next sections are testing¹.

5.3.1 Einstein-Podolsky-Rosen Paradox and Entanglement

In 1935, Einstein, Podolsky and Rosen (EPR) proposed a thought-experiment to highlight why they believed that quantum mechanics could not be a complete theory [14]. Their thought experiment was essentially the description of non-classical correlations from the last section, but using the formalism of quantum mechanics. The essence of the argument is as follows (the argument was originally framed in terms of continuous variables, but Bohm [164] re-framed it in terms of discrete spin variables, which is conceptually simpler). Two entangled particles are in the pure state

$$|\Phi^+\rangle = \frac{1}{\sqrt{2}}(|0_A 1_B\rangle + |1_A 0_B\rangle) \quad (5.1)$$

where the composite particles A and B are separated by lightyears. A measurement of particle A would seem to affect a measurement of particle B, in that if Alice

¹For a thorough exposition of the difference between classical and non-classical correlations, refer to Bell's paper "Bertlmann's socks and the nature of reality", which can be found in [13]

measures her particle to be in the state $|0\rangle$, it collapse the wave function of Bob's particle into the eigenstate $|0\rangle$. Einstein, who had previously developed the theory of relativity, believed that this “instantaneous collapse” effect was “spooky action at a distance”, and violated the principles of local realism. The realism assumption in local realism states that if there is a physical property or quantity associated with a system, which can be predicted with certainty without disturbing the system, then this physical quantity corresponds to an “element of reality”. The locality assumption states that there can be no action at a distance, so that a local measurement at A cannot disturb a space-like separated system B.

Einstein *et al.* were arguing for a local hidden variable model of reality, in which no effect can propagate faster than the speed of light, and the properties of a system are predetermined by variables, which are hidden prior to measurement. The paradox in the EPR experiment is the the system variables of A and B appear to depend on what is measured. Around this same time, Schrödinger also made influential contributions to the early these early discussions. He called the apparent influence by A on the wave function of the remote system B “steering”, and also coined the term “entanglement” to describe the inseparability (or unfactorizability) of the individual wave functions for the subsystems A and B [165]. In another thought experiment that carries his name (Schrödinger's cat paradox), he imagined a microscopic quantum system, such as an atom, entangled with a macroscopic object such as a cat. Since the microscopic object is generally in a superposition state, this implies that the macroscopic object must also exist in a superposition, leading to absurd conclusions, like the cat being in a superposition of a live and dead state [166]. The phenomenon of entanglement was central to the early development of quantum mechanics, and von Neumann later proposed that measurement-induced wave function collapse could be explained by the measurement apparatus becoming entangled with the measured system [167].

The EPR paradox set in motion a long-lasting debate over the interpretation of what quantum theory says about the nature of reality [168]. Although most standard interpretations assert that “realism”, or hidden variables, do not exist in nature, alternative interpretations have not definitively been ruled out. Perhaps the two most famous alternative interpretations are the Bohm-de Broglie interpretation [169, 170] and Everett's many-worlds interpretation [171].

5.3.2 Bell Inequalities

Since the original EPR paper, much effort has been devoted to developing quantitative models to constrain the types of theories that could describe how nature really works [172]. The most famous result in this line is Bell's theorem, due to John Bell in 1964 [12, 13]. Bell derived an inequality that all local hidden variable (LHV) theories must satisfy, and showed that quantum mechanics predicts that the inequality will be violated. Bell's theorem demonstrates the incompatibility of quantum mechanics and LHV theories.

Clauser *et al.* extended Bell's theorem in 1969, deriving an inequality that is somewhat simpler than Bell's original one, and could more easily be implemented in the laboratory [173]. The idea behind the CHSH inequality is presented, which is enough to understand the essential idea in Bell's theorem. Bell imagined the following scenario: Alice and Bob each have one particle of a pair of particles, which may be correlated in some way. Alice and Bob both also have two measurement apparatuses each: Alice's apparatuses are A_1 and A_2 , while Bob's are B_1 and B_2 . They agree together that they will both, independently but simultaneously, choose one measurement apparatus and measure their particle with it. It can conveniently be assumed that the possible measurement results are always ± 1 , without any loss of generality. Bell's inequality states that for a LHV theory

$$E(A_1B_1) + E(A_1B_2) + E(A_2B_1) + E(A_2B_2) \leq 2 , \quad (5.2)$$

where $E(A_jB_k)$ is the expectation value for Alice measuring A_j and Bob measures B_k . The only assumptions that enter into the derivation of this inequality are those of local realism: a) a measurement reveals a pre-existing element of physical reality, and b) a measurement made by Alice has no effect on a measurement made by Bob, when he is space-like separated from her. In other words, the inequality does not refer to quantum theory at all, and hence the inequality is theory-independent. The quantum mechanical prediction for the inequality is

$$E(A_1B_1) + E(A_1B_2) + E(A_2B_1) + E(A_2B_2) = 2\sqrt{2} > 2 , \quad (5.3)$$

violating the bound set by local realism. This demonstrates that, in order for quantum mechanics to accurately describe nature, which it has been repeatedly confirmed to do, one of the two assumptions in local realism must be abandoned. It is impossible for a LHV theory to accurately describe nature. Another influential result, complementary to Bell's theorem, is the Kochen–Specker theorem [174].

Kochen and Specker showed that quantum mechanical commutation relations are incompatible with a non-contextual hidden variable theory. Quantum mechanical observable can therefore not be considered elements of physical reality outside the context of how they are measured.

The earliest violation of the CHSH inequality with causally separated parties was demonstrated by Aspect *et al.* in 1982, using entangled photons. The test of Bell's theorem was convincing but not conclusive, as low detection efficiencies meant that measurements could only be performed on a post-selected sub-ensemble of events. Only very recently has a Bell inequality been conclusively violated [74, 75], with the detection loophole finally closed.

5.3.3 Steering Inequalities

Schrödinger originally coined the term “steering” in 1935 to refer to the EPR thought experiment. The phenomenon in the original thought experiment, whereby Alice affects, or “steers” Bob's state by choosing a basis to measure her own state in, was mostly superseded in popular discussion by Bell inequalities, which involve a slightly different scenario. A rigorous definition of steering was not established until 2007, when steering was defined operationally, in terms of a quantum information task, and a steering inequality was derived [160]. A hierarchy exists for entangled states, and steerable states were shown to be a strict superset of Bell nonlocal states, and a strict subset of all entangled (non-separable) states [161] (see Figure 5.1). The success of this approach highlights the advantage in operationally defining entanglement inequalities. In the remainder of this chapter, entanglement inequalities will be discussed as quantum information protocols, and the Bell and steering protocols are described below.

In the Bell inequality protocol (see Figure 5.2(a)), the aim is for Alice and Bob to convince an external referee, Charlie, that they share a Bell nonlocal state between them. An ensemble of identical bipartite states are prepared and distributed between Alice and Bob, who then separate to a space-like distance from each other. After the preparation step, communication is forbidden between Alice and Charlie. Alice and Bob will communicate with Charlie, who trusts quantum mechanics but does not trust either of them (represented by the black box covering Alice's and Bob's measurement devices in 5.2(a)). Alice and Bob proceed to simultaneously measure their quantum state one at a time, reporting their results to Charlie. If the correlations between their results are too strong to be explained by any LHV model, Charlie must conclude that they really do share entanglement above the Bell

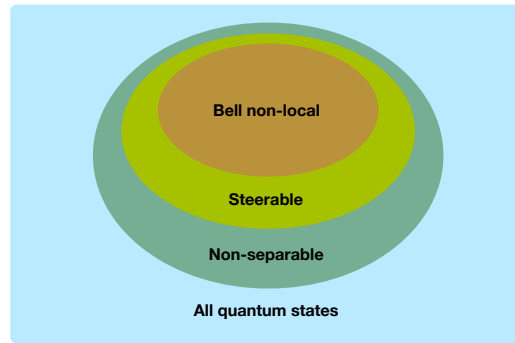


Figure 5.1: Hierarchy of entanglement. Bell non-local states, capable of violating a Bell inequality, are a strict subset of steerable states, only capable of violating a steering inequality. They are both strict subsets of non-separable states, which are quantum states with non-zero entanglement.

nonlocal threshold.

The steering protocol (see Figure 5.2(b)) is derived by weakening the Bell inequality protocol. Steering is asymmetric, unlike demonstrating Bell non-locality, and Charlie now trusts Bob while still not trusting Alice. The criteria Charlie uses to decide if Alice and Bob truly share entanglement is whether the correlations can be explained by any local hidden state (LHS) model for Bob. In a LHS model, Bob's system is in a definite state, and it is simply unknown to him. This could be the result of Alice cheating in the preparation stage by secretly giving Bob a local pure state that is known to her. Charlie can in principle perform quantum state tomography on Bob's state (because he trusts everything Bob tells him), and only concedes that Alice and Bob share entanglement if Alice can steer Bob's state. In other words, the correlations between their measurements must exceed the LHS bound set by the steering inequality [160].

Similarly, by weakening the criteria in the steering protocol, a protocol for determining non-separability can be arrived at (see Figure 5.2(c)). In this protocol, Charlie trusts both Alice and Bob, and can therefore perform quantum state tomography on both of their states. By reconstructing the full density matrix, it can be determined whether or not the state is separable [149, 175].

Early experimental investigations of steering [176–179] used continuous-variable states. More recently, steering was experimentally demonstrated using entangled polarisation qubits [81, 180]. In this experiment, the degree of entanglement could be tuned by preparing various Werner states [175], and the steering of a Bell local state was conclusively shown for the first time.

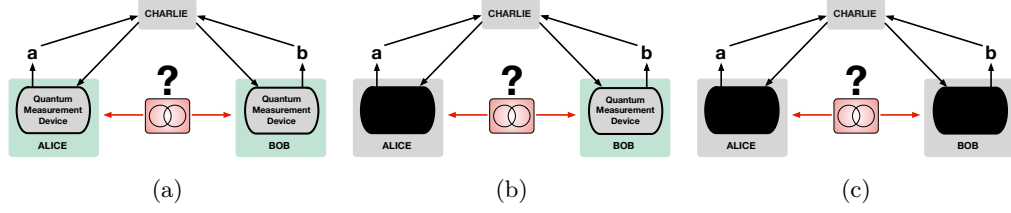


Figure 5.2: Comparing (a) standard QKD, (b) one-sided DIQKD and (c) DIQKD configurations. In standard QKD, Alice and Bob must both trust their measurement devices. One-sided DIQKD is an asymmetric protocol, in which only Bob must trust his device, and Alice can be untrusted (signified by the black box over her measurement device). Alice must prove to the referee, Charlie, that she can steer Bob’s state, and this is achieved by violating a steering inequality. In DIQKD, both Alice and Bob can be untrusted, and they prove to Charlie that they share entanglement by violating a Bell inequality. DIQKD has the most strenuous requirements, in terms of the strength of the correlation the parties must demonstrate, and detection efficiencies. Standard QKD has the weakest requirement, it only being necessary to show that Alice’s and Bob’s states are not separable, by each performing quantum state tomography on their systems.

5.4 Experimental Concept

In standard QKD, communication security is proven under the assumption that Alice and Bob can trust their measurement devices. Recently, the successful hacking [181, 182] of the BB84 protocol [41] has demonstrated the weakness of this assumption. Trust in one’s measurement device becomes unnecessary in a DIQKD protocol [79]: the measurement devices can be considered black boxes, as their specific inner workings are not relevant as long as a Bell inequality is violated.

DIQKD protocols impose strenuous requirements on overall detection efficiency [74, 75]. One-sided DIQKD protocols, which involve the violation of a steering inequality instead of a Bell inequality [159], impose somewhat lower detection efficiency requirements [71–73]. For Charlie to witness steering, however, he must trust Bob (and implicitly, Bob’s measurement device).

Generalising recent work [183] on non-local (or “semi-quantum”) games, and inspired by the work extending it to one-sided DIQKD [184, 185], a device-independent protocol to prove the steerability of a state has been developed [186], that no longer requires Charlie to trust Bob. It is believed that the protocol can be extended to quantum-refereed one-sided DIQKD, and this is being theoretically investigated. The experimental work presented in this chapter implements such a protocol to witness Bob steering Alice’s state. The details of the experimental protocol can be found in Section 5.4.1. A state from a class of mixed entangled states known as Werner states was used in the experiment, to demonstrate steering of a strictly Bell

local state.

5.4.1 Quantum-Refereed Steering Protocol

Pre-shared classical information can be used by Alice and Bob to mimic non-classical correlations, and convince the referee Charlie to erroneously assert that they share a steerable state. In the standard steering protocol (see Figure 5.3(a)), Charlie is required to trust Bob (and his measurement device) to verify that Alice and Bob share a steerable state. In Figure 5.3(a), a green box around Bob's apparatus indicates trust by Charlie, while the protocol is device-independent with respect to Alice, indicated by the black box. In the modified, quantum-refereed steering protocol (Figure 5.3(b)), Charlie is not required to trust Bob in order to verify steering, and steering can be verified in a fully adversarial context. Classical communication from Charlie to Bob in 5.3(a) is replaced by quantum communication in 5.3(b) (indicated by the red arrow from Charlie to Bob), and this quantum randomness effectively neutralises any pre-arranged cheating strategy that Alice and Bob could have agreed upon in the protocol's preparation stage [187]. The green box around Charlie in 5.3(b) indicates that Charlie must now trust his own ability to correctly prepare the quantum state he sends to Bob.

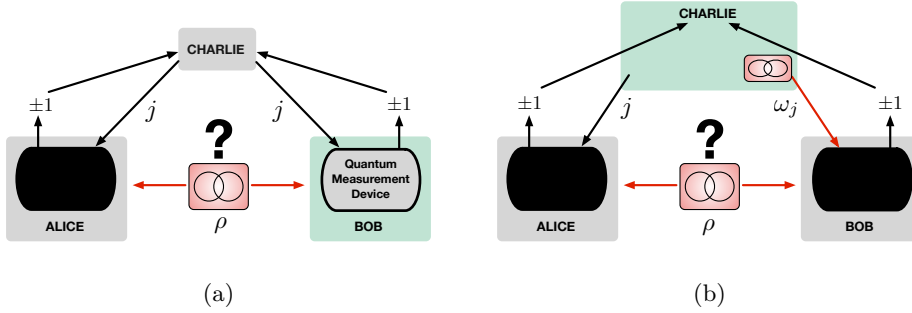


Figure 5.3: Comparing (a) one-sided DIQKD and (b) quantum-refereed one-sided DIQKD configurations. In one-sided DIQKD, the aim is for Bob, whom Charlie trusts (signified by the green box), and Alice to demonstrate that they share a steerable state ρ . Charlie communicates classical measurement settings j to both parties, and analyses the correlations of Alice's and Bob's results to see whether they violate a steering inequality, thus proving that Alice can steer Bob's state. In the quantum-refereed case, Charlie trusts neither Bob nor Alice, and must only trust his own ability to accurately prepare and send a quantum state. His trust in Bob is replaced by quantum communication (red arrow), by which he sends Bob a quantum state ω_j instead of a classical measurement setting, as he did in (a). Bob will make a joint measurement on $\rho_B \otimes \omega_j$ when trying to violate a steering inequality, which prevents him from conspiring with Alice to deceive Charlie.

Our modified steering protocol follows the general approach proposed in [184, 185].

Alice and Bob share a Werner state ρ , in polarisation space (see Section 5.5.1 for details). Charlie sends Bob the state ω_j , proportional to an eigenstate of one of the three Pauli operators σ_j ($j \in \{1, 2, 3\}$), and he sends Alice the measurement basis j (*i.e.* a classical signal). Alice can use her knowledge of the measurement basis to inform her own choice of measurement, and returns a dichotomic result $a_p = \pm 1$ to Charlie. Bob possesses the combined state $\rho_B \otimes \omega_j$, where ρ_B is Bob's half of the state ρ that he shares with Alice, and $\omega_j \equiv (\mathbb{1} \pm \sigma_j)/2$ is the state that Charlie sends to him. Bob projects his combined state onto the observable

$$B \equiv 2|\Psi^-\rangle\langle\Psi^-| - \mathbb{1} \otimes \mathbb{1} , \quad (5.4)$$

and also returns a dichotomic result ± 1 . In the original semiquantum game in [183], Bob performed a full Bell state measurement on his combined state. In [185], it was shown that a simple projection onto a maximally entangled state was enough in their protocol. The observable B corresponds to projecting Bob's combined state onto the singlet state $|\Psi^-\rangle$, which is the easiest measurement to implement experimentally. Charlie uses Alice's and Bob's reported results to construct the “payoff” function

$$P(\rho) \equiv \sum_p \left[s_p \langle a_p (\mathbb{1} \otimes \mathbb{1} + B) \rangle_{\rho_B \otimes \omega_p} - \frac{1}{\sqrt{3}} \langle (\mathbb{1} \otimes \mathbb{1} + B) \rangle_{\rho_B \otimes \omega_p} \right] , \quad (5.5)$$

where p is an index that can take one of six values: $p = \pm j \in \{\pm 1, \pm 2, \pm 3\}$, and s_p is the sign of p .

The payoff function will be positive for any steerable state, and negative for any non-steerable state. The payoff function is robust against any conspiratorial cheating strategy between Alice and Bob, since a non-steerable state combined with local operations and shared randomness still cannot yield a positive payoff [184, 187].

5.4.2 Werner States

Werner states are the best-known class of mixed entangled states, and can be expressed in terms of the three Pauli matrices:

$$W_\mu = \frac{1}{4} \left(\mathbb{1} \otimes \mathbb{1} - \mu \sum_{j=1}^3 \sigma_j \otimes \sigma_j \right) , \quad (5.6)$$

where the $\{\sigma_x, \sigma_y, \sigma_z\}$ Pauli matrices are indexed by $j \in \{1, 2, 3\}$, and $\mathbb{1}$ is the two-dimensional identity operator. A Werner state is entirely determined by the parameter $\mu \in [0, 1]$, with $\mu = 0$ corresponding to a completely mixed state, and

$\mu = 1$ corresponding to the singlet state, which is a maximally entangled state. Using the formula for the singlet state

$$|\Psi^-\rangle\langle\Psi^-| = \frac{1}{4} \left(\mathbb{1} \otimes \mathbb{1} - \sum_{j=1}^3 \sigma_j \otimes \sigma_j \right), \quad (5.7)$$

the Werner state can be expressed in a couple of different ways:

$$W_\mu = \mu |\Psi^-\rangle\langle\Psi^-| + \frac{1-\mu}{4} \mathbb{1} \otimes \mathbb{1} \quad (5.8a)$$

$$= \frac{1+3\mu}{4} |\Psi^-\rangle\langle\Psi^-| + \frac{1-\mu}{4} (\mathbb{1} \otimes \mathbb{1} - |\Psi^-\rangle\langle\Psi^-|), \quad (5.8b)$$

Thus, a Werner state is a weighted sum of the singlet state, which is a maximally entangled state, and symmetric (“white”) noise from the identity matrix, as in (5.8a). Alternatively, it can be considered a weighted mixture of a symmetric (singlet) subspace and an anti-symmetric (triplet) subspace, as in (5.8b). The Werner state has been a convenient model to use when deriving quantum information bounds, and it is known that a Werner state is entangled if and only if $\mu > 1/3$ [175], it can only violate the CHSH inequality if $\mu > 1/\sqrt{2} \simeq 0.707$ [173], and it cannot violate any Bell inequality if $\mu < 0.6595$ [188].

Steering inequalities have also been derived for Werner states [160]. These steering bounds generally depend on the number of measurement settings—how many bases Bob measures his state in. For three measurement settings (corresponding, for example, to the Pauli observables σ_x , σ_y , and σ_z), a Werner state is steerable if $\mu > 1/\sqrt{3} \simeq 0.5774$, and this is the Werner parameter bound we use in the experiment. For a larger number of measurement settings, the Werner parameter required for a steerable state is reduced, and asymptotes for an infinite number of settings at $\mu > 1/2$ [180]. Werner states are consequently ideally suited to be test states for proof-of-principle demonstrations of quantum information protocols, as their entanglement class is well-understood, easily measured and varied.

5.5 Experimental Setup

The experimental setup consists of: a polarisation-entangled photon source, which generates the state ρ to be distributed between Alice and Bob; a polarisation-unentangled source, which Charlie uses to send the state ω_j to Bob; and a Bell state analysis setup, with which Bob performs a joint measurement on his half of ρ and the state Charlie sends him. Details about these experimental components can be

found in the next sections.

The principle laser is a *Tsunami* model Ti:Sapphire laser manufactured by *Spectra-Physics*. This laser can provide approximately 2 W of frequency tuneable pulsed coherent light in the TEM₀₀ spatial mode. The repetition rate was 80 MHz, with a pulse width of ~ 100 fs. The laser was operated at 820 nm wavelength, and the output was sent to a BBO crystal to be up-converted to 410 nm, in a SHG process. These components are not picture in 5.4.

The 410 nm pump beam is split at the first PBS in Figure 5.4; half (~ 200 mW) of the optical power is sent to Alice's and Bob's (polarisation-entangled) source, and ~ 200 mW is sent to Charlie's (polarisation-unentangled) source. Two pairs of up-converted photons at 820 nm are used in the remainder of the experiment. Frequency filtering is applied at all output ports using tilted band-gap interference filters manufactured for a central wavelength of 810 nm (not pictured). All light is coupled into single-mode 820 nm optical fibre at the output ports (illustrated as green lines), and is detected using single photon counting modules (SPCM).

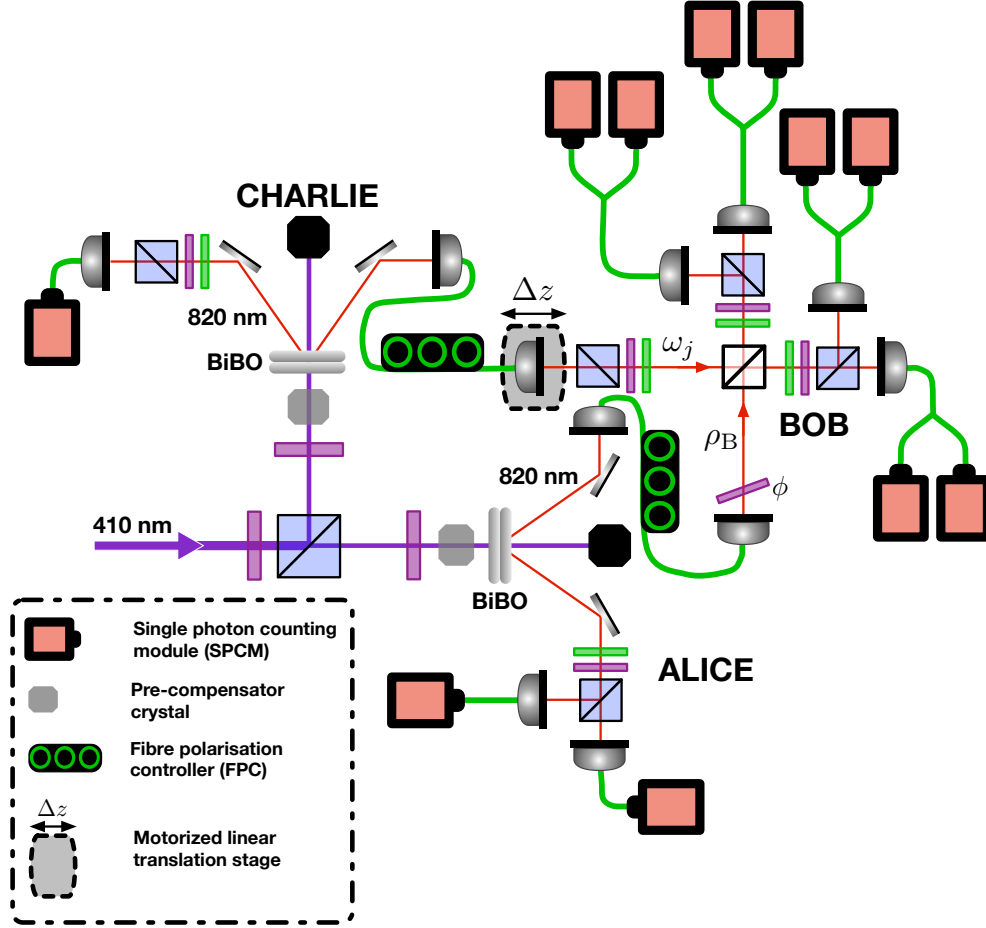


Figure 5.4: Both SPDC sources consist of a pair of 0.5 mm sandwiched BiBO crystals cut for type-I phase matching, with their optic axes perpendicularly oriented. Charlie's SPDC source is operated to generate polarisation-unentangled photons. One of Charlie's photons is sent straight to a SPCM, and heralds when the second photon arrives at the Bell state analysis setup. The other SPDC setup is configured to generate polarisation-entangled photons, creating the state ρ shared between Alice and Bob. The state from the SPDC source can be transformed into any of the four Bell states. This is done with a fibre polarisation control (FPC) on Bob's fibre, and a tilted HWP with its optic axis in the horizontal plane, that applies a phase ϕ between $|H\rangle$ and $|V\rangle$. Alice's photon is sent to her detection setup, while Bob's photon is coupled into single-mode fibre and sent to the Bell state analyser. The Bell state analyser, which takes as inputs Bob's half of the entangled state ρ and the state ω_j that Charlie sends him, consists of a central 50:50 beam splitter and polarisation analysers at its output ports. With pseudo-number resolving detectors, two of the four Bell states (including $|\Psi^-\rangle$) can be perfectly resolved, while the remaining two are imperfectly resolved (see text for details).

5.5.1 SPDC Sources

A sandwiched SPDC source [189] was used to generate polarisation-entangled photon pairs. In this source, two adjacent, thin (0.5 mm) Bismuth Borate (BiBO) crystals cut for type-I phase matching are oriented so their optic axes and the pump beam define perpendicular planes. That is, the first (second) crystal's optic axis and the pump beam define the vertical (horizontal) plane. The pump beam is diagonally polarised, and can generate a down conversion event in both crystals. The vertical polarisation component of the pump will produce horizontally polarised photon pairs (due to type-I coupling) in the first crystal, while the vertical component of the pump will generate vertically polarised photon pairs in the second crystal. As the two crystals are thin and directly adjacent to one another, the two down conversion light cones will be spatially indistinguishable from each other. In principle, no information exists to determine if a down-converted pair came from the first or second crystal, which means that the two down conversion processes are coherent². A down-converted photon pair is thus in an entangled state

$$|\psi\rangle = \frac{|H_1 H_2\rangle + e^{i\phi} |V_1 V_2\rangle}{\sqrt{2}}, \quad (5.9)$$

where the subscripts indicate collection modes, and the relative phase ϕ is determined by details of the phase matching condition. The state in (5.9) is maximally entangled, and can be transformed into any of the four Bell state $\{|\Psi^\pm\rangle, |\Phi^\pm\rangle\}$ by local operations, using wave plates and phase shifters.

Charlie's source of quantum states that he sends to Bob was an identical sandwiched type-I SPDC source, operated in the polarisation-unentangled mode, by setting the pump polarisation to effectively pumping only one crystal. Charlie prepares the signal photon in an eigenstate of one of the Pauli operators σ_j , and the idler photon acts as a herald, or external trigger, signalling that its pair has been delivered to the optical circuit. The idler photon must be measure in the same basis j . Charlie's ability to send the correct state ω_j to Bob was experimentally characterised. An average fidelity of $\mathcal{F}_{\text{av}} = 98.7 \pm 0.6\%$ was measured in the Bell state analysis setup for the six Pauli operator eigenstates from Charlie's source.

The singles rate from the entangled source was $(8.2 \pm 0.3) \times 10^4 \text{ s}^{-1}$ and a two-fold coincidence rate of $(4.2 \pm 0.1) \times 10^3 \text{ s}^{-1}$, while the singles rate from Charlie's

²The two crystals must be thin to allow for high spatial overlap of the down conversion cones. From a geometric argument [189], the spatial overlap will be high if $\theta_{dc} L/D \ll 1$, where θ_{dc} is the opening angle of the down conversion cone ($\sim 3^\circ$), L is the crystal thickness, and D is the pump beam diameter.

unentangled source was $(9.2 \pm 0.3) \times 10^4 \text{ s}^{-1}$, and the two-fold coincidence rate was $(4.2 \pm 0.3) \times 10^3 \text{ s}^{-1}$.

5.5.2 Bell State Analysis

Bob makes a joint projective measurement of his state $\rho_B \otimes \omega_j$ on the singlet subspace. Performing a full Bell state measurement that resolves all four Bell states is impossible using linear optics and post-selection [190]. Hong–Ou–Mandel interference can be used to filter the singlet state $|\Psi^-\rangle$: single photons will only anti-bunch if they are in a joint anti-symmetric state, and will bunch if they are in any of the three symmetric triplet states $|\Psi^+\rangle$, $|\Phi^\pm\rangle$. The signature of measuring $|\Psi^-\rangle$ is therefore a coincidence detection between the two output ports of the 50:50 beam splitter, and theoretically the efficiency of this measurement is only limited by the HOM interference visibility (see Section 5.6.1). The triplet states will all be measured as coincidences within one output port of the 50:50 beam splitter.

Polarisation modes are separated in each output arm after the 50:50 beam splitter using wave plates and PBSs. As a result, the $|\Psi^+\rangle = (|HV\rangle + |VH\rangle)/\sqrt{2}$ state can also be perfectly resolved, as its signature is a coincidence in a single output arm between different polarisation modes. The remaining two triplet states $|\Phi^\pm\rangle = (|HH\rangle \pm |VV\rangle)/\sqrt{2}$ cannot be perfectly resolved with the apparatus in 5.4. In these two states, the two photons will occupy the same output mode after the 50:50 beam splitter, and also be identically polarised, meaning that they will exit the same port after a PBS as well. A SPCM with number resolution could, in principle, distinguish the $|\Phi^\pm\rangle$ states from the other two Bell states, although it would still not be possible to resolve $|\Phi^+\rangle$ from $|\Phi^-\rangle$.

Fortunately, the quantum-refereed steering protocol only requires Bob to project his state onto the singlet subspace, with the orthogonal result combining all three triplet state projections. Measuring the aggregate of the projections onto $|\Phi^\pm\rangle$ is therefore acceptable. We implemented pseudo-number-resolving detection, by using 50:50 fibre beam splitters at the four output modes of the Bell state measurement, and using eight SPCM instead of the original four. With this strategy, there is a 50% probability that two photons in one output mode will be split at the fibre beam splitter, and register a coincidence in two detectors. In our data analysis, we therefore double the measured rate of $|\Phi^\pm\rangle$ detections, to account for the half of those states that we were unable to measure directly.

5.6 Experimental Results

A quantum-refereed steering inequality was violated with a Bell-local Werner state. The quantum-refereed steering protocol was also tested using a singlet state, and a maximum violation of the steering inequality was observed.

5.6.1 Characterising HOM Interference

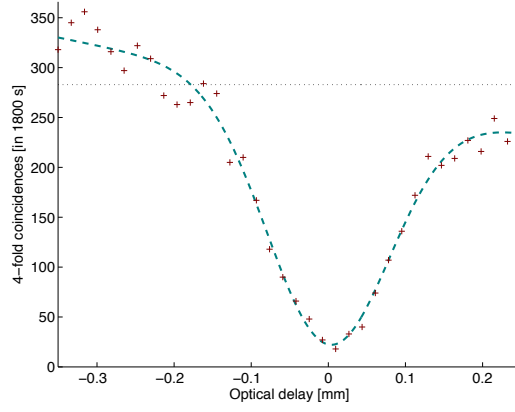


Figure 5.5: Measurement of the Hong–Ou–Mandel (HOM) interference visibility between Bob’s and Charlie’s photons, at the central 50:50 beam splitter in the Bell state analyser. The output coupler in Charlie’s arm was on a motorised linear translation stage, which temporally mode-matched the two photons. Data was collected in four-fold coincidence detection, and the collection time for each data point was 1800 seconds. A Gaussian function was fitted to the data set (see text for details), and the interference visibility was calculate to be 89%.

The Bell state analysis setup in 5.4 is based around a non-classical HOM interference between the ρ_B and ω_j photons at the central 50:50 beam splitter. It was necessary to characterise the HOM interference, as high interference visibility was required to effectively resolve the singlet state $|\Psi^-\rangle$ from the other three triplet Bell states—only the singlet state anti-bunches at the beam splitter. Bob performs a joint measurement on $\rho_B \otimes \omega_j$, and the fibre output coupler for the ω_j photon is on a linear z -translation stage, to match temporal modes between the ρ_B and ω_j photons.

As the ρ_B and ω_j photons are from independent SPDC sources, it was necessary to measure the HOM interference (see Figure 5.5) in four-fold coincidences. Thus, a photon detected in Alice’s detector heralds the presence of the ρ_B photon at the 50:50 beam splitter, and a detection in Charlie’s other detector heralds the presence of the ω_j photon.

A Gaussian function was fitted to the data set in Figure 5.5, and the interference visibility was calculated using the amplitude of the fitted function. As the output coupler was translated along the z -axis across the interference region, the coupling efficiency to the output couplers changed slightly due to imperfect alignment of the translation stage; this can be seen as a decrease in the coincidence rate outside the interference region (compare coincidence rates at $z = -0.3$ and $z = 0.2$). When fitting the Gaussian function to the data set, a linear background term was added to accommodate for this small variation in coupling efficiency. An average coincidence rate outside the interference region (dotted black line in Figure 5.5) was used in the visibility calculation: the visibility is the ratio of the fitted Gaussian function's amplitude to the average coincidence rate. A HOM interference visibility of 89% was calculated.

5.6.2 Characterising the Werner State

There are several different methods of generating polarisation Werner-states, including: the depolarised method, which consists of inducing a spatially dependent phase shift on one of the polarisation qubits with a prism, and then tracing over the spatial degree of freedom [180, 191]; the patchwork method, which consists of a double-passed type-I SPDC source and a series of phase shifting and decohering elements between and after the two passes [192]; or a method using fast variable polarisation rotators [193].

Our method to calculate the payoff function $P(\rho)$ for an experimental Werner state ρ is relatively straight-forward, and uses the fact that a Werner state can be expressed as a statistical mixture of all four Bell states. Data is taken when ρ is consecutively prepared in the four Bell states, and the data sets are aggregated to produce a value of the payoff function for the effective state ρ . The Werner parameter is tuned by weighting the data collection time for the singlet state compared to data collection time for the three triplet states (data collection time between the three triplet states is identical). For example, to test the payoff function using a completely mixed state ($\mu = 0$ from Section 5.4.2), data can be taken for an equal time with all four Bell states.

Payoff function data was collected for all six possible states ω_j that Charlie sends to Bob. For each ω_j , payoff function data was collected when $\rho = |\Psi^-\rangle$ for 9,000 seconds, and for each of the three triplet states $\rho = \{|\Psi^+\rangle, |\Phi^\pm\rangle\}$ for 860 seconds.

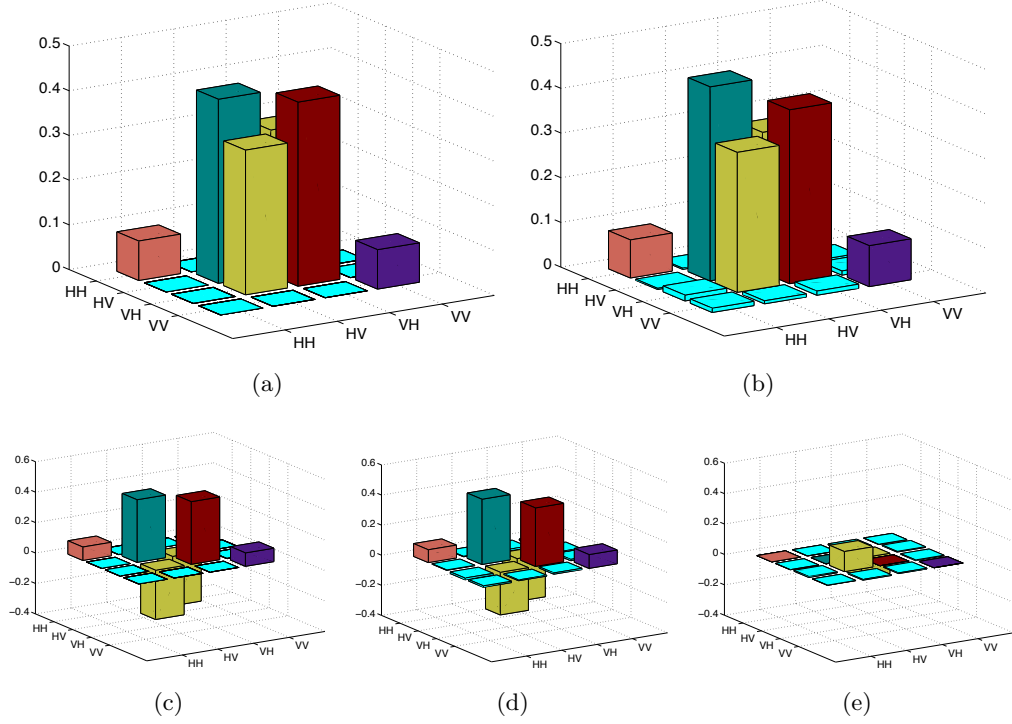


Figure 5.6: Comparison of the ideal Werner state W_μ with the experimentally reconstructed Werner state ρ_e . The absolute value of the density matrix elements for (a) W_μ and (b) ρ_e . (c) The real valued elements of the W_μ density matrix. The (d) real and (e) imaginary elements of the ρ_e density matrix.

Based on these data collection times, the effective state is expected to be

$$\rho = 0.777|\Psi^-\rangle\langle\Psi^-| + 0.223(\mathbb{1} \otimes \mathbb{1} - |\Psi^-\rangle\langle\Psi^-|), \quad (5.10)$$

which corresponds to roughly expecting $\mu = 0.703$, from (5.8b). This Werner parameter is above the desired range $0.5774 < \mu < 0.6595$, in which quantum-refereed steering of a Bell-local state can be demonstrated. This is deliberate, as we cannot prepare perfect Bell states, and the small amount of noise in each of the four Bell states adds together as symmetric noise in the aggregate ρ , further reducing the actual Werner parameter.

The quality of the four individual Bell states was characterised using quantum state tomography in the Bell state analysis setup, and the average fidelity was measured to be $\mathcal{F}_{\text{av}} = 0.976 \pm 0.017$, while the average purity was $\mathcal{P}_{\text{av}} = 0.955 \pm 0.003$. For further details, refer to Table 5.1

A Werner state density matrix was produced using the experimental density matrices

of the four Bell states. The initial weighting was based on the relative amount of data used from each Bell state that was used to calculate the payoff function $P(\rho)$, which is more accurate than using data collection time, as in (5.10). The ratio of data from the four Bell states contributing to the payoff function gave a preliminary value $\mu = 0.682$. A numerical search was then implemented to arrive at a more accurate value of μ .

ρ_e	$\mathcal{P}(\rho_e)$	$\mathcal{F}(\rho_e)$	$\mathcal{T}(\rho_e)$
$ \Psi^-\rangle\langle\Psi^- _e$	0.958 ± 0.004	0.977 ± 0.002	0.913 ± 0.009
$ \Psi^+\rangle\langle\Psi^+ _e$	0.955 ± 0.002	0.076 ± 0.001	0.911 ± 0.005
$ \Phi^-\rangle\langle\Phi^- _e$	0.950 ± 0.002	0.974 ± 0.001	0.898 ± 0.004
$ \Phi^+\rangle\langle\Phi^+ _e$	0.956 ± 0.003	0.977 ± 0.002	0.916 ± 0.006
Average	0.955 ± 0.003	0.976 ± 0.002	0.909 ± 0.008

Table 5.1: The average purity (\mathcal{P}), fidelity (\mathcal{F}) and tangle (\mathcal{T}) from the Monte Carlo simulations of the experimentally reconstructed states ρ_e . All four Bell states are measured.

In a Monte Carlo simulation of 200 iterations, the parameters are varied in the experimentally reconstructed density matrix

$$\rho_e = \frac{1+3\mu_e}{4}|\Psi^-\rangle\langle\Psi^-|_e + \frac{1-\mu_e}{4}(|\Psi^+\rangle\langle\Psi^+|_e + |\Phi^-\rangle\langle\Phi^-|_e + |\Phi^+\rangle\langle\Phi^+|_e) . \quad (5.11)$$

Quantum state tomography of the Bell states is based on measuring the Stokes parameters, and deriving a density matrix using maximum likelihood reconstruction (see Section 2.6.2). Uncertainty in the Stokes parameter measurements is determined by Poissonian statistics, as it is due to the shot noise of single photon detection events. The Stokes parameter measurements for each Bell state are varied within Poissonian uncertainty, to generate slightly different experimental Bell states $\{|\Psi^\pm\rangle_e, |\Phi^\pm\rangle_e\}$ in each iteration of the Monte Carlo simulation. At the same time, the estimated Werner parameter μ_e is also varied in each iteration, as the total singlet and triplet counts are changed within Poissonian uncertainty. In each iteration, an ideal Werner state of the form

$$W_\mu = \frac{1+3\mu}{4}|\Psi^-\rangle\langle\Psi^-| + \frac{1-\mu}{4}(|\Psi^+\rangle\langle\Psi^+| + |\Phi^-\rangle\langle\Phi^-| + |\Phi^+\rangle\langle\Phi^+|) \quad (5.12)$$

is fitted to the experimental Werner state ρ_e , by varying the parameter μ in (5.12) to maximise the fidelity between the ideal and experimental Werner state:

$$\mathcal{F}(\rho_e, W_\mu) = \text{tr} \left(\sqrt{W_\mu^{1/2} \rho_e W_\mu^{1/2}} \right)^2 . \quad (5.13)$$

After each iteration, the fitted Werner parameter μ and the fidelity $\mathcal{F}(\rho_e, W_\mu)$ are recorded. At the end of the 200 iterations, the average fitted Werner parameter and fidelity are calculated, as well as their standard deviations. The fitted Werner parameter was found to be $\mu = 0.6478 \pm 0.0045$, and this value is substituted for the estimate μ_e in (5.11).

The density matrices for the final ρ_e and W_μ are depicted in Figure 5.6. The absolute values of the density matrix W_μ (Figure 5.6(a)) and ρ_e (Figure 5.6(b)) are compared. The real-valued matrix elements of W_μ in Figure 5.6(c) can be compared to the real and imaginary density matrix elements of ρ_e in Figures 5.6(d) and 5.6(e), respectively. There is a slight imaginary component in the $|H\rangle\langle V|$ and $|V\rangle\langle H|$ elements of ρ_e , and this is likely due to small phase rotations from experimental components, and does not significantly impact the payoff function measurement.

5.6.3 Steering Inequality Measurement

Data for the payoff function $P(\rho)$ was collected in four-fold coincidence: Alice detects a photon in her detector, Charlie detects a photon in his triggering detector, and Bob measures a two-fold coincidence in the Bell state analysis setup. As mentioned, Charlie sends all six possible ω_j states to Bob, and for a given ω_j , singlet and triplet state detection events are separated in Bob's Bell state analysis. In the payoff function

$$P(\rho) \equiv \sum_p \left[s_p \langle a_p (\mathbb{1} \otimes \mathbb{1} + B) \rangle_{\rho_B \otimes \omega_p} - \frac{1}{\sqrt{3}} \langle (\mathbb{1} \otimes \mathbb{1} + B) \rangle_{\rho_B \otimes \omega_p} \right], \quad (5.14)$$

the index $p \in \{\pm 1, \pm 2, \pm 3\}$ corresponds to the six possible states that Charlie can send to Bob:

$$\omega_z = \frac{\mathbb{1} \pm \sigma_j}{2}, \quad j \in \{1, 2, 3\}. \quad (5.15)$$

The first term in the sum, $s_p \langle a_p (\mathbb{1} \otimes \mathbb{1} + B) \rangle$, is the correlation of Bob measuring a singlet state (from (5.4), it is clear that $\mathbb{1} \otimes \mathbb{1} + B = 2|\Psi^-\rangle\langle\Psi^-|$) and Alice's measurement result a_j . The sign factor s_p is in (5.5) to account for the fact that when Charlie changes from sending a positive eigenvalue eigenstate ω_j to a negative eigenvalue eigenstate ω_{-j} , the correct correlation in Alice's result will also switch sign. This sign factor is accounted for in the experiment, however, by correlating Alice's measurement projection with the state Bob sends to Charlie—Alice's result that is correctly correlated with Bob's measurement is thus always measured in the same detector, for all p .

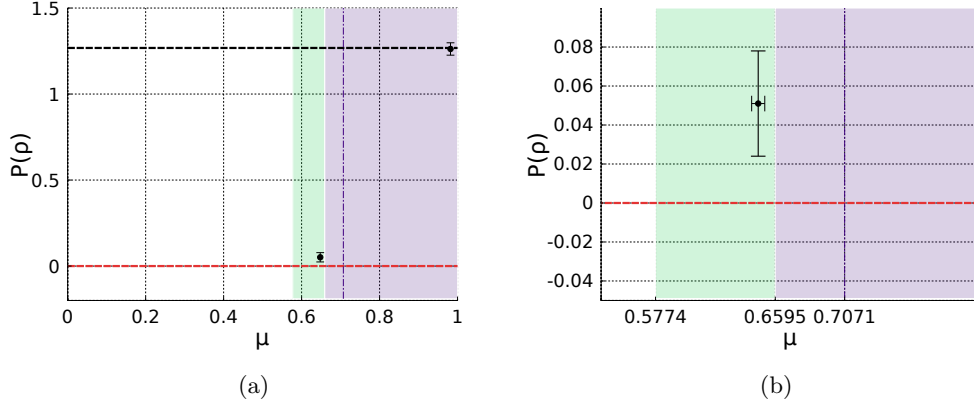


Figure 5.7: (a) Plotting the value of the payoff function $P(\rho)$ for a singlet state (Bell non-local, $\mu = 0.98$) and for a steerable Werner state (Bell local, $\mu = 0.6478 \pm 0.0045$). The dashed horizontal black line is the upper payoff limit for a maximally entangled state, and the dashed red line at $P(\rho) = 0$ shows the minimum payoff function value required to demonstrate that a state is steerable. The green region is the range of steerable states based on the Werner parameter μ , and the purple region is the range of Bell non-local states. The dashed vertical purple line shows the minimum Werner parameter needed to violate the CHSH inequality. (b) A magnified view of the steerable state data point. The payoff value is positive within error, as required to demonstrate quantum-refereed steering. It is also fully within the green region, which shows the range of steerable states based on the Werner parameter.

The payoff function is calculated for a Bell-nonlocal state, and for a state that is steerable but Bell-local. These two data points are presented in 5.7(a). To measure the Bell non-local case, a singlet state was prepared, and it was measured to have 98.2% fidelity with the ideal singlet. The payoff function for this state was calculated to be $P(\rho) = 1.262 \pm 0.036$, which reaches the theoretical limit $P_{\max}(\rho) = 3 - \sqrt{3} \simeq 1.2679$ for a maximally entangled state.

A magnified picture of the payoff data point for the steerable state is found in 5.7(b). As described in Section 5.6.2, the fitted Werner parameter for this state is $\mu = 0.6478 \pm 0.0045$, which lies in the range of steerable Werner states $0.5774 < \mu < 0.7071$, within uncertainty. The value of the payoff function for this state was calculated to be $P(\rho) = 0.051 \pm 0.027$, which is positive to within error. The payoff function is positive only for steerable states.

5.7 Discussion

This is the first demonstration of the violation of a steering inequality when neither party can be trusted. In all previous demonstrations, the asymmetric steering

steering task has involved implicit trust between Charlie, the referee, and Bob, the party whose quantum subsystem is being steered. Quantum randomness is added into the protocol, by replacing the classical instructions Charlie sends to Bob with quantum instructions, in the form of a quantum state the Bob uses to perform a joint measurement. This invalidates the requirement of trust between Charlie and Bob, since no pre-arranged cheating strategy between Alice and Bob exists by which they can deceive Charlie in the new protocol.

One-sided DIQKD is an extension of standard DIQKD; based on the violation of a steering inequality, such an asymmetric protocol could be directly applicable to scenarios in which a secure central server trades information with many unsecured terminals. Recently, a quantum access network architecture was investigated [128]—a nodal network with point-to-multipoint connections, demonstrating a resource-efficient strategy for practical realisation of multi-user QKD technology. One-sided DIQKD could be applied in just such a scenario. It has been shown that one-sided DIQKD is secure against the most general (*i.e.* coherent) attacks [159, 194, 195], under only a few assumptions (memoryless devices [196], integrity of location). Loophole-free tests of a Bell inequality are at the very limit of what is possible using current technology [74, 75], while violating steering inequalities have the advantage of less strenuous detection efficiency requirements [71–73].

Secure quantum communication will become ever more integrated with other quantum information tasks [115, 130], as the range [197] and resilience [198] of protocols increases. The experimental result presented in this chapter is an important addition to the array of techniques for securing the distribution of quantum information in different scenarios.

Chapter 6

Frequency Conversion of Squeezed States

6.1 Acknowledgements

The work presented in this chapter was carried out over the course of three months, while visiting Professor Roman Schnabel’s laboratory in the Max Planck Institute for Gravitational Physics (Albert Einstein Institute), at the Leibniz Universität Hannover. Prior to arriving, some of the experimental set up (Figure 6.7) had been constructed and used in previous experiments [199].

My main contributions to the experiment were in the frequency conversion efficiency measurement (6.6.1), and the first measurement of squeezed vacuum at 1550 nm (6.6.2). I also built two homodyne tomography setups, HD₁₅₅₀ and HD₅₃₂, as well as various optical paths in the setup. In addition, I modified the SFG cavity to increase conversion efficiency. All of the work was done together with Petrisa Zell and Christina Vollmer, with significant assistance from Christoph Baune and Axel Schönbeck.

6.2 Introduction

Frequency conversion of quantum states of light is a topic of long-standing interest [200], with potential applications in fields such as gravitational wave detection [201–205] and quantum computing [206–208]. Common sources of non-classical light, such as SPDC setups or quantum dots, commonly emit at IR or near-IR wavelengths.

Quantum memories that are being developed for quantum networking, and to facilitate full-scale quantum computing, are mostly incompatible with these light sources. An array of different systems are being investigated as potential quantum memories: rare-earth ion doped crystals ($\text{Pr}^{3+}:\text{Y}_2\text{SiO}_5$) using gradient echo [209], or EIT [210], at wavelengths ~ 606 nm; atomic frequency combs in $\text{Nd}:\text{Y}_2\text{SiO}_5$ crystals [211], with wavelengths ~ 883 nm, and in $\text{Ti}:\text{Tm}:\text{LiNbO}_3$ waveguides [212], at ~ 795 nm; warm atomic vapour using gradient echo [213], at ~ 795 nm; and Faraday interaction in Caesium vapour [214], at ~ 860 nm. In general, most quantum memories are being developed in the optical regime from 500–900 nm [215, 216]. In addition, although high-efficiency detectors for telecommunication wavelengths are being developed [217, 218], currently available single photon detector for visible wavelengths have significantly higher quantum efficiency than commercially available photon detectors at IR wavelengths [107]. Finally, generating squeezed states at shorter wavelengths is directly applicable in gravitation wave detection, as the phase sensitivity of an interferometer scales inversely with wavelength.

Frequency conversion and frequency entanglement are thus important techniques for connecting quantum technologies [219, 220]. As new approaches to distributed quantum computation are explored [130], in which a client can securely implement a quantum computation task through a remote server, quantum computing and quantum communication will merge into the same task. Quantum information is best transmitted at telecommunication wavelengths, around 1500 nm where the optical loss is lowest, and this will be a critical constraint on distributed ground-based protocols. Wavelength flexibility could also be desirable as recently proposed satellite-based quantum communication protocols [221] and experiments [222] are developed.

The aim of the experiment was to demonstrate frequency conversion of a squeezed state, and the verification of entanglement between squeezed vacuum at 1550 nm and at 532 nm. A squeezed state is versatile, with applications in quantum communication, computing and measurement, but it is also very sensitive to loss. Successful frequency conversion of squeezing demonstrates that the process is suitable for highly fragile non-classical states. The experimental work presented in this chapter includes the first results of the experiment—characterising the frequency conversion efficiency, and generating the squeezed state. The frequency conversion of squeezed vacuum and measurement of frequency mode entanglement, which are the main results, are not presented in this thesis, as I did not participate in collecting that data. Details about the full experiment can be found in [223]. The results presented here do, however, represent the key steps necessary to achieve squeezing and entanglement

conversion.

6.3 Quantum Optical Theory in Continuous Variables

Previous chapters in this thesis discussed quantum optics experiments in discrete variables—single photons—and the techniques associated with controlling and measuring them. In continuous-variable quantum optics experiments, light is considered to be a wave, generally comprised of a macroscopic number of photons in a mode. In the simplest case, the light wave is in a coherent state, introduced in 2.4.1. A coherent state is a minimum uncertainty state, meaning that its variance is equal to that of the vacuum state. The variance of an observable \hat{x} is defined in the following way:

$$\mathcal{V}(\hat{x}) = \langle \Delta \hat{x}^2 \rangle = \langle \hat{x}^2 \rangle - \langle \hat{x} \rangle^2 . \quad (6.1)$$

In classical mechanics, a non-zero variance of the observable \hat{x} is associated with noise, or imperfect preparation of the system with the desired property. An ideally prepared quantum system will still have non-zero variance, however, due to the probabilistic nature of quantum measurement. The variance, in this case, can be thought of as quantum noise, since it is a fundamental property of the system. When a state is represented in phase space, as in 2.5.1, the width of a quadrature is given by the variance of the state at that measurement angle.

In continuous-variable experiments, the quantum noise is often the property of interest. Squeezed states of light, a frequent topic of such experiments, are states with variance below the vacuum noise in one quadrature, and a correspondingly increased variance in the orthogonal quadrature. When the noise correlation is between quadratures of a single mode, it is known as a single-mode squeezed state. When the noise correlations are between two different modes, which might be at separate optical frequencies for example, it is known as a two-mode squeezed state. There is a rich variety of continuous-variable quantum states, and their applications can be found in every field of quantum optics and quantum information. Continuous and discrete variables can be used in the same experiment, and hybrid quantum optics is a growing field that is garnering much interest [224, 225].

6.3.1 Sum-Frequency Conversion

The classical theory of sum-frequency conversion was presented in 2.3.1. In this chapter, SFG is described semi-classically, using quantum operators to describe the

signal and idler modes, and only making the parametric approximation to treat the pump classically. By explicitly treating the inputs as quantum states, it is shown that the process is coherent and does not collapse the states. The interaction Hamiltonian describing SFG is

$$\mathcal{H} = i\hbar\xi (\hat{a}_1^\dagger \hat{a}_2 e^{-i\omega_0 t} - \hat{a}_1 \hat{a}_2^\dagger e^{i\omega_0 t}) . \quad (6.2)$$

The pump field at ω_0 is treated classically in (6.2), and the coupling constant ξ is therefore proportional to the nonlinear coefficient $\chi^{(2)}$ and the intensity of the pump field. The equations of motion in the Heisenberg picture for the two fields are

$$\begin{aligned} \frac{d\hat{a}_1}{dt} &= \frac{i}{\hbar} [\mathcal{H}, \hat{a}_1] + \frac{\partial \hat{a}_1}{\partial t} & \frac{d\hat{a}_2}{dt} &= \frac{i}{\hbar} [\mathcal{H}, \hat{a}_2] + \frac{\partial \hat{a}_2}{\partial t} \\ &= -\xi \hat{a}_2 , & &= \xi \hat{a}_1 . \end{aligned} \quad (6.3a)$$

These are two coupled differential equations with solutions

$$\hat{a}_1(t) = \cos(\xi t) \hat{a}_1(0) - \sin(\xi t) \hat{a}_2(0) , \quad (6.4a)$$

$$\hat{a}_2(t) = \cos(\xi t) \hat{a}_2(0) + \sin(\xi t) \hat{a}_1(0) . \quad (6.4b)$$

According to (6.4), full quantum state transfer will occur between frequency modes ω_1 and ω_2 after a characteristic time that depends on the interaction length and the coupling strength. The fact that the time-dependent annihilation operators at both frequencies can explicitly be expressed in terms of the initial conditions confirms that the converted output is also a pure quantum state.

6.3.2 Optical Parametric Amplification

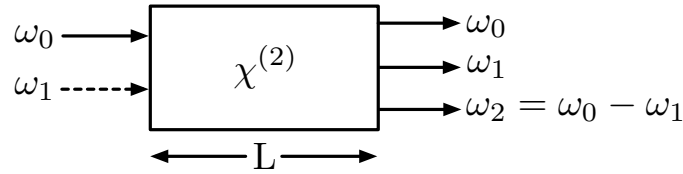


Figure 6.1: Input and output optical frequencies in an optical parametric amplifier (OPA), consisting of a $\chi^{(2)}$ nonlinear material of length L . Due to energy conservation, the signal frequency ω_1 and the generated idler frequency ω_2 must add to the pump frequency ω_0 . Thus, it is a difference-frequency generation (DFG) process. If the input amplitude of the ω_1 seed field is zero, this becomes the familiar SPDC configuration, where phase matching determines the generated frequencies ω_1 and ω_2 .

The SPDC process was discussed in 2.3.4, and it was indicated that the zero-point

energy fluctuation of the vacuum field facilitates the generation of light at a new frequency. The new light exhibits sub-Poissonian photon statistics, and is known as a squeezed vacuum state. When a low-intensity field is added to the input of the $\chi^{(2)}$ material alongside the strong pump field, it is known as an optical parametric amplifier (OPA). This is a DFG process, in which the “seed” or signal field intensity is much lower than the classical pump field intensity. The signal field is amplified, and an idler field at the difference frequency is also generated. Supplementary details can be found in [226]. The interaction Hamiltonian describing the OPA process is:

$$\mathcal{H} = i\hbar\xi (\hat{a}_1^\dagger \hat{a}_2^\dagger e^{-i\omega_0 t} - \hat{a}_1 \hat{a}_2 e^{i\omega_0 t}) , \quad (6.5)$$

where ξ is the coupling constant for the interaction (proportional to $\chi^{(2)}$ and the pump intensity), the pump field is treated classically, and \hat{a}_1 , \hat{a}_2 are the annihilation operators for the signal and idler modes, respectively. The equations of motion in the interaction picture are:

$$\dot{\hat{a}}_1 = -\frac{i}{\hbar}[\hat{a}_1, \mathcal{H}] = \xi \hat{a}_2^\dagger , \quad \dot{\hat{a}}_2^\dagger = -\frac{i}{\hbar}[\hat{a}_2^\dagger, \mathcal{H}] = \xi \hat{a}_1 . \quad (6.6)$$

The solutions to these equations of motion are:

$$\hat{a}_1(t) = \cosh(\xi t) \hat{a}_1(0) + \sinh(\xi t) \hat{a}_2^\dagger(0) , \quad (6.7a)$$

$$\hat{a}_2(t) = \cosh(\xi t) \hat{a}_2(0) + \sinh(\xi t) \hat{a}_1^\dagger(0) . \quad (6.7b)$$

The time-dependent mode operators in (6.7) recall the time-dependent complex amplitudes (2.35) in the classical description of DFG. By once again taking a semi-classical approach and treating the signal field as a quantum state, the OPA process is shown to be coherent. If we assume the initial coherent states $|\alpha_1, \alpha_2\rangle$ in modes ω_1 and ω_2 , the average photon number in the signal mode is:

$$\langle n_1(t) \rangle = \langle \alpha_1, \alpha_2 | a_1^\dagger(t) a_1(t) | \alpha_2, \alpha_1 \rangle \quad (6.8a)$$

$$= |\alpha_1 \cosh(\xi t) + \alpha_2^* \sinh(\xi t)|^2 + \sinh^2(\xi t) . \quad (6.8b)$$

The photon number in either one of the output modes depends on the amplitude of both the input modes, as well as the relative phase between them. In the absence of any input signal, the output still grows exponentially due to the last term in (6.8). This situation—a strong classical pump combined with vacuum states in the signal and idler inputs—is the familiar SPDC configuration from Chapter 2. The zero point energy fluctuations of the vacuum state input combine with the strong pump to generate photons in the output, the number being proportional to $\sinh(\xi t)$

after a time t .

If the OPA is phase matched for a degenerate output, it acts as a phase-sensitive amplifier, amplifying one quadrature and attenuating the other, depending on the relative phase of the input states. Here, the squeezing and anti-squeezing are directly on the quadratures of the fundamental beam, since $\hat{a}_1 = \hat{a}_2 = \hat{a}$ and the Hamiltonian no longer yields two coupled equations of motion (6.7). In the interaction picture, the unitary operator for time evolution of the degenerate OPA is

$$U(t) = \exp \left[\frac{-i\mathcal{H}t}{\hbar} \right] = \exp \left[\xi t (\hat{a}^{\dagger 2} - \hat{a}^2) \right]. \quad (6.9)$$

This is the single-mode squeezing operator, with squeeze parameter $r = \xi t$. As mentioned earlier, a coherent state is a minimum-uncertainty state, with identical variance in both quadratures equal to the vacuum noise. The squeezing operator transforms a coherent state into a squeezed state, which is another minimum-uncertainty state with reduced variance in one quadrature, at the expense of increased variance in the other. The squeezing parameter determines the amount by which the variance of the quadrature is squeezed and anti-squeezed:

$$\mathcal{V}(\hat{Q}, t) = e^{2\xi t} \mathcal{V}(\hat{Q}, 0), \quad \mathcal{V}(\hat{P}, t) = e^{-2\xi t} \mathcal{V}(\hat{P}, 0). \quad (6.10)$$

Here \hat{Q} and \hat{P} are the amplitude and phase quadrature defined in (2.62) of Chapter 2. If the OPA is non-degenerate, the time evolution operator is

$$U(t) = \exp \left[\xi t (\hat{a}_1^\dagger \hat{a}_2^\dagger - \hat{a}_1 \hat{a}_2) \right], \quad (6.11)$$

which is the two-mode squeezing operator. The output of the OPA will be a two-mode squeezed state, where the squeezing and anti-squeezing can be observed in the sum of the quadratures:

$$\hat{Q}^+ = \frac{\hat{Q}_1 + \hat{Q}_2}{\sqrt{2}}, \quad \hat{P}^+ = \frac{\hat{P}_1 + \hat{P}_2}{\sqrt{2}}, \quad (6.12)$$

with $\hat{Q}_{1,2}$ and $\hat{P}_{1,2}$ denoting the amplitude and phase quadratures in modes ω_1 and ω_2 . In this case, there will not be any squeezing on the individual beams. The correlation between the noise in the two beams is quantum entanglement of the type discussed in the EPR paradox. In the limit of infinite squeezing, a measurement of one beam at a certain phase angle yields perfect information about the quadrature of the other beam. Another phase angle could have been measured instead, however, yielding perfect information about the second beam at a new

angle. Thus, information can be gained about non-commuting variables of the second beam, by only measuring the first beam.

6.3.3 Cavity Equation of Motion

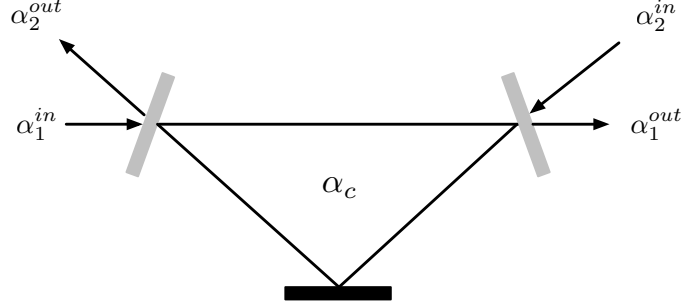


Figure 6.2: Three mirror ring cavity configuration. The two side mirrors have identical amplitude reflection and transmission coefficients \sqrt{R} and \sqrt{T} , respectively, while the middle mirror is assumed to be purely reflective. The coefficient γ_j represents loss to mode j due to leakage out of the cavity, while μ_j represents loss due to other internal processes such as absorption or scattering. The coefficient $\gamma'_j = \gamma_j + \mu_j$ includes all cavity losses in mode j .

A cavity resonator only supports specific frequency modes, and if the cavity contains a nonlinear material, its periodic mode structure has a strong influence on the nonlinear interaction, as in the case of an optical parametric oscillator for example. For this reason, the equation of motion of a field in a cavity must be taken into account. It is conceptually convenient to consider a three mirror ring cavity, as depicted in Figure 6.2.

Input fields α_1^{in} and α_2^{in} enter the cavity through the two end mirrors. It is assumed that both end mirrors have high amplitude reflectivity: $\sqrt{R} = \sqrt{1 - T} \simeq 1$. This ensures that the change to a wave after one round trip is small. If τ is the round trip period for the circulating cavity field α_c , the change after one round trip is

$$\alpha_c(t + \tau) = \sqrt{(1 - T_1)(1 - T_2)(1 - \Lambda)} e^{i\phi} \alpha_c(t) \quad (6.13a)$$

$$+ \sqrt{(T_1)(1 - T_2)} e^{i\phi} \alpha_1^{in}(t) + \sqrt{T_2} e^{i\phi} \alpha_2^{in}(t). \quad (6.13b)$$

The fields acquire a phase ϕ after one round trip, and near a cavity resonance $\phi \simeq \text{mod}[2\pi]$. The factor Λ in (6.13), which is assumed to be very small ($\Lambda \ll 1$), accounts for internal loss in the cavity due to absorption or scattering. Expanding $\alpha_c(t + \tau)$ to first order gives $\alpha_c(t) + \tau \dot{\alpha}_c(t)$, while the transmission terms can be

expressed as a Taylor series to first order, in order to linearise into:

$$\tau \dot{\alpha} = (i\phi - \gamma_1 - \gamma_2 - \mu_1 - \mu_2) \alpha + \sqrt{2\gamma_1} \alpha_1^{in} + \sqrt{2\gamma_2} \alpha_2^{in} , \quad (6.14)$$

where $\gamma_j = T_j/2$ and $\mu_j = \Lambda_j/2$ are the leakage and internal loss coefficients for mode j , and the subscript has been dropped from α_c . Equation (6.14) describes the field inside the cavity, which is related to the field exiting the cavity through:

$$\alpha_j^{out} = \sqrt{T_j} \alpha - \sqrt{1 - T_j} \alpha_j^{in} \quad (6.15a)$$

$$\simeq \sqrt{2\gamma_j} \alpha - \alpha_j^{in} . \quad (6.15b)$$

Different approaches have been used to rigorously establish the quantum equations of motion for cavity modes. A relatively simple method is to apply the canonical quantisation rules to the classical equation of motion in (6.14). For convenience, the cavity is assumed to be at resonance, and $\phi = 0$. A total loss coefficient is also introduced: $\gamma'_j = \gamma_j + \mu_j$. Finally, when considering the quantum modes, the vacuum mode $\hat{\Gamma}$ that is coupled into the cavity due to internal losses must be included. The quantum equation of motion for cavity modes is thus:

$$\tau \dot{\hat{a}}_j + \gamma'_j \hat{a}_j = \sqrt{2\gamma} \hat{a}_j^{in} + \sqrt{2\mu} \hat{\Gamma}_j . \quad (6.16)$$

Resonator cavities are often used in continuous-variable quantum optics experiments to prepare the mode of a laser beam. A beam of light can only have a high transmission through a cavity if it is spectrally and spatially well mode-matched to the cavity. To see that this is the case, consider a resonant, lossless and symmetric cavity: $\phi = 0$, $\mu = 0$ and $\gamma_1 = \gamma_2 = \gamma$. The equation of motion (6.16) is expressed in the frequency domain via a Fourier transform, and the boundary condition (6.15) is used to derive the cavity output:

$$\hat{a}_1^{out}(\omega) = \frac{\gamma \hat{a}_2^{in}(\omega) + i\omega\tau \hat{a}_1^{in}(\omega)}{\gamma - i\omega\tau} , \quad (6.17a)$$

$$\hat{a}_2^{out}(\omega) = \frac{\gamma \hat{a}_1^{in}(\omega) + i\omega\tau \hat{a}_2^{in}(\omega)}{\gamma - i\omega\tau} . \quad (6.17b)$$

We assume that a single photon, with a broad frequency distribution centred at the cavity resonance frequency, is sent to the cavity. If the reflected port is considered “lost”, the transmitted field will be a mixture of vacuum, and a single photon with

a Lorentzian frequency distribution that depends on the cavity parameter γ :

$$|\langle \hat{a}_1^{out}(\omega) | \hat{a}_1^{out}(\omega) \rangle|^2 \propto \frac{\gamma^2}{\gamma^2 + (\omega\tau)^2} \quad (6.18)$$

This shows that a cavity can filter out a specific frequency mode of an incoming radiation field, and only let the desired mode through. The characteristics of the filtered frequency mode can be tuned using the cavity parameters, represented in (6.18) by γ and τ .

6.3.4 Optical Parametric Oscillation

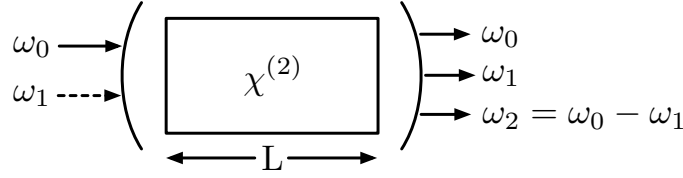


Figure 6.3: Input and output optical frequencies in an OPO, consisting of a $\chi^{(2)}$ nonlinear material of length L inside a linear resonator cavity. This is represented as a DFG process, where the signal (ω_1) and idler (ω_2) frequencies must add to the pump (ω_0) frequency. The threshold parameter σ is the point at which the pump power equals the rate of energy loss in the OPO system. If the pump power significantly exceeds threshold, there is positive feedback and the fields generated via the OPO interaction tend towards bright coherent states. If the OPO is driven at or below threshold, the cavity output fields are squeezed states, with maximal (in principle infinite) squeezing occurring at exactly threshold. If the OPO is degenerate ($\omega_1 = \omega_2 = \omega$), single-mode squeezing is produced. If the OPO is non-degenerate (a NOPO), the two-mode squeezing is in the sum of the different mode quadratures.

An optical parametric oscillator (OPO) consists of a nonlinear material placed inside a cavity resonator. If the cavity mirrors are highly reflective at both fundamental frequencies ω_1 and ω_2 , it is known as a doubly resonant oscillator. If the mirrors are highly reflective at only one of the fundamental frequencies, the device is called a singly resonant oscillator. Below the threshold condition, the equations describing the OPO are linear, and the pump field can be treated classically.

The Hamiltonian for a non-degenerate OPO is:

$$\mathcal{H} = \mathcal{H}_I + \mathcal{H}_P + \mathcal{H}_S + \mathcal{H}_L \quad (6.19a)$$

$$\mathcal{H}_I = i\hbar\chi^{(2)} (\hat{a}_s^\dagger \hat{a}_i^\dagger \hat{a}_p - \hat{a}_s \hat{a}_i \hat{a}_p^\dagger) \quad (6.19b)$$

The full system Hamiltonian is composed of the following parts: \mathcal{H}_I describes the

coupling between the fundamental and harmonic frequencies, \mathcal{H}_S and \mathcal{H}_P describe the driving fields at the signal and pump frequencies, and \mathcal{H}_L describes the cavity losses for all modes.

The outline of a derivation of the equations of motion in a non-degenerate OPO is presented in Appendix B. This closely follows the approach in [227, 228], while a detailed solution of the degenerate case can be found in [226]. The cavity equation of motion (6.16) is combined with \mathcal{H}_I , the coupling term of the Hamiltonian from (6.19). The equations of motion due to \mathcal{H}_I are:

$$\dot{\hat{a}}_0 = \chi^{(2)} \hat{a}_1 \hat{a}_2 \quad (6.20a)$$

$$\dot{\hat{a}}_1 = -\chi^{(2)} \hat{a}_0 \hat{a}_2^\dagger \quad (6.20b)$$

$$\dot{\hat{a}}_2 = -\chi^{(2)} \hat{a}_0 \hat{a}_1^\dagger \quad (6.20c)$$

The two fundamental modes are coupled through these equations of motion. A non-degenerate OPO can therefore produce two-mode squeezing, a concept introduced in 6.3.2 and further developed in Appendix B. Squeezing and anti-squeezing can be measured in the sum of the quadratures (6.12), while there will be no single-mode squeezing of the individual quadratures.

Two-mode squeezing is generally only observed when the OPO is not driven too far above threshold. The threshold condition is the point at which the rate of incoming pump energy balances the rate of energy loss due to leakage and internal loss processes. By finding the stationary solutions (B.4) to the mean field equations of motion, the threshold condition is obtained:

$$\sigma = \sqrt{P/P_0} = 2\sqrt{(2\chi^2\gamma_0)/(\gamma_0'^2\gamma_1'\gamma_2')} \alpha_0^{in} . \quad (6.21)$$

The incoming pump intensity is P , and $P_0 = (\gamma_0'^2\gamma_1'\gamma_2')/(8\chi^2\gamma_0)$ is the threshold intensity. The coefficients γ_j' and γ_j are again the total loss and leakage loss coefficients for a single pass through the OPO cavity, as in (6.16). The OPO operates above threshold when $\sigma > 1$, or when the incoming harmonic intensity exceeds the total losses in the system. Above threshold, the fundamental beams tend towards uncorrelated coherent states, and hence two-mode squeezing tends towards zero. However, two-mode squeezing has been shown near but still above threshold [229].

The squeezing spectrum for a non-degenerate OPO is shown in (B.10):

$$\mathcal{V}_{\hat{Q}^+}^{\text{out}}(\omega) = 1 - \frac{4\gamma\gamma'}{\omega^2\tau^2 + 4\gamma'^2\sigma^2} \quad (6.22a)$$

$$\mathcal{V}_{\hat{P}^+}^{\text{out}}(\omega) = 1 + \frac{4\gamma\gamma'}{\omega^2\tau^2 + 4\gamma'^2(\sigma - 1)^2} . \quad (6.22b)$$

This shows two-mode squeezing and anti-squeezing on the sum of the quadratures \hat{Q}^+ and \hat{P}^+ defined in (6.12). Squeezing is measured in the laboratory using a homodyne tomography setup, introduced in 6.4.1. The measurement does not need to be constant, but can be made at any frequency, and this measurement frequency is the ω in the denominator of (6.22). In the ideal case, the maximum squeezing is always measured at zero frequency, but for technical reasons a higher squeezing value can often be measured at non-zero frequencies. The highest squeezing value is expected when the OPO is driven at the threshold σ .

In deriving equations (6.22), the cavity parameters for the two fundamental modes were set to be identical, for simplicity. Thus, the squeezing spectrum for a degenerate OPO would look identical to (6.22), with the key difference being that it would be single-mode squeezing and anti-squeezing, meaning that $\hat{Q}^+ \rightarrow \hat{Q}$ and $\hat{P}^+ \rightarrow \hat{P}$, where \hat{Q} and \hat{P} are defined in (2.62). In the degenerate single-mode case, there can be no inter-beam correlations or EPR entanglement as previously mentioned, since two modes would be required. While two-mode squeezing could be used in certain quantum information protocols, such as continuous-variable QKD or Schrödinger cat state quantum computation, single-mode squeezed states can enhance the phase sensitivity of interferometers, and have been proposed for gravitational wave detection [201].

6.4 Experimental Techniques

Cavity resonators and homodyne detection are two common features of continuous variable experiments. These components are generally absent from discrete variable experiments, and the experimental techniques associated with them have therefore not been previously discussed in this thesis. The next sections briefly present the main details of balanced homodyne detection and cavity stabilisation. Further details can be found in [228].

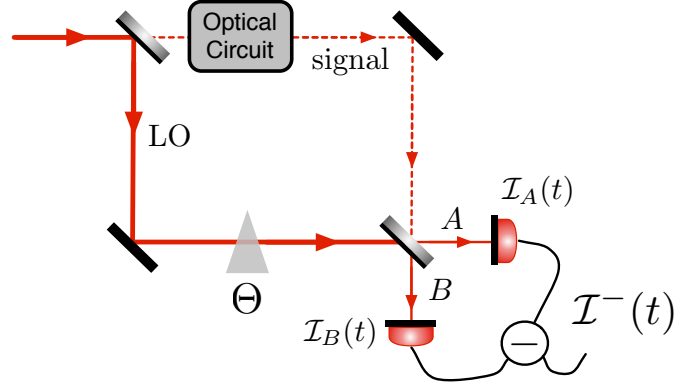


Figure 6.4: Balanced homodyne tomography apparatus. The signal field and local oscillator (LO), which is phase matched to the signal, are mixed on a 50:50 beam splitter. The average intensities $\langle n_A \rangle$ and $\langle n_B \rangle$ in modes A and B are converted to photo-currents $\mathcal{I}_A(t)$ and $\mathcal{I}_B(t)$. The difference current $\mathcal{I}^-(t) = \mathcal{I}_A(t) - \mathcal{I}_B(t)$ is directly proportional to the noise of the signal, scaled by the amplitude of the LO. The relative phase Θ between the LO and signal determines in which quadrature the noise is being measured.

6.4.1 Balanced Homodyne Tomography

Balanced detection of a single-mode beam consists of sending it to a 50:50 beam splitter, with a detector at each output port. This can give information about the the field's total (classical and quantum) noise, but it cannot differentiate between the field quadratures. To measure a specific quadrature of the signal beam, a phase reference is required. A local oscillator (LO) in the other input port of the beam splitter fulfils that requirement, and turns it into a balanced homodyne tomography setup. In providing a phase reference, the LO must be phase locked to the signal beam, so that the relative phase of the LO determines the quadrature angle that is being measured (see (2.63) in Chapter 2). For this reason, the LO often originates from the same pump beam that generates the signal, as shown in Figure 6.4, to make spectral and spatial mode matching easier.

Both detectors in Figure 6.4 generate a photo-current that is proportional to the intensity of the field in that port: $\mathcal{I}_A \propto \langle \hat{n}_A \rangle$. The difference of the two macroscopic photo-currents, processed electronically, is the quantity of interest in homodyne tomography:

$$\mathcal{I}^-(t) \simeq 2\alpha_{LO} [\delta\hat{Q}_{in}(t) \cos(\Theta) + i\delta\hat{P}_{in}(t) \sin(\Theta)] . \quad (6.23)$$

This expression is valid as long as the local oscillator amplitude is far stronger than the signal. The difference current is the ideal quantity to measure, because it is proportional to the noise of the signal scaled by the amplitude of the LO. The noise of the LO and the amplitude of the signal are entirely absent from (6.23),

as desired. A spectrum analyser is used to measure the variance of the difference current: $\mathcal{V}(\mathcal{I}^-) = (\Delta\mathcal{I}^-(t))^2$. By correctly choosing the measurement angle with the LO phase, the variance of the difference current will be directly proportional to one of the quadrature variances.

It is actually the beating between the LO and signal fields that is measured in balanced homodyne detection. If the measurement frequency of the spectrum analyser is ω , the beating is measured between the LO and the correlated sidebands at $\omega_0 \pm \omega$ on the signal beam. The expression for the squeezing spectrum (6.22) suggests that the squeezing is highest at zero measurement frequency. In practice, the presence of other noise sources in an experiment, which are not fundamental properties of the signal, often means that higher squeezing can be observed at non-zero measurement frequencies.

6.4.2 Cavity Stabilization

The Pound–Drever–Hall (PDH) technique is a widely used method of stabilising a laser’s frequency to a cavity linewidth, or alternatively, of stabilising the length of a cavity that is resonant with a laser beam [230]. It is a key component of gravitational wave interferometers, among its other uses. In the experiment presented in this chapter, it was the technique used to stabilise cavity lengths.

If an incident field is initially resonant with a cavity, a straightforward way to measure fluctuations in the cavity’s length would be to monitor the reflected intensity, and keep it at zero—if the cavity length changes slightly, the incoming field is no longer perfectly on resonance, and part of the field will be reflected. The problem with this method is that the intensity of the reflected beam is symmetric about resonance, and there is no way to immediately determine in which direction the cavity length must be shifted to bring it back on resonance. The phase of the reflected beam is not symmetric about resonance, however, and measuring this phase yields enough information to move directly back onto resonance.

Measuring a phase requires a phase reference, and to this end, sidebands are created on the incident beam. Sidebands can be created using an electro–optic modulator (EOM), which can simply consist of a crystal between capacitor plates, whose index of refraction is a function of the local electric field strength. If the voltage applied to the capacitor varies sinusoidally with frequency Ω and small amplitude β , the

time-dependent electric field is:

$$E(t) = E_0 e^{i(\omega t + \beta \sin \Omega t)} \quad (6.24a)$$

$$\simeq E_0 e^{i\omega t} (1 + i\beta \sin \Omega t) \quad (6.24b)$$

$$= E_0 \left(e^{i\omega t} + \frac{\beta}{2} e^{i(\omega+\Omega)t} - \frac{\beta}{2} e^{i(\omega-\Omega)t} \right) \quad (6.24c)$$

The phase modulation creates two sidebands above and below the carrier frequency. The envelope of the carrier wave will exhibit a beat pattern at the modulation frequency Ω , and this is used in PDH stabilisation as an error signal. If the modulation frequency is high enough, the sideband frequencies are out of resonance with the cavity, and they will be completely reflected. The reflected beam is measured with a fast photodetector, and the modulation at Ω is isolated in the signal by applying a mixer and a low-pass filter to the photodetector current. The

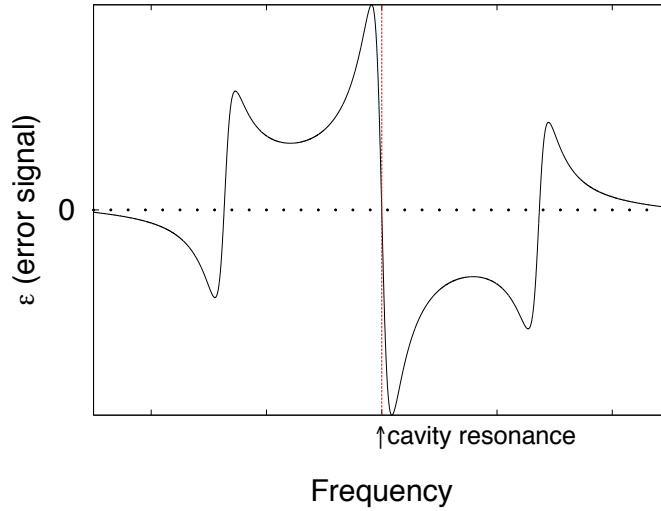


Figure 6.5: A simulation of the error signal ϵ used in PDH stabilisation, produced in the reflected port (high frequency modulation) of a cavity when the modulation frequency Ω is large compared to the cavity linewidth.

reflection coefficient for a symmetric cavity without losses is the ratio of reflected to incident amplitude:

$$\gamma(\omega) = \frac{E_{\text{ref}}}{E_{\text{in}}} . \quad (6.25)$$

If the modulation frequency is high enough to move the sidebands out of resonance with the cavity, then the power of the modulation signal in the reflected beam is proportional to

$$P(\Omega) \propto \text{Im} [\gamma(\omega) \gamma^*(\omega + \Omega) - \gamma^*(\omega) \gamma(\omega - \Omega)] . \quad (6.26)$$

This is the error signal that is used to lock the cavity length, $\epsilon = P(\Omega)$. The function ϵ has a large constant derivative around resonance, making it anti-symmetric about the resonance point, which is ideal for an error signal used to stabilise cavity length on resonance.

6.5 Experimental Setup

In the following sections, the full setup in Figure 6.7 is divided into stages, and technical details about each stage are presented.

6.5.1 Laser Preparation

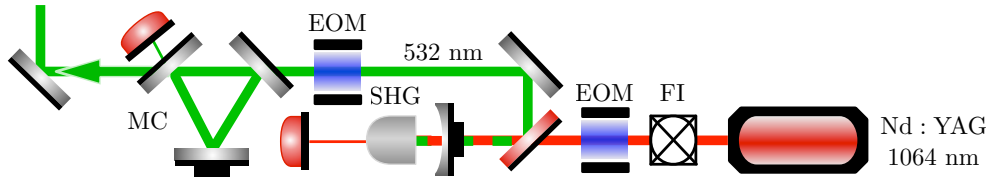


Figure 6.6: The laser preparation stage of the setup. The main laser source was a commercial Nd:YAG solid-state laser emitting ~ 2 W of coherent radiation at 1064 nm, in a single spatial mode. This beam was used to pump an SHG cavity, and produce ~ 1 W of optical power at 532 nm, also in a single spatial mode. The 532 nm light passes through a mode cleaner cavity for additional filtering of its spatial and frequency modes, after which approximately 700 mW of optical power is left to be used as a pump beam for the next stage of the setup.

The initial laser in the experimental setup was a Neodymium-doped Yttrium Aluminum Garnet (Nd:YAG) laser. The laser was the *Mephisto* model manufactured by *Inno-light*. This laser provided approximately 2 W of continuous wave (c.w.) optical power at 1064 nm wavelength. The light from this laser passed through a Faraday isolator (FI), to prevent back reflections from re-entering the laser cavity. It then passed through an electro-optical modulator (EOM), which modulated at a sideband frequency of 15 MHz. The light next entered the SHG cavity, which consisted of a 7% doped MgO:LiNbO₃ crystal with a curved back surface and a coupling mirror. The coupling mirror had a reflectivity of 90% at 1064 nm, and less than 4% at 532 nm. The flat surface of the crystal had anti-reflective coating ($R < 0.05\%$), and the curved surface had high-reflective coating for both wavelengths ($R > 99.96\%$). The SHG cavity was stabilised using the PDH locking technique, with the sidebands from the EOM. Approximately 1 W of optical power at 532 nm was produced from the SHG. This light was sent through a three-mirror ring cavity

with 1.3 MHz linewidth, known as a mode cleaner (MC), in order to filter a well-defined TEM_{00} spatial mode and to suppress technical frequency noise. The MC was again locked using the PDH technique, with 29.5 MHz sidebands. This initial setup provided a strong coherent beam at 532 nm, which was used to pump the non-degenerate OPO.

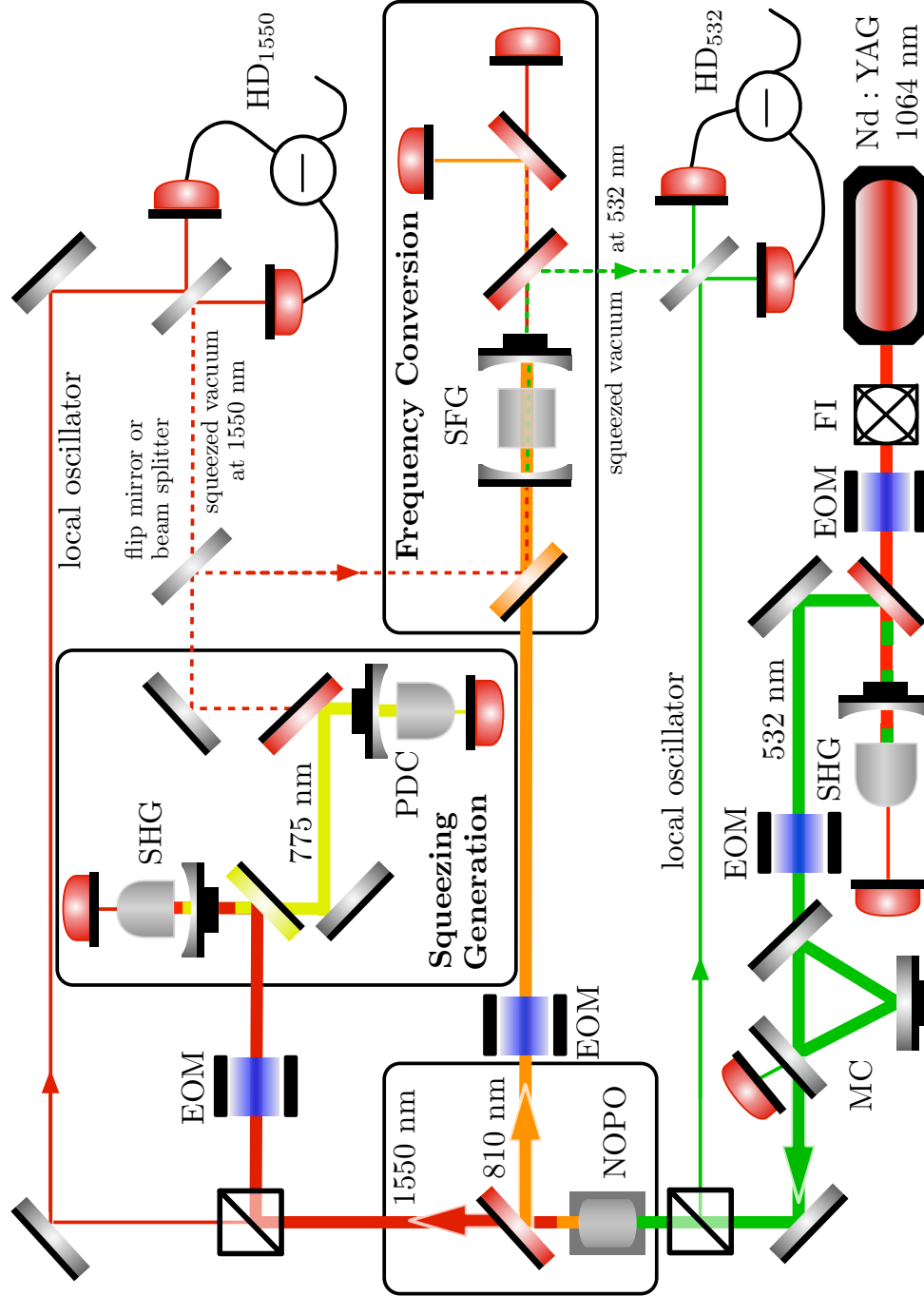


Figure 6.7: The full experimental setup for frequency conversion of a squeezed vacuum state at 1550 nm to a squeezed vacuum state at 532 nm. The details of the experimental stages—laser preparation to generate a 532 nm pump field and LO, NOPO to generate 1550 nm and 810 nm pump fields and LOs, squeezing generation to produce a squeezed vacuum at 1550 nm, and frequency conversion to convert it to a squeezed vacuum at 532 nm—are each described in their own section.

6.5.2 Non-degenerate OPO

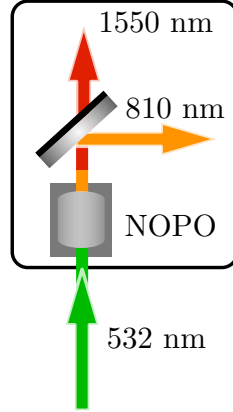


Figure 6.8: The non-degenerate OPO consists of a PPKTP crystal in a monolithic cavity. It is driven above threshold, with approximately 700 mW of 532 nm pump light, to produce two coherent (un-entangled) beams at 1550 nm and 810 nm. The frequencies are then separated with a dichroic mirror.

In order for oscillation to occur in a non-degenerate (doubly-resonant) OPO, the cavity must simultaneously be resonant at both fundamental frequencies. Cavity resonance modes—Airy functions—occur periodically in the frequency spectrum, and the field transmitted through a cavity will have a Lorentzian frequency distribution (6.18). Adjacent transmission peaks are separated by a frequency known as the free spectral range (FSR), and the width of the Lorentzian peak is determined by the finesse of the cavity. In general, resonance modes of one fundamental frequency will not overlap with resonance modes of the other fundamental frequency, and this is the case depicted in Figure 6.9(a). By temperature-tuning the nonlinear material in the cavity, and thus changing its length, the resonance modes of the two fundamental frequencies can be overlapped. Note that the axes of the two frequency modes increase in opposite directions. This is due to the fact that adding the frequencies at any two corresponding points must satisfy energy conservation: $\omega_1 + \omega_2 = \omega_0$.

The phase matching condition of the nonlinear material inside the OPO, discussed in 2.3.1, must also be considered—parametric oscillation only occurs when the resonance modes overlap within the phase matching region 6.9(b). The probability of generating oscillatory behaviour in the OPO grows with increasing overlap between the two resonance modes and the phase matching region 6.10.

As the material's phase matching is temperature tuned, different fundamental resonance modes overlap within the phase matching region—moving from one overlap

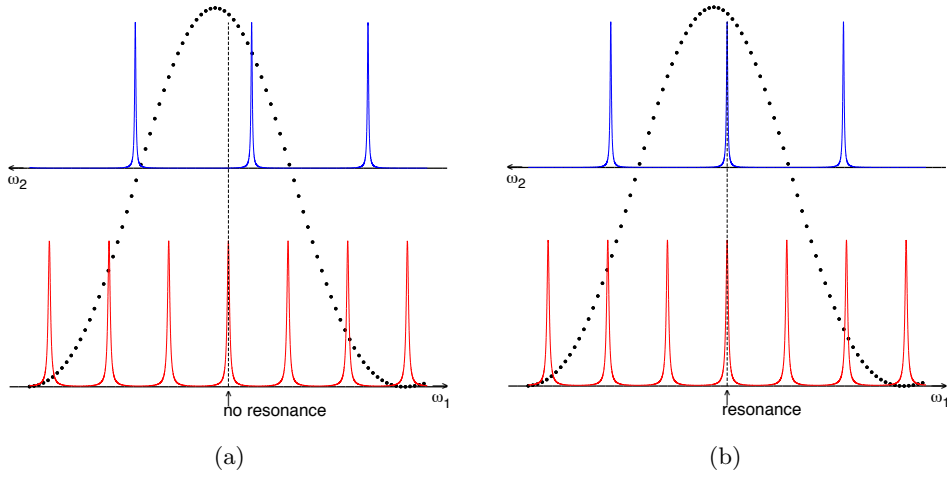


Figure 6.9: (a) Simulation of a NOPO with no modes overlapping within the phase matching region (dotted curve). A frequency comb exists for each fundamental frequency (the frequencies at every point along their axes add up to the pump frequency ω_0), and the cavity modes will not generally overlap. (b) Cavity modes at the fundamental frequencies overlap. These two frequencies add to the pump frequency, conserving energy.

condition to the next one is called a mode hop. The general trend is that a resonance overlap that begins on the left side of the phase matching region will progress via mode hops towards the right side of the region. As this happens, one fundamental frequency is increasing, while the other is decreasing by the same amount. Eventually, the last mode hop will be too far outside the phase matching region on the right, and a new resonance overlap on the left side of the phase matching condition will be the dominant oscillation—this is known as a cluster jump. The process continues in this pattern throughout temperature tuning, with each new mode hop and cluster jump corresponding to a new pair of fundamental frequencies.

The 532 nm beam from the SHG was used to pump the NOPO above threshold, and generate two unentangled coherent beams at 810 nm and 1550 nm. The non-linear material was a 8.9 mm long periodically-poled Potassium Titanyl Phosphate (PPKTP) crystal, whose two curved end surfaces formed a monolithic standing-wave cavity for both output fields. The front surface was 99.9% reflective at 810 nm and 1550 nm, and the back surface was 94% reflective. This created a cavity with a finesse of $\mathcal{F} = 100$, a linewidth of 91 MHz and a FSR of 9.15 GHz. The back surface of the PPKTP was highly reflective at 532 nm, and its front surface was highly transmissive, meaning that the pump beam passed through the crystal twice. The threshold power of the NOPO, which depends on the phase matching

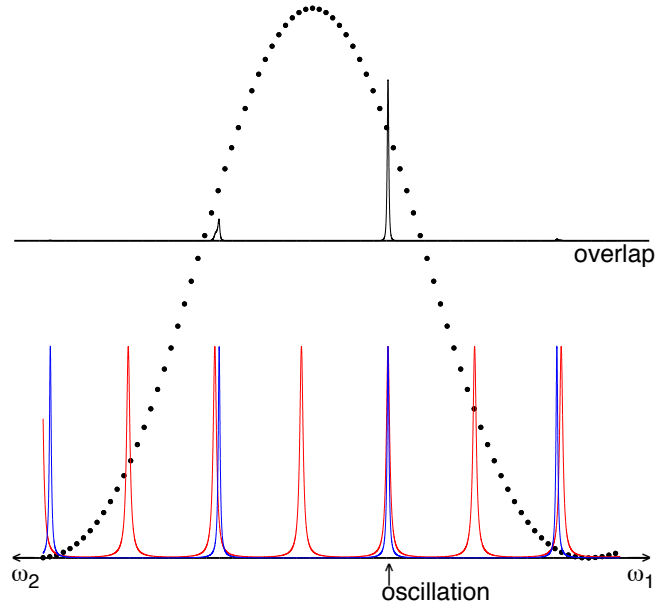


Figure 6.10: The overlap of the cavity modes with the phase matching function must be taken into account, as the overlap of all three functions determines the strength of the interaction in the NOPO.

condition and the spatial mode quality of the pump beam, was typically between 70 mW and 130 mW. The PPKTP temperature, which determined the phase matching, was controlled with a Peltier element and held around 60° C. The phase matching condition determined the outgoing wavelengths—this behaviour was generally linear for mode hops, but it was step-like at cluster jumps, making the exact wavelengths from the NOPO difficult to predict. Further details about the incremental behaviour can be found in [199].

6.5.3 Squeezing Generation

The 1550 nm output beam from the NOPO pumped a PPKTP crystal, phase matched for SHG. The PPKTP crystal had a curved back surface with highly reflective coating for 1550 nm and 775 nm, and a flat front surface with anti-reflection coating at both wavelengths. A coupling mirror formed a linear cavity with the back surface, and this mirror had 85% reflectivity at 1550 nm and 97.5% reflectivity at 775 nm. The cavity length was stabilised using sidebands on the 1550 nm field, and the temperature of the crystal was generally held at $\sim 50^\circ$ C.

The 775 nm coherent light generated from the SHG cavity pumped another PPKTP crystal, phase matched for parametric down conversion (PDC). The PPKTP crystal

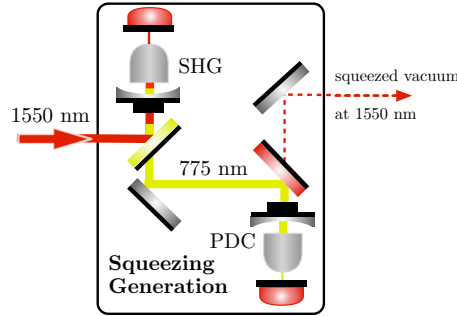


Figure 6.11: The squeezing generation stage consists of an SHG cavity and a parametric down conversion (PDC) cavity, which together convert an incoming 1550 nm coherent beam into a squeezed vacuum state at 1550 nm. The entire process is mediated by 775 nm light, which is created in the SHG and used as a pump in the PDC.

and cavity were identical to the SHG setup in everything but the phase matching, forming a doubly-resonant cavity for 775 nm and 1550 nm. The system, operating below threshold, behaved like a vacuum-seeded OPA, and the 775 nm light was down-converted back to 1550 nm, but in a squeezed vacuum state. The threshold power for a doubly-resonant OPO is generally lower than for a singly-resonant OPO, and the threshold power to induce oscillation in the PDC was expected to be around 15 mW based on simulations¹. The typical PDC pump power used in the experiment was ~ 10 mW, below threshold.

6.5.4 Frequency Conversion

The quantum up-conversion from 1550 nm to 532 nm was achieved using sum-frequency generation. A 9.3 mm PPKTP crystal, anti-reflection coated at 810 nm, 1550 nm and 532 nm, was placed inside a linear cavity. The crystal temperature was generally held at $\sim 70^\circ$ C. The back mirror was highly reflective at 1550 nm and 810 nm ($R > 99.9\%$), and the front mirror had 97% reflectivity at 810 nm and 91% reflectivity at 1550 nm. The front mirror was highly reflective at 532 nm ($R > 99.9\%$) and the back mirror was highly anti-reflective ($R < 0.1\%$), ensuring that all the converted light exited the cavity through the back mirror. The cavity length was stabilised using PDH locking, with 24.5 MHz sidebands on the 810 nm field. Using sum-frequency conversion, the squeezed vacuum at 1550 nm would eventually be converted to a squeezed vacuum at 532 nm. As a first step, however, we measured

¹Later, ~ 25 mW of pump power was sent into the cavity without reaching threshold. Threshold conditions are sensitive to many factors, including crystal temperature, imperfect mode matching and the exact wavelength from the NOPO, so threshold powers from simulations tend to be somewhat approximate.

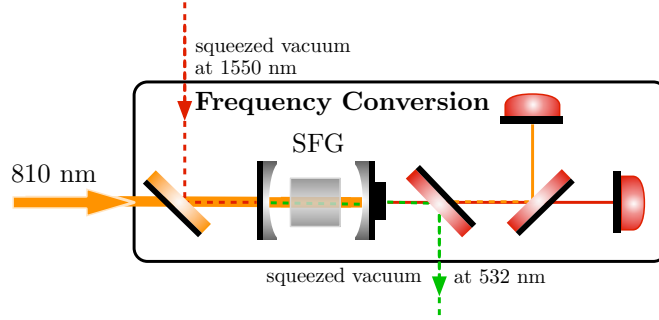


Figure 6.12: The frequency conversion is achieved using a SFG setup consisting of a PPKTP crystal in a cavity. Using the coherent 810 nm beam from the NOPO as a pump, an incoming squeezed vacuum state at 1550 nm (or a weak coherent 1550 nm field in 6.6.1) is up-converted to 532 nm at the output.

the quantum conversion efficiency of the SFG process, using a dim 1550 nm signal field and a strong 810 nm pump field, to ensure that the process would be parametric. Details about this measurement can be found in Section 6.6.1.

6.6 Results

In the following sections, experimental results that I participated in collecting while in Hannover are presented. Data collected by others after I left Hannover is not included in this thesis, but details can be found in [223]. The results presented here demonstrate the key experimental steps necessary for converting a squeezed vacuum state from 1550 nm to 532 nm, and for measuring entanglement between squeezed vacuum states at the two wavelengths.

6.6.1 Frequency Conversion Efficiency

The frequency conversion efficiency was characterised using a weak 1550 nm signal beam and a strong 810 nm pump beam, ensuring that the pump would be undepleted throughout the process. The intensities of the optical fields were measured with photo-detectors, which were calibrated using power meters. The conversion efficiency was calculated as the ratio of converted 532 nm photons to 1550 nm input photons:

$$\eta_R = \frac{\langle n \rangle_{532}}{\langle n \rangle_{1550}} = \frac{532 \cdot P_{532}}{1550 \cdot P_{1550}} = \Upsilon \cdot \frac{532 \cdot P_{532}^{\text{meas}}}{1550 \cdot P_{1550}^{\text{meas}}} . \quad (6.27)$$

The correction factor Υ accounts for error in the absolute calibration of the photo-detectors with the power meters. To determine this factor, the depletion of the signal field was recorded by monitoring the 1550 nm light reflected at the input of the cavity and transmitted through the cavity. With the 810 nm pump initially blocked, the 1550 nm signal beam reflected from the front mirror when the cavity was far off resonance ($P_{\text{refl,max}}$), and the transmitted signal when the cavity was at resonance ($P_{\text{trans,max}}$), were both measured. The relative depletion is thus

$$\eta_D = 1 - \frac{P_{\text{refl}} + P_{\text{trans}}}{P_{\text{in}}} \quad (6.28a)$$

$$= 1 - \left(\frac{P_{\text{refl}}}{P_{\text{refl,max}}} + \underbrace{\frac{P_{\text{trans,max}}}{P_{\text{refl,max}}}}_{\kappa} \cdot \frac{P_{\text{trans}}}{P_{\text{trans,max}}} \right), \quad (6.28b)$$

which should, in principle, yield the same result as η_R . In practice, the two methods differ slightly² in Figure 6.13(a), and data using both methods is used to derive a best estimate for the real conversion efficiency. The measured data sets were compared to a theoretical model by numerically simulating the SFG system. A nonlinear cavity simulator program [231] was written to provide a theoretical model based on system parameters such as wavelengths, beam powers, waist size, mirror reflectivity's and crystal properties. This model was then fitted simultaneously to the power ratio data and the signal depletion data, using a *Python* script from [199]. The numerical optimisation produces the correction factor Υ .

The data presented in Figure 6.13(b), which is the data in Figure 6.13(a) adjusted by the correction factor Υ , was produced in [223]. The maximum uncorrected conversion efficiency was found to be 91.7%, and the true maximum conversion efficiency after correction was found to be 89.2%, with a 810 nm pump power of 165 mW and an 1550 nm input signal power of 2 mW.

As theoretically predicted, the energy oscillates between the interacting modes (6.4), which explains the gradual decrease in conversion efficiency after the maximum is reached at $P_{810} = 165$ mW. The conversion efficiency curve depends on the temperature (phase matching) of the SFG cavity, as well as the temperature of the NOPO cavity. As discussed in 6.5.2, when the phase matching of the NOPO is temperature tuned, the wavelengths of the two fundamental resonance modes that overlap also change by small amounts. This is to ensure that energy is also conserved in the conversion process. The SFG system parameters are generally

²The ratio method (η_R) of determining conversion efficiency depends on the accuracy of power meters, and the depletion method (η_D) includes absorption and scattering. By using two different methods, a more accurate efficiency curve can be fitted to the data.

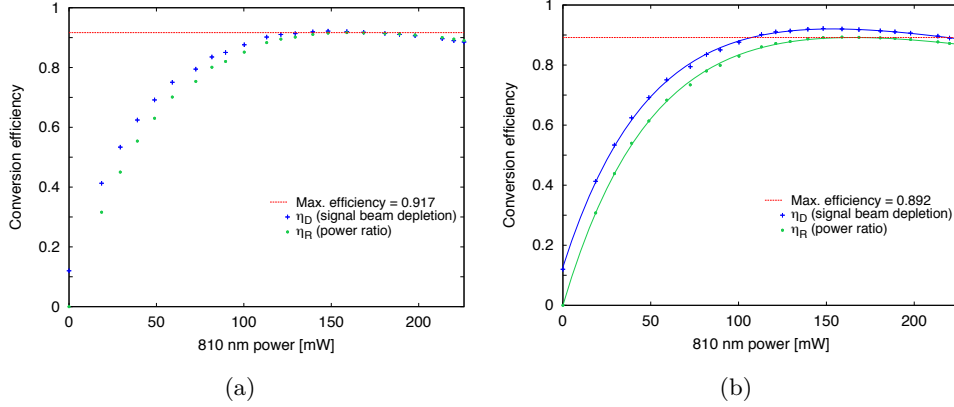


Figure 6.13: Frequency conversion efficiencies measured using η_R and η_D . (a) Uncorrected conversion efficiencies, showing a maximum efficiency of 91.7%. (b) Conversion efficiencies scaled by the factor Υ , showing the true maximum conversion efficiency of 89.4%. The solid curves show the theoretical simulation of the nonlinear cavity, fitted simultaneously to both the η_R and η_D data.

wavelength sensitive, so these small changes to the NOPO output wavelengths can significantly affect the conversion efficiency in the SFG. While data was collected for the conversion efficiency measurement, care was taken to ensure that the NOPO did not undergo any mode hops or cluster jumps, to ensure that the wavelengths were constant throughout.

The overall efficiency of converting a squeezed vacuum state at 1550 nm to a squeezed vacuum state at 532 nm is expected to be somewhat lower than the measured 89.2% quoted above. This is due to the fact that the squeezing parameter of a squeezed state is extremely sensitive to loss, and reduction in squeezing is due to losses in the optical path between the SFG and the HD₅₃₂. A total loss of $\sim 56\%$ in the optical path between the SFG and homodyne measured was determined in [223] for the homodyne detector and the conversion process. Since the HD₅₃₂ detectors could not be oriented at their Brewster angle in the setup, their effective quantum efficiency was effectively $\sim 79\%$.

6.6.2 Single-Mode Squeezing

The quadrature noise of a squeezed vacuum state at 1550 nm was measured using the balanced homodyne tomography setup HD₁₅₅₀. The 1550 nm squeezed vacuum is the output field from the OPA in the squeezing generation stage of the experimental setup 6.7. A spectrum analyser measured the squeezed and anti-squeezed quadratures of the field at a sideband frequency $f = 8\text{MHz}$, with a resolution bandwidth

$\Delta f = 300\text{kHz}$ and a video bandwidth $v = 300\text{Hz}$. The phase was controlled manually

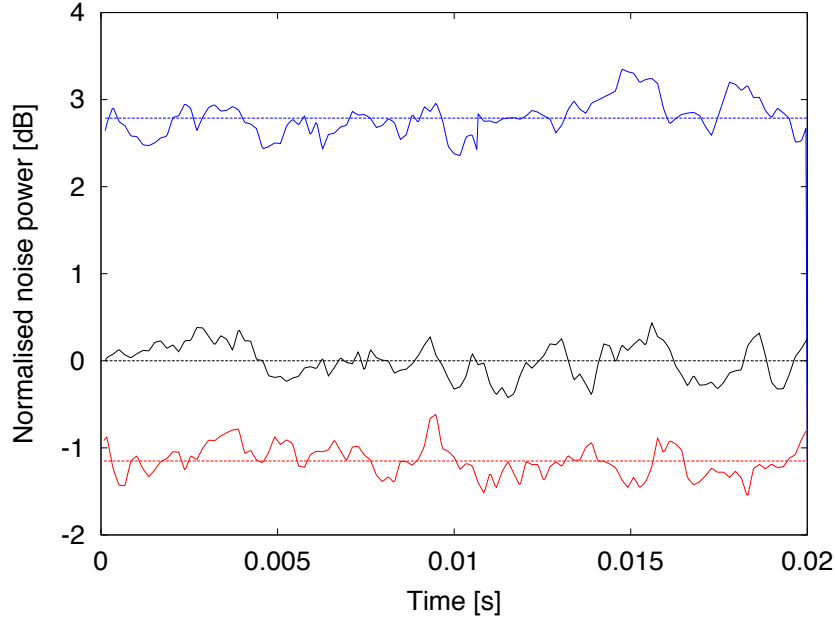


Figure 6.14: Quadrature noise traces of the squeezed 1550 nm field, measured using a network analyser. Quadrature noise is relative to vacuum noise power, which is set to be the zero noise level. The red trace shows noise in the squeezed quadrature, the blue shows the anti-squeezed quadrature, and the black trace is vacuum noise.

to measure the squeezing and anti-squeezing in Fig. 6.14. The detectors in HD_{1550} were two InGaAs photo-diodes from *OSI Optoelectronics* (FC InGaAs-300) with a quantum efficiency of 80%. The homodyne detector was custom made, and it was confirmed by measurement that its noise power increased linearly with increasing LO power, within the optical power regime used in the experiment (2–8 mW). The traces in Figure 6.14 are normalised to the vacuum noise, which was measured by blocking the signal field before the detector. From the average of the traces, the measured squeezing was 1.1 dB and the anti-squeezing was 2.9 dB, which is not corrected for dark noise in the detectors. In Figure 6.15, the quadrature noise changes as a function of the measurement angle, which was manually varied. For comparison, the average squeezing and anti-squeezing values calculated from Figure 6.14 are included as dashed lines on the plot. The value of the quadrature noise fluctuates between the maximum attained squeezing and anti-squeezing, as expected.

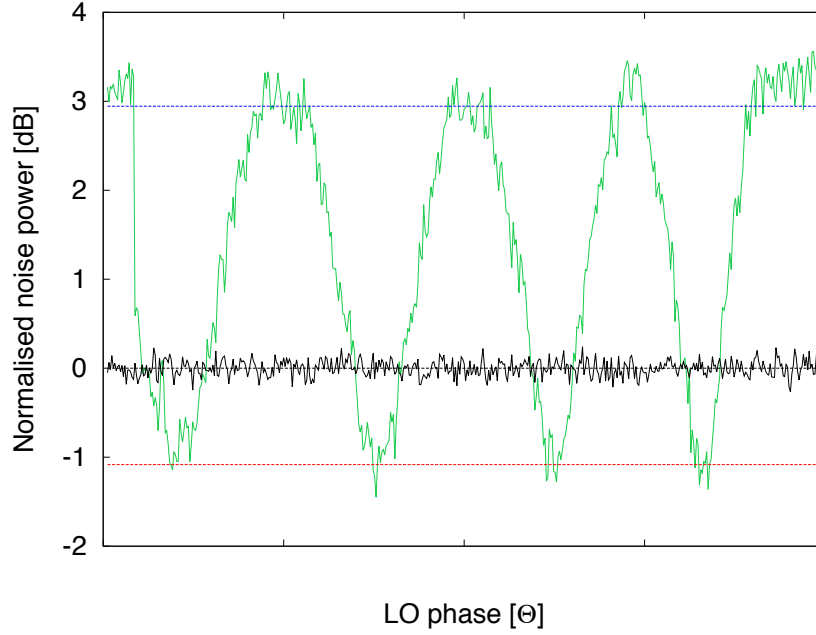


Figure 6.15: Quadrature noise measurement, as LO phase Θ is varied. The black trace shows the vacuum noise reference, and the green trace shows the noise on the 1550 nm field, which dips below vacuum noise when the squeezed quadrature is measured. The dashed red and blue lines are the squeezing and anti-squeezing values from 6.14, and are included as a reference.

6.7 Discussion

The results presented in 6.6.1 and 6.6.2 represent the key steps towards converting a squeezed vacuum state from 1550 nm to 532 nm. After I left Hannover, the 1550 nm squeezed vacuum was split at a 50:50 beam splitter (picture after the squeezing generation stage in 6.7), and half of the field was sent to HD_{1550} , while the other half was sent to the SFG and up-converted to 532 nm, to finally be measured at HD_{532} . Once part of the 1550 nm squeezed vacuum is converted to 532 nm, a two-mode squeezed state has been created. In a two-mode squeezed state, the variance in quadratures is correlated between the two modes. In 2000, Duan *et al.* derived an inseparability criterion [232] for two EPR-like operators:

$$\hat{u} \equiv |a| \hat{Q}_1 + \frac{1}{a} \hat{Q}_2 \quad (6.29a)$$

$$\hat{v} \equiv |a| \hat{P}_1 - \frac{1}{a} \hat{P}_2, \quad (6.29b)$$

where a is an arbitrary non-zero real number, and 1 and 2 index two modes. Duan *et al.* showed that the variance of these operators obeys the following inequality for

all separable states:

$$\langle(\Delta\hat{Q})^2\rangle + \langle(\Delta\hat{P})^2\rangle \geq \frac{1}{2} \left(a^2 + \frac{1}{a^2} \right) . \quad (6.30)$$

The violation of this inequality is a sufficient condition to demonstrate entanglement of a continuous-variable state. Setting $a = 1$ expresses the above inequality in its mostly intuitive form:

$$\langle(\Delta(\hat{Q}_1 + \hat{Q}_2))^2\rangle + \langle(\Delta(\hat{P}_1 - \hat{P}_2))^2\rangle \geq 1 . \quad (6.31)$$

Using this criterion, a final entanglement of 1.4 dB was measured between squeezed vacuum states at 1550 nm and 532 nm [223]. In this way, single-mode squeezing on the 1550 nm squeezed vacuum state was converted to two-mode entanglement between widely separated frequencies, with one in the telecommunication range and the other in the visible regime.

This work investigates an efficient and coherent process for converting the frequency of a quantum state, or for two-mode frequency entanglement from single-mode entanglement. The results significantly improve upon previously demonstrated frequency conversion efficiency of non-classical states of light [233]. The process is tuneable in principle, has the potential to give access to quantum states in previously unattainable frequency regimes, as well as to facilitate the integration of quantum communication and quantum storage technologies.

Chapter 7

Conclusion

The fundamental questions about the role of information in physics raised over 50 years ago have persisted as fascinating and fruitful topics of investigation. With technological and theoretical breakthroughs over the past half-century, researchers have been able to isolate and control quantum systems with ever-increasing precision. These practical advances have, in turn, enabled new generations of experiments in basic physics. In the past decade: experiments have verified Landauer's principle by measuring the energy cost of erasing information from a memory [234], as well as converting measurement information into work [235, 236]; Bell's inequality has been experimentally violated with causally independent photons, while closing the detection loophole [74, 75]; and the first demonstrations of practical quantum computation tasks have been demonstrated, with Shor's quantum factoring algorithm [237–240] and the simulation of quantum systems with a basic quantum computer [241, 242].

In the middle of the last century, the diversity of applications that the emerging field of quantum information would encompass could not be fully appreciated. Pioneering figures in the field were, however, able to guess at the future direction of research. Over twenty years ago, it was apparent that quantum techniques would need to be integrated, in order for quantum technologies to be viable. This idea is illustrated in the 1993 paper [33] introducing the theory of quantum teleportation:

Although it is currently unfeasible to store separated EPR particles for more than a brief time, if it becomes feasible to do so, quantum teleportation could be quite useful.

Based on this quotation, the usefulness of quantum teleportation would appear to

have been somewhat underestimated at first [43, 243, 244], but the essential point that the authors were making continues to be valid. Integration of current quantum techniques will play a major role in the future of quantum information science.

The first experimental result in this thesis is the heralded noiseless amplification of a qubit. The restriction against noiseless amplification of a quantum state is embedded in the structure of quantum mechanics [39], but as is often the case, the constraint is not as absolute as it may at first seem, and noiseless amplification is in fact achievable within certain parameters. As discussed in Chapter 3, a qubit is the quintessential model for encoding quantum information. Two noiseless linear amplification stages were used to coherently amplify the modes of a photon polarisation qubit, which were recombined at the output of the optical circuit. The amplification is non-deterministic but heralded, meaning that when amplification is successful, the output qubit is available for further quantum information processing. This is a powerful and robust technique, that has direct applications to secure quantum communication protocols such as DIQKD [77]. The limits on noiseless amplification of a qubit were experimentally investigated, to characterise the achievable performance with current single photon sources and detectors.

The next result, presented in Chapter 4, investigated a linear optical technique for mitigating the effect of photon loss in quantum networks. This experiment adapted the optical circuit from Chapter 3, using one NLA stage as a single-mode amplifier and the other as a stage to swap mode entanglement. Two different configurations of the circuit, corresponding to the position at which single-mode loss was added, were investigated and characterised. In the first configuration, where the loss and amplification were in the channel between a photon source and a potential quantum memory, a significant distillation of the concurrence between modes was measured. In the second configuration, where the loss and amplification were between a photon source and the entanglement swapping stage, a clear increase was observed in the coherence between modes, although it was not enough to increase the concurrence. We concluded that imperfect ancilla states can largely explain the limitations of our second configuration.

The advantage of the technique presented in Chapter 4 can be seen in the context of the quantum repeater proposed in Ref. [113]. This approach uses heralded qubit amplifiers, of the type demonstrated in Chapter 3, to construct elementary links similar to those first introduced in the DLCZ repeater protocol [123]. These elementary links consist of two quantum memories (atomic ensembles are most commonly considered) separated by a minimum linkage distance, that share

entanglement—mode entanglement in Ref. [123], and EPR entanglement in Ref. [113]. In contrast to the original DLCZ repeater, the approach presented in [113] requires both quantum memories to successfully store a photon in order to form an elementary link, and a qubit amplifier can be used to herald this. The first configuration in Chapter 4 could address this scenario, by adding another quantum memory close to the first photon source in Fig. 4.5, in the C_1 (entanglement swap) channel. In general, the first configuration ensures that a pure state is sent into a quantum memory. This could also be important if the memory is used for quantum information processing, in which case high-purity states are generally required. The advantage of the second configuration can be seen in a scenario where long-range EPR entanglement has already been established, and is being extended to the next node via a Bell state (two-photon) measurement. In this case, any transmission loss in the new channel leading to the Bell state measurement should be corrected using the NLA stage, before the entangled quantum memory releases its state. The NLA stage thus increases the probability of successfully swapping states, and maintaining the long-range entanglement.

The technique in Chapter 4 could be applied to a variety of quantum repeater architectures, and is not limited to the scenarios discussed here. Although mode entanglement is used in Chapter 4, extending the NLA stage to form a qubit amplifier, to be directly applicable in the proposal of Ref. [113], was studied in Chapter 3. A small difference in the optical circuit’s behaviour in Chapter 4 compared to Chapter 3, due to the effect of state renormalisation after the amplification stage, is discussed in Appendix A. Taken together, the work in Chapters 3 and 4 set a benchmark for linear optical techniques aimed at facilitating long-range entanglement protocols in the presence of imperfect transmission channels. A quantum erasure-correcting code that preserves coherence despite transmission loss has been experimentally demonstrated for continuous-variable states [138], and our work addresses a similar problem for discrete variables. Our results also underscore the great potential benefits of the next generation of single photon sources and detectors. With high-quality, on-demand single photon sources, the techniques based on NLA stages would no longer be limited to relatively small amplitude states [106]. In principle, with deterministic ancillary sources, attenuated states could be amplified arbitrarily close to a single photon [60]. These techniques will also benefit from improved single photon detectors: higher detection efficiency will translate directly to higher amplification success rates. As the NLA is based around the concept of projection synthesis [92], a potentially interesting direction for future research could be to use single photon detectors with number-resolution, in order

to operate on a broader class of non-classical states. Another interesting extension of the work in Chapters 3 and 4, which has been proposed in Ref. [112], is to adapt these techniques to the high-fidelity teleportation of non-classical continuous-variable states. Hybrid techniques, combining elements from discrete and continuous variable quantum optics, have been successfully used to recently achieve important milestones in quantum information science [225, 245]. These hybrid techniques show promise in harnessing the advantages of discrete and continuous variable quantum optics to overcome the limitations in both [224].

In Chapter 5, a quantum-refereed steering protocol was demonstrated. The violation of a steering inequality enables one-sided DIQKD, but demonstrating steering required one of the parties, Bob, to be completely trustworthy. Inspired by work on semi-quantum games [183], modifications to the standard one-sided DIQKD procedure have been studied [184, 185]. We derive a modified steering inequality [186] that accounts for the referee Charlie sending Bob a quantum state, instead of the usual classical measurement setting. Due to this quantum randomness, Charlie can distrust both Alice and Bob, and must now only trust his own ability to accurately prepare a quantum state. Using this quantum-refereed protocol, we experimentally violated a steering inequality, when Alice and Bob shared a Bell-local state. The advantage of one-sided DIQKD is that fully symmetric DIQKD imposes extremely rigorous experimental requirements, that are still at the frontier of what is technologically possible [74, 75], while one-sided DIQKD is far more feasible [71–73]. Furthermore, it is the natural solution for nodal networks, such as the quantum access network architecture recently demonstrated [128]. Our proof-of-principle demonstration of quantum-refereed steering is a versatile modification of one-sided DIQKD, requiring one less key assumption, and hereby enhancing communication security. It thus expands the range of scenarios to which one-sided DIQKD could be applied.

The final experiment in Chapter 6 involved coherently converting the frequency of a squeezed vacuum state from 1550 nm to 532 nm. Frequency conversion of non-classical states is necessary to be able to interface different quantum technologies. Quantum information is transmitted in optical modes, at the telecommunication frequency regime around 1550 nm, where absorption and scattering is lowest. Quantum memories, on the other hand, are based on atomic transitions in alkali metals, with frequencies in the visible spectrum. A conversion efficiency of 89.2% was measured for a weak (~ 2 mW) coherent field, using a sum-frequency generation process [200]. In the end, entanglement of 1.4 dB was measured between the squeezed vacuum at 1550 nm and 532 nm. In previous experiments, frequency conversion of single

photons from telecommunication to visible wavelengths has been demonstrated with $\sim 5\%$ efficiency [233]. Quantum memories have narrow acceptance bandwidths that are typically very difficult to match to the spectral bandwidth of single photons, while still maintaining a bright enough photon source. Recent work has begun to address this issue [246], but compressing the spectral bandwidth of a single photon down to the range of quantum memories, or appropriately filtering the sources using cavities, remains a challenge. Entangled squeezed states, on the other hand, are often generated in cavity-based sources and consist of many frequency channels, each of which can be narrowband. Frequency conversion of squeezed states might be regarded as an attractive method of interfacing non-classical optical states and quantum memories.

The term quantum information science covers a multitude of sub-fields. A unifying theme is the precise preparation, control and measurement of quantum systems, either to probe and elucidate fundamental aspects of quantum theory, or to exploit these non-classical features in the service of practical applications. The experimental work in this thesis represents a step towards connecting quantum information technologies, in order to expand the range of quantum systems that can be studied.

Appendices

Appendix A

Effect of State Renormalisation in NLA Experiments

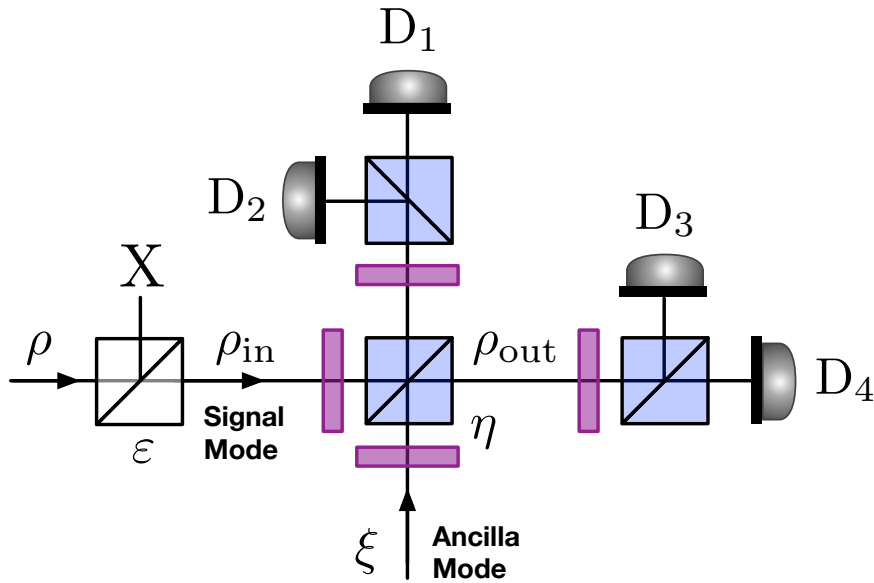


Figure A.1: Conceptual diagram of a noiseless linear amplification stage based on the generalised quantum scissors

Two noiseless linear amplification (NLA) stages are used in Chapter 3 to noiselessly amplify a qubit, and in Chapter 4 to correct for loss and swap entanglement between single-mode states. Both experiments use generalised-quantum-scissors-type amplifiers [62, 92].

In Figure 4.13 of Chapter 4, the single photon component of the input state is

relatively large, and a saturation effect is observed at the output of the first NLA stage. The aim had been to use one NLA stage to equalise the polarisation mode states of the single photon, and the $\langle H|\rho_{\text{out}}|H\rangle$ and $\langle V|\rho_{\text{out}}|V\rangle$ probabilities are equalised as desired, but while $\langle H|\rho_{\text{in}}|H\rangle$ is amplified, $\langle V|\rho_{\text{in}}|V\rangle$ is somewhat de-amplified in the process. This de-amplification effect is not observed in the qubit amplifier of Chapter 3, even though we studied it in the saturation regime as well. Here we discuss why it should be expected in Chapter 4 but not in Chapter 3. Throughout the discussion we will refer to the single NLA stage depicted in Figure A.1.

We start with the mixed state in the signal mode

$$\rho = \gamma_0|0\rangle\langle 0| + \gamma_H|H\rangle\langle H| + \gamma_V|V\rangle\langle V| + \gamma_{HV}(|H\rangle\langle V| + |V\rangle\langle H|) , \quad (\text{A.1})$$

where the total single photon probability is $\gamma_1 = \gamma_H + \gamma_V$. The coherence terms in the polarisation state are not important in this analysis, and can be neglected in the following, for convenience. Similarly, the mixed state in the ancilla mode is

$$\xi = \alpha_0|0\rangle\langle 0| + \alpha_1|1\rangle\langle 1| . \quad (\text{A.2})$$

In both signal and ancilla modes, the vacuum term dominates: $\gamma_0 > \gamma_1$, $\alpha_0 > \alpha_1$. Higher order terms can be neglected, and the states are effectively normalised: $\gamma_0 + \gamma_1 \simeq \alpha_0 + \alpha_1 \simeq 1$.

As in Chapter 4, polarisation-dependent loss is applied by passing ρ through a HWP and PPBS. The attenuation factor in the $|H\rangle$ mode is denoted by ε , and ρ is transformed into the input state

$$\rho_{\text{in}} = \gamma_0|0\rangle\langle 0| + \varepsilon\gamma_H|H\rangle\langle H| + \gamma_V|V\rangle\langle V| . \quad (\text{A.3})$$

It is clear that the state in (A.3) is not a normalised state. The re-normalised state after loss is

$$\rho_{\text{in}}^r = \frac{\gamma_0|0\rangle\langle 0| + \varepsilon\gamma_H|H\rangle\langle H| + \gamma_V|V\rangle\langle V|}{\gamma_0 + \varepsilon\gamma_H + \gamma_V} \quad (\text{A.4a})$$

$$= \gamma'_0|0\rangle\langle 0| + \gamma'_H|H\rangle\langle H| + \gamma'_V|V\rangle\langle V| . \quad (\text{A.4b})$$

Since $\gamma_0 + \varepsilon\gamma_H + \gamma_V = N_1 < 1$, the relation between the re-normalised probabilities and the original probabilities is: $\gamma'_0 = \gamma_0/N_1 > \gamma_0$, $\gamma'_H > \gamma_H$ and $\gamma'_V > \gamma_V$.

The $|H\rangle$ mode of the state ρ_{in}^r is then amplified in the NLA stage by a factor G . The

output state thus becomes

$$\rho_{\text{out}} = \gamma'_0|0\rangle\langle 0| + G\gamma'_H|H\rangle\langle H| + \gamma'_V|V\rangle\langle V|. \quad (\text{A.5})$$

The state in (A.5) is once again not a normalised state, and must be re-normalised:

$$\rho_{\text{out}}^r = \frac{\gamma'_0|0\rangle\langle 0| + G\gamma'_H|H\rangle\langle H| + \gamma'_V|V\rangle\langle V|}{\gamma'_0 + G\gamma'_H + \gamma'_V} \quad (\text{A.6a})$$

$$= \gamma''_0|0\rangle\langle 0| + \gamma''_H|H\rangle\langle H| + \gamma''_V|V\rangle\langle V|. \quad (\text{A.6b})$$

Now $\gamma'_0 + G\gamma'_H + \gamma'_V = N_2 > 1$, since $G > 1$. After re-normalisation, the vacuum term has decreased in the mixture: $\gamma''_0 = \gamma'_0/N_2 < \gamma'_0$. The $|H\rangle$ mode has increased: $\gamma''_H > \gamma'_H$, although it is by a factor less than G . The $|V\rangle$ mode, on the other hand, has decreased: $\gamma''_V < \gamma'_V$. Overall, the single photon component of the state has increase (the vacuum has decreased), but the amplification in mode $|H\rangle$ has somewhat de-amplified mode $|V\rangle$. This is effect is not observed in the qubit amplifier of Chapter 3, because there both modes are amplified, and the de-amplification of the opposite modes are cancelled out. The saturation effect in the qubit amplifier is therefore manifested as a levelling off of the achievable gain, as the output state size approaches the ancilla efficiency. In the remainder of this Appendix, we used various observed photon rates in the optical circuit of Chapter 3 to calculate the approximate degree of de-amplification we should expect in mode $|V\rangle$. Our analysis is consistent with the degree of de-amplification observed in Figure 4.13 of Chapter 4.

The gain G of the NLA stage is set to compensate the loss: $G = \varepsilon^{-1}$. In A.1, the gain is determined by the ratio of reflected to transmitted intensity, with η as the reflected intensity coefficient:

$$G = \frac{\eta}{1 - \eta}, \quad (\text{A.7})$$

implying that in the ideal case $\eta = (1 - \varepsilon)^{-1}$ in order for the gain to compensate for the loss.

One way in which the performance of the optical circuit is characterised in Chapters 3 and 4 is by experimentally comparing the size of the $|H\rangle$ and $|V\rangle$ modes in ρ_{in} and ρ_{out} . As ρ_{out} is a heralded state, it is the heralded probabilities of detecting $|H\rangle$ and $|V\rangle$ that are compared. To make the comparison with ρ_{in} , the heralded probabilities of detecting modes $|H\rangle$ and $|V\rangle$ are measured in the input state as well, with the ancilla photon just acting as an independent trigger. The coincidence detection rate (\mathcal{C}_2) between the heralding and output detectors is measured, and

the heralded probability is the coincidence detection rate normalised by the single photon detection rate in the heralding detectors. The ratio is

$$\mathcal{R} = \frac{\mathcal{C}_2(D_{1+2}, D_{3+4})}{D_{1+2}}. \quad (\text{A.8})$$

The heralded probabilities in ρ_{in} are measured by sending the ancilla mode directly to the heralding detectors without any mode splitting, and the signal mode likewise directly through the NLA stage to the output detectors. The heralded rate of measuring the $|H\rangle$ signal mode is the coincidence detection rate between D_4 and D_{1+2} , while the heralded rate of measuring the $|V\rangle$ signal mode is the coincidence detection rate between D_3 and D_{1+2} . The integration time for all detection rates is one second.

The symbol A_1 is used to represent the rate of detected single photons per second from the ancilla mode $A1$. Another rate that will be important is the rate of single photons per second detected in the initial (unattenuated) state ρ , and it is denoted by the symbol S_1 . The heralded probabilities (denoted by the subscript h) of $|H\rangle$ and $|V\rangle$ in the input state are given by the ratios

$$\langle H|\rho_{\text{in}}|H\rangle_{\text{h}} = \frac{\mathcal{C}_2\{\langle 1|\xi|1\rangle, \langle H|\rho_{\text{in}}|H\rangle\}}{A_1}, \quad (\text{A.9a})$$

$$\langle V|\rho_{\text{in}}|V\rangle_{\text{h}} = \frac{\mathcal{C}_2\{\langle 1|\xi|1\rangle, \langle V|\rho_{\text{in}}|V\rangle\}}{A_1}. \quad (\text{A.9b})$$

The coincidence rates in the numerators of (A.9) can be estimated from the coincidence efficiency v between ρ and A_1 , and the measured singles rates in these modes:

$$v \equiv \frac{\mathcal{C}_2\{\langle 1|\xi|1\rangle, \langle 1|\rho|1\rangle\}}{\sqrt{S_1^2 + A_1^2}} \quad (\text{A.10})$$

The single photon subspace of the initial state ρ is in an equal superposition of $|H\rangle$ and $|V\rangle$, and the loss attenuates $|H\rangle$ by the factor ε . This implies:

$$\mathcal{C}_2\{\langle 1|\xi|1\rangle, \langle H|\rho_{\text{in}}|H\rangle\} = \frac{\varepsilon \mathcal{C}_2\{\langle 1|\xi|1\rangle, \langle 1|\rho|1\rangle\}}{2} \quad (\text{A.11a})$$

$$\simeq \frac{\varepsilon v \sqrt{S_1^2 + A_1^2}}{2}, \quad (\text{A.11b})$$

and

$$\mathcal{C}_2\{\langle 1|\xi|1\rangle, \langle V|\rho_{\text{in}}|V\rangle\} = \frac{\mathcal{C}_2\{\langle 1|\xi|1\rangle, \langle 1|\rho|1\rangle\}}{2} \quad (\text{A.12a})$$

$$\simeq \frac{v \sqrt{S_1^2 + A_1^2}}{2}. \quad (\text{A.12b})$$

The heralded probabilities of $|H\rangle$ and $|V\rangle$ in the input state are thus

$$\langle H|\rho_{\text{in}}|H\rangle_{\text{h}} \simeq \frac{\varepsilon v \sqrt{S_1^2 + A_1^2}}{2A_1} \quad (\text{A.13a})$$

$$\langle V|\rho_{\text{in}}|V\rangle_{\text{h}} \simeq \frac{v \sqrt{S_1^2 + A_1^2}}{2A_1} \quad (\text{A.13b})$$

To measure ρ_{out} , the $|H\rangle$ mode in ρ_{in} is sent to the heralding detectors D_{1+2} , while the $|V\rangle$ mode is sent to the output detectors D_3 . Using a HWP, an effective reflectivity η is set at the central beam splitter, sending $\eta\xi$ to D_4 and transmitting $(1-\eta)\xi$ to D_{1+2} . The single detection rate in D_{1+2} is approximately $(1/2)\varepsilon S_1 + (1-\eta)A_1$. Substituting into (A.8) yields

$$\langle H|\rho_{\text{out}}|H\rangle_{\text{h}} = \frac{\mathcal{C}_2\{D_{1+2}, D_4\}}{D_{1+2}} \quad (\text{A.14a})$$

$$\simeq \frac{\mathcal{C}_2\{\langle H|\rho_{\text{in}}|H\rangle, \langle 1|\eta\xi|1\rangle\}}{\langle H|\rho_{\text{in}}|H\rangle + \langle 1|(1-\eta)\xi|1\rangle} \quad (\text{A.14b})$$

$$\simeq \frac{\varepsilon v \eta \sqrt{S_1^2 + A_1^2}}{\varepsilon S_1 + 2(1-\eta)A_1}, \quad (\text{A.14c})$$

and

$$\langle V|\rho_{\text{out}}|V\rangle_{\text{h}} = \frac{\mathcal{C}_2\{D_{1+2}, D_3\}}{D_{1+2}} \quad (\text{A.15a})$$

$$\simeq \frac{\mathcal{C}_2\{\langle V|\rho_{\text{in}}|V\rangle, \langle 1|(1-\eta)\xi|1\rangle\}}{\langle H|\rho_{\text{in}}|H\rangle + \langle 1|(1-\eta)\xi|1\rangle} \quad (\text{A.15b})$$

$$\simeq \frac{v(1-\eta) \sqrt{S_1^2 + A_1^2}}{\varepsilon S_1 + 2(1-\eta)A_1}. \quad (\text{A.15c})$$

Estimates of the probabilities $\langle H|\rho_{\text{out}}|H\rangle_{\text{h}}$ and $\langle V|\rho_{\text{out}}|V\rangle_{\text{h}}$ are expressed in terms of a few experimental parameters in (A.14) and (A.15). Substituting the typically observed rates $S_1 \simeq 5.5 \cdot 10^4 \text{ s}^{-1}$ and $A_1 \simeq 8.5 \cdot 10^4 \text{ s}^{-1}$ with a coincidence efficiency $v \simeq 0.175$, and assuming a loss factor $\varepsilon = 1/2$ and $\eta = 2/3$, the estimated heralded

probabilities become:

$$\langle H|\rho_{\text{in}}|H\rangle_{\text{h}} \simeq 0.05 \qquad \langle H|\rho_{\text{out}}|H\rangle_{\text{h}} \simeq 0.07 \qquad (\text{A.16 a,b})$$

$$\langle V|\rho_{\text{in}}|V\rangle_{\text{h}} \simeq 0.10 \qquad \langle V|\rho_{\text{out}}|V\rangle_{\text{h}} \simeq 0.07 \qquad (\text{A.16 c,d})$$

The NLA stage increases $|H\rangle$ from a heralded input probability ~ 0.05 to a heralded output probability ~ 0.07 . Furthermore, the two polarisations are balanced in ρ_{out} after amplification, as desired. The $|V\rangle$ mode, however, has been de-amplified in the process: $\langle V|\rho_{\text{in}}|V\rangle_{\text{h}} > \langle V|\rho_{\text{out}}|V\rangle_{\text{h}}$. This is the saturation effect presented in 4.13. The ratio of the heralded output to input probability for the $|V\rangle$ mode is

$$\frac{\langle V|\rho_{\text{out}}|V\rangle_{\text{h}}}{\langle V|\rho_{\text{in}}|V\rangle_{\text{h}}} = \frac{2(1-\eta)A_1}{\varepsilon S_1 + 2(1-\eta)A_1} . \qquad (\text{A.17})$$

The saturation effect becomes negligible, or $\langle V|\rho_{\text{out}}|V\rangle_{\text{h}}/\langle V|\rho_{\text{in}}|V\rangle_{\text{h}} \rightarrow 1$, when $\varepsilon S_1 \ll 2(1-\eta)A_1$. The single photon rate in the ancilla mode must be much greater than the single photon rate in the signal mode to avoid saturation effects.

In the case of the qubit amplifier presented in Chapter 3, the $|V\rangle$ signal mode is amplified in the first NLA stage while the $|H\rangle$ mode passes through the stage, and $|H\rangle$ is amplified in the second NLA stage while $|V\rangle$ pass through. If the input state size is too large, both polarisations are alternately amplified and de-amplified in the NLA stages. Saturation in the qubit amplifier therefore manifests itself as asymptotically approaching a maximum gain factor, determined by the ancilla efficiency relative to the state size.

Appendix B

Dynamics of Optical Parametric Oscillators

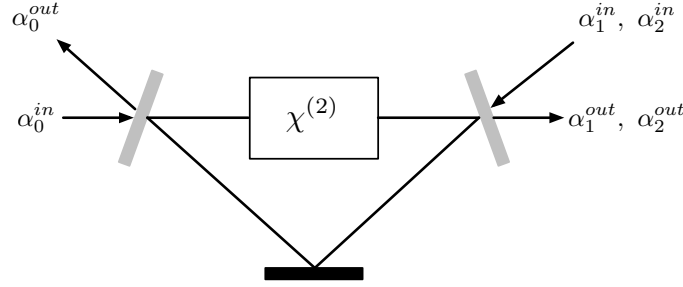


Figure B.1: Optical parametric oscillator in a three-mirror ring cavity. See text for details.

We investigate a system consisting of a nonlinear $\chi^{(2)}$ material inside a ring cavity, as shown in Figure B.1. A strong pump field with frequency ω_0 couples into the cavity, and two other fields at frequencies ω_1 and ω_2 are generated from the interaction between the pump and the nonlinear material. The single-pass loss parameters in the cavity are given by γ_i and μ_i , associated with loss through the mirror and all other loss mechanisms (*e.g.* absorption), respectively.

The equation of motion of a field in an empty cavity was derived in 6.3.3. The interaction Hamiltonian for a non-degenerate OPO was give in 6.3.4. The dynamics of an OPO can be approximately described by combining the cavity equation of motion with the equations of motion from the interaction Hamiltonian. In the following, all fields will be represented as classical (complex-valued) amplitudes, which can be decomposed into a mean amplitude and a fluctuation term: $\alpha = \bar{\alpha} + \delta\alpha$. We take τ to be the time for all fields to complete a single pass through the cavity.

The evolution of the fields on that time scale is:

$$\tau \dot{\alpha}_0 + \gamma'_0 \alpha_0 = \chi^{(2)} \alpha_1 \alpha_2 + \sqrt{2\gamma_0} \alpha_0^{in} + \sqrt{2\mu_0} \Gamma_0^{in} \quad (\text{B.1a})$$

$$\tau \dot{\alpha}_1 + \gamma'_1 \alpha_1 = -\chi^{(2)} \alpha_0 \alpha_2^* + \sqrt{2\gamma_1} \alpha_1^{in} + \sqrt{2\mu_1} \Gamma_1^{in} \quad (\text{B.1b})$$

$$\tau \dot{\alpha}_2 + \gamma'_2 \alpha_2 = -\chi^{(2)} \alpha_0 \alpha_1^* \sqrt{2\gamma_2} \alpha_2^{in} + \sqrt{2\mu_2} \Gamma_2^{in} \quad (\text{B.1c})$$

The equations (B.1) describe the fields inside the cavity. The final measurements will be made on the fields at the cavity output, and the condition relating the input, internal and output fields is:

$$\alpha_i^{out} = \sqrt{2\gamma} \alpha_i - \alpha_i^{in} \quad (i = 0, 1, 2) . \quad (\text{B.2})$$

We first consider the stationary mean field solutions to (B.1). We assume that there is only one field α_0^{in} initially coupling into the OPO. The stationary mean field equations are therefore:

$$\gamma'_0 \bar{\alpha}_0 = 2\chi \bar{\alpha}_1 \bar{\alpha}_2 + \sqrt{2\gamma_0} \bar{\alpha}_0^{in} \quad (\text{B.3a})$$

$$\gamma'_1 \bar{\alpha}_1 = -2\chi \bar{\alpha}_0 \bar{\alpha}_2 \quad (\text{B.3b})$$

$$\gamma'_2 \bar{\alpha}_2 = -2\chi \bar{\alpha}_0 \bar{\alpha}_1 \quad (\text{B.3c})$$

The coefficient $\gamma'_i = \gamma_i + \mu_i$ groups together losses due to escaping the cavity and absorption. Between (B.1) and (B.3), we have made the substitution $\chi^{(2)} = 2\chi$ for convenience. The phases in (B.3) can be chosen in the above equations to ensure that all the mean field amplitudes are real. The solutions to (B.3) are:

$$\bar{\alpha}_0 = \frac{\gamma'_1 \gamma'_2}{4\chi^2} \quad (\text{B.4a})$$

$$\bar{\alpha}_1 = \frac{\gamma'_0 \gamma'_2}{4\chi^2} (\sigma - 1) \quad (\text{B.4b})$$

$$\bar{\alpha}_2 = \frac{\gamma'_0 \gamma'_1}{4\chi^2} (\sigma - 1) \quad (\text{B.4c})$$

In the above equations, the pump parameter $\sigma = 2\sqrt{(2\chi^2\gamma_0)/(\gamma_0'^2\gamma_1'\gamma_2')} \alpha_0^{in}$. The pump parameter can be expressed as $\sigma = \sqrt{P/P_0}$, where $P = |\alpha_0^{in}|^2$ is the incoming pump intensity, and $P_0 = (\gamma_0'^2\gamma_1'\gamma_2')/(8\chi^2\gamma_0)$ is the threshold intensity. If $\sigma > 1$, then the OPO is operating *above threshold*, and the fundamental fields α_1^{out} and α_2^{out} at the cavity's output will approach coherent states. We now look at the dynamics of the field fluctuation terms. At this point we make the simplifying assumption that the loss coefficients for the fundamental fields are equal: $\gamma'_i = \gamma'$, ($i = 1, 2$). Keeping

this in mind, the fluctuation terms in Equation (B.1) become:

$$\tau \delta \dot{\alpha}_0 + \gamma'_0 \delta \alpha_0 = -\sqrt{\gamma'_0 \gamma'(\sigma - 1)} \delta \alpha_2 - \sqrt{\gamma'_0 \gamma'(\sigma - 1)} \delta \alpha_1 \quad (\text{B.5a})$$

$$+ \sqrt{2\gamma_0} \delta \alpha_0^{in} + \sqrt{2\mu_0} \delta \Gamma_0^{in} \quad (\text{B.5b})$$

$$\tau \delta \dot{\alpha}_1 + \gamma' \delta \alpha_1 = \gamma' \delta \alpha_2^* + \sqrt{\gamma'_0 \gamma'(\sigma - 1)} \delta \alpha_0 + \sqrt{2\gamma} \delta \alpha_1^{in} + \sqrt{2\mu} \Gamma_1^{in} \quad (\text{B.5c})$$

$$\tau \delta \dot{\alpha}_2 + \gamma' \delta \alpha_2 = \gamma' \delta \alpha_1^* + \sqrt{\gamma'_0 \gamma'(\sigma - 1)} \delta \alpha_0 + \sqrt{2\gamma} \delta \alpha_2^{in} + \sqrt{2\mu} \delta \Gamma_2^{in} \quad (\text{B.5d})$$

To further simplify the calculation, we make another assumption that the cavity finesse for the pump field is much lower than for the fundamental fields: $\gamma'_0 \gg \gamma'$. This implies that the pump field amplitude evolves on a much longer time scale than the fundamental fields, and its time derivative in (B.5) can be adiabatically eliminated:

$$\gamma'_0 \delta \alpha_0 = -\sqrt{\gamma'_0 \gamma'(\sigma - 1)} (\delta \alpha_1 + \delta \alpha_2) + \sqrt{2\gamma_0} \delta \alpha_0^{in} + \sqrt{2\mu_0} \delta \Gamma_0^{in}. \quad (\text{B.6})$$

This stationary value for $\delta \alpha_0$ is substituted into (B.5). The first-order differential equations for $\delta \alpha_1$ and $\delta \alpha_2$ can be converted to algebraic equations using the following property of the Fourier transform: $\mathcal{F}[\dot{f}(t)] = -i\omega \mathcal{F}[f(t)]$. We obtain two coupled equations in the frequency domain:

$$(\gamma' \sigma - i\omega \tau) \delta \tilde{\alpha}_1 = \gamma' \delta \tilde{\alpha}_2^* + \gamma'(1 - \sigma) \delta \tilde{\alpha}_2 + \sqrt{2\gamma_0 \gamma'(\sigma - 1)/\gamma'_0} \delta \tilde{\alpha}_0^{in} \quad (\text{B.7a})$$

$$+ \sqrt{2\mu_0 \gamma'(\sigma - 1)/\gamma'_0} \delta \tilde{\Gamma}_0^{in} + \sqrt{2\gamma} \delta \tilde{\alpha}_1^{in} + \sqrt{2\mu} \delta \tilde{\Gamma}_1^{in} \quad (\text{B.7b})$$

$$(\gamma' \sigma - i\omega \tau) \delta \tilde{\alpha}_2 = \gamma' \delta \tilde{\alpha}_1^* + \gamma'(1 - \sigma) \delta \tilde{\alpha}_1 + \sqrt{2\gamma_0 \gamma'(\sigma - 1)/\gamma'_0} \delta \tilde{\alpha}_0^{in} \quad (\text{B.7c})$$

$$+ \sqrt{2\mu_0 \gamma'(\sigma - 1)/\gamma'_0} \delta \tilde{\Gamma}_0^{in} + \sqrt{2\gamma} \delta \tilde{\alpha}_2^{in} + \sqrt{2\mu} \delta \tilde{\Gamma}_2^{in} \quad (\text{B.7d})$$

The following variables can now be defined:

$$p_i = \delta \alpha_i + \delta \alpha_i^* \quad q_i = -i(\delta \alpha_i - \delta \alpha_i^*) \quad (i = 0, 1, 2) \quad (\text{B.8})$$

In terms of these new variables:

$$\gamma' \sigma \tilde{p}_1 + \omega \tau \tilde{q}_1 = \gamma'(2 - \sigma) \tilde{p}_2 + \sqrt{2\gamma_0 \gamma'(\sigma - 1)/\gamma'_0} \tilde{p}_0^{in} \quad (\text{B.9a})$$

$$+ \sqrt{2\mu_0 \gamma'(\sigma - 1)/\gamma'_0} \tilde{p}_0^{in'} + \sqrt{2\gamma} \tilde{p}_1^{in} + \sqrt{2\mu} \tilde{p}_1^{in'} \quad (\text{B.9b})$$

$$\gamma' \sigma \tilde{p}_2 + \omega \tau \tilde{q}_2 = \gamma'(2 - \sigma) \tilde{p}_1 + \sqrt{2\gamma_0 \gamma'(\sigma - 1)/\gamma'_0} \tilde{p}_0^{in} \quad (\text{B.9c})$$

$$+ \sqrt{2\mu_0 \gamma'(\sigma - 1)/\gamma'_0} \tilde{p}_0^{in'} + \sqrt{2\gamma} \tilde{p}_2^{in} + \sqrt{2\mu} \tilde{p}_2^{in'} \quad (\text{B.9d})$$

Equation (B.9) shows that the amplitude and phase quadratures of the fundamental

fields are coupled. In other words, the quantum noise in the generated beams will be correlated, and it is interesting to look at the fluctuation variance for the sum of the phase quadratures and the sum of the amplitude quadratures: $Q^+ = (q_1 + q_2)/\sqrt{2}$ and $P^+ = (p_1 + p_2)/\sqrt{2}$. It is also clear from (B.9) that the noise in the cavity depends directly on the noise of the input fields \tilde{p}_i^{in} . Assuming the inputs are all coherent states, their variances can be normalised: $\mathcal{V}_{p_i}^{in}(\omega) = \langle |\tilde{p}_i^{in}|^2 \rangle = 1$ and similarly for $\mathcal{V}_{q_i}^{in}(\theta)$. Recalling the relation between the internal field and the cavity output (B.2), the noise variance in the sum of quadratures is:

$$\mathcal{V}_{Q^+}^{out}(\omega) = \langle |q^{out}(\omega)|^2 \rangle = 1 - \frac{4\gamma\gamma'}{\omega^2\tau^2 + 4\gamma'^2\sigma^2} \quad (\text{B.10a})$$

$$\mathcal{V}_{P^+}^{out}(\omega) = \langle |p^{out}(\omega)|^2 \rangle = 1 + \frac{4\gamma\gamma'}{\omega^2\tau^2 + 4\gamma'^2(\sigma - 1)^2} \quad (\text{B.10b})$$

The minimum uncertainty for both quadratures is $\mathcal{V}_{q_i, p_i}^{in}(\omega) = 1$, which describes a coherent state. The variance in the fundamental fields' amplitude quadrature decreases below this level, and it is said to be squeezed. To still satisfy the quantum uncertainty relation, the variance in the complementary phase quadrature must increase, and this quadrature is said to be anti-squeezed. Equations (B.10) show the squeezing spectrum in the sum of the \hat{Q} and \hat{P} quadratures. Thus, there is a correlation between the noise of the fundamental fields generated in the non-degenerate OPO.

References

- [1] J. N. Wilford. “Men Walk on Moon: Astronauts Land on Plain; Collect Rocks, Plant Flag”. *The New York Times*, Monday 21 July, 1969.
- [2] H. Pick. “Beatle hysteria hits US”. *The Guardian*, Saturday 8 February 1964.
- [3] K. Christitch, B. Girod de l’Ain, and J.-P. Quelin. “Le nuit des barricades”. *Le Monde*, 12-13 Mai 1968.
- [4] M. A. Nielsen and I. L. Chuang. *Quantum Computation and Quantum Information*. Cambridge University Press, First edition, 2000.
- [5] R. Landauer. Irreversibility and Heat Generation in the Computing Process. *IBM Journal of Research and Development*, 5(3):183, 1961.
- [6] J. C. Maxwell. *Theory of Heat*. Longmans, Green and Co., London, 1871.
- [7] K. Maruyama, F. Nori, and V. Vedral. Colloquium: The physics of Maxwell’s demon and information. *Reviews of Modern Physics*, 81(1):1–23, 2009.
- [8] L. Szilard. On the decrease of entropy in thermodynamic systems by the intervention of intelligent beings. *Zeitschrift für Physik*, 53:840–856, 1929.
- [9] R. Landauer. Information is Physical. *Physics Today*, 1991.
- [10] R. Landauer. The physical nature of information. *Physics Letters A*, 217:188–193, 1996.
- [11] C. E. Shannon. A Mathematical Theory of Communication. *The Bell System Technical Journal*, 27:379–423, 623–656, 1948.
- [12] J. S. Bell. On the Einstein-Podolsky-Rosen paradox. *Physics*, 1:195–200, 1964.
- [13] J. S. Bell. *Speakable and Unspeakable in Quantum Mechanics*. Cambridge University Press, Cambridge, 1988.

- [14] A. Einstein, B. Podolsky, and N. Rosen. Can Quantum-Mechanical Description of Physical Reality Be Considered Complete? *Physical Review*, 47:777–780, 1935.
- [15] R. J. Glauber. The Quantum Theory of Optical Coherence. *Physical Review*, 130(6):2529–2539, 1963.
- [16] R. J. Glauber. Coherent and Incoherent States of the Radiation Field. *Physical Review*, 131(6):2766–2788, 1963.
- [17] R. Loudon. *The Quantum Theory of Light*. Oxford University Press, Oxford, Third edition, 2000.
- [18] T. H. Maiman. Stimulated Optical Radiation in Ruby. *Nature*, 187:493–494, 1960.
- [19] A. L. Schawlow and C. H. Townes. Infrared and Optical Masers. *Physical Review*, 112(6):1940–1940, 1958.
- [20] Nobelprize.org. “The Nobel Prize in Physics 1964”.
- [21] R. W. Boyd. *Nonlinear Optics*. Elsevier, Amsterdam, Third edition, 2008.
- [22] C. H. Bennett. The Thermodynamics of Computation-a Review. *International Journal of Theoretical Physics*, 21(12):905–940, 1982.
- [23] R. P. Feynman. Simulating Physics with Computers. *International Journal of Theoretical Physics*, 21(6):467–488, 1982.
- [24] H. J. Kimble, M. Dagenais, and L. Mandel. Photon Antibunching in Resonance Fluorescence. *Physical Review Letters*, 39(11):691–695, 1977.
- [25] A. Aspect, P. Grangier, and G. Roger. Experimental Tests of Realistic Local Theories via Bell’s Theorem. *Physical Review Letters*, 47:460–463, 1981.
- [26] A. Aspect, P. Grangier, and G. Roger. Experimental Realization of Einstein-Podolsky-Rosen-Bohm Gedankenexperiment: A New Violation of Bell’s Inequalities. *Physical Review Letters*, 49:91–94, 1982.
- [27] A. Aspect, J. Dalibard, and G. Roger. Experimental Test of Bell’s Inequalities Using Time-Varying Analyzers. *Physical Review Letters*, 49:1804–1807, 1982.
- [28] C. K. Hong, Z. Y. Ou, and L. Mandel. Measurement of Subpicosecond Time Intervals between Two Photons by Interference. *Physical Review Letters*, 59(18):2044–2046, 1987.

- [29] R. P. Feynman, R. B. Leighton, and M. Sands. *The Feynman Lectures on Physics*, volume I-III. Reading: Addison-Wesley, Boston, 1965.
- [30] P. G. Kwiat, A. M. Steinberg, and R. Y. Chiao. Observation of a “quantum eraser”: A revival of coherence in a two-photon interference experiment. *Physical Review A*, 45:7729–7739, 1992.
- [31] A. M. Steinberg, P. G. Kwiat, and R. Y. Chiao. Dispersion cancellation in a measurement of the single-photon propagation velocity in glass. *Physical Review Letters*, 68:2421–2424, 1992.
- [32] P. G. Kwiat. *Nonclassical Effects from Spontaneous Parametric Down-Conversion: Adventures in Quantum Wonderland*. PhD thesis, University of California at Berkeley, 1993.
- [33] C. H. Bennett, G. Brassard, C. Crépeau, R. Jozsa, A. Peres, and W. K. Wootters. Teleporting an unknown quantum state via dual classical and epr channels. *Physical Review Letters*, 70:1895–1899, 1993.
- [34] S. L. Braunstein and A. Mann. Measurement of the Bell operator and quantum teleportation. *Physical Review A*, 51(3):R1721–R1730, 1995.
- [35] H. Weinfurter. Experimental Bell-state analysis. *Europhysics Letters*, 25:559–564, 1994.
- [36] D. Bouwmeester, J.-W. Pan, K. Mattle, M. Eible, H. Weinfurter, and A. Zeilinger. Experimental quantum teleportation. *Nature*, 390:575–579, 1997.
- [37] D. Boschi, S. Branca, F. De Martini, L. Hardy, and S. Popescu. Experimental Realization of Teleporting an Unknown Pure Quantum State via Dual Classical and Einstein-Podolsky-Rosen Channels. *Physical Review Letters*, 80(1121), 1998.
- [38] J.-W. Pan, D. Bouwmeester, H. Weinfurter, and A. Zeilinger. Experimental Entanglement Swapping: Entangling Photons That Never Interacted. *Physical Review Letters*, 80(18):3891–3894, 1998.
- [39] W. K. Wootters and W. H. Zurek. A single quantum cannot be cloned. *Nature*, 299:802–803, 1982.
- [40] D. Dieks. Communication by EPR devices. *Physics Letters*, 92A(6):271–272, 1982.

- [41] C. H. Bennett and G. Brassard. Quantum Cryptography: Public key distribution and coin tossing. In *Proceedings of the IEEE International Conference on Computers, Systems and Signal Processing, Bangalore, India*, page 175, New York, 1984. IEEE.
- [42] A. K. Ekert. Quantum cryptography based on bell's theorem. *Physical Review Letters*, 67:661–663, 1991.
- [43] E. Knill, R. Laflamme, and G. J. Milburn. A scheme for efficient quantum computation with linear optics. *Nature*, 409:46–52, 2001.
- [44] J. L. O'Brien, G. J. Pryde, A. G. White, T. C. Ralph, and D. Branning. Demonstration of an all-optical quantum controlled-NOT gate. *Nature*, 426:264–267, 2003.
- [45] J. C. Maxwell. *A Treatise on Electricity and Magnetism*, volume I-II. Oxford, 1873.
- [46] J. C. Maxwell. A Dynamical Theory of the Electromagnetic Field. *Philosophical Transactions of the Royal Society of London*, 155:459–512, 1865.
- [47] M. Planck. On the theory of the law of energy distribution in the normal spectrum. *Verhandlungen der Deutschen Physikalischen Gesellschaft*, 2:237–245, 1900.
- [48] A. Einstein. On a Heuristic Point of View about the Creation and Conversion of Light. *Annalen der Physik*, 17(6):132–148, 1905.
- [49] J. P. Gordon, H. Z. Zeiger, and C. H. Townes. The Maser-New Type of Microwave Amplifier, Frequency Standard, and Spectrometer. *Physical Review*, 99(4):1264–1274, 1955.
- [50] J. S. Lundeen. *Generalized Measurement and Post-selection in Optical Quantum Information*. PhD thesis, University of Toronto, 2006.
- [51] M. Born and E. Wolf. *Principles of Optics: Electromagnetic Theory of Propagation, Interference and Diffraction of Light*. Cambridge University Press, Cambridge, 7th edition, 1999.
- [52] W. E. Lamb, Jr. Anti-photon. *Applied Physics B: Lasers and Optics*, 60:77–84, 1995.
- [53] H. Goldstein, C. P. Poole, and J. L. Safko. *Classical Mechanics*. Addison-Wesley, Third edition, 2001.

- [54] C. Cohen-Tannoudji, B. Diu, and F. Laloë. *Quantum mechanics*, volume I-II. Collection Enseignement des Sciences, Paris, 1973.
- [55] N. K. Langford. *Encoding, Manipulating and Measuring Quantum Information in Optics*. PhD thesis, University of Queensland, 2007.
- [56] C. C. Gerry and P. L. Knight. *Introductory Quantum Optics*. Cambridge University Press, 2005.
- [57] U. Leonhardt. *Measuring the Quantum State of Light*. Cambridge University Press, Cambridge, 1997.
- [58] H. Fearn and R. Loudon. Quantum theory of the lossless beam splitter. *Optics Communications*, 64(6):485–490, 1987.
- [59] B. E. A. Saleh and M. C. Teich. *Fundamentals of Photonics*. Wiley, New Jersey, Second edition, 2007.
- [60] S. Kocsis, G. Y. Xiang, T. C. Ralph, and G. J. Pryde. Heralded noiseless amplification of a photon polarisation qubit. *Nature Physics*, 9:23–28, 2013.
- [61] C. M. Caves. Quantum limits on noise in linear amplifiers. *Physical Review D*, 26(8):1817–1839, 1982.
- [62] G. Y. Xiang, T. C. Ralph, A. P. Lund, N. Walk, and G. J. Pryde. Heralded noiseless linear amplification and distillation of entanglement. *Nature Photonics*, 4:316–319, 2010.
- [63] F. Ferreyrol *et al.* Implementation of a Nondeterministic Optical Noiseless Amplifier. *Physical Review Letters*, 104(123603), 2010.
- [64] A. Zavatta, J. Fiurášek, and M. Bellini. A high-fidelity noiseless amplifier for quantum light states. *Nature Photonics*, 5:52–60, 2010.
- [65] M. A. Usuga *et al.* Noise-powered probabilistic concentration of phase information. *Nature Physics*, 6:767–771, 2010.
- [66] C. I. Osorio. Heralded photon amplification for quantum communication. *Physical Review A*, 86(023815), 2012.
- [67] M. Mičuda *et al.* Noiseless loss suppression in quantum optical communication. *Physical Review Letters*, 109:180503, 2012.
- [68] A. Shaji and C. M. Caves. Qubit metrology and decoherence. *Physical Review A*, 76(032111), 2008.

- [69] W.-B. Gao *et al.* Experimental demonstration of a hyper-entangled ten-qubit Schrödinger cat state. *Nature Physics*, 6:331–335, 2010.
- [70] P. G. Kwiat, P. H. Eberhard, A. M. Steinberg, and R. Y. Chiao. Proposal for a loophole-free Bell inequality experiment. *Physical Review A*, 49:3209–3220, 1994.
- [71] A. J. Bennet *et al.* Arbitrarily Loss-Tolerant Einstein-Podolsky-Rosen Steering Allowing a Demonstration over 1 km of Optical Fiber with No Detection Loophole. *Physical Review X*, 2:031003, 2012.
- [72] D. H. Smith *et al.* Conclusive quantum steering with superconducting transition-edge sensors. *Nature Communications*, 3:625–631, 2012.
- [73] B. Wittmann *et al.* Loophole-free Einstein-Podolsky-Rosen experiment via quantum steering. *New Journal of Physics*, 14(053030), 2012.
- [74] B. G. Christensen *et al.* Detection-Loophole-Free Test of Quantum Nonlocality, and Applications. *Physical Review Letters*, 111(130406), 2013.
- [75] M. Giustina *et al.* Bell violation using entangled photons without the fair-sampling assumption. *Nature*, 497:227–230, 2013.
- [76] A. E. Lita, A. J. Miller, and S. W. Nam. Counting near-infrared single-photons with 95% efficiency. *Optics Express*, 16(5):3032–3040, 2008.
- [77] N. Gisin, S. Pironio, and N. Sangouard. Proposal for Implementing Device-Independent Quantum Key Distribution Based on a Heralding Qubit Amplifier. *Physical Review Letters*, 105:070501, 2010.
- [78] D. Pitkaens, X. Ma, R. Wickert, P. van Loock, and N. Lütkenhaus. Efficient heralding of photonic qubits with applications to device-independent quantum key distribution. *Physical Review A*, 84(022325), 2011.
- [79] A. Acín, N. Brunner, N. Gisin, S. Massar, S. Pironio, and V. Scarani. Device-Independent Security of Quantum Cryptography against Collective Attacks. *Physical Review Letters*, 98(230501), 2007.
- [80] A. Acín, N. Gisin, and L. Masanes. From Bell’s Theorem to Secure Quantum Key Distribution. *Physical Review Letters*, 97:120405, 2006.
- [81] D. J. Saunders. *Quantum Correlations: Experimental EPR-Steering, Bilocality and Weak Tomography in Photonic Information Science*. PhD thesis, Griffith University, 2012.

- [82] H. P. Yuen. Amplification of quantum states and noiseless photon amplifiers. *Physics Letters*, 113A(8):405–407, 1986.
- [83] D. Dieks. Overlap and distinguishability of quantum states. *Physics Letters*, 126(5):303–306, 1988.
- [84] G. M. D’Ariano and H. P. Yuen. Impossibility of Measuring the Wave Function of a Single Quantum System. *Physical Review Letters*, 76(16):2832–2835, 1996.
- [85] H. Barnum, C. M. Caves, C. A. Fuchs, R. Jozsa, and B. Schumacher. Noncommuting Mixed States Cannot Be Broadcast. *Physical Review Letters*, 76(15):2818–2821, 1996.
- [86] L.-M. Duan and G.-C. Guo. Probabilistic Cloning and Identification of Linearly Independent Quantum States. *Physical Review Letters*, 80(22):4999–5002, 1998.
- [87] V. Scarani, S. Iblisdir, and N. Gisin. Quantum cloning. *Reviews of Modern Physics*, 77:1225–1256, 2005.
- [88] C. Simon, G. Weihs, and A. Zeilinger. Optimal Quantum Cloning via Stimulated Emission. *Physical Review Letters*, 84(13), 2000.
- [89] M. Barbieri, F. Ferreyrol, R. Blandino, R. Tualle-Brouri, and P. Grangier. Nondeterministic noiseless amplification of optical signals: a review of recent experiments. *Laser Physics Letters*, 8(6):411–417, 2011.
- [90] V. Parigi, A. Zavatta, M. Kim, and M. Bellini. Probing Quantum Commutation Rules by Addition and Subtraction of Single Photons to/from a Light Field. *Science*, 317:1890–1893, 2007.
- [91] A. Zavatta, V. Parigi, M. S. Kim, H. Jeong, and M. Bellini. Experimental Demonstration of the Bosonic Commutation Relation via Superpositions of Quantum Operations on Thermal Light Fields. *Physical Review Letters*, 103:140406, 2009.
- [92] D. T. Pegg, L. S. Philips, and S. M. Barnett. Optical state truncation by projection synthesis. *Physical Review Letters*, 81:1604–1606, 1998.
- [93] F. Ferreyrol, R. Blandino, M. Barbieri, R. Tualle-Brouri, and P. Grangier. Experimental realization of a nondeterministic optical noiseless amplifier. *Physical Review A*, 83:063801, 2011.

- [94] N. Bruno, V. Pini, A. Martin, and R. T. Thew. A complete characterization of the heralded noiseless amplification of photons. *New Journal of Physics*, 15:093002, 2013.
- [95] K. J. Resch, J. S. Lundeen, and A. M. Steinberg. Quantum State Preparation and Conditional Coherence. *Physical Review Letters*, 88(11):113601, 2002.
- [96] S. J. van Enk. $|0\rangle|1\rangle + |1\rangle|0\rangle$, 2005. arXiv:quant-ph/0507189v4.
- [97] H. M. Wiseman and J. A. Vaccaro. Entanglement of Indistinguishable Particles Shared between Two Parties. *Physical Review Letters*, 91(9):097902, 2003.
- [98] Y. Aharonov and L. Vaidman. Nonlocal aspects of a quantum wave. *Physical Review A*, 61:052108, 2000.
- [99] S. A. Babichev, J. Ries, and A. I. Lvovsky. Quantum scissors: Teleportation of single-mode optical states by means of a nonlocal single photon. *Europhysics Letters*, 64:1–7, 2003.
- [100] C. J. Villas-Bôas, N. G. de Almeida, and M. H. Y. Moussa. Teleportation of a zero- and one-photon running-wave state by projection synthesis. *Physical Review A*, 60:2759–2763, 1999.
- [101] M. Koniorczyk, Z. Kurucz, A. Gábris, and J. Janszky. General optical state truncation and its teleportation. *Physical Review A*, 62:013802, 2000.
- [102] Ş. K. Özdemir, A. Miranowicz, M. Koashi, and N. Imoto. Quantum scissors device for optical state truncation: A proposal for practical realization. *Physical Review A*, 64:063818, 2001.
- [103] Ş. K. Özdemir, A. Miranowicz, M. Koashi, and N. Imoto. Pulse-mode quantum projection synthesis: Effects of mode mismatch on optical state truncation and preparation. *Physical Review A*, 66(053809), 2002.
- [104] T. C. Ralph and A. P. Lund. Nondeterministic noiseless linear amplification of quantum systems. In A. I. Lvovsky, editor, *Proceedings of the 9th International Conference on Quantum Communication Measurement and Computing*, pages 155–160. AIP, 2009.
- [105] Y.-H. Kim, Y. Yu, S. P. Kulik, Y. Shih, and M. O. Scully. Delayed “Choice” Quantum Eraser. *Physical Review Letters*, 84:1–5, 2000.
- [106] D. W. Berry and A. I. Lvovsky. Preservation of loss in linear-optical processing. *Physical Review A*, 84:042304, 2011.

- [107] M. D. Eisaman, J. Fan, A. Migdall, and S. V. Polyakov. Invited Review Article: Single-photon sources and detectors. *Review of Scientific Instruments*, 82:071101, 2011.
- [108] M. Tanida, R. Okamoto, and S. Takeuchi. Highly indistinguishable heralded single-photon sources using parametric down conversion. *Optics Express*, 20(14):15275–15285, 2012.
- [109] M. Da Cunha Pereira, F. E. Becerra, B. L. Glebov, J. Fan, S. W. Nam, and A. Migdall. Demonstrating highly symmetric single-mode, single-photon heralding efficiency in spontaneous parametric downconversion. *Optics Letters*, 38(10):1609–1611, 2013.
- [110] G. Harder *et al.* An optimized photon pair source for quantum circuits. *Optics Express*, 21(12):13975–13985, 2013.
- [111] J. B. Spring *et al.* On-chip low loss heralded source of pure single photons. *Optics Express*, 21(11):13522–13532, 2013.
- [112] U. L. Andersen and T. C. Ralph. High-Fidelity Teleportation of Continuous-Variable Quantum States Using Delocalized Single Photons. *Physical Review Letters*, 111:050504, 2013.
- [113] J. Minář, H. de Riedmatten, and N. Sangouard. Quantum repeaters based on heralded qubit amplifiers. *Physical Review A*, 85:032313, 2012.
- [114] R. Blandino, A. Leverrier, M. Barbieri, J. Etesse, P. Grangier, and R. Tualle-Broui. Improving the maximum transmission distance of continuous-variable quantum key distribution using a noiseless amplifier. *Physical Review A*, 86:2012, 2012.
- [115] H. J. Kimble. The quantum internet. *Nature*, 453:1023–1030, 2008.
- [116] N. Sangouard, C. Simon, H. de Riedmatten, and N. Gisin. Quantum repeaters based on atomic ensembles and linear optics. *Rev. Mod. Phys.*, 83:33–80, Mar 2011.
- [117] S. Ritter *et al.* An elementary quantum network of single atoms in optical cavities. *Nature*, 484:195–201, 2012.
- [118] J. Hofmann *et al.* Heralded Entanglement Between Widely Separated Atoms. *Science*, 337(6090):72–75, 2012.

- [119] M. Riebe *et al.* Deterministic quantum teleportation with atoms. *Nature*, 429:734–737, 2004.
- [120] M. D. Barrett *et al.* Deterministic quantum teleportation of atomic qubits. *Nature*, 429:737–739, 2004.
- [121] J. F. Sherson *et al.* Quantum teleportation between light and matter. *Nature*, 443:557–560, 2006.
- [122] L. Steffen *et al.* Deterministic quantum teleportation with feed-forward in a solid state system. *Nature*, 500:319–322, 2013.
- [123] L.-M. Duan, M. D. Lukin, J. I. Cirac, and P. Zoller. Long-distance quantum communication with atomic ensembles and linear optics. *Nature*, 414:413–418, 2001.
- [124] D. Salart, A. Baas, C. Branciard, N. Gisin, and H. Zbinden. Testing the speed of ‘spooky action at a distance’. *Nature*, 454:861–864, 2008.
- [125] D. Salart, A. Baas, J. A. W. van Houwelingen, N. Gisin, and H. Zbinden. Spacelike Separation in a Bell Test Assuming Gravitationally Induced Collapse. *Physical Review Letters*, 100:220404, 2008.
- [126] A. Cuevas *et al.* Long-distance distribution of genuine energy-time entanglement. *Nature Communications*, 4(2871):1–6, 2013.
- [127] C. Simon and W. T. M. Irvine. Robust Long-Distance Entanglement and a Loophole-Free Bell Test with Ions and Photons. *Physical Review Letters*, 91(11):110405, 2003.
- [128] B. Fröhlich *et al.* A quantum access network. *Nature*, 501:69–73, 2013.
- [129] A. Broadbent, J. F. Fitzsimmons, and E. Kashefi. Universal blind quantum computation. In *Proceedings of the 50th Annual IEEE Symposium on Foundations of Computer Science*, pages 517–527, Los Alamitos, USA, 2009. IEEE Computer Society.
- [130] S. Barz, E. Kashefi, A. Broadbent, J. F. Fitzsimmons, A. Zeilinger, and P. Walther. Demonstration of Blind Quantum Computing. *Science*, 335(6066):303–308, 2012.
- [131] H.-J. Briegel, W. Dür, J. I. Cirac, and P. Zoller. Quantum repeaters: The role of imperfect local operations in quantum communication. *Physical Review Letters*, 81(26):5932–5935, 1998.

-
- [132] J. Simon, H. Tanji, J. K. Thompson, and V. Vuletić. Interfacing Collective Atomic Excitations and Single Photons. *Physical Review Letters*, 98:183601, 2007.
- [133] N. Sangouard *et al.* Robust and efficient quantum repeaters with atomic ensembles and linear optics. *Physical Review A*, 77(062301), 2008.
- [134] M. Lobino, C. Kupchak, E. Figueroa, and A. I. Lvovsky. Memory for Light as a Quantum Process. *Physical Review Letters*, 102(203601), 2009.
- [135] P. W. Shor. Scheme for reducing decoherence in quantum computer memory. *Physical Review A*, 52(R2493), 1995.
- [136] A. M. Steane. Error correcting codes in quantum theory. *Physical Review Letters*, 77:793, 1996.
- [137] T. Aoki *et al.* Quantum error correction beyond qubits. *Nature Physics*, 5(541), 2009.
- [138] M. Lassen *et al.* Quantum optical coherence can survive photon losses using a continuous-variable quantum erasure-correcting code. *Nature Photonics*, 4(700), 2010.
- [139] T. Yamamoto, K. Hayashi, Ş. K. Özdemir, M. Koashi, and N. Imoto. Robust photonic entanglement distribution by state-independent encoding onto decoherence-free subspace. *Nature Photonics*, 2:488–491, 2008.
- [140] R. Ikuta, Y. Ono, T. Tashima, T. Yamamoto, M. Koashi, and N. Imoto. Efficient Decoherence-Free Entanglement Distribution over Lossy Quantum Channels. *Physical Review Letters*, 106:110503, 2011.
- [141] T. B. Pittman, B. C. Jacobs, and J. D. Franson. Demonstration of quantum error correction using linear optics. *Physical Review A*, 71(052332), 2005.
- [142] C. C. Gerry. Nonlocality of a single photon in cavity QED. *Physical Review A*, 53(6):4583–4585, 1996.
- [143] C. H. Bennett, H. J. Bernstein, S. Popescu, and B. Schumacher. Concentrating partial entanglement by local operations. *Physical Review A*, 53(4):2046–2052, 1996.
- [144] A. P. Lund, T. C. Ralph, and H. L. Haselgrove. Fault-Tolerant Linear Optical Quantum Computing with Small-Amplitude Coherent States. *Physical Review Letters*, 100:030503, 2008.

- [145] A. P. Lund and T. C. Ralph. Nondeterministic gates for photonic single-rail quantum logic. *Physical Review A*, 66:032307, 2002.
- [146] E. Lombardi, F. Sciarrino, S. Popescu, and F. De Martini. Teleportation of a Vacuum-One-Photon Qubit. *Physical Review Letters*, 88(7):070402, 2002.
- [147] S. J. Jones and H. M. Wiseman. Nonlocality of a single photon: Paths to an Einstein-Podolsky-Rosen-steering experiment. *Physical Review A*, 84:012110, 2011.
- [148] P. Kok, W. J. Munro, K. Nemoto, T. C. Ralph, J. P. Dowling, and G. J. Milburn. Linear optical quantum computing with photonic qubits. *Reviews of Modern Physics*, 79:135–174, 2007.
- [149] R. Horodecki, P. Horodecki, M. Horodecki, and K. Horodecki. Quantum entanglement. *Reviews of Modern Physics*, 81:865–942, 2009.
- [150] C. H. Bennett, D. D. DiVincenzo, J. A. Smolin, and W. K. Wootters. Mixed-state entanglement and quantum error correction. *Physical Review A*, 54(6):3824–3851, 1996.
- [151] M. Horodecki, P. Horodecki, and R. Horodecki. Limits of Entanglement Measures. *Physical Review Letters*, 84(9):2014–2017, 2000.
- [152] W. K. Wootters. Entanglement of Formation of an Arbitrary State of Two Qubits. *Physical Review Letters*, 80(10):2245–2248, 1998.
- [153] C. W. Chou, H. de Riedmatten, D. Felinto, S. V. Polyakov, S. J. van Enk, and H. J. Kimble. Measurement-induced entanglement for excitation stored in remote atomic ensembles. *Nature*, 438:828–832, 2005.
- [154] L. Vaidman. Teleportation of quantum states. *Physical Review A*, 49:1473–1476, 1994.
- [155] A. Furusawa *et al.* Unconditional Quantum Teleportation. *Science*, 282(5389):706–709, 1998.
- [156] V. Vedral. *Introduction to Quantum Information Science*. Oxford University Press, First edition, 2006.
- [157] K. S. Choi, H. Deng, J. Laurat, and H. J. Kimble. Mapping photonic entanglement into and out of a quantum memory. *Nature*, 452:67–72, 2008.
- [158] D. Gottesman, T. Jennewein, and S. Croke. Longer-Baseline Telescopes Using Quantum Repeaters. *Physical Review Letters*, 109:070503, 2012.

- [159] C. Branciard, E. G. Cavalcanti, S. P. Walborn, V. Scarani, and H. M. Wiseman. One-sided device-independent quantum key distribution: Security, feasibility, and the connection with steering. *Physical Review A*, 85:010301, 2012.
- [160] H. M. Wiseman, S. J. Jones, and A. C. Doherty. Steering, Entanglement, Nonlocality, and the Einstein-Podolsky-Rosen Paradox. *Physical Review Letters*, 98:140402, 2007.
- [161] S. J. Jones, H. M. Wiseman, and A. C. Doherty. Entanglement, Einstein-Podolsky-Rosen correlations, Bell nonlocality, and steering. *Physical Review A*, 76:052116, 2007.
- [162] E. G. Cavalcanti, S. J. Jones, H. M. Wiseman, and M. D. Reid. Experimental criteria for steering and the Einstein-Podolsky-Rosen paradox. *Physical Review A*, 80(032112), 2009.
- [163] J. F. Fitzsimons, E. G. Rieffel, and V. Scarani. The Quantum Frontier. arXiv:1206.0785, 2013.
- [164] D. Bohm. *Quantum Theory*. Prentice-Hall, New York, 1951.
- [165] E. Schrödinger. Discussion of probability relations between separated systems. *Proceedings of the Cambridge Philosophical Society*, 31:555–563, 1935.
- [166] E. Schrödinger. Die gegenwärtige Situation in der Quantenmechanik (The present situation in quantum mechanics). *Naturwissenschaften*, 23:807, 1935.
- [167] J. von Neumann. *Mathematische Grundlagen der Quantenmechanik (Mathematical foundations of quantum mechanics)*. Springer, Berlin, 1955.
- [168] M. D. Reid *et al.* Colloquium: The Einstein-Podolsky-Rosen paradox: From concepts to applications. *Reviews of Modern Physics*, 81:1727–1751, 2009.
- [169] D. Bohm. A Suggested Interpretation of the Quantum Theory in Terms of “Hidden” Variables. I. *Physical Review*, 85:166–179, 1952.
- [170] D. Bohm. A Suggested Interpretation of the Quantum Theory in Terms of “Hidden” Variables. II. *Physical Review*, 85:180–193, 1952.
- [171] H. Everett. “Relative State” Formulation of Quantum Mechanics. *Rev. Mod. Phys.*, 29:454–462, 1957.
- [172] N. D. Mermin. Hidden variables and the two theorems of John Bell. *Reviews of Modern Physics*, 65(3):803–815, 1993.

- [173] J. F. Clauser, M. A. Horne, A. Shimony, and R. A. Holt. Proposed Experiment to Test Local Hidden-Variable Theories. *Physical Review Letters*, 23(15):880–884, 1969.
- [174] S. Kochen and E. P. Specker. The problem of hidden variables in quantum mechanics. *Journal of Mathematics and Mechanics*, 17:59–87, 1967.
- [175] R. F. Werner. Quantum states with Einstein-Podolsky-Rosen correlations admitting a hidden-variable model. *Physical Review A*, 40(8):4277–4281, 1989.
- [176] Z. Y. Ou, S. F. Pereira, H. J. Kimble, and K. C. Peng. Realization of the Einstein-Podolsky-Rosen paradox for continuous variables. *Physical Review Letters*, 68:3663–3666, 1992.
- [177] J. Hald, J. L. Sørensen, C. Schori, and E. S. Polzik. Spin Squeezed Atoms: A Macroscopic Entanglement Ensemble Created by Light. *Physical Review Letters*, 83:1319–1322, 1999.
- [178] W. P. Bowen, R. Schnabel, P. K. Lam, and T. C. Ralph. Experimental Investigation of Criteria for Continuous Variable Entanglement. *Physical Review Letters*, 90:043601, 2003.
- [179] J. C. Howell, R. S. Bennink, S. J. Bentley, and R. W. Boyd. Realization of the Einstein-Podolsky-Rosen Paradox Using Momentum- and Position-Entangled Photons from Spontaneous Parametric Down Conversion. *Physical Review Letters*, 92:210403, 2004.
- [180] D. J. Saunders, S. J. Jones, H. M. Wiseman, and G. J. Pryde. Experimental EPR-steering using Bell-local states. *Nature Physics*, 6:845–849, 2010.
- [181] I. Gerhardt *et al.* Full-field implementation of a perfect eavesdropper on a quantum cryptography system. *Nature Communications*, 2(349), 2011.
- [182] L. Lydersen *et al.* Hacking commercial quantum cryptography systems by tailored bright illumination. *Nature Photonics*, 4:686–689, 2010.
- [183] F. Buscemi. All Entangled Quantum States Are Nonlocal. *Physical Review Letters*, 108:200401, 2012.
- [184] E. G. Cavalcanti, M. J. W. Hall, and H. M. Wiseman. Entanglement verification and steering when Alice and Bob cannot be trusted. *Physical Review A*, 87:032306, 2013.

- [185] C. Branciard, D. Rosset, Y.-C. Liang, and N. Gisin. Measurement-Device-Independent Entanglement Witness for All Entangled Quantum States. *Physical Review Letters*, 110:060405, 2013.
- [186] S. Kocsis, A. J. Bennet, M. J. W. Hall, and G. J. Pryde. Quantum refereed steering for enhanced security. *Manuscript in preparation*, 2014.
- [187] D. Rosset, C. Branciard, N. Gisin, and Y.-C. Liang. Entangled states cannot be classically simulated in generalized Bell experiments with quantum inputs. *New Journal of Physics*, 15:053025, 2013.
- [188] A. Acín, N. Gisin, and B. Toner. Rothendieck’s constant and local models for noisy entangled quantum states. *Physical Review A*, 73:062105, 2006.
- [189] P. G. Kwiat, E. Waks, A. G. White, I. Appelbaum, and P. H. Eberhard. Ultrabright source of polarization-entangled photons. *Physical Review A*, 60(2):773–776, 1999.
- [190] J. Calsamiglia and N. Lütkenhaus. Maximum efficiency of a linear-optical Bell-state analyzer. *Applied Physics B: Lasers and Optics*, 72:67–71, 2001.
- [191] G. Puentes, D. Voigt, A. Aiello, and J. P. Woerdman. Tunable spatial decoherers for polarization-entangled photons. *Optics Letters*, 31(13):2057–2059, 2006.
- [192] M. Barbieri, F. De Martini, G. Di Nepi, P. Mataloni, G. M. D’Ariano, and C. Macchiavello. Detection of Entanglement with Polarized Photons: Experimental Realization of an Entanglement Witness. *Physical Review Letters*, 91(22):227901, 2003.
- [193] J. Dai, Y. L. Len, Y. S. Teo, L. A. Krivitsky, and B.-G. Englert. Controllable generation of mixed two-photon states. *New Journal of Physics*, 15:063011, 2013.
- [194] M. Tomamichel and R. Renner. Uncertainty Relations for Smooth Entropies. *Physical Review Letters*, 106:110506, 2011.
- [195] M. Tomamichel, C. C. W. Lim, N. Gisin, and R. Renner. Tight finite-key analysis for quantum cryptography. *Nature Communications*, 3(634), 2012.
- [196] L. Masanes, S. Pironio, and A. Acín. Secure device-independent quantum key distribution with causally independent measurement devices. *Nature Communications*, 2(238), 2011.

-
- [197] X.-S. Ma *et al.* Quantum teleportation over 143 kilometers using active feed-forward. *Nature*, 489:269–273, 2012.
- [198] Z. Zhang, M. Tengner, T. Zhong, F. N. C. Wong, and J. H. Shapiro. Entanglement’s Benefit Survives an Entanglement-Breaking Channel. *Physical Review Letters*, 111:010501, 2013.
- [199] A. Samblowski. *State Preparation for Quantum Information Science and Metrology*. PhD thesis, Leibniz Universität Hannover, 2013.
- [200] P. Kumar. Quantum frequency conversion. *Optics Letters*, 15(24):1476–1478, 1990.
- [201] C. M. Caves. Quantum mechanical noise in an interferometer. *Physical Review D*, 23(8):1693–1708, 1981.
- [202] R. Schnabel, N. Mavalvala, D. E. McClelland, and P. K. Lam. Quantum metrology for gravitational wave astronomy. *Nature Communications*, 1(121), 2010.
- [203] The LIGO Scientific Collaboration and The Virgo Collaboration. An upper limit on the stochastic gravitational-wave background of cosmological origin. *Nature*, 490:990–994, 2009.
- [204] K. Arai *et al.* Status of Japanese gravitational wave detectors. *Classical and Quantum Gravity*, 26:204020, 2009.
- [205] H. Vahlbruch, A. Khalaidovski, N. Lastzka, C. Gräf, K. Danzmann, and R. Schnabel. The GEO 600 squeezed light source. *Classical and Quantum Gravity*, 27(084027), 2010.
- [206] N. K. Langford, S. Ramelow, R. Prevedel, W. J. Munro, G. J. Milburn, and A. Zeilinger. Efficient quantum computing using coherent photon conversion. *Nature*, 478:360–363, 2011.
- [207] M. Pysher, Y. Miwa, R. Shahrokhshani, R. Bloomer, and O. Pfister. Parallel Generation of Quadripartite Cluster Entanglement in the Optical Frequency Comb. *Physical Review Letters*, 107:030505, 2011.
- [208] N. C. Menicucci, S. T. Flammia, and O. Pfister. One-Way Quantum Computing in the Optical Frequency Comb. *Physical Review Letters*, 97:110501, 2006.

- [209] M. P. Hedges, J. J. Longdell, Y. Li, and M. J. Sellars. Efficient quantum memory of light. *Nature*, 465:1052–1056, 2010.
- [210] G. Heinze, C. Hubrich, and T. Halfmann. Stopped light and image storage by electromagnetically induced transparency up to the regime of one minute. *Physical Review Letters*, 111:033601, Jul 2013.
- [211] C. Clausen *et al.* Quantum storage of photonic entanglement in a crystal. *Nature*, 469:508–511, 2011.
- [212] E. Saglamyurek *et al.* Broadband waveguide quantum memory for entangled photons. *Nature*, 469:512–515, 2011.
- [213] M. Hosseini, G. Campbell, B. M. Sparkes, P. K. Lam, and B. C. Buchler. Unconditional room-temperature quantum memory. *Nature Physics*, 7:794–798, 2011.
- [214] K. Jensen *et al.* Quantum memory for entangled continuous-variable states. *Nature Physics*, 7:13–16, 2011.
- [215] C. Simon *et al.* Quantum memories. *The European Physical Journal D*, 58:1–22, 2010.
- [216] A. I. Lvovsky, B. C. Sanders, and W. Tittel. Optical quantum memory. *Nature Photonics*, 3:706–714, 2009.
- [217] W. H. P. Pernice *et al.* High-speed and high-efficiency travelling wave single-photon detectors embedded in nanophotonic circuits. *Nature Communications*, 3:1–10, 2012.
- [218] F. Marsili *et al.* Detecting single infrared photons with 93% system efficiency. *Nature Photonics*, 7:210–214, 2013.
- [219] A. G. Radnaev *et al.* A quantum memory with telecom-wavelength conversion. *Nature Physics*, 6:894, 2010.
- [220] J. S. Pelc, Q. Zhang, C. R. Phillips, Y. Yamamoto, and M. M. Fejer. Cascaded frequency upconversion for high-speed single-photon detection at 1550 nm. *Optics Letters*, 37(4):476, 2012.
- [221] J.-P. Bourgoin *et al.* A comprehensive design and performance analysis of low earth orbit satellite quantum communication. *New Journal of Physics*, 15(2):023006, 2013.

- [222] D. Rideout *et al.* Fundamental quantum optics experiments conceivable with satellites—reaching relativistic distances and velocities. *Classical and Quantum Gravity*, 29(22):224011, 2012.
- [223] C. E. Vollmer. *Non-Classical State Engineering for Quantum Networks*. PhD thesis, Leibniz Universität Hannover, 2013.
- [224] P. van Loock. Optical hybrid approaches to quantum information. *Laser & Photonics Reviews*, 5(2):167–200, 2011.
- [225] S. Takeda, T. Mizuta, M. Fuwa, P. van Loock, and A. Furusawa. Deterministic quantum teleportation of photonic quantum bits by a hybrid technique. *Nature*, 500:315–318, 2013.
- [226] D. F. Walls and G. J. Milburn. *Quantum Optics*. Springer-Verlag, Second edition, 2004.
- [227] C. Fabre, E. Giacobino, A. Heidmann, and S. Reynaud. Noise characteristics of a non-degenerate Optical Parametric Oscillator—Application to quantum noise reduction. *Journal de Physique*, 50:1209–1225, 1989.
- [228] H.-A. Bachor and T. C. Ralph. *A Guide to Experiments in Quantum Optics*. Wiley-VCH, Second edition, 1994.
- [229] A. Sambrowski, C. E. Laukötter, N. Grosse, P. K. Lam, and R. Schnabel. Two Color Entanglement. In *AIP Conference Proceedings*, volume 1363, pages 219–222. American Institute of Physics, 2011.
- [230] E. D. Black. An introduction to Pound-Drever-Hall laser frequency stabilization. *American Journal of Physics*, 69(1):79–87, 2000.
- [231] N. Lastzka. *Numerical Modelling of Classical and Quantum Effects in Non-linear Optical Systems*. PhD thesis, Leibniz Universität Hannover, 2010.
- [232] L.-M. Duan, G. Giedke, J. I. Cirac, and P. Zoller. Inseparability Criterion for Continuous Variable Systems. *Physical Review Letters*, 84:2722, 2000.
- [233] S. Tanzilli *et al.* A photonic quantum information interface. *Nature*, 437:116–120, 2005.
- [234] A. Bérut, A. Arakelyan, A. Petrosyan, S. Ciliberto, R. Dillenschneider, and E. Lutz. Experimental verification of landauer’s principle linking information and thermodynamics. *Nature*, 483:187–190, 2012.

- [235] S. Toyabe, T. Sagawa, M. Ueda, E. Muneyuki, and M. Sano. Experimental demonstration of information-to-energy conversion and validation of the generalized Jarzynski equality. *Nature Physics*, 6:988–992, 2012.
- [236] V. Serreli, C.-F. Lee, E. R. Kay, and D. A. Leigh. A molecular information ratchet. *Nature*, 445:523–527, 2007.
- [237] C.-Y. Lu, D. E. Browne, T. Yang, and J.-W. Pan. Demonstration of a Compiled Version of Shor’s Quantum Factoring Algorithm Using Photonic Qubits. *Physical Review Letters*, 99:250504, 2007.
- [238] B. P. Lanyon *et al.* Experimental Demonstration of a Compiled Version of Shor’s Algorithm with Quantum Entanglement. *Physical Review Letters*, 99:250505, 2007.
- [239] A. Politi, J. C. F. Matthews, and J. L. O’Brien. Shor’s Quantum Factoring Algorithm on a Photonic Chip. *Science*, 325(5945):1221, 2009.
- [240] E. Lucero *et al.* Computing prime factors with a Josephson phase qubit quantum processor. *Nature Physics*, 8:719–723, 2012.
- [241] B. P. Lanyon *et al.* Towards quantum chemistry on a quantum computer. *Nature Chemistry*, 2:106–111, 2010.
- [242] B. P. Lanyon *et al.* Universal Digital Quantum Simulation with Trapped Ions. *Science*, 334(6052):57–61, 2011.
- [243] D. Gottesman and I. L. Chuang. Demonstrating the viability of universal quantum computation using teleportation and single-qubit operations. *Nature*, 402:390–393, 1999.
- [244] R. Raussendorf and H. J. Briegel. A One-Way Quantum Computer. *Physical Review Letters*, 86:5188–5191, 2001.
- [245] N. Lee *et al.* Teleportation of Nonclassical Wave Packets of Light. *Science*, 332:330–333, 2011.
- [246] J. Lavoie, Y. M. Donohue, L. G. Wright, A. Fedrizzi, and K. J. Resch. Spectral compression of single photons. *Nature Photonics*, 7:363–366, 2013.